Novel Capabilities for Gas-Phase Laser-Induced Gratings



Priyav Shah
Jesus College
University of Oxford

A thesis submitted in partial fulfilment of the requirements for the degree of Doctor of Philosophy

Trinity 2021

To my mother, who passed before I embarked on this journey;

and my father, who departed before its conclusion.

Acknowledgements

This dissertation is the culmination of a journey that I would not have been able to navigate without the guidance and support of numerous people. The list of names is endless, but I would like to take this opportunity to name a few. Firstly, I would like to thank Dr Ben Williams for giving me the opportunity to pursue a DPhil, and showing unwavering faith in my ability to succeed in the face of adversity. I also extend my gratitude to Professor Paul Ewart for allowing me the use of his laboratory and equipment while I was 'lableless' and Professor Richard Stone for taking me under his wing at the beginning of my DPhil.

I am fortunate to have worked with, and alongside, such a talented group of individuals. I would like to thank Dr Francesca De Dominco for being an excellent collaborator for part of the work presented in Chapter 3 of this thesis. I am also grateful to the members of the Thermal Propulsion Systems Research Group, who have been a pleasure to work with. In particular, my thanks to Dr Chris Willman and Dr Laurent Le Page for being ever-present to offer guidance and assistance, and Li Shen for his friendship and enthusiasm. To Hannah Rana, Kharthik Chakravarthy and Maruthi Malladi: it was an honour to navigate the trials and tribulations of research alongside you (not to mention a pandemic and so many other things). It is impossible to overstate the positive impact you have each had on me, and the number of times your friendship, support and work have astounded me.

I have also been extremely lucky to meet many incredible people along this journey. Santiago and Peter, thank you for the endless memories from Kame House, the crazy Booch experiments, the Terraforming and for overall being the best lockdown mates I could have asked for. To Caro for being my right-hand and always turning up (late); Tanaya for being the life of the party and a pillar of support; Wouter for being a true planner and a great friend (even through rainy hikes); Arjun for the great parties, football, cricket, Hi-Lo and not Hawaii Five-0; Sandy, Hank and Maxwell for keeping me sane and the many remarkable friends I've made through the Jesus College MCR.

Thanks also to Anna, Doug, Kiran, Ollie and Susan for the adventures and memories over the years; I look forward to future exploits. To Mike, Rishi and Shrey for always keeping me entertained; and to Suraj and Sangeet for your friendship since the very beginning.

I owe a debt of gratitude to my brother, Nirav, for *everything*; without him, none of this would have been possible. I would also like to acknowledge Emily for her support, and Aneeta, Jasmine, and Emmanuel for always providing a reason to smile. I am thankful to Ashni and Mihir, who have always been by my side; Manjri and Rajesh, whose kindness knows no bounds; and to the rest of my family, whose support I am truly appreciative of.

Finally, I will be eternally grateful to my parents for doing everything in their power to enable my successes.

Abstract

Laser-Induced Grating Spectroscopy (LIGS) is a non-intrusive optical diagnostic primarily used for temperature measurements in the gas phase. The technique boasts excellent accuracy and precision, achieved at relatively low cost and complexity, compared to similar diagnostics.

A drawback of the technique is its temporal resolution, which has generally been limited to 10 Hz without compromising the accessibility of the technique (through the use of toxic tracer species or expensive lasers). The discovery of a new LIGS tracer species, biacetyl, which enables the use of accessible high repetition rate lasers is presented. Temperature measurements, obtained at a rate of 1 kHz, and the application of the technique to study thermoacoustic instabilities, have been demonstrated.

A significant problem for LIGS is an inherently poor spatial resolution due to an elongated (in the axial direction) measurement region. A novel approach enabling simultaneous 1-D spatially-resolved LIGS measurements in the axial direction is presented. This capability can be incorporated into standard LIGS experiments with a negligible increase in cost or complexity, thus preserving the accessibility of the technique. A computational model for the approach was developed and validated. A preliminary experiment demonstrated a 93 % improvement in axial spatial resolution, as well as a three-fold increase in the number of single-shot measurements obtained, when compared to a standard LIGS configuration.

To exploit the significant advantages of the technique by enhancing its accessibility, a unique transportable LIGS system (named PILOT) was designed, manufactured and characterised. The mobile, self-contained system is capable of collecting tracer-free LIGS measurements at a rate of 400 Hz. An accuracy of <0.37 % and precision of ± 0.7 % was demonstrated for temperature measurements in room air. Characterisation experiments showed that the use of an avalanche photodetector for signal detection would permit the use of the system in scattering environments. A novel systematic investigation of tracer-free LIGS in different gases highlighted the polarisability of a gas as a key indicator for performance of the technique. These findings will inform experimental design for future applications. Finally, the deployment of PILOT in a research facility was demonstrated.

Contents

1 Introduction **1**

1.1 Motivations 1

1.2 Thesis structure 3

2 Background **4**

2.1 Theory of LIGS 4

2.1.1 Laser-Induced Thermal Grating Spectroscopy (LITGS) 4

2.1.2 Laser-Induced Electrostrictive Grating Spectroscopy (LIEGS) 8

2.1.3 Experimental uncertainty considerations 9

2.2 Origins of LIGS 11

2.3 Literature Review 12

2.3.1 Relevant optical diagnostic techniques 12

3 Temporally-Resolved Biacetyl LITGS **21**

3.1 Motivations 21

3.2 Selection of absorbing species and proof-of-concept 22

3.3 Characterising the effect of beam heating 25

3.3.1 Experimental setup 25

3.3.2 Experimental results 27

3.3.3 Theoretical estimate 29

3.3.4 Concentration 33

3.4 Application of biacetyl LITGS to measure entropy spots 36

3.4.1 Experiments using a steady jet 37

3.4.1.1 Characterising the effect of biacetyl concentration 39

3.4.1.2 Temperature measurements 41

3.4.1.3 Characterising LITGS frequency for different gases 42

3.4.1.4 Measuring steady composition variations 44

3.4.1.5 Time-resolved composition variation measurements 46

3.4.2 Time-resolved measurements in an entropy generation duct 48
3.4.2.1 Detection of composition spots 50
3.4.2.2 Detection of temperature spots 53
3.5 Summary 55

4 Axially-resolved LIGS: Theory and Modelling 57
4.1 Motivations 57
4.2 Concept overview 59
4.3 Scheimpflug imaging 62
4.4 Experimental design for characterisation 67
4.5 Computational model 70
4.5.1 LITGS geometry 71
4.5.2 Imaging geometry 72
4.5.3 Generating the signal beam 73
4.5.4 Imaging the signal beam 74
4.5.5 Implementing the detection fibres 76
4.5.5.1 Grating length per fibre 76
4.5.5.2 Grating pitch 77
4.5.6 Simulating the experiment 79
4.5.6.1 Simulating grating intensity variation 79
4.5.6.2 Simulating signal beam generation 81
4.5.6.3 Simulating signal beam intensity variation 82
4.5.6.4 Simulating signal beam detection 86
4.6 Parametric investigation of spatial resolution 88
4.6.1 Varying the angle of the detector plane 89
4.6.1.1 Detector plane coincident to image plane 89
4.6.1.2 Rotating the detector plane about the optical axis 93
4.6.2 Varying the angle of the lens plane 98
4.6.2.1 Detector plane coincident to expected image plane 98
4.6.2.2 Detector plane coincident to adjusted image plane 102

4.6.2.3 Detector plane not coincident with image plane 104
4.6.3 Varying the distance between the grating and the imaging lens . . . 107
4.6.3.1 Detector plane coincident to image plane 107
4.6.3.2 Detector plane not coincident with image plane 109
4.7 Summary 111

5 Axially-resolved LIGS: Experimental validation 113

5.1 Experimental setup 113
5.2 Characterisation of fringe spacing variation 118
5.3 Computational model inputs 120
5.4 Signal beam size 121
5.4.1 Computational Results 121
5.4.2 Experimental Results 123
5.4.3 Discussion 124
5.5 Magnification 124
5.5.1 Computational Results 124
5.5.2 Experimental Results 125
5.5.3 Discussion 125
5.6 Characterisation using 'large' optical fibres 127
5.6.1 Computational Results 127
5.6.2 Experimental results 129
5.6.3 Discussion 131
5.7 Characterisation using 'small' optical fibres 133
5.7.1 Computational Results 133
5.7.2 Experimental results 135
5.7.3 Discussion 137
5.8 Simultaneous axially-resolved LITGS temperature measurements 138
5.8.1 Experimental setup 138
5.8.2 Steady-state temperature measurements with the heater off 142
5.8.3 Steady-state temperature measurements with the heater on 145

5.8.4 Transient temperature measurements as the heater is turned on . . . 151
5.9 Summary . . . 152

6 Development of a transportable LIGS system (PILOT) 155

6.1 Motivations . . . 155
6.2 Design and development . . . 156
6.2.1 Laser selection . . . 156
6.2.2 Laser integration . . . 157
6.2.3 Pump beam optical layout . . . 158
6.2.4 Probe and signal tracing beams optical layouts . . . 160
6.2.5 Alignment optics . . . 160
6.2.6 Mechanical considerations and peripherals . . . 163
6.3 Optimising and characterising the PILOT system . . . 164
6.3.1 Delay line . . . 164
6.3.1.1 Experimental setup . . . 164
6.3.1.2 Results and discussion . . . 166
6.3.2 Scaling probe/pump beam power/energy . . . 167
6.3.2.1 Experimental setup . . . 167
6.3.2.2 Results and discussion . . . 169
6.3.3 Spatial resolution . . . 170
6.3.3.1 Experimental setup . . . 171
6.3.3.2 Results and discussion . . . 174
6.3.4 Temperature measurement comparison with thermocouples . . . 177
6.3.4.1 Experimental setup . . . 177
6.3.4.2 Steady-state temperature measurement . . . 179
6.3.4.3 Impulse temperature measurements . . . 180
6.4 Practical and environmental considerations . . . 183
6.4.1 Window damage thresholds . . . 183
6.4.1.1 Experimental setup . . . 184
6.4.1.2 Results . . . 187

6.4.1.3 Discussion . . . 189
6.4.2 Measurements in scattering environments . . . 190
6.4.2.1 Experimental setup . . . 191
6.4.2.2 Results . . . 194
6.4.2.3 Discussion . . . 202
6.4.3 Characterising different gases for use with LIEGS . . . 203
6.4.3.1 Experimental setup . . . 204
6.4.3.2 Results . . . 206
6.5 Applying PILOT in research facilities . . . 209
6.5.1 Imperial College London wind tunnel . . . 209
6.5.1.1 Experimental setup . . . 210
6.5.1.2 Results . . . 213
6.5.2 Future applications . . . 214
6.6 Summary . . . 215

7 Conclusions **218**
7.1 Temporally-Resolved Biacetyl LITGS . . . 218
7.2 Axially-Resolved LIGS . . . 219
7.3 Development of PILOT system . . . 221

8 Future Prospects **224**

Bibliography **226**

A Validation of axially-resolved LITGS experimental design **240**

1 Introduction

The research presented in this thesis describes the development and demonstration of novel capabilities for gas-phase laser-induced gratings. The particular application of these gratings, via an optical diagnostic technique known as Laser-Induced Grating Spectroscopy (LIGS), for gas-phase measurements is considered.

This chapter first investigates the motivations behind the use of optical diagnostic methods. Next, the objectives of the work reported here are stated and the structure of the thesis is explained.

1.1 Motivations

The scientific method is widely accepted as being fundamental to further our civilisation's understanding of the natural world and push forward our technological development. A key component of this method is the ability to physically measure phenomena to either discover connections or demonstrate (validate) theories [1]. These measurements must be made in a manner that will not inherently affect and change the characteristic being investigated.

Optical diagnostic techniques are an excellent choice for such measurements due to their ability to non-intrusively interrogate processes and environments. A wide range of versatile techniques now play important roles in a variety of applications. For example, the ability to optically detect molecular species has been widely exploited in the biomedical field to characterise cellular processes and detect viral agents, bacterial pathogens and various types of cancer [2]. Additionally, *in situ* species identification by optical diagnostics has found applications in the thin film industry which is essential to the success of, among other things, the microelectronics industry [3]. Optical temperature and pressure measurements have played a vital role in improving the efficiency and cleanliness of combustion processes [4]. The particular importance of this research to internal combustion engine design, due to the effect of emissions on climate change, has come to the forefront in recent times with governments pledging to take action through treaties such as The Paris Agreement [5]. Similar measurements have also been used to optimise alternative energy systems such as fuel

cells [6]. The ability to optically obtain spatially- and temporally-resolved temperature and pressure measurements in high-speed non-reacting flows [7] has been important for designing technologies such as space vehicles. In subsonic flows, similar measurements have been beneficial for applications such as metal foam design which is used in fields ranging from cryogenics to cladding design for buildings [8]. Furthermore, optical velocimetry measurements have been employed in far-reaching applications such as characterising the air flow within buildings [9]. Optical diagnostic methods have also been used to characterise sprays which are encountered in a huge range of applications from cosmetics to agriculture [10].

The work presented in this thesis focuses on developing novel capabilities for an optical diagnostic technique called Laser-Induced Grating Spectroscopy (LIGS). This diagnostic has primarily been used to obtain point temperature [11] and pressure [12] measurements in gases, but has also been successfully employed for species detection [13] and velocimetry [14] measurements. The objectives of the research discussed here were to:

- Enhance the temporal resolution (rate at which measurements are obtained) of the technique while retaining its relatively low cost and practical applicability.
- Improve the spatial resolution (size of the region measured) of the technique while retaining its relatively low complexity.
- Increase the dimension of the technique (from single point to one-dimensional measurements).
- Further the accessibility of the technique by developing a self-contained, mobile device to be deployed in previously impracticable applications.

1.2 Thesis structure

Section 1.1 set out the motivations for the use of optical diagnostic techniques in a variety of applications. The objectives of this thesis, in developing novel capabilities for an optical diagnostic technique known as Laser-Induced Grating Spectroscopy (LIGS), were also introduced.

Having explored the practical relevance of optical diagnostic techniques, and introduced LIGS as the focus of the work presented in this thesis, the first part of Chapter 2 provides a detailed explanation of how the technique works. A contextual overview of the origins of LIGS is also provided. Following this, the relevance of the technique in comparison to alternative optical diagnostics is explored. The unique advantages of LIGS are identified, as are the key drawbacks that the work presented in subsequent chapters addresses.

Chapter 3 details the novel use of biacetyl as a tracer species for LIGS, which enables the practical use of accessible high-repetition lasers for enhanced temporal resolution. The technique is demonstrated and characterised before being successfully applied in a research facility to characterise the evolution of so-called 'entropy spots'.

Next, the concept behind axially-resolved LIGS (which enables simultaneous, spatially-resolved measurements in the axial direction) is introduced in Chapter 4. The chapter considers the use of concepts from 'Scheimpflug imaging', and describes the development of a computational model of the technique. The model is then employed to perform a parametric study of the technique.

Following on from the development of the model, Chapter 5 describes experiments that were conducted to validate and further refine it. The results from two additional experiments that demonstrate the practical application of the technique are also presented.

Chapter 6 describes the design of a transportable LIGS system (named 'PILOT'). Experiments to characterise and optimise PILOT are presented, before its performance in select practical applications is considered. Finally, its successful deployment in a research facility is presented.

Conclusions from the work presented in this thesis are drawn in Chapter 7, before suggestions for future work are discussed in Chapter 8.

2 Background

Chapter 1 set out the motivations for the use of optical diagnostic techniques, and explained how this thesis is concerned with the development of novel capabilities for Laser-Induced Grating Spectroscopy (LIGS). This chapter first delves into the theory behind this technique and provides a high-level overview of its origins. Following this, existing literature is reviewed to compare LIGS with other relevant optical diagnostic techniques. The advantages of LIGS are identified, as are the key drawbacks which are addressed by the work presented in this thesis.

2.1 Theory of LIGS

The LIGS technique has two variants - Laser-Induced Thermal Grating Spectroscopy (LITGS) and Laser-Induced Electrostrictive Grating Spectroscopy (LIEGS). This section explains the theory behind both of them when applied in the gas phase.

2.1.1 Laser-Induced Thermal Grating Spectroscopy (LITGS)

To carry out a LITGS temperature measurement of a gas, the first step is to cross two coherent, pulsed laser beams at the point at which the measurement is required. The angle at which the beams cross, referred to as the 'crossing angle', is assigned the symbol θ_x. Within the area where these 'pump' beams cross over, hereafter referred to as the interaction region, a fringe pattern is produced. Bright fringes are formed where there is constructive superposition between the waves from both beams (and therefore a high intensity of light) and dark fringes are formed by the destructive superposition of the waves. This setup is shown in sub-diagram **a** of Figure 2.1. The fringe spacing (Λ), which is the distance between consecutive bright fringes, is determined by the wavelength of the pump beams (λ) and the crossing angle (θ_x) according to the following equation:

$$\Lambda = \frac{\lambda}{2\sin\left(\frac{\theta_x}{2}\right)} \tag{2.1}$$

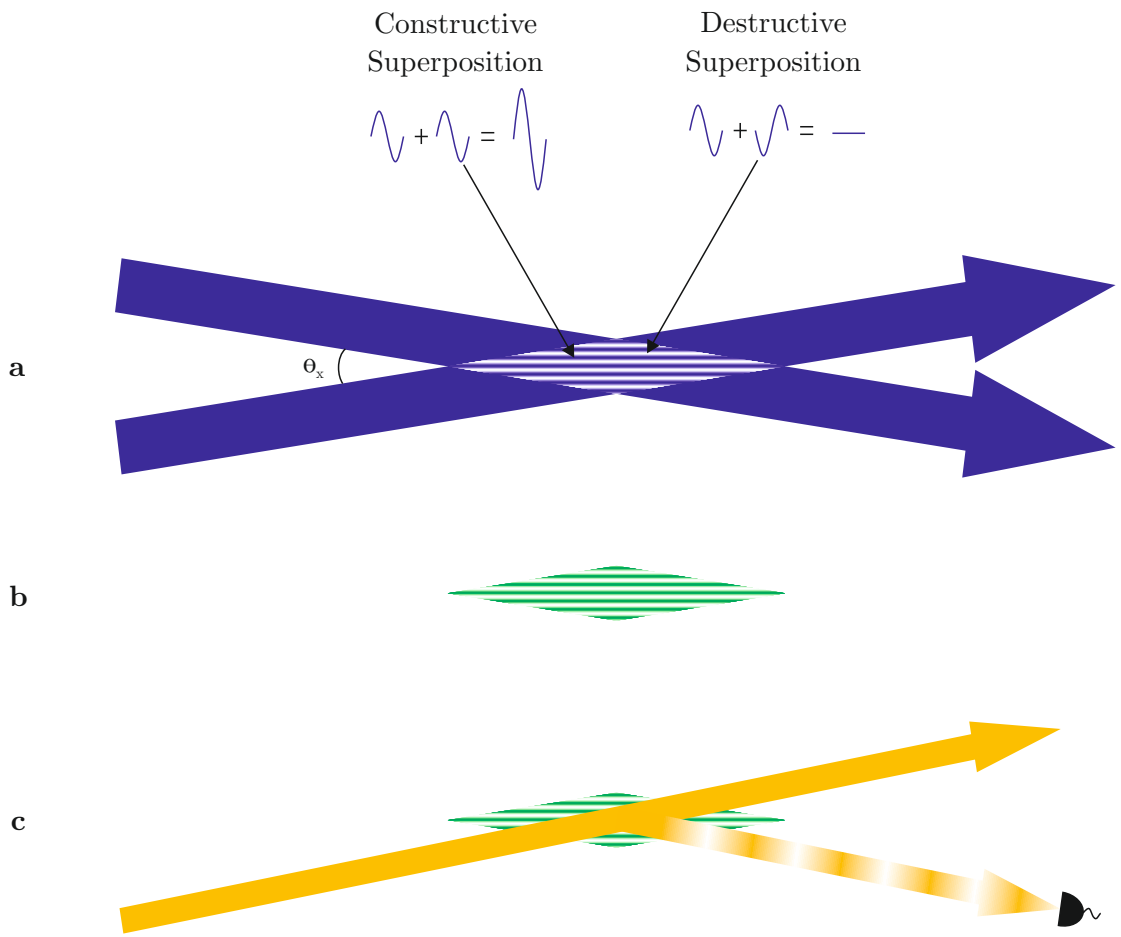


Figure 2.1: Diagrammatic explanation of the theory behind LITGS (adapted from [15]):
a Two pump beams are crossed at an angle θ_x, creating a fringe pattern within the interaction region.
b Molecular absorption of the laser energy, and subsequent quenching, leads to the formation of a thermal grating.
c The periodically- and coherently-scattered signal from a probe beam is collected by a detector.

Within the high-intensity regions (the bright fringes), energy from the beams is absorbed and temporarily stored in the excited states of the molecules of a constituent of the gas which has an electronic resonance tuned to the wavelength of the pump laser (or, if such a constituent is non-existent for the wavelengths available, the gas is seeded with a suitable absorbing species). Subsequent quenching (the non-radiative transfer of energy as an excited molecule relaxes back down to its ground state) of these molecules results in localised heating which generates a time-varying spatial density modulation within the interference region called a thermal grating (sub-diagram **b** of Figure 2.1). This thermal grating is made up of

two components:

1. Temperature: The localised heating results in a temperature, and thus density, modulation. Therefore, this component resembles the same geometry as the interference fringe pattern. Over time, due to diffusion processes, the visibility of this modulation component decays [15].

2. Acoustic: The sudden increase in localised pressure due to the quenching of the molecules results in sound waves propagating in the direction through the grating planes, creating a standing wave. The amplitude of this density modulation oscillates sinusoidally with time at a frequency determined by the speed at which the waves are travelling, as well as decaying over time due to viscous effects [15].

As the acoustic component oscillates, it has the effect of alternatively amplifying and negating the temperature component. This means that the overall thermal grating 'appears' and 'disappears' at a frequency determined by the speed at which the acoustic waves travel through the gas. The density modulation within the thermal grating results in a corresponding variation in the index of refraction. When a third 'probe' beam is directed at the grating at the first-order Bragg-angle (θ), it may be coherently scattered (due to the variation in refractive index) into the same angle (on the same side of the normal), creating a laser-like signal beam which is detected as shown in sub-diagram **c** of Figure 2.1. The angle required is dependent on the fringe spacing, determined from the following equation:

$$\theta = \sin^{-1}\left(\frac{\lambda}{2\Lambda}\right) \tag{2.2}$$

This coherent scattering only occurs when the grating is visible, leading to an oscillation in intensity of the signal beam. The oscillation frequency of the signal beam (F) is determined by the speed at which the acoustic waves are travelling through the gas (i.e. the speed of sound). To make a temperature measurement, it is necessary to relate the speed of sound (and hence the oscillation frequency F) to the temperature of the gas. For an ideal

gas, this relationship is given by the equation

$$T = \frac{\Lambda^2 M F^2}{\gamma k_{\mathrm{B}}} \tag{2.3}$$

where M is the molar mass of the gas, γ is the heat capacity ratio for the gas, and k_{B} is Boltzmann's constant.

Experience suggests that the oscillation frequency, F, at room temperature for most gases is around 50 MHz which necessitates the use of a highly sensitive detector capable of a short response time. Given these conditions, a photomultiplier tube (PMT) is often used with the signal subsequently digitised by an oscilloscope. Figure 2.2 shows a typical experimental LITGS signal obtained using a PMT. The oscillations caused by the acoustic standing wave are visible, as is a steady overall decay in the signal. This is due to the deterioration of the temperature and acoustic components caused by diffusive and viscous effects respectively.

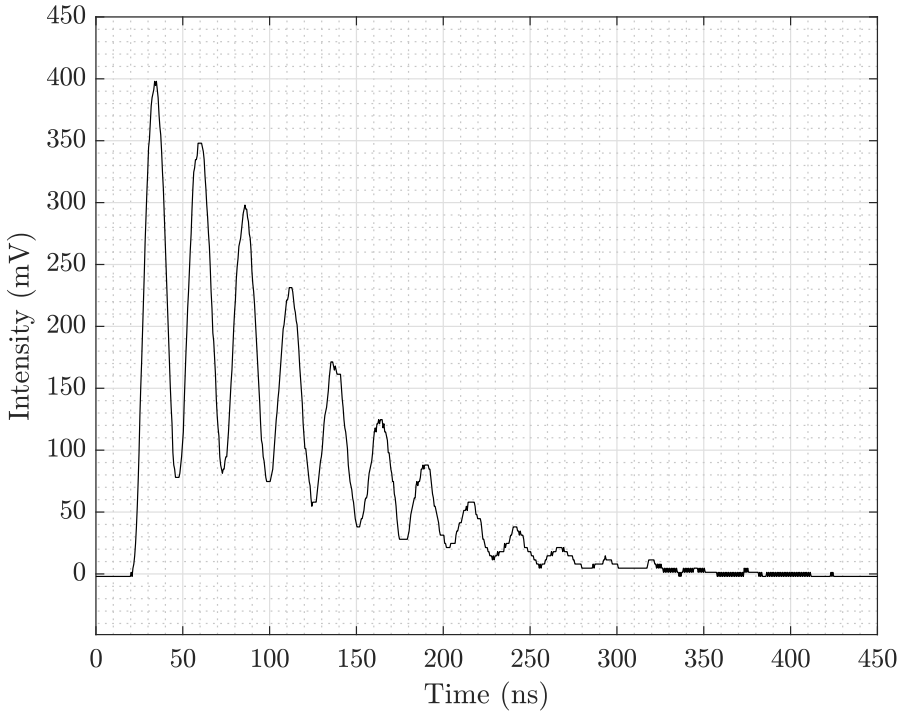


Figure 2.2: Experimental LITGS signal recorded by a photomupltiplier tube and digitised using an oscilloscope.

To extract the oscillation frequency from the digitised signal, a Fast Fourier Transform (FFT) algorithm is applied. The resulting power spectrum will contain information averaged over the duration of the signal (generally of the order of 1 µs), and will also include low frequency content due to the slow decay of the signal. Applying a bandpass filter to the spectrum allows the low frequency content to be suppressed and returns the dominant frequency which can then be converted to a temperature.

2.1.2 Laser-Induced Electrostrictive Grating Spectroscopy (LIEGS)

A laser-induced electrostrictive grating is created using the same optical geometry described in Section 2.1.1. The difference between the techniques lies in the way that a density perturbation is 'written' into the gas within the measurement region. While LITGS is based upon the absorption and subsequent non-radiative release of laser energy, LIEGS relies on the process of electrostriction which is defined as the mechanical deformation of a dielectric material (one that has a high polarisability and low conductivity) in the presence of an electric field. First, the electric field pattern created by the interference of the pump beams polarises the dielectric gas. The continued presence of the inhomogeneous electric field causes a spatially periodic deformation of the gas, resulting in the generation of a spatially periodic density perturbation. The rapid creation of this density variation launches acoustic waves that travel normal to the grating planes, forming a standing wave oscillating at a frequency determined by the speed at which they are travelling through the gas. An oscillating acoustic grating is therefore formed, similar in characteristics to that produced by the LITGS technique. However, unlike the thermal grating produced in LITGS, the temperature component is negligible [16].

Having set up an oscillating grating, the probe beam can be scattered off the grating in the same way as it is for a LITGS measurement, as described in Section 2.1.1. The analysis of the resulting signal beam is also carried out in an identical manner. Finally, the temperature (T) is derived from the oscillation frequency (F) of the signal beam by

$$T = \frac{\Lambda^2 M \left(\frac{F}{2}\right)^2}{\gamma k_{\mathrm{B}}} \tag{2.4}$$

where M is the molar mass of the gas, γ is the heat capacity ratio for the gas, and k_B is Boltzmann's constant. It is important to note that the key difference between Equations 2.3 and 2.4 is the halving of the signal frequency term (F) for the LIEGS temperature calculation.

As discussed in Section 2.1.1, the application of LITGS often requires the addition of an absorbing species as a tracer. However, the non-resonant nature of LIEGS means that tracer-free measurements can be taken. While this advantage may appear to render the use of the LITGS technique obsolete, it should be noted that LIEGS requires the use of a pulsed laser to generate pump beams with energies that are generally one order of magnitude larger than required for LITGS [17]. The resonant nature of LITGS can also be exploited to derive the concentration of certain species at the measurement point [17]. These considerations therefore show that both methods are relevant, and the selection of one over the other depends on the application.

2.1.3 Experimental uncertainty considerations

Sections 2.1.1 and 2.1.2 introduced how the frequency of oscillations within a LIGS signal is a measure of the speed of sound at the measurement point. Equations 2.3 and 2.4 can then be applied to derive a temperature measurement. This section considers the impact of experimental uncertainties on a LIGS measurement due to the form of these equations.

The primary source of uncertainty in turbulent applications, such as unsteady combustion, is a variation in the local gas composition. This variation leads to a change in the ratio between molar mass and heat capacity within equations 2.3 and 2.4. The calculated temperature varies linearly with this ratio, and so large fluctuations will lead to significant errors in measurement.

Another source of experimental uncertainty is a variation in the crossing angle of the two pump beams. Equation 2.1 shows how this affects the fringe spacing for a given setup, which would then lead to an error in the calculated temperature. Given the small crossing angles generally used in LIGS experiments ($\sim 2^\circ$), the relative error in crossing angle can be approximated to equal the relative error in fringe spacing. However, due to the form of Equations 2.3 and 2.4, this relative uncertainty is doubled for the calculated temperature.

To overcome this problem, a LIGS setup can first be calibrated by taking a measurement in a gas at a known temperature, and then applying Equations 2.3 and 2.4 to calculate the experimental fringe spacing. In practice, the alignment method employed for LIGS experiments (explained in detail in Section 3.2) limits this error to a negligible amount.

The final source of uncertainty comes from the accuracy with which the Fast Fourier Transform algorithm is able to extract the frequency from the LIGS signal. As with all signal processing routines, a large signal-to-noise ratio is desirable. As shown in Sections 6.3.2, increasing the pump and probe beam irradiance can help to increase the signal level[1]. Another way to increase the signal strength is to ensure that the two pump beams are phase-matched to maximise the wave interference that leads to the formation of the grating. Common LIGS setups have one pump beam travelling a further distance than the other, and so care needs to be taken to ensure that the difference in path lengths does not exceed the coherence length of the laser. This is further explored and quantified in Section 6.3.1. Finally, the spectral irradiance and divergence of the probe beam should be narrowed and minimised respectively. This is due to the form of Equation 2.2, which shows that the angle of the probe beam is tuned to the desired fringe spacing for a given wavelength. Therefore, light at a different wavelength (due to a broad spectral irradiance) or different angle (due to a large beam divergence) will not be scattered into the signal beam efficiently.

[1]This is valid to a certain extent as extremely high irradiance can lead to gas breakdown. For LITGS, high pump beam energies can also lead to systematic error for temperature measurements due to 'beam heating'; this is further explored in Section 3.3.

2.2 Origins of LIGS

This section provides some historical context for the the LIGS technique. In the 1970s, the use of two beams to create a thermal grating, and subsequent scattering off the grating, was termed 'Forced Rayleigh Scattering' [18]. This method was used extensively to study thermal diffusivity in solids [18–21] and liquids [19, 22], as well as examining other characteristics and phenomena such as 'second sound' (the wavelike propagation of heat pulses) [23]. In these applications, only the decay of the thermal grating was analysed. In 1980 Nelson and Fayer [24] developed a new technique, which they called Laser Induced Phonon Spectroscopy (LIPS), to measure the speed of sound in crystals and liquids. The theory behind it is similar to that of LIGS; two pump beams are crossed over to form either thermal or electrostrictive gratings [25], and then a third probe beam is diffracted from the induced grating to produce an oscillating signal beam. The distinction of the difference in frequency of oscillations depending on whether an electrostrictive or thermal grating is present was also reported [26, 27]. In his PhD thesis submitted in 1992, Buntine [28] presented results showing a LITGS signal in the gas phase (water vapour)[2]. Subsequently in 1994 Cummings [29] demonstrated the use of the technique, now coined 'Laser Induced Thermal Acoustics' (LITA), to generate resonant (in NO_2) and non-resonant (in air) signals in the gas phase (LITGS and LIEGS, respectively). A measured sound speed accuracy of 0.5 % was reported.

Since then, the technique has been developed and applied extensively under the interchangeable names of LIGS or LITA. In addition to being used to measure gas transport properties and relaxation dynamics [31, 32], it has been used for species detection [13, 33–35] and gas velocimetry [14, 36, 37]. The diagnostic has also been employed to measure gas-phase pressures [12, 38–40]. Primarily, though, LIGS has been used as a temperature diagnostic in chemically reacting [11, 41–44] and non-reacting [43, 45–47] flows.

[2]The thesis also refers to a technique known as 'Two-Colour Laser-Induced Grating Spectroscopy', which is referred to elsewhere as LIGS [30]. This is a two colour variation on the Degenerate Four-Wave Mixing technique, where the probe laser wavelength is spectrally scanned. It explains the presence of the word 'spectroscopy' in the LIGS technique described in his thesis, where the probe laser is a different wavelength to the pump beams, even though the technique is not spectroscopic in nature. This nomenclature has persisted to the present day.

2.3 Literature Review

Having described the theory behind both variants of LIGS, and explored their origins, this section introduces and assesses relevant alternative optical diagnostic techniques. It then concludes by explaining the relative advantages and drawbacks of the LIGS technique, which the work presented in this thesis aims to exploit and address, respectively.

2.3.1 Relevant optical diagnostic techniques

The family of optical diagnostic techniques can be split into linear and non-linear groups, based on the response of the induced molecular polarisation to the incident electric field [15]. The transition from linear to non-linear response occurs as the incident intensity increases.

An example of a linear technique is laser absorption spectroscopy (LAS) which relies on the fundamental theory of photon absorption by atoms and molecules. Absorption of a photon occurs when its energy (determined by the frequency of the light) is equal to the spacing between two discrete ro-vibrational states. The number of photons absorbed is proportional to the number density of molecules in these states, and is experimentally measured by directing a spectrally narrow probe beam through a sample and measuring the reduction in intensity of the beam after it exits the sample. The theory is depicted in Figure 2.3. The number density populating these states is dependent on temperature (a gas at a higher temperature contains more internal energy, and therefore a larger proportion of molecules at higher energies) and is characterised in databases which can be used to derive a temperature from the measured absorption [48]. Alternatively, the ratio between the absorption at two different frequencies (which is related to the ratio in number density between two different electronic transitions) can be measured and used to calculate the temperature [49]. However, the spatial resolution of this technique is inherently limited as it gives an average temperature along its 'line of sight' rather than the temperature of a point in space [50–53], which makes it unsuitable for applications where the measurement medium is non-uniform.

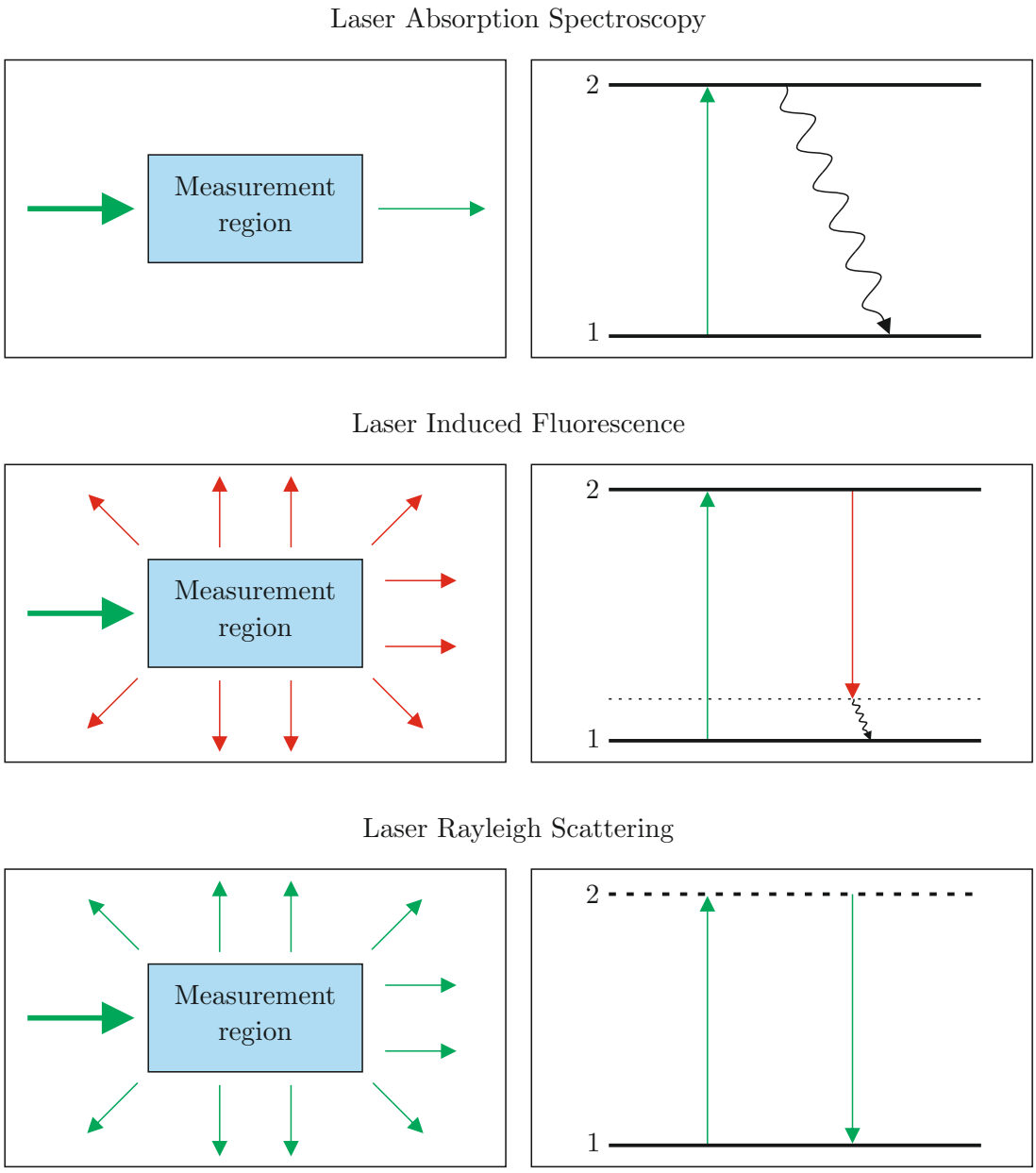


Figure 2.3: Theory behind three linear laser diagnostic techniques. The diagrams on the left show how, in each case, a probing beam directed at the measurement region produces a signal as shown by the arrows directed out of the region. The diagrams on the right represent the molecular processes as electronic transitions between two states at different energies (state 2, the excited state, is at a higher energy than state 1, which is the ground state). Solid up and down arrows show the absorption and emission of a photon respectively, while a wavy arrow signifies the non-radiative transfer of energy as a molecule relaxes back down to its ground state.

Another linear technique is Laser-Induced Fluorescence (LIF). Typically, a tracer species is introduced into the sample. A laser beam, spectrally tuned to an absorption feature of the tracer, is directed at the sample and results in the spontaneous fluorescence of the tracer. This fluorescence is caused by the absorption of photons by molecules, thus promoting them into an excited state, followed by the emission of photons as the molecules relax back down to their ground states. The wavelength of the emitted light will be at an equal or longer wavelength than that absorbed (i.e. the emitted photons will have an equal or lower energy than those absorbed). Figure 2.3 depicts the case whereby the fluorescence is at a different wavelength. The intensity of the fluorescence is used to infer the number density in a given state, and a temperature can then be calculated in a similar manner as described for LAS. To overcome the considerable problem of varying tracer number density, two-colour LIF may be applied where the temperature is derived from the ratio between two different wavelengths within the fluorescence spectrum [54]. Forming the incident laser beam into a sheet further allows for a 2D temperature measurement.

However, LIF also has its drawbacks. The temperature is calculated based on the detected fluorescence strength which can be difficult in 'dirty' environments such as an optically-accessible engine, where the windows are likely to be fouled by combustion products during operation. Furthermore, intensity is lost when the molecules release their energy through non-radiative processes (such as quenching and collisional broadening) instead of fluorescing, which is difficult to correct for [15, 55]. As a result of this, quantitative data is very hard to recover *a priori*. This can be overcome by calibrating the signal, but this can be cumbersome to achieve in practice. Lastly, using the two-colour method inherently reduces the signal intensity (as only two narrow spectral bands of the signal are used while the rest is discarded), resulting in a reduced signal-to-noise ratio.

Similarly to LIF, Laser Rayleigh scattering (LRS) requires a laser beam to be directed at the sample. The light is then elastically scattered (i.e. the light is scattered at the same wavelength) by the molecules, and the resulting signal is detected. This process is depicted in Figure 2.3. The spatial variation in intensity relates to the variation in number density of scattering molecules. Prior knowledge of the pressure and composition of the gas allows for the temperature to be calculated using the ideal gas law [4]. The major

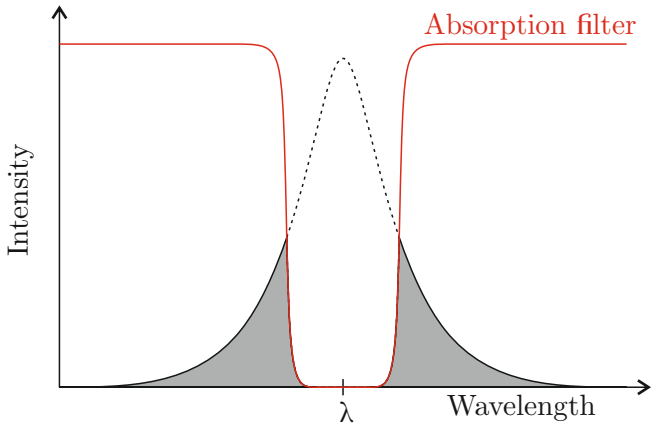


Figure 2.4: Diagrammatic explanation of the theory behind FRS. The black curve shows a broadened Rayleigh scatter spectrum, and the red curve imposed over it shows the wavelengths surpressed by the filtering cell. The wavelength designated by λ refers to that of the probe laser. Only the shaded parts of the signal are transmitted through the cell.

drawback of this method is its sensitivity to stray light (i.e. scattering from surfaces and particles) [4]. To overcome this, filtered Rayleigh scattering (FRS) uses a molecular cell which suppresses all the elastically scattered light. The light scattered from the gas being probed, however, will be spectrally broadened and frequency-shifted due to the thermal motion of the molecules and fluctuations in the gas density, meaning that some of it will be transmitted through the filter cell [56]. This effect is shown in Figure 2.4. Although this approach goes a long way to solving the problem of background scatter, the method reduces the signal-to-noise ratio as a large amount of the signal is also suppressed by the filtering cell. It also requires an accurate model of the Rayleigh scattering's spectral distribution, which is then convolved with the absorption spectrum of the filter cell to quantify the transmitted intensity [57]. Additionally, the technique requires a very accurate knowledge of the gas composition due to its effect on the Rayleigh scattering cross section [58, 59]. Another linear technique, Raman scattering, has been used to identify the major species in the sample before applying Rayleigh scattering to measure its temperature. Raman scattering relies on the inelastic scattering (i.e. the light is scattered at a different wavelength) of light from molecules. Since the scattered light from different molecules will have a characteristic intensity distribution across the frequency spectrum, analysis of the frequency content in the signal can be used to characterise the gas composition in the probed volume. Kearney

et al. [60] conducted temperature measurements in a diffusion flame using a combination of the Filtered Rayleigh and Raman scattering techniques, and reported an accuracy of 4–6 %. However, both techniques were not applied simultaneously and a flamelet model was still required to approximate the gas composition. Additionally, the application of Raman scattering is non-trivial as the signal strength is orders of magnitude lower than Rayleigh scattering.

In general, linear techniques that are not line-of-sight produce an incoherent output whereby the signal is emitted in all directions. Non-linear techniques, on the other hand, can provide coherent, laser-like signal beams which enable detectors to be placed further away from the measurement region and offer better discrimination against background noise [52]. The subset of four-wave mixing techniques (which includes LIGS) is particularly relevant.

Degenerate Four-Wave Mixing (DFWM) is a non-linear technique that relies on three in-phase beams crossing at the measurement point to create a fourth 'signal' beam. The three beams have the same wavelength, and so a single laser together with beam splitters can be used to generate them. DFWM can be thought of as a kind of grating process that is similar to LIGS, whereby the first two 'pump' beams are crossed at a certain angle to create a fringe pattern [52]. Absorption of the light by a resonant species in the gas leads to the formation of a population grating (which consists of a modulation in the population difference between excited and ground states). The third 'probe' beam is then scattered off this grating to generate the signal beam. Figure 2.5 depicts this process, and compares it with other relevant four wave mixing techniques[3]. The key difference between LIGS and DFWM is the presence of a population grating rather than a thermal grating [61], and therefore the requirement for the probe beam to be at the resonant frequency of the molecular species. When the wavelength is matched to an allowed molecular transition[4] within the gas being probed, the DFWM signal experiences a strong resonant enhancement. Therefore, by scanning the laser through different wavelengths, the relative distribution of molecules in different ro-vibrational states can be determined. This information is then

[3]The geometry shown for DFWM in Figure 2.5 is an example of a 'forward pump geometry'. This configuration produces the largest signal intensity, but can suffer from the Doppler effect causing the beams to appear 'off-resonance' to some molecules. An alternative geometry which uses two counter-propagating pump beams has been demonstrated [52].

[4]The availability of molecular transitions is governed by certain selection rules as explained by Eckbreth [4].

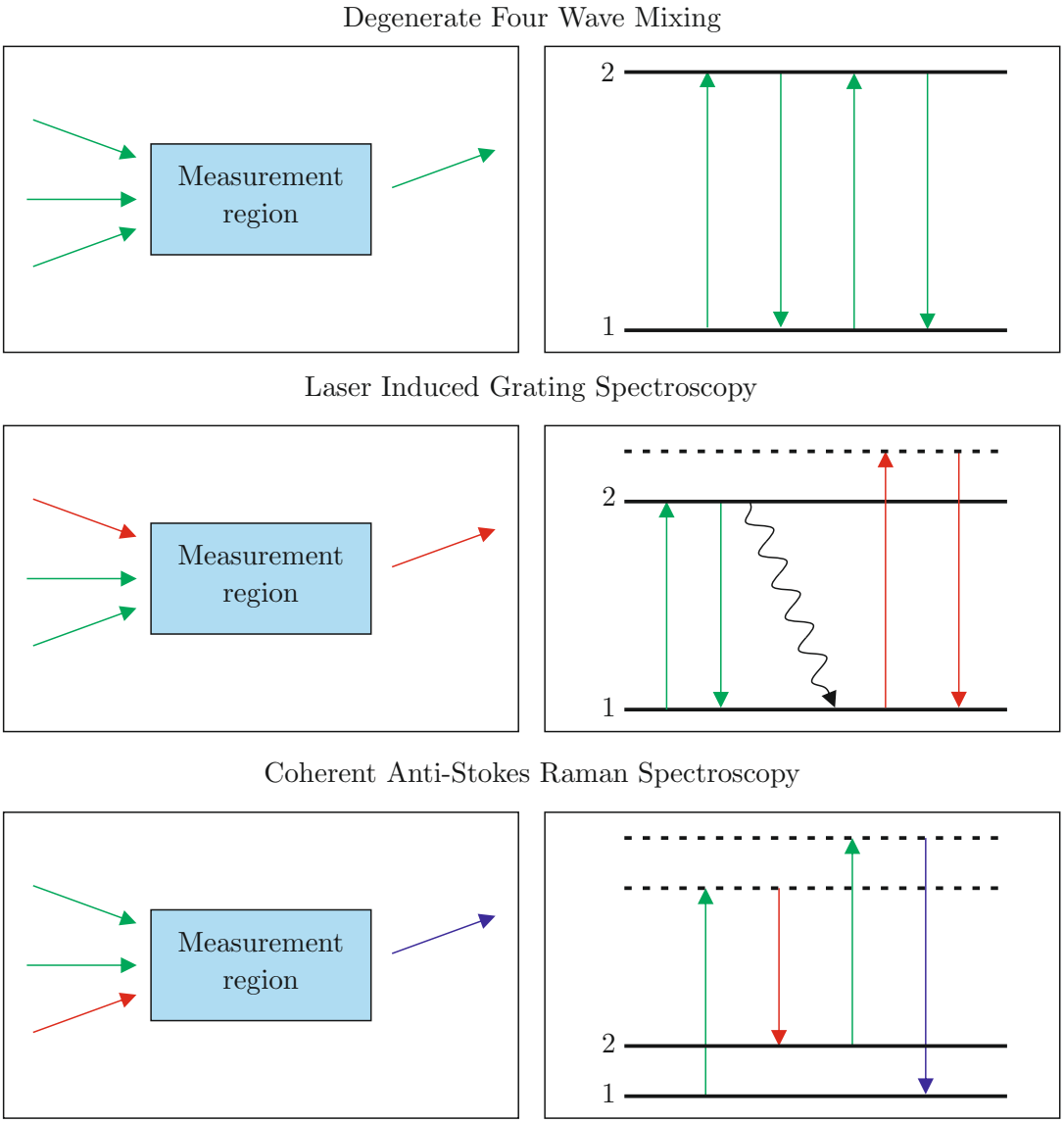


Figure 2.5: Theory behind three non-linear four-wave mixing laser diagnostic techniques. The diagrams on the left show how, in each case, the interaction of three beams produces a coherent, laser-like fourth beam that contains information relating to the probed point. The diagrams on the right depict the molecular process as transitions between two states at different energies (state 2, the excited state, is at a higher energy than state 1, which is the ground state). Solid arrows represent processes involving photons, while a wavy arrow signifies the non-radiative transfer of energy as a molecule relaxes back down to its ground state.

correlated with the theoretical distribution expected at different temperatures to derive the temperature of the probed volume. Time-averaged 2D temperature measurements have been presented by Ewart *et al.* [62], as have single-shot measurements using a broadband laser [63].

A significant drawback of the DFWM technique is the degradation of signal intensity at elevated pressures due to increased molecular collisions which lead to the formation of thermal gratings. The presence of a thermal grating then leads to the formation of a LITGS signal which dominates the DFWM signal. Latzel *et al.* [44] reported that this limit was reached at 3 bar for single shot temperature measurements in a high-pressure flame. Interfering elastic light scatter from unwanted sources is also an issue due to all three pump and probe beams being at the same wavelength as the signal beam [64]. Furthermore, variations in laser intensity have been shown to affect the derived temperature [65]. This means that shot-to-shot intensity variations need to be considered when performing a spectral scan, or pulse-to-pulse mode intensity fluctuations if using a broadband laser[5] for a single-shot measurements. The use of a modeless laser can help alleviate this problem, but since most of the energy within the bandwidth of the laser does not contribute to the DFWM signal, a resultant low signal-to-noise ratio can limit the accuracy of the measurements [64]. Finally, as with all intensity-based spectral measurements, absorption of light at a specific wavelength within the spectrum of interest must be accounted for. This was evident in the temperature measurements of a flame conducted by Ewart [66], where the error due to absorption was predicted to be 10 % . The accuracy of the corrected DFWM temperature measurements, when compared to values obtained using a thermocouple, was reported to be 5 % while the precision was 15 %. These values correlate well to the accuracy and precision of 4 % and 14 % reported by Jefferies *et al.* [67] for methane/air flame measurements. Due to the aforementioned difficulties, and the relatively low accuracy and precision, this technique has rarely been applied for temperature measurements over the last couple of decades.

Instead, the most widely-used four-wave mixing technique for temperature measurements is Coherent Anti-Stokes Raman Scattering (CARS). The CARS technique employs three beams, at frequencies ω_1, ω_2 and ω_3, which are crossed over in a phase-matching geometry to create a fourth output beam with a frequency ω_4. Phase-matching ensures that the signals generated at different points will all be in phase, and therefore constructively

[5] In fact, Yip *et al.* [68] reported that shot-to-shot mode intensity fluctuations meant that DFWM signals were present in only 15 % of their measurements.

interfere rather than decaying. The difference in frequencies ω_1 and ω_2 is tuned to match a vibrational or rotational Raman transition within the probed gas species via a 'virtual' state. Absorption of a photon from the third beam, with frequency ω_3, and subsequent relaxation back to the ground state results in the emission of the output beam at a frequency ω_4 which is equal to $\omega_1 - \omega_2 + \omega_3$. This process is depicted in Figure 2.5[6]. The temperature of the gas can then be derived by spectrally scanning the second pump beam and recording the signal, followed by fitting to known molecular parameters [4, 15, 52]. Single shot measurements can be obtained by using a broadband laser to generate the entire CARS spectrum of the probed gas species [4].

Compared to CARS, LIGS boasts a superior accuracy[7] for single-shot temperature measurements. Stevens and Ewart [69] reported a LIGS temperature measurement accuracy of 0.42 % for measurements of NO_2/N_2 mixtures in a cell between 300–400 K. In comparison, accuracies of 2–3 % (for temperatures ranging from 500–1400 K) [70] and 2.5–8.5 % (for a temperature range between ambient and 2000 K) [71] have been presented for vibrational N_2 CARS in air, while a 3 % accuracy (for temperatures ranging from 300–1600 K) [71] was reported for rotational N_2 CARS in air. Comparing the results from the same experiments also shows that LIGS is capable of a better precision (standard deviation of 0.16 % [69]) than vibrational CARS (standard deviations of 3.5–5 % [70] and 3–11 % [71]) and rotational CARS (standard deviation of 1.4–2.8 % [71]).

From an experimental perspective, the CARS technique is significantly more challenging to implement compared to LIGS due to the requirement of fine optical alignment and high wavelength accuracy [17]. CARS is also more costly because of the need for a highly sensitive spectrometer (for signal detection) and tunable laser (or stable 'modeless' broadband laser for single-shot thermometry); this is further exacerbated by the use of picosecond and femtosecond lasers for increased accuracy [72]. The analysis of CARS data, which requires accurate spectral fitting routines, is far more complex and computationally expensive compared to the frequency extraction required from LIGS signals. Accurate knowledge

[6]The geometry shown in Figure 2.5, which is the most commonly employed configuration, is termed 'BOXCARS'. Other variations are possible [4].

[7]This is based on the available literature for calibration measurements, which have been conducted at different temperature ranges. It should be noted that a direct comparison has not been conducted.

of the molecular processes occurring in the probed conditions is required, and the general limitations of intensity-based spectral measurements as discussed for DFWM (e.g. modal intensity fluctuations in the laser) also apply to CARS. On the other hand, LIGS is a frequency-based measurement technique which means that it can operate in conditions where intensity fluctuations are prevalent due to the environment. This also limits the impact of 'beam steering'[8], which is a common issue for techniques based on crossing multiple beams and leads to variations in signal intensity.

However, CARS temperature measurements obtained at rates of the order of 1 kHz have been extensively reported [73–75], whereas LIGS measurement rates have generally been limited to the order of 10 Hz [76]. Although measurement rates higher than 10 Hz have recently been demonstrated for LIGS, they have been achieved alongside an undesirable increase in experimental cost and complexity. The work presented in Chapter 3 was undertaken to alleviate this problem.

Relative to LIGS, CARS is capable of excellent spatial resolution. The standard BOXCARS arrangement is generally capable of 1–3 mm [77], but variations on the geometry can offer a spatial resolution of the order of micrometers — the review article written by Roy *et al.* [78] claims a possible resolution of better than 25 µm, Bohlin and Kliewer [79] carried out an experiment with a spatial resolution of ∼500 µm, and Bohlin *et al.* [80] reported a resolution of better than 50 µm. For comparison, the spatial resolution of a typical LIGS experiment is of the order of centimetres. Addressing this drawback is the focus of the work presented in Chapters 4 and 5.

[8]Beam steering is the deviation in direction of a beam due to its transmission through a medium of varying refractive index. For example, this could happen if a beam travels through a flame.

3 Temporally-Resolved Biacetyl LITGS

This chapter begins by explaining the motivations behind the use of biacetyl as a tracer species for LITGS, referred to as 'biacetyl LITGS', to enable temporally-resolved LITGS measurements. Next, the characterisation of this approach is described. Finally, an application where a high repetition rate laser was employed to conduct biacetyl LITGS is presented.

3.1 Motivations

As described in Section 2.1, LIGS temperature measurements are inherently temporally averaged over the duration of the LIGS signal, which is typically of the order of 1 µs (determined by the decay rate of the thermal/electrostrictive grating). The rate at which measurements can be collected (the temporal resolution of the technique) is therefore theoretically capped in the order of 1 MHz. In reality, the temporal resolution of LIGS is determined by the repetition rate at which the pump beams (and probe beam, if using a pulsed laser to generate it) are fired. Until recently, LIGS measurements had been limited to the 10 Hz repetition rate of the high-energy pulsed lasers being used (compared to the kHz-rate resolution of CARS as mentioned in Section 2.3) [76]. However, this temporal resolution is not suitable for many transient applications, such as turbulent flows [81]. Although advances in technology have now made high repetition rate Nd:YAG lasers more easily accessible, it is undesirable to operate them at the 4^{th} harmonic due to the short operating lifetimes of the doubling crystals which essentially make them consumables. Not being able to employ the 266 nm wavelength output is a significant barrier for LITGS as it rules out the use of common absorbing tracer species such as toluene and acetone. The remaining wavelengths are 1064 nm, 532 nm and 355 nm. Stevens and Ewart [38] demonstrated the use of nitrogen dioxide (NO_2), which absorbs light at 532 nm. However, the high toxicity of NO_2 [82] makes this solution undesirable in many systems. Therefore, a practically usable

tracer species which absorbs at wavelengths of 1064 nm, 532 nm or 355 nm (to make use of relatively accessible high repetition rate Nd:YAG lasers) is required.

It should be noted that while this work was carried out, Förster *et al.* [76] presented results showing the application of LIGS at a rates of up to 10 kHz (using NO_2). Since this work was carried out, De Domenico and co-workers [83] have successfully demonstrated the use of a pulse-burst laser to obtain LIGS measurements at 100 kHz.

3.2 Selection of absorbing species and proof-of-concept

Biacetyl (also known as diacetyl) is a chemical that absorbs light at 355 nm, and has already been widely used by the community for Laser-Induced Fluorsecence (LIF) measurements [84, 85]. Its use as a flavouring additive in microwave popcorn makes it easily available and, despite links to lung cancer from exposures in large quantities [86], it is a non-toxic option as a tracer species. Biacetyl was therefore suggested for use as a novel tracer species for LITGS.

The next step was to obtain a LITGS signal from biacetyl vapour. The experimental setup used is shown in Figure 3.1. To create the pump beams, an Nd:YAG laser[1] operating in the third harmonic (355 nm) was used. The output beam from the laser was passed through a lens (with 600 mm focal length), and then equally split into two beams by a beam splitter. One beam was passed through a fused silica compensator plate to account for the difference in path lengths between both beams, and then they were both directed through a crossing lens (with 300 mm focal length). The use of two lenses, acting in tandem as a telescope, in each beam path ensured collimation of the beams at the crossing point. The difference in focal length of the two lenses also halved the beam sizes. The crossing angle used for the experiment was 2.3°, resulting in a fringe spacing of 8.8 µm. A diode-pumped solid state laser[2], operating at 671 nm, was used to produce a 300 mW continuous wave probe beam. This beam also passed through a lens before arriving at the crossing lens (to ensure collimation at the crossing point). A beam sampler was used to create a fourth beam from the probe laser, with much lower intensity, to trace the path of the signal beam

[1]The Minilite II model from Continuum was used.
[2]The MLL-III-671 model from CNI was used.

for alignment purposes only. The crossing lens was used to cross all three beams, with the required LITGS geometry, at the measurement point.

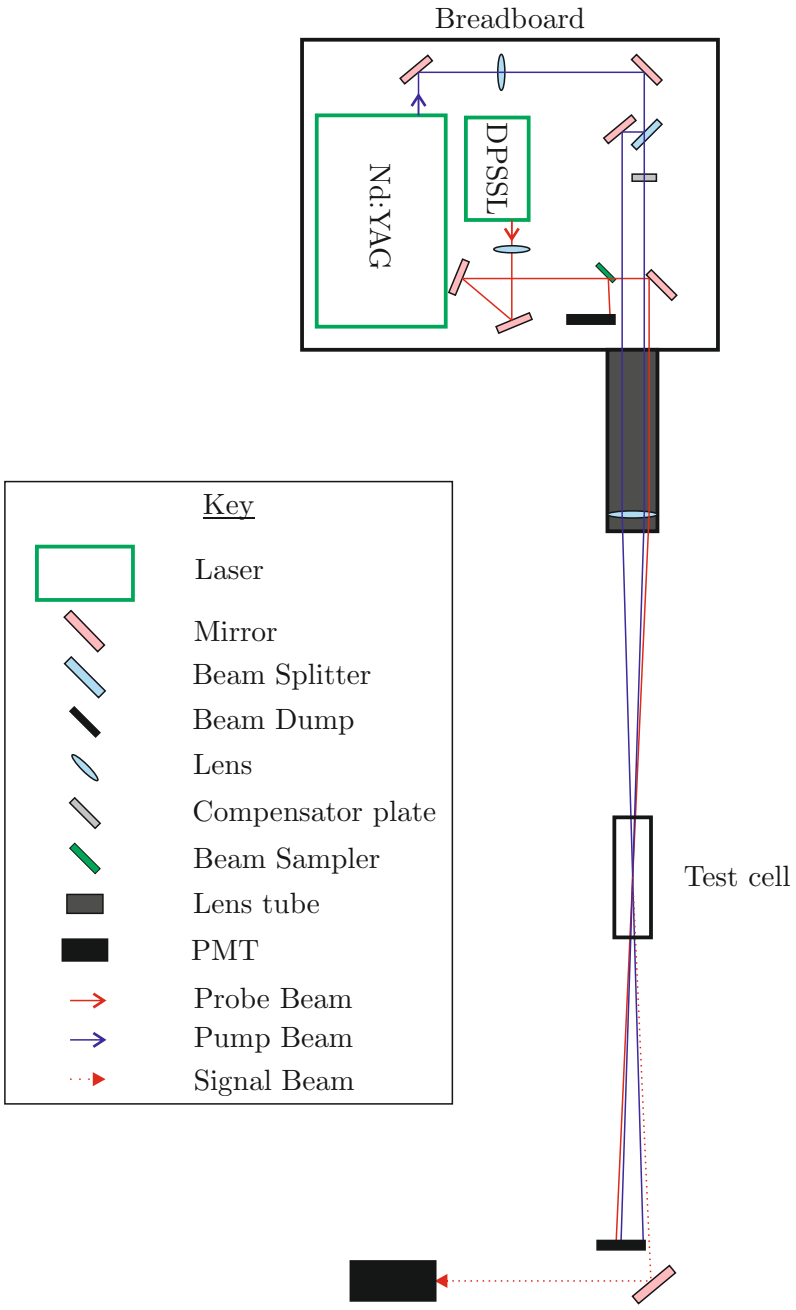


Figure 3.1: Schematic showing the experimental setup for the LITGS experiment. Note that the beam sampler is only used to align the detector, hence why a beam dump is placed in front of it during the experiment.

To align the experiment, the crossing lens was removed and two 'masks' were employed to ensure all four beams were travelling parallel to each other along the optical table. The first mask, placed at the output of the lens tube, was a metal plate with four holes drilled into it to allow the beams to pass through. The hole spacing was chosen such that when the crossing lens was introduced into the setup, all four beams would cross (at the focal point of the crossing lens) at the required angles. The second mask was a metal plate with four targets printed onto it at the same spacing as the holes for the first mask. It was placed further down the optical table, at a distance roughly equal to twice the crossing lens focal length from the output of the lens tube. Initial alignment was then achieved by adjusting the positions and angles of the optics to ensure that all four beams passed through the holes in the first mask to land on their respective targets on the second mask.

Next, the first mask was removed and the crossing lens was introduced into the setup. A pinhole was placed at the focal point of the crossing lens (i.e. the position at which both pump beams were able to pass through it and still land on the targets on the second mask). Due to chromatic aberration, the probe and signal tracing beams did not come to a focus at the same position. The relevant optics were therefore adjusted to ensure that both beams also passed through the pinhole and landed on their respective targets on the second mask. Once this was achieved, the pinhole and second mask were removed from the setup and the beam dump and detector optics were placed. The signal tracing beam was used to determine where the detector was positioned. Optical alignment was then complete, and the signal tracing beam was blocked off immediately after being reflected from the beam sampler optic (since it was only used for alignment, and was not required for the LITGS experiment). Finally, a test cell containing saturated biacetyl vapour at room temperature and pressure was placed at the measurement point.

A photomultiplier tube[3] was chosen as the detector for this experiment due to its fast rise time (under 1 ns) and high sensitivity ($\sim$40 A/mW). The data was recorded using an oscilloscope[4] capable of recording 4 Gs/s and a specified bandwidth of 750 MHz. An example LITGS signal obtained from the experiment is shown in Figure 3.2.

[3]The H6780-20 module from Hamamatsu was used.
[4]The Wavesurfer 3074 model from Teledyne LeCroy was used.

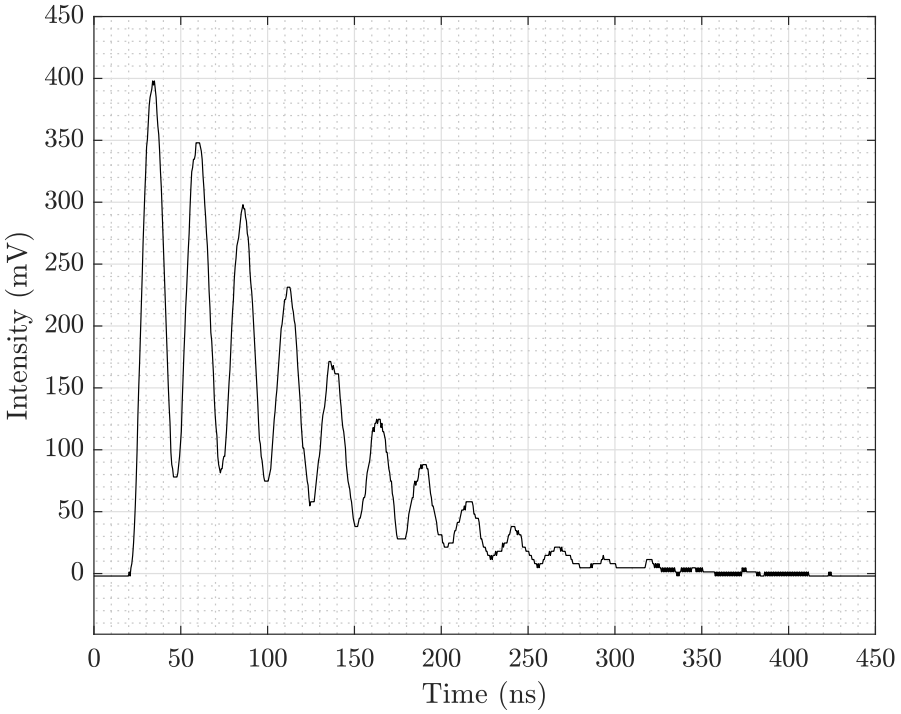


Figure 3.2: Example LITGS signal using biacetyl vapour as the absorbing species.

3.3 Characterising the effect of beam heating

As explained in Section 2.1, the cornerstone of LITGS is the deposition of energy from the pump beams into a gas to produce a thermal grating. However, this input of energy causes the temperature of the gas within the grating to increase - a phenomenon called 'beam heating'. This introduces a systematic error in the temperature measured for the gas, and so it was important to quantify this error when using biacetyl and 355 nm pump beams. This was initially determined experimentally, and then a theoretical approach was used to predict the error and the two results were compared.

3.3.1 Experimental setup

The same experimental setup shown in Figure 3.1 in Section 3.2 was used. The pump beams were crossed at an angle (θ_x) of 2.3° to create a grating with a fringe spacing (Λ) of 8.7 µm. A cylindrical cell (of length 31 cm and diameter 4 cm) with windows on each end was placed at the crossing point of the two beams so that the entire grating was contained within

it. Before conducting any experiments, the loss in energy of the beams as they travelled through the cell windows was quantified.

To calculate the fraction of the total beam energy that passed through each window (the 'transmittance' of the window), a power meter was used to take measurements of the pulse energy of the pump beams before (E_{before}) and after (E_{after}) the cell. The transmittance (T) of each test cell window was calculated to be 81.96 % using the following equation:

$$T = \sqrt{\frac{E_{\text{after}}}{E_{\text{before}}}} \tag{3.1}$$

Having quantified the loss in energy due to the test cell windows, an initial experiment was conducted to determine the concentration of biacetyl in the test cell to be used for the subsequent beam heating experiments. A droplet of biacetyl was inserted into the cell and allowed to fully evaporate in air, and then the beam pulse energy measurements were repeated. After correcting for the loss in energy from the windows, the incident and exit beam pulse energies to and from the gas mixture in the cell were found to be 5.6 mJ and 5.5 mJ, respectively. The concentration of biacetyl (c) in the cell was then calculated by using the following equation, derived by applying the Beer-Lambert law:

$$c = \frac{1}{\sigma N_{\text{A}} l} \ln\left(\frac{E_{\text{incident}}}{E_{\text{exit}}}\right) \tag{3.2}$$

where E was the pulse energy of the pump beams, l was the length of the cell, N_{A} was Avogadro's constant, and σ was the attenuation cross section for biacetyl ($0.771 \times 10^{-20}\,\text{cm}^2$ per molecule as found by Horowitz *et al.* [87]). The concentration, c, was calculated to be $9.92 \times 10^{-8}\,\text{mol/cm}^3$.

To verify this concentration, an alternative approach using a best-guess calculation of the volume of biacetyl added to the test cell was also performed. Assuming the droplet to be spherical with the same diameter (3 mm) as the syringe used to inject it into the test cell, its volume (V_{droplet}) was calculated to be $0.0141\,\text{cm}^3$.

The number of moles of biacetyl (n) in this volume was found to be 1.62 x 10^{-4} by using

$$n = \frac{V_{\text{droplet}}\rho}{M} \tag{3.3}$$

where ρ was the density of biacetyl (0.990 g/cm^3 at 15 °C [88]) and M was the molecular mass of biacetyl (86.1 g/mol [88]). As the volume of the test cell was calculated to be 390 cm^3, the concentration of biacetyl in the test cell using this method was predicted to be 41.7×10^{-8} mol/cm^3. Given the simple assumptions used in this calculation, the fact that both figures were within the same order of magnitude supported the accuracy of the calculated concentration of 9.92×10^{-8} mol/cm^3.

In order to express this concentration as a mole fraction, biacetyl vapour and air were both assumed to behave as ideal gasses. The partial pressure (P_{B}) of the biacetyl was calculated to be 0.2417 kPa by using the formula

$$P_{\text{B}} = cRT \tag{3.4}$$

where R was the universal gas constant and T was room temperature (293.15 K).

Assuming the total pressure (P_{T}) in the cell to be atmospheric, the mole fraction (X) of biacetyl was calculated to be 2.39 x 10^{-3} using the following equation:

$$X = \frac{P_{\text{B}}}{P_{\text{T}}} \tag{3.5}$$

3.3.2 Experimental results

Having characterised the transmittance of the test cell windows and concentration of biacetyl, the setup described in Section 3.3.1 was used to determine beam heating effects. LITGS signals at 7 different pump beam pulse energies between 1.6 mJ and 6.4 mJ (roughly 50 shots taken at each intensity) were collected and analysed. Figure 3.3 shows the mean temperature calculated for each beam energy, with the error bars signifying one standard deviation of the data from the mean. The temperature was calculated from the frequency of oscillations of the signals by assuming the mole fraction of biacetyl vapour to air in the

cell to be 2.39 x 10^{-3} as presented in Section 3.3.1. The maximum deviation in the mean measured temperature over the range of beam energies was 0.4 K, but there was no evidence of a systematic increase proportional to the pump beam energy. This suggests that the error in temperature measurement caused by beam heating is negligible when using 355 nm pump beams (with measured beam diameters of 1 mm) and biacetyl as the absorbing species at these conditions.

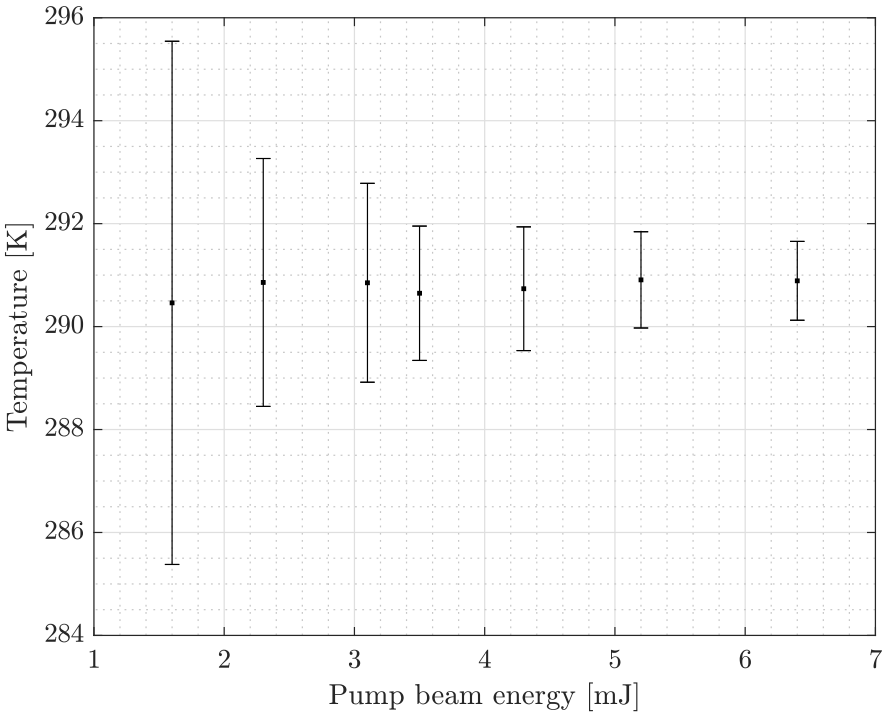


Figure 3.3: Temperature calculated from LITGS signals produced with different pump beam energies. The error bars show one standard deviation of the data from the mean.

The increased precision in the temperature measurements at higher beam energies was correlated with an increase in signal strength, as shown in Figure 3.4. This was to be expected, as the use of higher pump beam energies results in an increase in signal intensity. This improves the signal-to-noise ratio, which is beneficial for extracting the frequency from the signal.

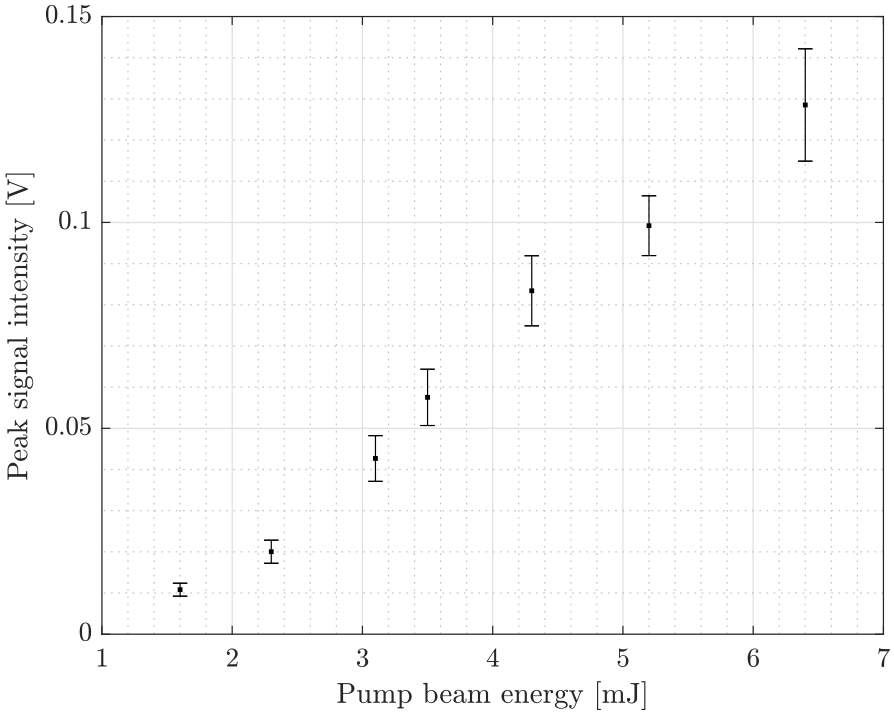


Figure 3.4: Peak signal intensity calculated from LITGS signals produced with different pump beam energies.The error bars show one standard deviation of the data from the mean.

3.3.3 Theoretical estimate

Having presented experimental results showing a negligible temperature variation due to energy deposition, a theoretical approach was taken to calculate the total beam heating taking place at the maximum pump beam energy available. To do this, the amount of energy deposited in the grating had to be calculated.

As described in Section 3.3.1, the concentration of biacetyl in the test cell was found to be $9.92 \times 10^{-8}\,\mathrm{mol/cm^3}$. For this calculation, a pump beam pulse energy of 6.8 mJ incident to the cell was used. Since the entire grating was contained within the cell, the next step was to calculate the incident and exit beam energies to and from the grating (rather than the cell). This was to account for absorption in the gas, within the cell, before the grating. To calculate the dimensions of the grating, the nomenclature shown in Figure 3.5 was used.

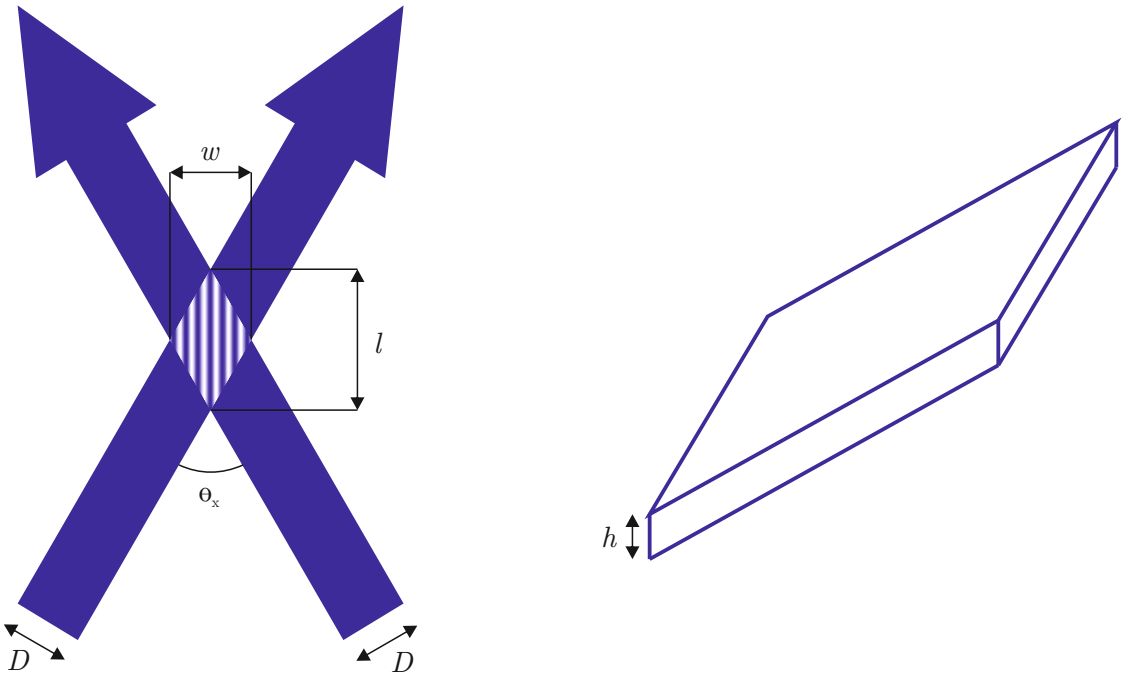


Figure 3.5: Diagrams showing the size and shape of the interaction region formed by the two pump beams, of diameter D, crossed over at an angle θ_x. The length (l) and width (w) are shown on the left (where the interaction region is depicted by blue fringes), while the diagram on the right shows the region in 3D with the height depicted by h. The height is constant due to the assumption of square beams.

The length (l) and width (w) of the grating were calculated to be 49.0 mm and 1.0 mm, respectively, by using the following equations (the diameter of the pump beams, D, was measured to be 1 mm):

$$l = \frac{2D \sin\left(90 - \frac{\theta_x}{2}\right)}{\sin\left(\theta_x\right)} \tag{3.6}$$

$$w = \frac{2D \cos\left(90 - \frac{\theta_x}{2}\right)}{\sin\left(\theta_x\right)} \tag{3.7}$$

The two pump beams were measured to cross 2.7 cm before the centre of the cell. Given that the cell was 31.0 cm long, this meant that the distance between the cell window and the beginning of the grating (l) was 12.8 cm. The incident beam energy (E_1) to the grating was calculated to be 5.541 mJ by using the equation

$$E_1 = \frac{E_0}{\mathrm{e}^{\sigma N_\mathrm{A} lc}} \tag{3.8}$$

where E_0 was the incident beam energy to the cell. The same formula was used to calculate the exit beam energy from the grating (E_2) as 5.528 mJ, meaning that 0.012 mJ had been deposited in the grating.

Having calculated the concentrations of air and biacetyl in the mixture and the total energy deposited within the grating, the final quantity required was the total mass of the gas in the grating volume. To find this, first the volume of the interaction region was calculated. The shape of the region, using the assumption of a top-hat profile for the beams, is shown in Figure 3.5.

For pump beams of height 1 mm, the total interaction volume (V) was calculated to be 24.5 mm^3 using the following formula:

$$V = h(0.5lw) \tag{3.9}$$

Next, the previously calculated concentration of biacetyl was used to find that there were 2.431 x 10^{-9} moles of biacetyl in the interaction region. Using the mole fraction of biacetyl which was also calculated earlier, it was found that there were 1.015 x 10^{-6} moles of air in the interaction region. Using the molar masses for both (0.0861 kg/mol for biacetyl and 0.0289 kg/mol for air), the total mass of gas (M) in the interaction region was calculated to be 2.96×10^{-8} kg.

Finally, by assuming the specific heat (c_p) of the gas mixture in the interaction region to be the same as that for air (since the mixture was >99 % air), the total temperature change within the interaction volume could be calculated by:

$$\Delta T = \frac{E_1 - E_2}{c_{p,\mathrm{air}} M} \tag{3.10}$$

This calculation produced a temperature change of 0.42 K. From room temperature (293.15 K), this is a variation of only 0.14 %. Considering the assumptions in this method, some observations can be made. Firstly, this calculation ignored the Gaussian nature of

the laser beams - a property which has the effect of making the interaction region shorter than expected (since the beams have a low intensity at the edges, the contribution from the corners of the grating is minimal). This means that the total energy deposited in the grating will be less than expected. In fact, Equation 3.8 shows that decreasing the length of the interaction region will decrease the incident energy of the beams (E_1) exponentially and increase the exit energy of the beams (E) exponentially. This means that the numerator in Equation 3.10, and therefore the beam heating, will decrease exponentially. On the other hand, decreasing the length of the interaction region means that its volume, and therefore the mass of gas contained in it, also decrease linearly. Therefore while the numerator in Equation 3.10 increases exponentially due to the reduced interaction length, the denominator also decreases linearly. The overall effect of a decreased interaction length is thus a lower value of beam heating, making the calculated 0.14 % temperature rise a conservative estimate.

The effect of another simplifying assumption should also be considered. As shown in Figure 3.6, the intensities used in Equation 3.10 include energy absorbed outside of the interaction region (shown as areas A, B, C and D in Figure 3.6). Therefore the numerator of Equation 3.10 was larger than it should have been, and thus the calculated temperature change is larger than expected.

That said, the Gaussian nature of the beams also has the effect of making the temperature rise within the interaction region uneven (it will be greater at the centre than the edges). So, while the 0.14 % is a conservative 'average' value, it is possible that the centre of the interaction region will experience this level of beam heating.

To verify the theoretical approach, the method was used to calculate the beam heating for beam pulse energies of 6.4 mJ and 1.6 mJ (the two extremes used in the experiment). For the 6.4 mJ beam, a beam heating value of 0.40 K was calculated while the 1.6 mJ was expected to increase the gas temperature within the grating by 0.10 K. This gave a variation between the two of 0.3 K, compared with the 0.4 K that was found experimentally. This further verified that the measured discrepancy in the experimental data was within the accuracy of the measurement technique rather than being due to beam heating.

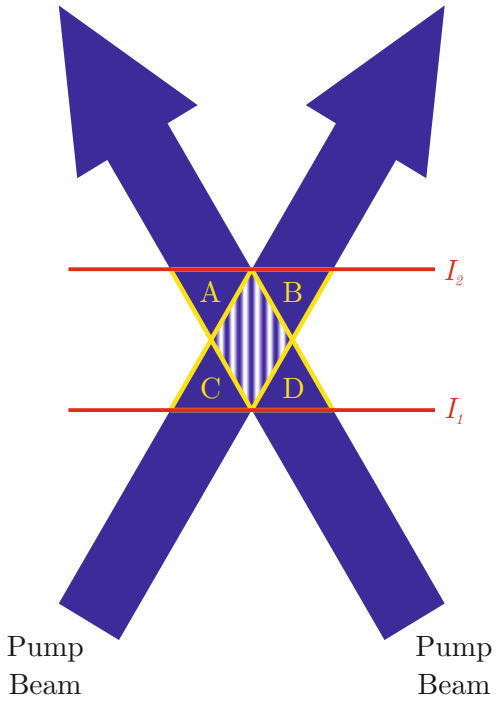


Figure 3.6: Diagram showing the values used for I_1 and I_2 in Equation 3.10 - they are taken as the total intensity along the lines shown. Note the areas A, B, C and D that are included in the calculation for the total energy deposited in the interaction region (despite not being part of the grating which is shown as blue fringes).

3.3.4 Concentration

The impact of increasing the concentration of biacetyl on beam heating was also considered. Using the theory presented in Section 3.3.3, a Matlab script was written to predict how varying the concentration of biacetyl would affect beam heating. In addition to beam heating, a prediction of the intensity of the signal produced was valuable (since maximising this is beneficial for the accuracy and precision of the frequency derived from the signal). To implement this, the experimental data was used to find the relationship between peak signal intensity and the amount of energy deposited in the grating. The energy deposited was found by using the the theoretical approach explained in Section 3.3.3, and the resulting plot is displayed in Figure 3.7. A least-squares linear fit has been applied. By extrapolating this fit, the expected signal intensity for any concentration of biacetyl could be predicted.

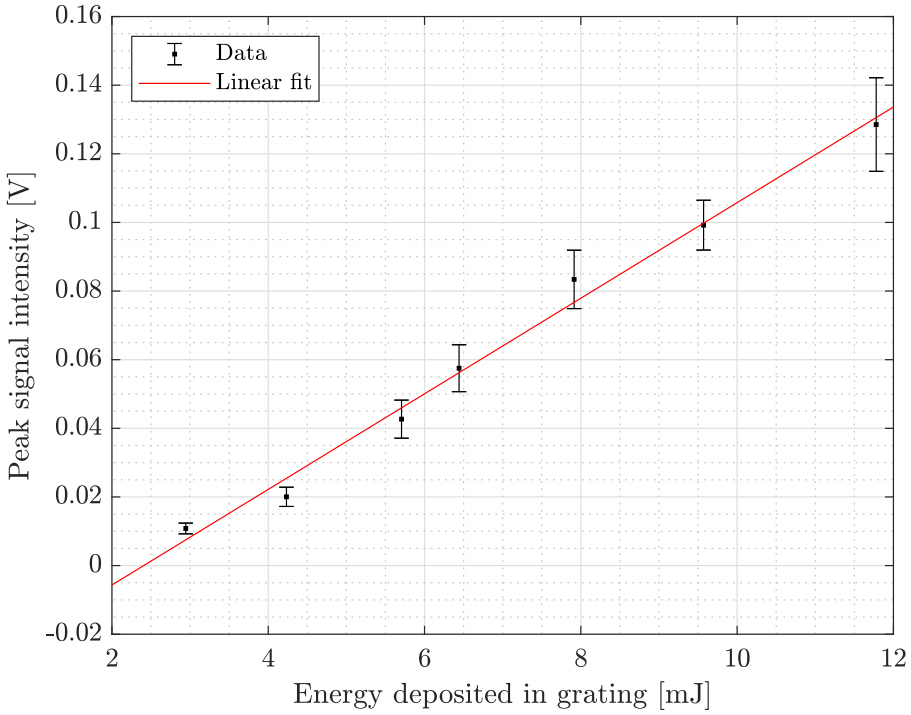


Figure 3.7: The relationship between the laser energy deposited in the grating and the peak intensity of the resulting LITGS signal. The error bars display the standard deviation of the data, and the red line is a least-squares linear fit.

A plot showing how the concentration of biacetyl affects the beam heating and signal intensity is shown in Figure 3.8. As expected, at first both the signal intensity and beam heating increase with concentration. However, the signal intensity then peaks and begins to fall. This is due to the increased absorption of the laser energy by the biacetyl *before* the beam arrives at the interaction region, meaning that less energy is being deposited in the grating itself. The beam heating also peaks and begins to fall; however, the total mass of the gas mixture increases with concentration (as biacetyl is heavier than air) and so the beam heating decreases at an increased rate compared to the signal intensity. Although it appears preferable to operate in this region where a large signal intensity and small beam heating is achievable, the large concentration of biacetyl would have the undesirable consequence of significantly affecting the properties of the gas mixture being investigated.

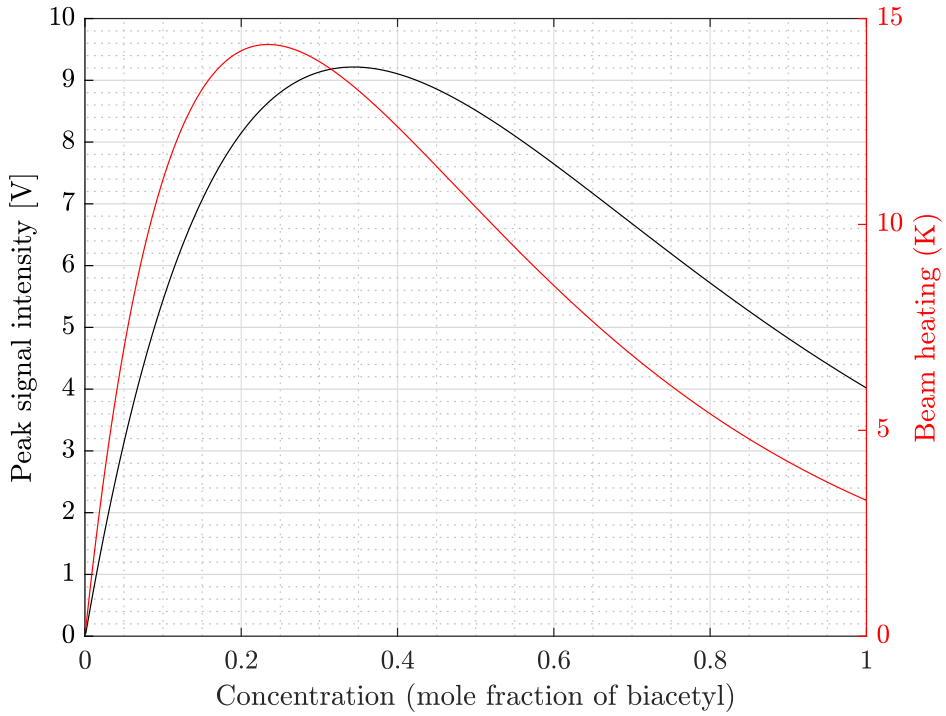


Figure 3.8: The effect of varying the concentration of biacetyl, expressed as a mole fraction of the mixture, on the predicted LITGS signal intensity. Beam heating is expressed as an absolute temperature difference.

Biacetyl has a lower flammability limit of 2.4 %, so Figure 3.9 shows the practically achievable concentration variation. In this case, as the concentration is increased both the beam heating and the signal intensity increase almost linearly. However, even at the upper limit of biacetyl concentration the absolute temperature change is below 4 K which would be negligible for most applications. Furthermore, for applications at higher temperatures the absolute systematic error would remain constant (as it is only dependent on the laser energy being deposited in the grating) while the relative error would diminish to a negligible value.

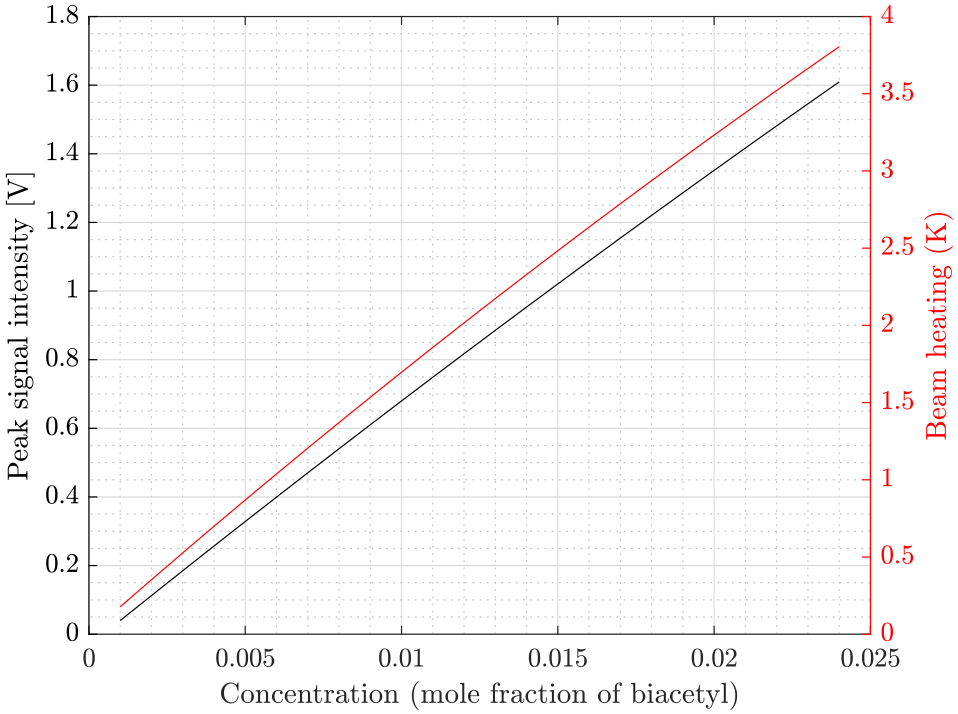


Figure 3.9: The effect of varying the concentration of biacetyl, expressed as a mole fraction of the mixture, on the predicted LITGS signal intensity. Beam heating is expressed as an absolute temperature difference. The concentration is only plotted up to the lower flammability limit for biacetyl.

3.4 Application of biacetyl LITGS to measure entropy spots

The recent push to regulate emissions from aerospace combustion applications has led to the use of lean premixed prevaporised combustors. Although they produce less NO_x, they also burn more unsteadily which can lead to the formation of so-called 'entropy spots'. The advection of these spots to the first stage of the gas turbine results in the formation of acoustic waves which contribute to the overall noise emission of the system. Characterising the properties of such spots is an active area of research at the Cambridge University Engineering Department, where they have designed and built an 'Entropy Generator'. In order to detect the passage of synthetic entropy and composition spots in the facility, a non-intrusive optical diagnostic technique capable of temperature and composition measurements with a temporal resolution between 0.5 and 1 kHz was required.

Having investigated the use of biacetyl as a suitable absorbing species, this provided a good opportunity to characterise its use with a high repetition rate laser emitting at 355 nm. First, temporally-resolved temperature and species concentration measurements in a steady jet were obtained. Following this, the technique was used to monitor the passage of entropy and composition spots in a flow. This work was conducted in collaboration with researchers from Cambridge University. The author was actively involved in designing and running the experiments, but only reviewed the data analysis and final publication. The findings have already been published; the remainder of this chapter mainly presents [89] in the author's own words to suit the context of this thesis.

3.4.1 Experiments using a steady jet

The first experiments carried out at the facility employed a steady jet to characterise the effect of gas composition (by varying the concentration of biacetyl in the bulk gas, and also using different bulk gasses) on the accuracy of the technique, as well as taking temperature and species concentration measurements. For this set of experiments, an identical optical setup as shown in Figure 3.1 in Section 3.3.1 was used, but with the Minilite II laser replaced by an Edgewave IS200-2-L laser. This laser was capable of a maximum repetition rate of 150 kHz, but at the expense of decreased pulse energy; to ensure pulse energies of up to 4 mJ at 355 nm, the laser was run at a maximum of 1 kHz. To create a steady jet with a variable concentration of biacetyl, the setup shown in Figure 3.10 was used.

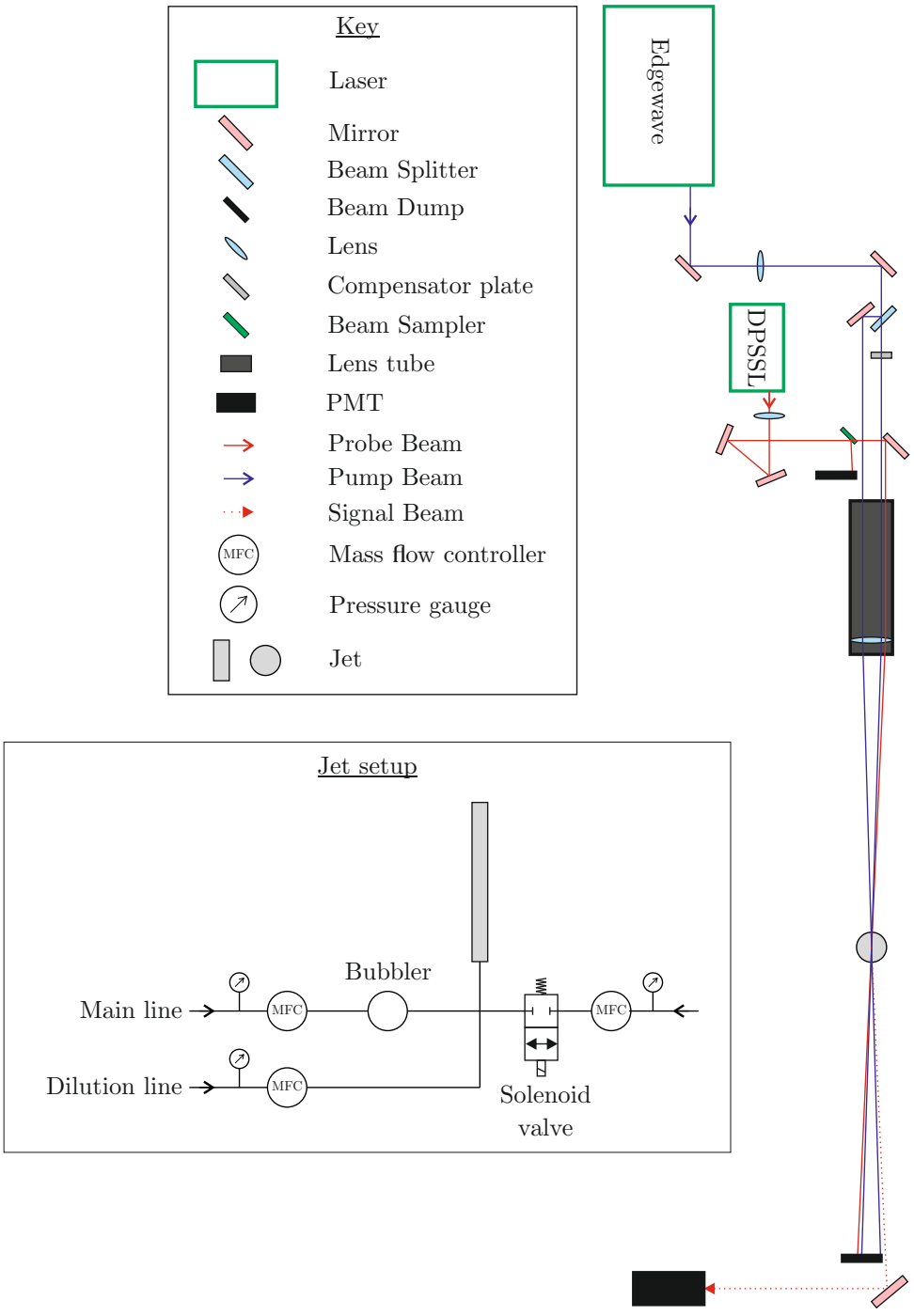


Figure 3.10: Schematic showing the experimental setup for characterising a steady jet. The inset schematic, showing the jet setup, explains how a steady jet was created. Gas flowing in the main line passes through the bubbler and becomes saturated with biacetyl vapour. This flow is then diluted by gas passing through the dilution line. The diluted gas then flows out of the jet, shown in grey. The LITGS measurements are taken at the crossing point of the beams, which is just above the opening of the jet.

3.4.1.1 Characterising the effect of biacetyl concentration

As explained in Section 2.1, the frequency of oscillations of the LITGS signal is a direct measure of the speed of travel for acoustic waves in the medium. The derivation of a temperature from this frequency is done by making use of Equation 2.3 from Section 2.1. This requires a knowledge of the local gas properties; in particular, the mean molecular mass (M) and mean ratio of specific heats (γ). When a tracer species is introduced into a gas, as is the case for biacetyl LITGS, then the concentration of the tracer will affect these gas properties. The extent of the effect for biacetyl LITGS is determined by the difference in γ and M, respectively, between the tracer species and the bulk gas. If unaccounted for, this variation in local gas composition, as identified in Section 2.1.3, would be a significant source of uncertainty for the technique.

The first experiment conducted at the facility was to characterise the effect of biacetyl concentration when it was used as a tracer species in air. Air was passed through the bubbler to seed it with saturated biacetyl vapour. This flow was then diluted by air that flowed through the dilution line. The dilution ratio δ was defined as

$$\delta = \frac{\dot{m}_{\text{tot}}}{\dot{m}_{\text{bub}}} \tag{3.11}$$

where $\dot{m}_{\text{tot}}$ was the total mass flow rate and $\dot{m}_{\text{bub}}$ was the mass flow rate through the bubbler. Figure 3.11**a** shows how the LITGS signal strength decreased as the dilution ratio was increased from 1 to 6. This is because a lower concentration of biacetyl results in a weaker thermal grating. The experimental data in Figure 3.11**b** shows that the measured frequency increased as the dilution ratio was increased, despite the temperature of the flow remaining constant. This was expected due to the difference in γ and M between air and biacetyl[5], as is shown by the dashed curves which represent theoretical predictions for different molar concentrations of the saturated biacetyl.

These results highlight how increasing the concentration of biacetyl in the flow results in a trade-off between increased signal intensity and decreased accuracy (unless the exact

[5]By holding the temperature, T, constant in Equation 2.3 in Section 2.1.1 a change in the ratio between M and γ must lead to a change in the frequency of oscillations F.

gas composition is known). Put another way, at higher biacetyl concentrations the derived temperature becomes more precise (due to increased signal intensity) but may suffer an increased systematic error.

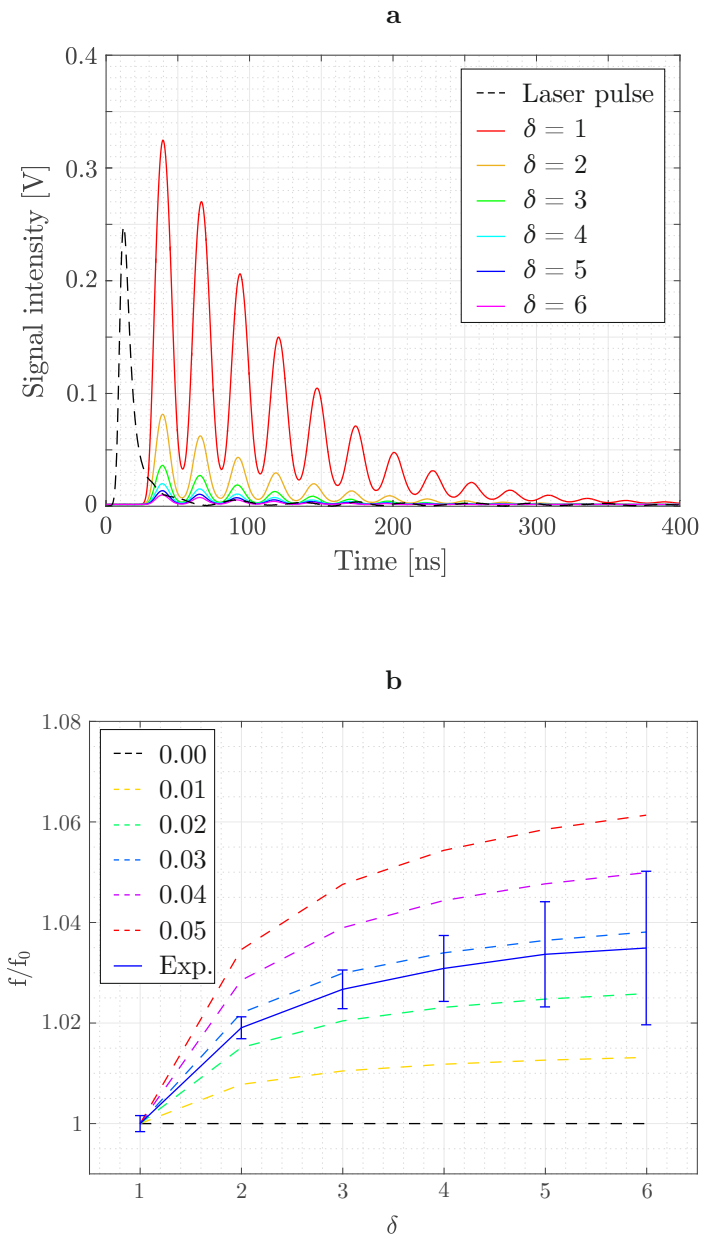


Figure 3.11: Figure **a** shows ensemble averaged LITGS signals obtained with varying dilution ratios (δ). Figure **b** shows how the frequency of the signals varied with dilution. The frequencies have been normalised by the frequency at zero dilution (f_0). The solid line shows the experimental data, while the dashed lines are predictions based on molar concentrations of saturated, undiluted biacetyl as given in the legend. The error bars show the standard deviation of the data from the mean.

3.4.1.2 Temperature measurements

For this experiment, a base flow of 40 slpm of air was passed through the bubbler, with no dilution added, and then through an in-line resistive heater with a variable voltage applied. Once the heater was set at a certain voltage, thermocouple measurements were taken without any biacetyl seeding (to reduce the consumption of biacetyl). The seeding was then turned on (by diverting the flow through the bubbler), and LITGS measurements were recorded. Figure 3.12 displays the results. The red dots represent the LITGS measurements in the seeded air, while the dashed line signifies an equal relationship between both measurements. The thermocouple measurements were taken in pure air, while the LITGS measurements required the addition of trace amounts of biacetyl. However, the heat transfer from the resistive heater to the gas mixture was constant for both measurements which explains why the LITGS temperature measurements were colder (extra energy was required to heat up the additional biacetyl vapour). The blue triangles show a calculated equivalent temperature in pure air from the LITGS measurements by accounting for this cooling effect of the biacetyl vapour.

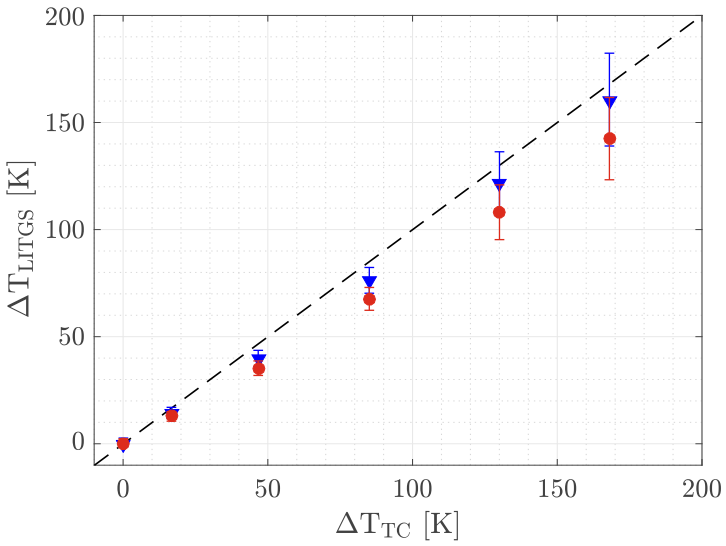


Figure 3.12: Measured temperature rise from ambient using LITGS ($\Delta T_{\mathrm{LITGS}}$), plotted against the thermocouple measurements (ΔT_{TC}). The dashed line demonstrates an equal relationship between both measurements. The red dots represent the LITGS measurements in seeded air. The blue triangles show the calculated equivalent temperature increase in a pure air jet from the LITGS measurements.

The results show a good correlation between the LITGS and thermocouple temperature measurements in a steady jet. However, the requirement of a tracer for the LITGS measurements must be accounted for if comparing temperature measurements with those taken without a tracer. The precision of the LITGS measurements also decreases at higher temperatures, which can be attributed to shortened signals due to an increased decay rate of the thermal grating from diffusive effects[6].

3.4.1.3 Characterising LITGS frequency for different gases

Equation 2.3 in Section 2.1.1 showed how the temperature of a gas is calculated from the measured frequency of a LITGS signal. The equation can be re-arranged to calculate the ratio of the molar mass of the gas, M, to the heat capacity ratio for the gas, γ, as being

$$\frac{M}{\gamma} = \frac{Tk_{\mathrm{B}}}{\Lambda^2 F^2} \tag{3.12}$$

where k_{B} is Boltzmann's constant, T is the temperature and F is the frequency of oscillations. Since this ratio is unique for different species, the frequency of oscillations for LITGS measurements taken in different gasses at a known temperature can be used to identify the gas composition.

For this experiment, there was no flow through the dilution line, so that the jet contained a saturated vapour of biacetyl. Mass flow rates of 5 slpm of air, carbon dioxide (CO_2), argon (Ar) and helium (He), respectively, were passed through the main line. Figure 3.13**a** shows the ensemble averaged LITGS signal for each gas. The difference in peak signal intensity is due to the quenching efficiency of each gas, which determines the rate and quantity of energy transferred to the gas. Figure 3.13**b** shows the derived frequency, obtained through a Fast Fourier Transform (FFT), of each ensemble averaged signal. For helium, because the signal did not have distinct oscillations, a frequency was not resolved by the FFT routine. The frequency was therefore determined manually by looking at the time period (τ) between the first two peaks as shown in the inset of Figure 3.13**a**, which is likely to explain the deviation from the best fit line.

[6]The shortened signals reduce the accuracy of the Fast Fourier Transform routine in extracting the frequency of oscillations from the signal, which was identified as a source of experimental uncertainty in Section 2.1.3.

The results show that the composition of the bulk gas affects the derived frequency of oscillations (and therefore the speed of sound through the gas) as expected by theory. Due to characteristic variations in quenching efficiencies between different gases, some offer 'better' performance (larger signal intensity and duration) for LITGS experiments. Of the gases tested, carbon dioxide was found to be the best while helium was the worst.

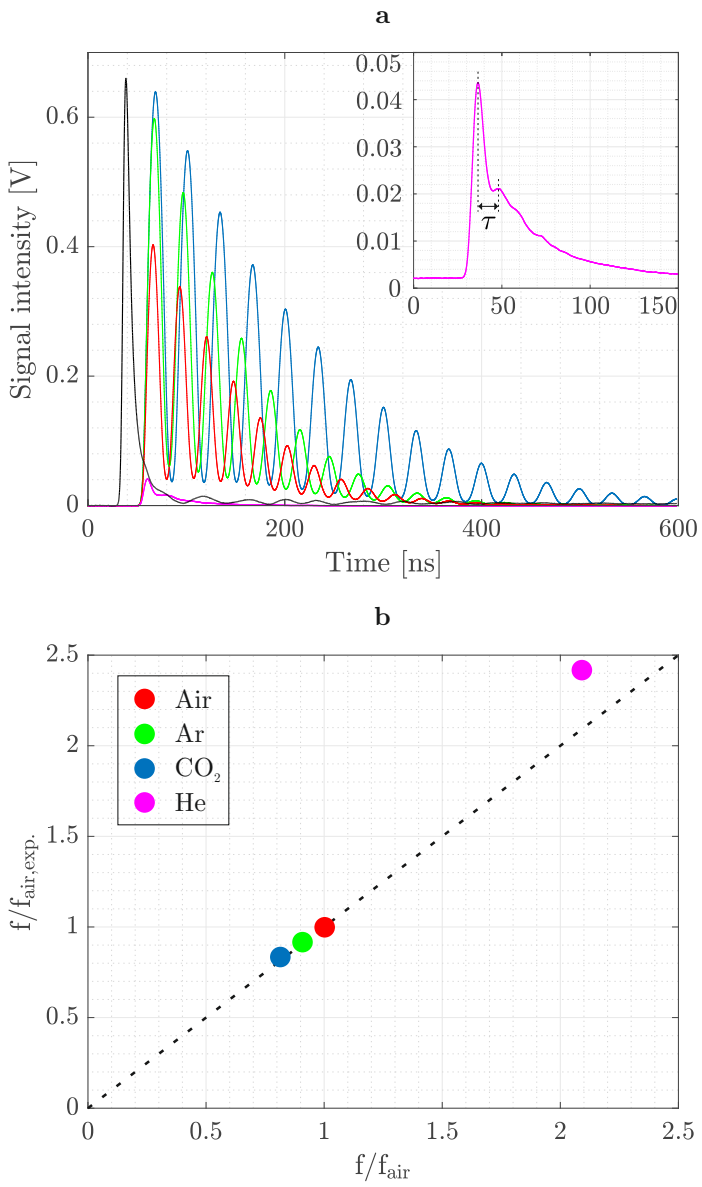


Figure 3.13: Figure **a** shows ensemble-averaged LITGS signals acquired in a jet of biacetyl-saturated air, argon, carbon dioxide, and helium. The inset image shows a zoomed-in helium signal. Figure **b** Shows the ratio between the peak frequencies obtained with different gases (y axis), normalised by that with air, compared to the theoretical expectation (x axis). The same colour coding, defined in the legend in Figure **b**, is used for both figures.

3.4.1.4 Measuring steady composition variations

The variation in measured frequency for different gases allows LITGS to be used to measure small compositional changes in a flow at known temperature. To demonstrate this, a non-diluted flow of air with saturated biacetyl vapour was mixed with varying flow rates of carbon dioxide (CO_2) and argon (Ar), respectively. This setup allowed LITGS measurements to be made of a steady flow with differing molar concentrations (X_i) of CO_2 and Ar. The molar concentration was calculated under the assumption that the mean signal frequency was composed of a weighted linear combination of the frequencies of both gasses. The results, displayed in Figure 3.14a, show good agreement with theoretical calculations.

The density variation ($\Delta\rho$) in the mean flow (ρ_0) due to the addition of the CO_2 and Ar flows, respectively, was calculated from the molar concentrations of each gas. Figure 3.14b shows how, using this method, the density variation in a flow due to the presence of a different (known) gas can be measured using LITGS.

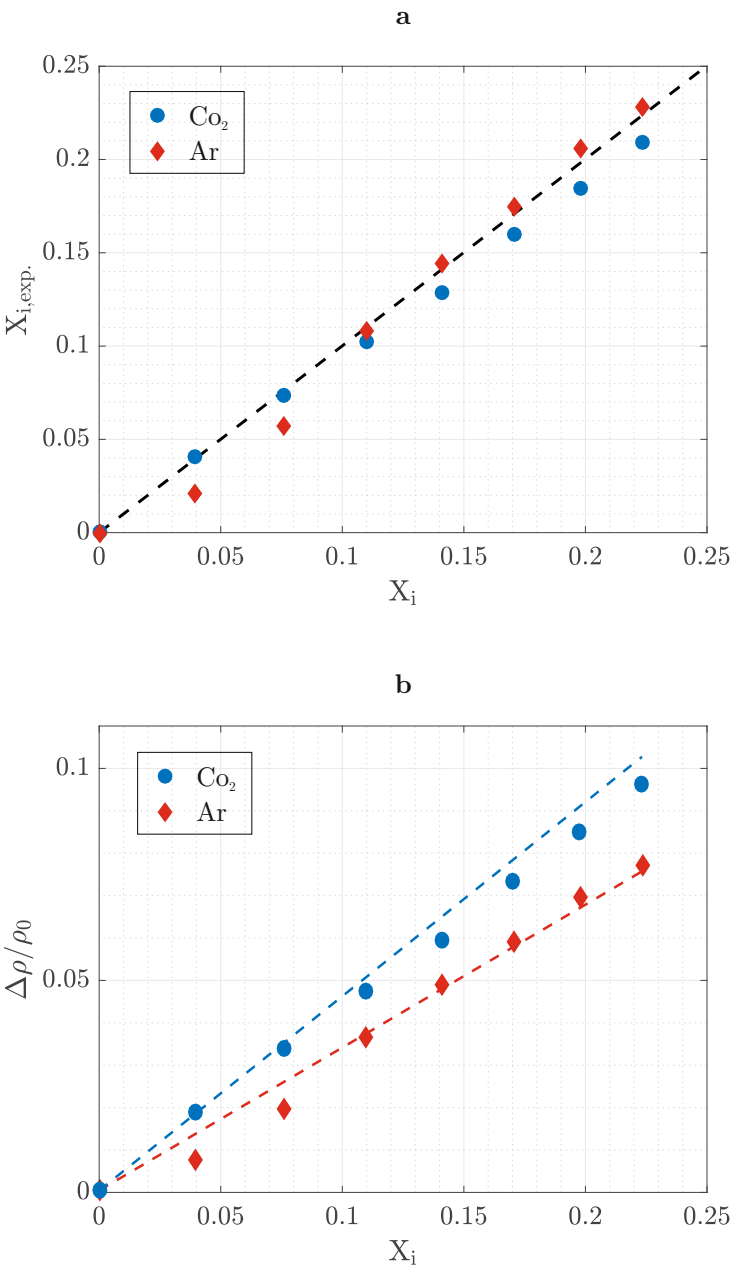


Figure 3.14: Figure **a** shows the measured mean molar concentrations in a jet of air of CO_2 and Argon (y axis) compared to theoretically calculated values (x axis). The dashed line indicates an equal correlation. Figure **b** shows the mean density variations using LITGS (y axis), relative to the expected concentrations based on dilution ratios (x axis). The dashed lines show the expected density through theoretical calculations.

3.4.1.5 Time-resolved composition variation measurements

For this experiment, a flow of 12 slpm of air was passed through the bubbler while another 5 slpm of air was directed through the dilution line. Packets of a different gas were periodically injected at the base of the jet using a fast response valve[7]. The alternative gases used were carbon dioxide (CO_2), argon (Ar) and helium (He). The frequency of the pulses was set to 3 Hz with a duty cycle of 20 %. Figure 3.15 shows the LITGS measurements taken at 1 kHz over 1 second.

The shape and amplitude of the gas pulses can be clearly identified in the frequency traces, including the characteristic rise and decay times. However, while the pulses of CO_2 and Ar are well defined, the He data shows a large amount of scatter near the peaks. This is due to the large quantity of He present in the flow at these times, causing a shorter signal with a smaller number of oscillations as explained in Section 3.4.1.3. The interpolation envelope shown by the solid black line in Figure 3.15**a**, calculated from the root-mean-square of 30 consecutive points, was therefore applied to the He data. The mole fraction (X_i) of the injected gas corresponding to each LITGS frequency was determined using the characterisation carried out in Section 3.4.1.4, and plotted in Figure 3.15**b**. The volumetric flow rates injected by the valve for the three gases, shown as the areas beneath each peak, are similar for the different gases as expected. The density variation at each point is obtained from the molar fraction. As the density of He differs substantially from air, the change in density due to the He pulses is much higher than for CO_2 and Ar.

[7] HSM2L7H50V model from Asco Numatics.

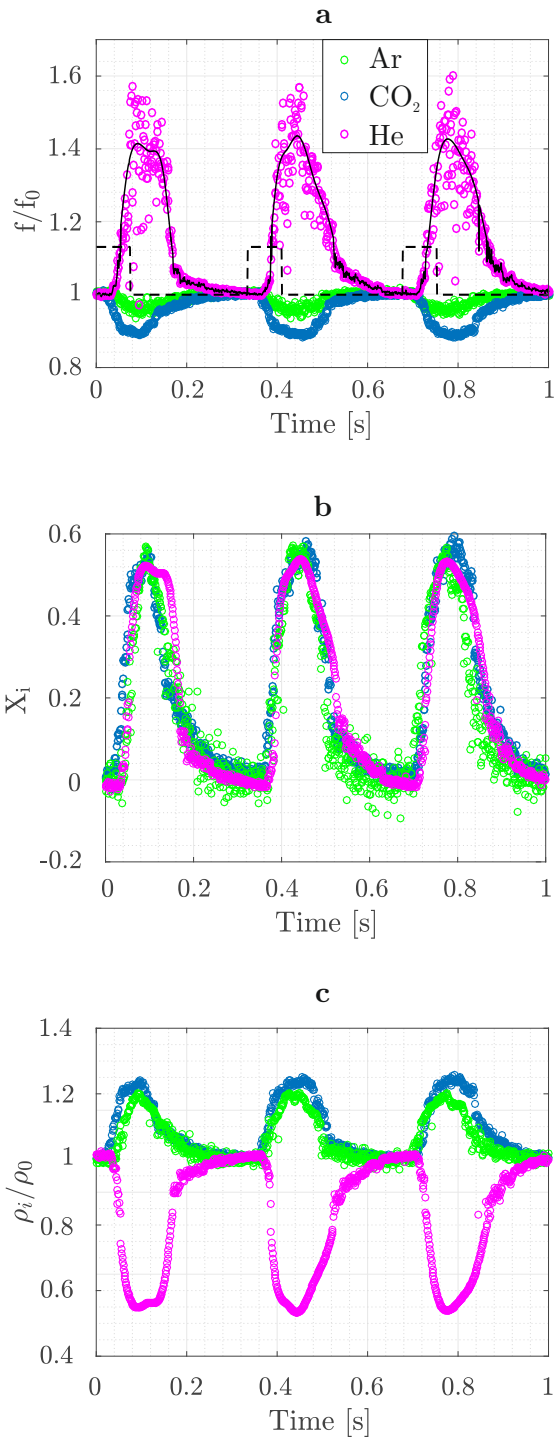


Figure 3.15: Figure **a** shows the normalised, time-resolved LITGS frequency variation in the jet flow as packets of gases were introduced via a valve (all three experiments are displayed together). The dashed line shows when the valve was opened. Figures **b** and **c** show the corresponding mole fraction and density variations as derived from the LITGS frequency measurements.

3.4.2 Time-resolved measurements in an entropy generation duct

For measurements in the entropy generator the same optical setup shown in Figure 3.10 in Section 3.4.1 was used. A schematic of the experimental layout is displayed in Figure 3.16. The LITGS beams were directed through the quartz tube, and crossed over within the tube along the centreline. The entire rig was on a traverse, which allowed measurements to be taken at the 5 positions x1–x5.

The mass flow rate of air in the experiment was set to 80 slpm. Nearly saturated or saturated air flows, with low or no dilution, respectively, were used. The laser pulse frequency was set to 500 Hz to allow the acquisition of longer periods of time in the data set due to the maximum number of samples that could be stored in the oscilloscope[8] memory buffer.

[8]The oscilloscope used for these experiments was a 4-channel LeCroy 6104A model, capable of a sampling rate of 10 Gs/s, 1 GHz bandwidth and a maximum of 40 million points real time memory.

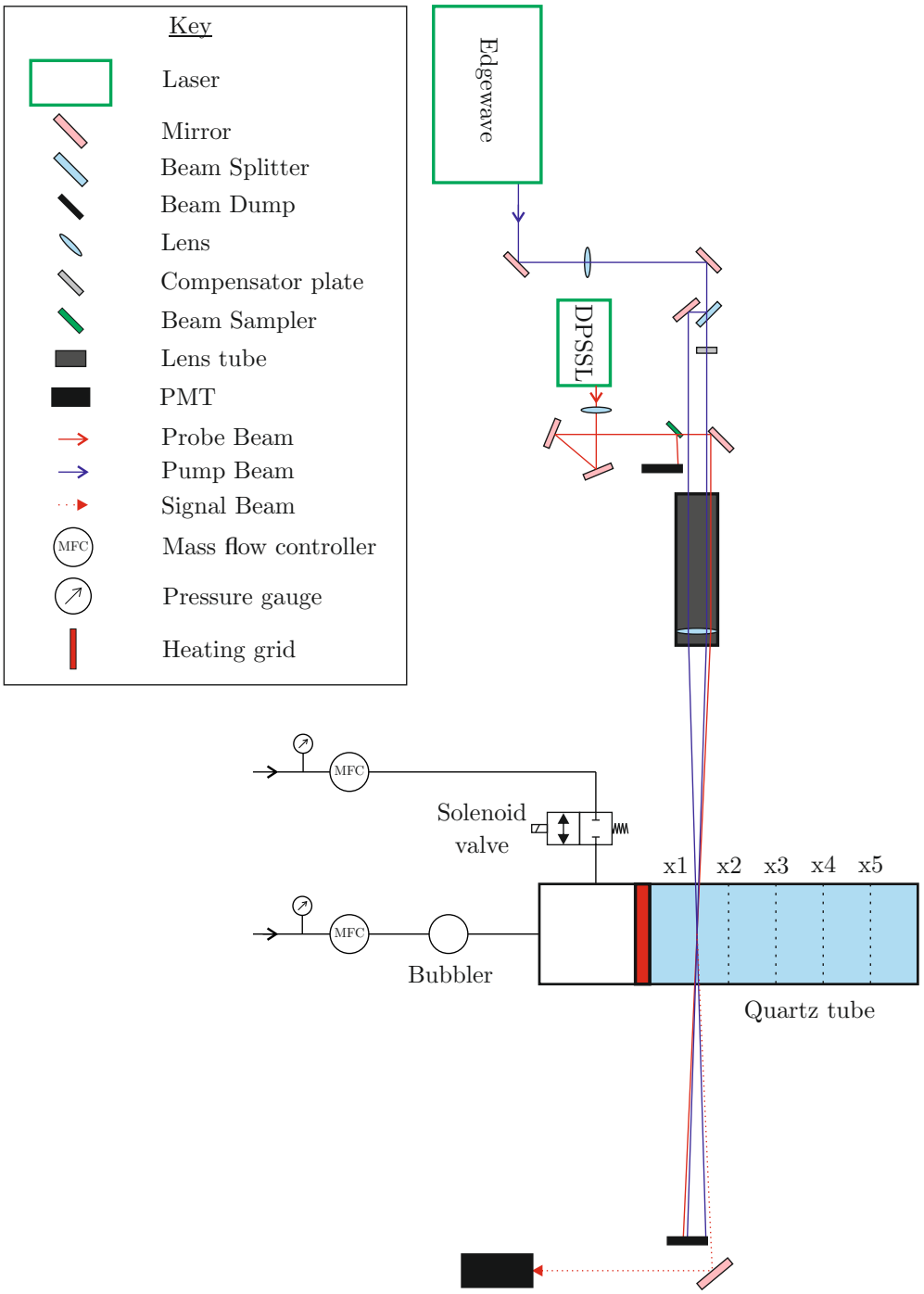


Figure 3.16: Schematic of the experimental setup used for the entropy spot generator (with a quartz tube to allow optical access). The positions x1-x5 show where LITGS measurements were taken. The beams were introduced transverse to the quartz tube and crossed along its centreline.

3.4.2.1 Detection of composition spots

Composition spots were detected using LITGS in the quartz tube at the five positions indicated in Figure 3.16. Three different gases (carbon dioxide, argon and helium) were injected into the mean flow via the solenoid valve at a frequency of 1 Hz and a duty cycle of 20 %. At each point, the passage of about 30 spots was recorded.

The results are presented in Figure 3.17. The first row shows the instantaneous time-resolved traces at the five locations for pulses of carbon dioxide, argon and helium. The passage of spots can be clearly identified in these signals. The consumption of biacetyl in the bubbler generates a small shift in the base flow frequency. As the level of biacetyl in the bubbler drops, its vaporisation becomes less efficient leading to a decrease in the concentration of biacetyl in the mean flow. This change in concentration therefore has to be taken into account to properly evaluate the mean flow properties at each location. This was achieved by evaluating the change in the frequency of the mean flow. After applying this correction, the 30 composition spot pulses were phase averaged to obtain clearer information on the shape and amplitude of the spots; this data is shown in row 3 of the figure.

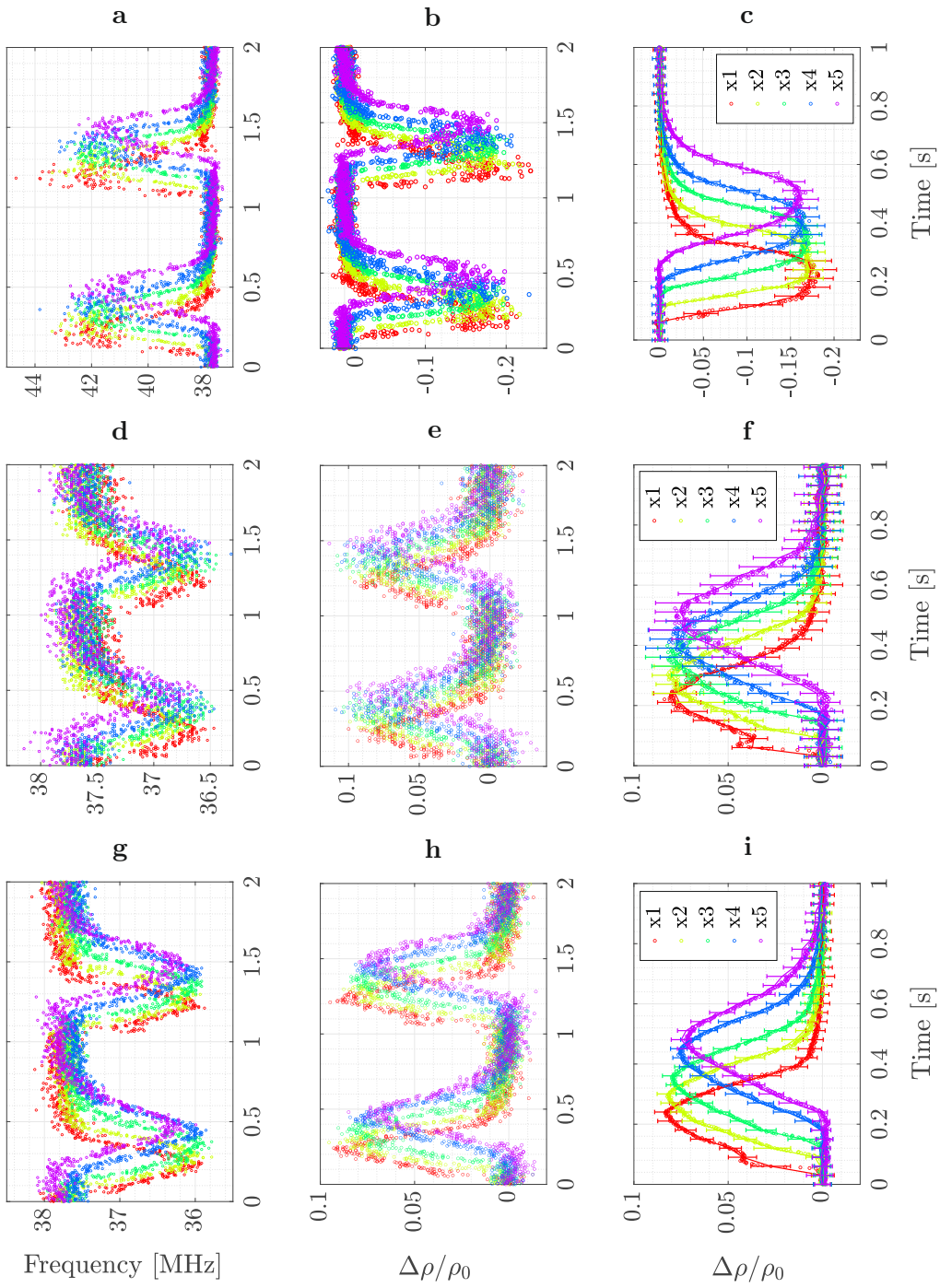


Figure 3.17: Detection of composition spots. The rows, from top to bottom, show data for helium, argon and carbon dioxide respectively at five locations along the quartz tube. Figures **a**,**d** and **g** show the time-resolved frequencies derived from the LITGS signals. Figures **b**, **e** and **h** show the time-resolved normalised density variations. Figures **c**, **f** and **i** show the ensemble-averaged normalised density variations.

Some features of the injected pulses were observed directly from the instantaneous mea-

surements. For example, the signals acquired in position x1 display a small 'hump' in the first few milliseconds, which corresponds to the first bounce of the composition spot off the opposite wall after being injected. This feature disappears in the subsequent positions. Some effects of dispersion can also be observed in the pulses, despite the short distance within the five measurements locations. The spots at x1 have a sharper shape, while at x5 they are more spread out. For the helium, as expected, the signals are more noisy relative to those for carbon dioxide and argon. It can also be observed (by the lack of a 'hump' in the data collected at position x1 and the generally more 'rounded' nature of the curves) that diffusive effects have a higher impact on helium than on carbon dioxide and argon. This was expected because helium is a smaller and lighter molecule with a higher diffusive coefficient.

3.4.2.2 Detection of temperature spots

The experiment detailed in Section 3.4.2.1 was isothermal. For the experiment detailed here, a heating grid was used to impose temperature variations onto the mean flow. These temperature spots were advected and dispersed along the flow and then characterised by LITGS at locations x1, x3, and x5 in Figure 3.16. The experimental conditions for this experiment were chosen to be comparable to the experimental case C1 reported by De Domenico *et al.* [90] to allow for a comparison of the LITGS results with the temperature data previously acquired with thermocouples and anemometers. Pulses of duration 200 ms and input power 35 V × 21 A on the power supply were delivered into the heating grid. The mass flow rate and duct dimensions were also chosen to be similar — a mass flow rate of 80 slpm flowing into a 42 mm inner-diameter rig was used here, compared to a mass flow rate of 78 slpm and a 42.6 mm inner-diameter rig as reported in [90]. The temperature measurements were also acquired at similar locations.

Figure 3.18**a** shows the time-resolved frequency traces obtained with LITGS. To reduce the scatter, the signal is averaged over 30 phase-locked traces (Figure 3.18**c**). After correcting for the base flow frequency shift due to a drop in biacetyl concentration as discussed in Section 3.4.2.1, the temperature increase ΔT was calculated (Figure 3.18**b**) The averaged temperature traces obtained in this way were then compared with the measurements in [90] (Figure 3.18**d**). The comparison between the thermocouple and LITGS measurements was good, even though the measurements were acquired in different facilities with different flow rates at slightly different positions. In [90], the thermocouple measurements were corrected using a faster hotwire, and an inaccuracy of the order of 1–2 K was expected. The LITGS measurements reported here captured the rise and fall of the temperature well. It can be noted, however, that the LITGS measurements recorded a systematically lower temperature than the thermocouples. In addition to differences between the two experimental setups, this discrepancy could be due to the poor spatial resolution of the LITGS setup which contained temperature contributions over a distance of ∼75 mm (which was the total length of the LITGS grating).

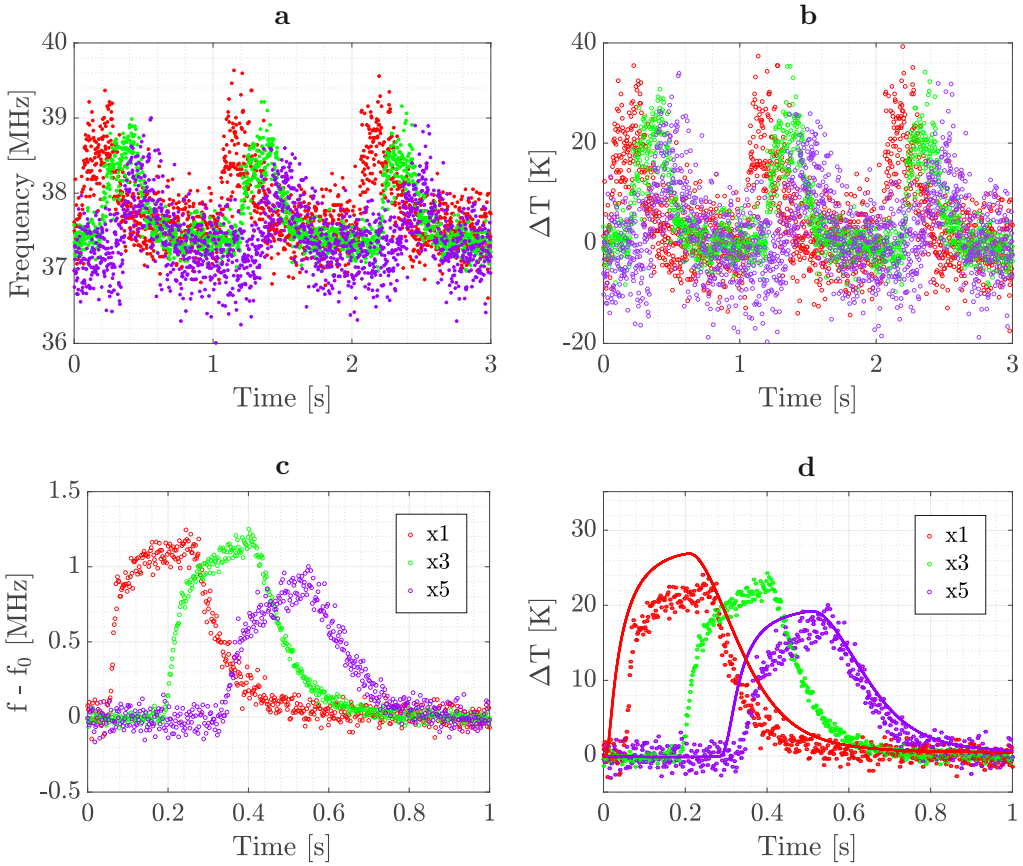


Figure 3.18: Measured time-resolved temperature fluctuations. Figure **a** displays the frequency fluctuations in the LITGS signals, Figure **b** shows the derived temperature deviation from the initial value, Figure **c** shows the averaged frequency variation, and Figure **d** shows the ensemble-averaged temperature obtained with LITGS (circles) and with an anemometer and thermocouples (lines) from [90].

3.5 Summary

The work presented in this Chapter has demonstrated the novel use of biacetyl as a tracer species for Laser-Induced Thermal Grating Spectroscopy (LITGS) using a pump laser emitting at 355 nm. Biacetyl is already established as a commonly used tracer for Laser-Induced Fluorescence (LIF), and facilitates the practical use of accessible high repetition rate lasers which allows for temporally-resolved LITGS measurements.

The addition of a tracer species into a flow introduces a systematic error in temperature measurements due to the effect of 'beam heating'. Section 3.3 explained how the impact of beam heating, when using biacetyl, was investigated. The results showed a negligible induced error for laser pulse energies up to 6.4 mJ. A theoretical evaluation of the effect of beam heating at different concentration levels of biacetyl also showed that its use as a tracer species (molar concentration of below 2.4 %) would result in a temperature variation of under 1 % due to beam heating effects.

The technique was then characterised using a steady jet. It was found that increasing the concentration of biacetyl (as the tracer) in a flow was correlated with an improved LITGS signal intensity, but also an increased systematic deviation of the frequency of the signal due to the change in gas composition. Quantifying the concentration of biacetyl is therefore an important consideration when using it as a tracer for LITGS. Temperature measurements were conducted in the jet and showed a good fit with measurements taken by a thermocouple. Next, isothermal LITGS measurements were taken in four different gases (air, argon, carbon dioxide and helium), all seeded with biacetyl vapour, to characterise the speed of sound (and therefore LITGS signal frequency) in each gas. The experimental results showed a good correlation with theoretical values, although the low LITGS signal intensity in helium reduced the accuracy of its frequency measurement. The disparity in frequency for different gases, when measured at the same temperature, was exploited to determine the concentration of different gases in a binary mixture. In two different experiments, varying concentrations of argon and carbon dioxide, respectively, were added to a bulk flow of air seeded with biacetyl vapour, and the frequencies derived from LITGS measurements were used to determine the molar concentrations of each gas in the flows. The results

showed a good fit with theoretical predictions, which demonstrates the potential for LITGS to measure species concentrations at known temperatures. Time-resolved concentration measurements, collected at 1 kHz, were obtained over three experiments by introducing pulses of argon, carbon dioxide and helium, respectively, into the bulk flow.

Having characterised the technique for temperature and isothermal concentration measurements, it was applied at the Cambridge University Engineering Department's 'Entropy Generator' facility. Pulsed variations were introduced into a bulk flow of air seeded with biacetyl vapour travelling down a duct, and time-resolved (collected at 500 Hz) temperature and concentration measurements were obtained at five different positions along the duct. Pulses of heated air were added for the temperature measurements, while pulses of a different gas (argon, carbon dioxide and helium, respectively) were introduced for the concentration measurements. The results showed that the pulsed variations were well resolved, and the effects of dispersion could be viewed as they travelled along the duct. The characterisation of the temperature pulses showed good agreement with data collected previously using thermocouples. However, the LITGS temperature measurements were systematically lower which could be due to the poor spatial resolution of the technique in this setup.

4 Axially-resolved LIGS: Theory and Modelling

This chapter introduces the inherent spatial resolution problem of LIGS, and explains how imaging of the LIGS signal can be used to obtain spatially-resolved measurements in the axial direction. The application of concepts from Scheimpflug imaging is introduced, and the theory behind this imaging technique is explored. Finally, a computational model of the technique is developed and used to conduct a parametric investigation.

4.1 Motivations

Chapter 2 presented LIGS as a relatively cheap, accurate and precise optical diagnostic method for (primarily) temperature measurements compared to the widely-used CARS technique. The most significant disadvantage of the technique, its spatial resolution, was also introduced. Figure 4.1 defines the geometrical directions used throughout this thesis.

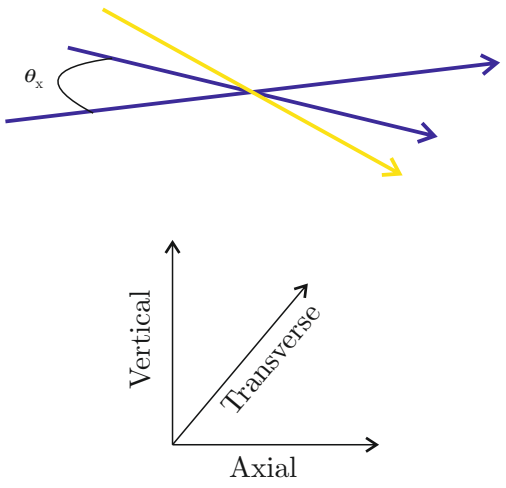


Figure 4.1: Diagram showing the definition of directions used when referring to the spatial geometry of LIGS. The blue arrows represent the pump beams, crossed at an angle θ_x, and the yellow arrow is the probe beam.

In the vertical direction, Stevens and Ewart [39] were able to achieve simultaneous 1-D measurements with a spatial resolution of 150 µm. However, the use of a streak camera for detection meant that the measurements were time-averaged over several shots. More recently, Willman and Ewart [91] presented simultaneous 1-D single-shot temperature measurements with a spatial resolution of 1 mm. In the transverse direction, the spatial resolution is limited by the width of the beams used. This can be easily minimised to be <1 mm by using lenses to focus the beams.

The spatial resolution in the axial direction is inherently poor. To understand the reason for this, a closer look at the generation of the signal beam is required. As described in Section 2.1, the temperature of the gas is derived from the oscillation frequency of the signal beam. This signal beam is produced by the coherent scattering of the probe beam by the grating, as shown in Figure 4.2. However, Figure 4.2 also shows that rather than the signal beam originating from a point in space, it is generated by the scattering of the probe beam along the entire length of intersection between the probe beam and the grating. The resulting signal frequency (and temperature calculated from it) is therefore derived from an extended region, giving rise to an undesirably poor spatial resolution. To give an idea of the magnitude of this spatial resolution, geometrical considerations show that a typical non-focused LIGS setup, with pump beams which are 1 mm in diameter and crossed over at an angle of 2.3°, would have an interaction region which is about 50 mm long.

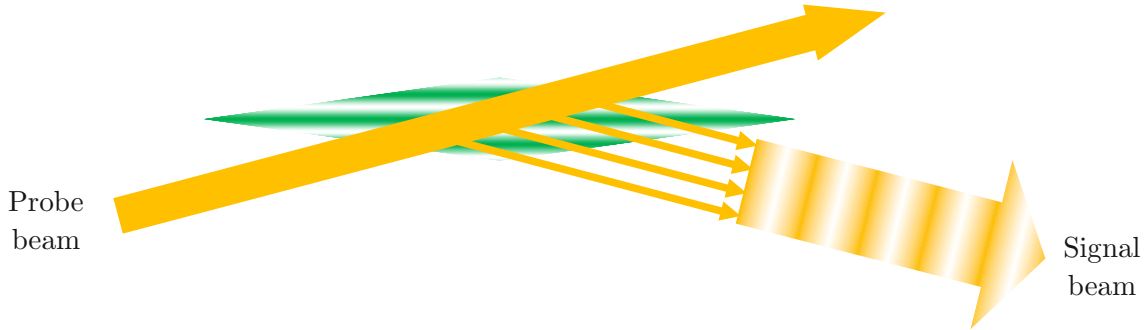


Figure 4.2: Diagram showing how the LIGS signal beam is generated. A probe beam is directed at the grating (shown in green) and coherently-scattered by the grating, at the first-order Bragg-angle, to produce the signal beam.

One way to reduce the length of the interaction region would be to increase the crossing angle of the two pump beams. However, as Equation 2.1 shows, this would have the effect of reducing the fringe spacing. This is somewhat tolerable, but ultimately a very small fringe spacing creates a very high frequency signal which is beyond the detector bandwidth. Furthermore, for a minimal fringe spacing, the diffusion process which destroys the temperature grating would occur rapidly resulting in very short signal lifetimes (again with the implication that the frequency would be unrecoverable, this time due to the absence of oscillations).

4.2 Concept overview

Section 4.1 introduced how the LIGS signal beam is produced over the entire intersecting region of all three laser beams (two pumps and one probe) resulting in an inherently low spatial resolution. As shown in Figure 4.3, a solution is to divide the signal beam into sub-elements and analyse each 'sub-signal' individually. By using a suitable imaging system each sub-signal can be traced back to its origin, thereby offering a way to simultaneously obtain multiple 1-D spatially resolved temperature measurements every time the lasers are fired.

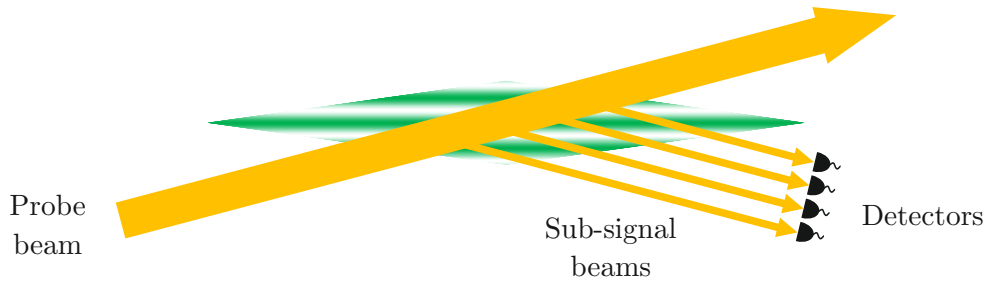


Figure 4.3: Diagram showing a solution to increasing the spatial resolution of LIGS. A probe beam is directed at the grating (shown in green) and coherently-scattered by the grating, at the first-order Bragg-angle, to produce the signal beam. Detectors analyse parts of the signal beam ('sub-signals') separately to obtain a measurement for a smaller region.

The need for an imaging system is illustrated by Figure 4.4. Figure 4.4**a** shows how the 'sub-signal' beams are divergent (due to diffraction at the grating) which results in interference between the sub-signals by the time they reach the detector. A solution to this, shown in Figure 4.4**b**, is to use a lens to image the origin of each sub-signal onto the detector.

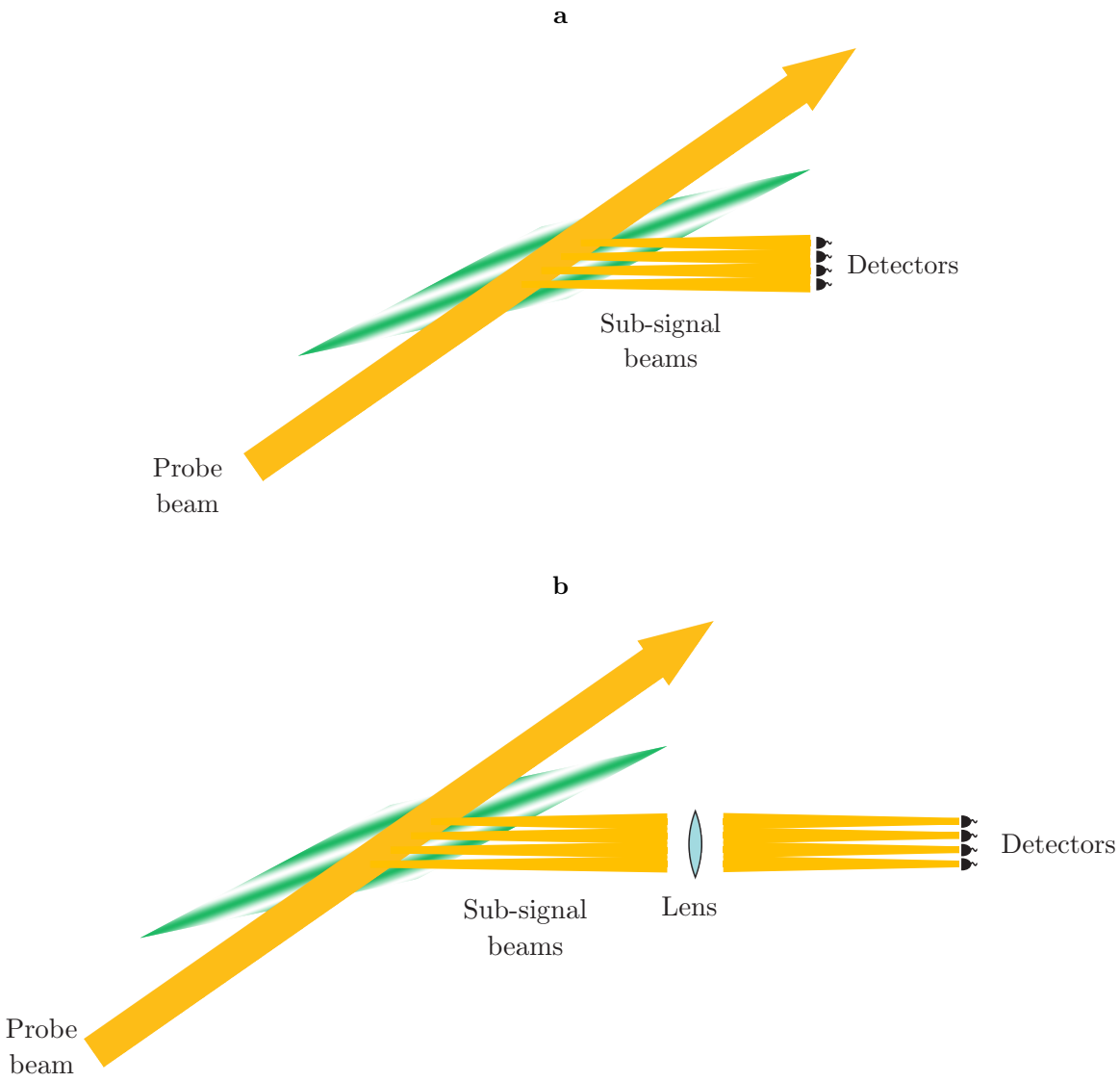


Figure 4.4: Diagram **a** illustrates how, in reality, the 'sub-signal' beams are divergent. Diagram **b** shows how a lens can be used to image the beams onto the detectors.

Unfortunately, this imaging is not trivial. As Figure 4.5 illustrates, if the plane along which the sub-signals were created (object plane) was perpendicular to their propagation direction, then the lens plane (the plane along which the imaging lens would be placed) and image plane (the plane in which a focused image is produced) would also be perpendicular to the propagation direction. This would mean that the lens and detectors could be placed perpendicular to the sub-signals. However, as Figure 4.6 shows, the object plane in a typical LIGS experiment would be at an angle. This kind of imaging problem can be solved using so-called 'Scheimpflug' imaging.

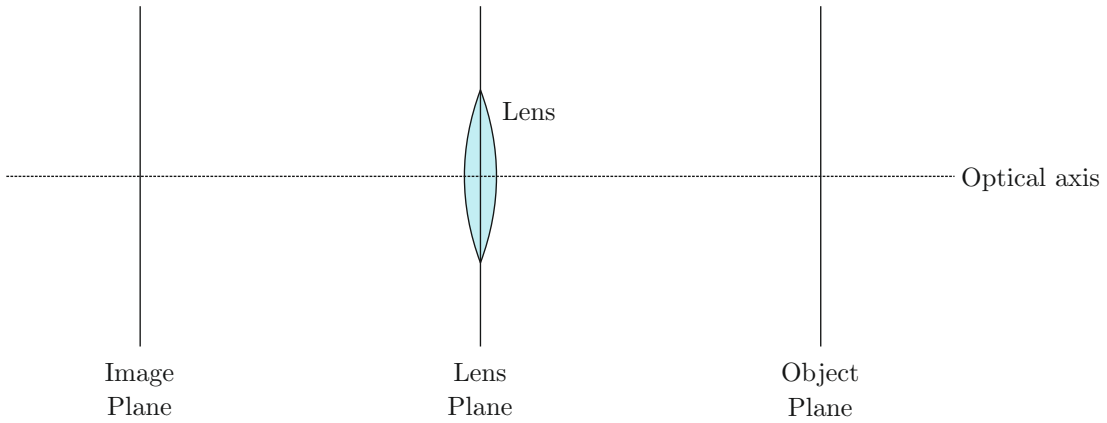


Figure 4.5: 'Standard' imaging setup where an object placed on the object plane will be in focus on the image plane.

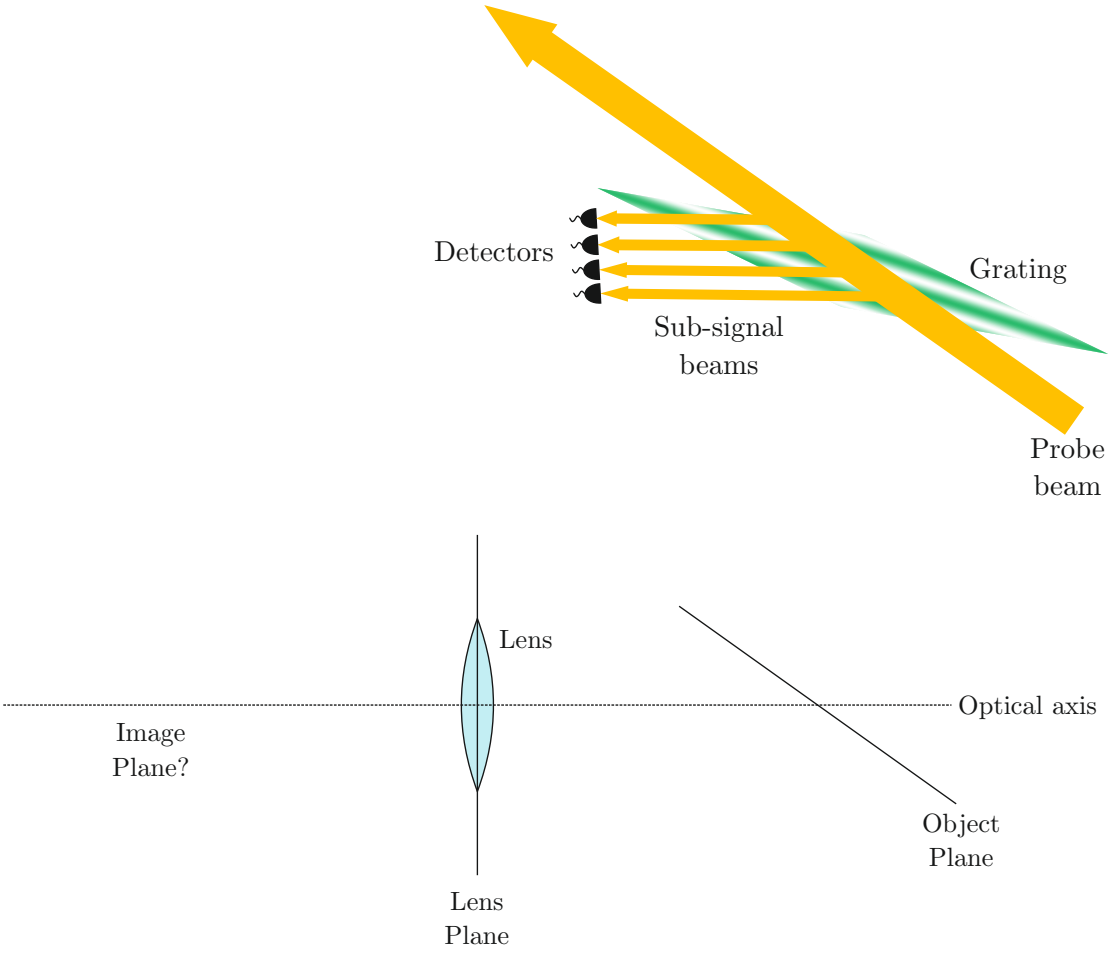


Figure 4.6: Imaging setup required to image sub-signals. Setting the sub-signal beams to propagate parallel to the optical axis, the object plane (along which the sub-signals originate) is now angled. The image plane (along which the detectors must be placed) will no longer be perpendicular to the optical axis.

4.3 Scheimpflug imaging

As introduced in Section 4.2, Scheimpflug imaging is required to obtain sharp, in-focus images of objects along a tilted plane. This section will describe the theory behind the Scheimpflug principle. Although the principle is eponymous of Theodor Scheimpflug[1] following his explanation of it in a patent application [92], this thesis will use the nomenclature presented by Merklinger [93] since it seems to be more widely accepted.

[1]Scheimpflug was not the first person to present this idea, even by his own admission [94].

There are two rules that must be followed when applying this principle to image an angled object plane. The first, known as the 'Scheimpflug rule', simply satisfies the thin lens equation which defines the relationship between the focal length of the lens (f), the distance of the object from the lens (u) and the distance of the image from the lens (v):

$$\frac{1}{f} = \frac{1}{u} + \frac{1}{v} \tag{4.1}$$

When this relationship is applied to a tilted object plane, a simplified statement of the rule can be made - the object, lens and image planes must all intersect as shown in Figure 4.7.

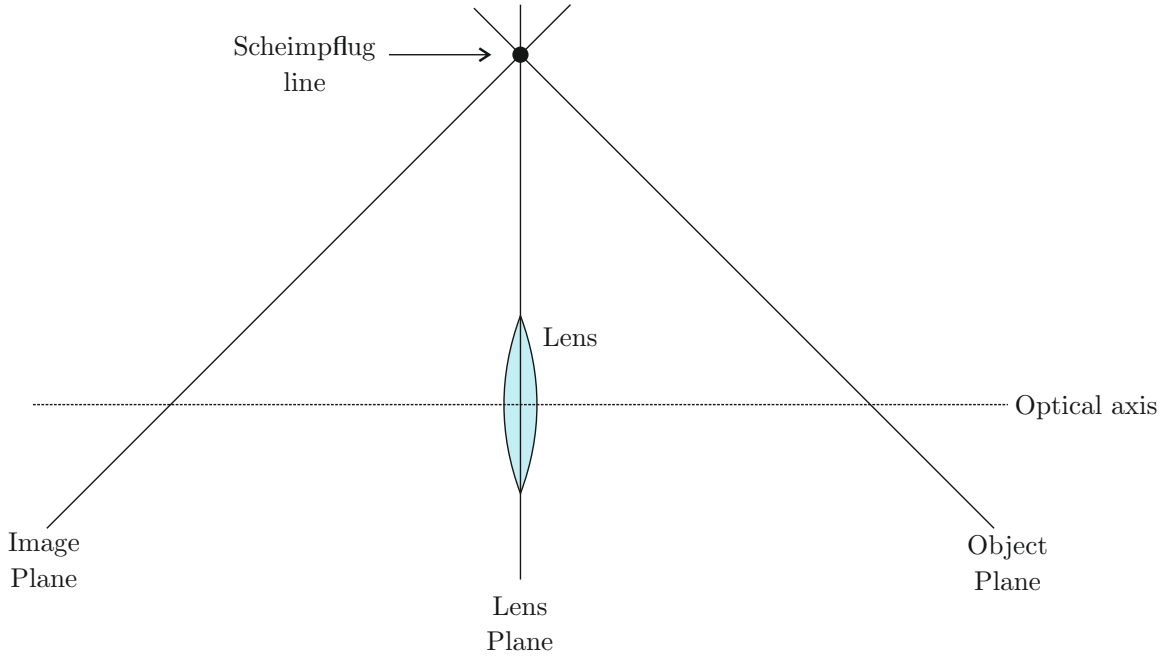


Figure 4.7: Depiction of the 'Scheimpflug rule'. The Scheimpflug line is where the object, lens and image planes intersect. Note that even though it appears as a point in this diagram, in reality it is a line that extends into the paper since we are dealing with planes.

To explain the second rule, two new planes must be introduced. The first one is a plane that is parallel to the image plane, but runs through the centre of the lens. Merklinger [95] called this the 'parallel-to-film plane', but for clarity it is referred to as the 'parallel-to-image (PTI) plane' in this thesis, as shown in Figure 4.8. The light rays from any object placed along this plane, and passing through the centre of the lens, would be incident on the image plane at an infinite distance from the centre of the lens. This idea becomes clear when

considering the 'standard' case where all the planes are vertical; the lens and PTI planes would be coincident and so any rays travelling from the PTI plane through the centre of the lens would be vertical. The second plane, called the 'front focal plane', is parallel to the lens but one focal length in front of it. Any object along this plane would be brought to a focus at an infinite distance behind the lens. This is more intuitive, and can be shown by a simple ray tracing diagram. The second rule, referred to as the 'hinge rule', states that the PTI, front focal, and object planes must all intersect as shown in Figure 4.8. This rule is also somewhat intuitive since any object placed on this intersection line (the 'hinge line') would be brought to a focus on the image plane at an infinite distance behind the lens.

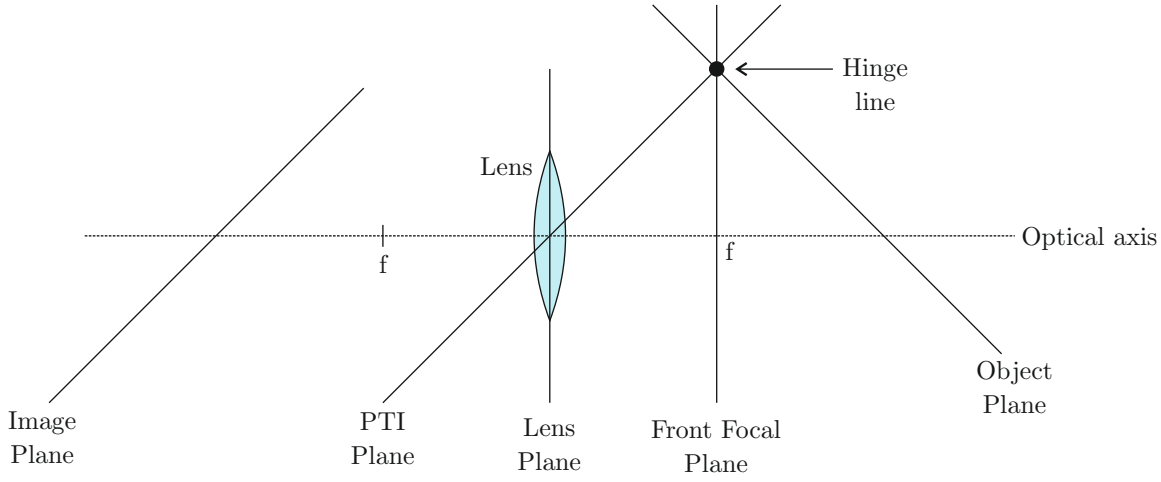


Figure 4.8: Figure showing the hinge rule. Note that 'f' is the focal length of the lens.

The complete Scheimpflug solution, satisfying both rules, is shown in Figure 4.9. If the angles of the lens and image plane are fixed, then moving the image plane forwards and backwards along the optical axis results in the Scheimpflug line moving up and down along the lens plane, while the object plane rotates about the hinge line.

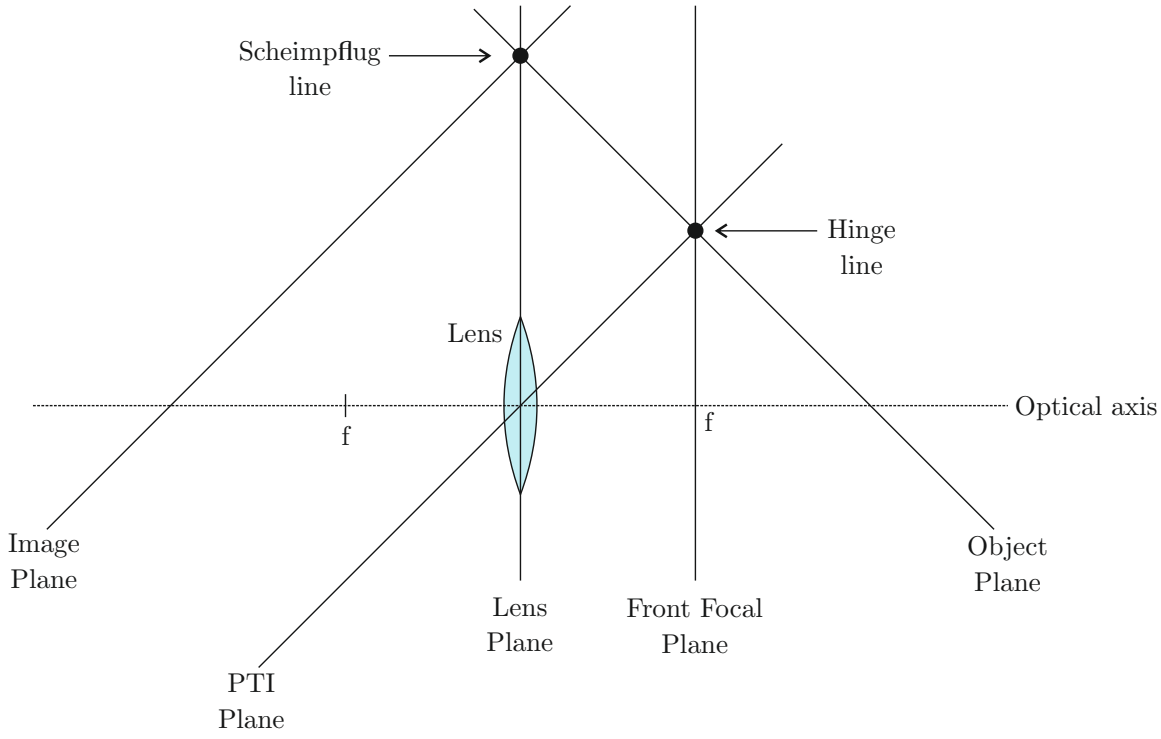


Figure 4.9: Figure showing the complete Scheimpflug solution.

In order to calculate the angle of the image plane for a given Scheimpflug imaging problem, the coordinates of the hinge line must be determined. First, the horizontal distance (H_x) of the hinge line from the centre of the lens is calculated using the equation:

$$H_x = \frac{u\tan(\theta) - \frac{f}{\tan\Delta}}{\tan(\theta) - \frac{1}{\tan\Delta}} \tag{4.2}$$

where u is the distance (along the optical axis) between the object (in our case the grating) and the lens, θ is the angle between the object plane and the optical axis (in our case the probe angle), f is the focal length of the lens and Δ is the angle between the lens plane and the vertical plane that is perpendicular to the optical axis. These definitions are presented in Figure 4.10. The next step is to calculate the vertical distance (H_y) of the hinge line from the centre of the lens, which is given by:

$$H_y = \tan(\theta)(u - H_x) \tag{4.3}$$

The angle of the image plane (γ) can then be calculated by:

$$\gamma = \tan^{-1}\left(\frac{H_y}{H_x}\right) \tag{4.4}$$

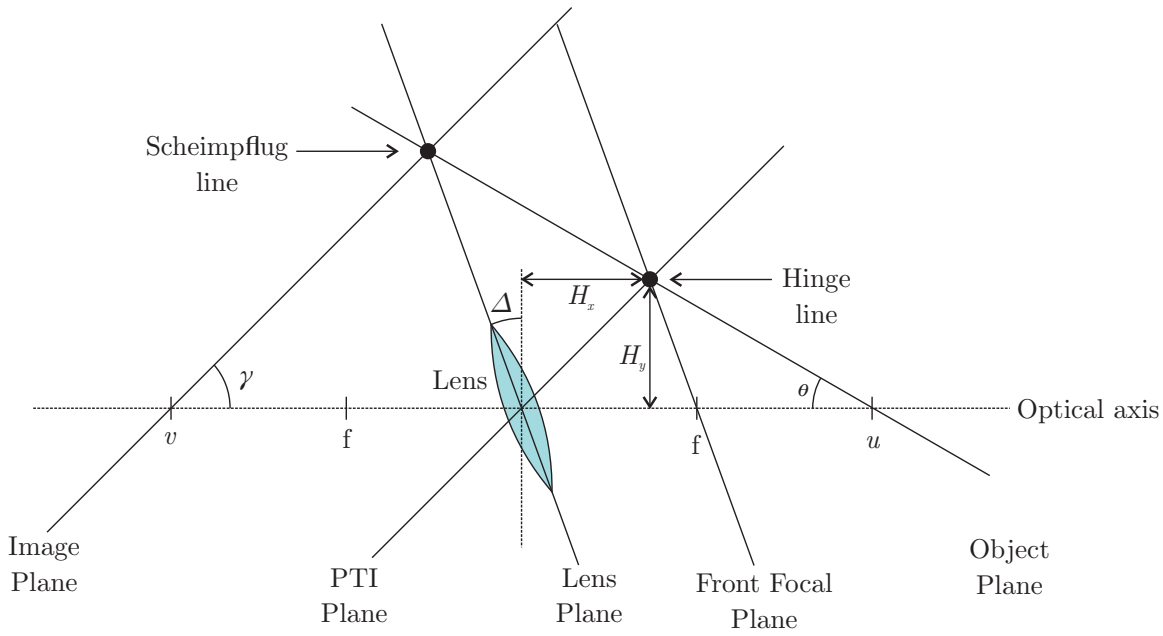


Figure 4.10: Figure showing the complete Scheimpflug solution, as well as the angles and distances used in calculations. Note that u, v and f are absolute horizontal distances from the centre of the lens.

The final imaging concept that is of interest here is the depth of field of the system. This can be defined as the distance from the image plane at which the image can still be considered to be in focus. This limit is somewhat subjective and dependent on the permissible error in its application. The calculation is outside the scope of this description[2], but the shape of the field is worth noting. As shown in Figure 4.11, the depth of field for the system can be determined by two lines that also intersect with the hinge line resulting in a wedge-shaped field which offers some freedom in the distance of the object from the lens when placed along the optical axis.

[2]Merklinger [93] includes a clear explanation of the calculation and derivation of the depth of field.

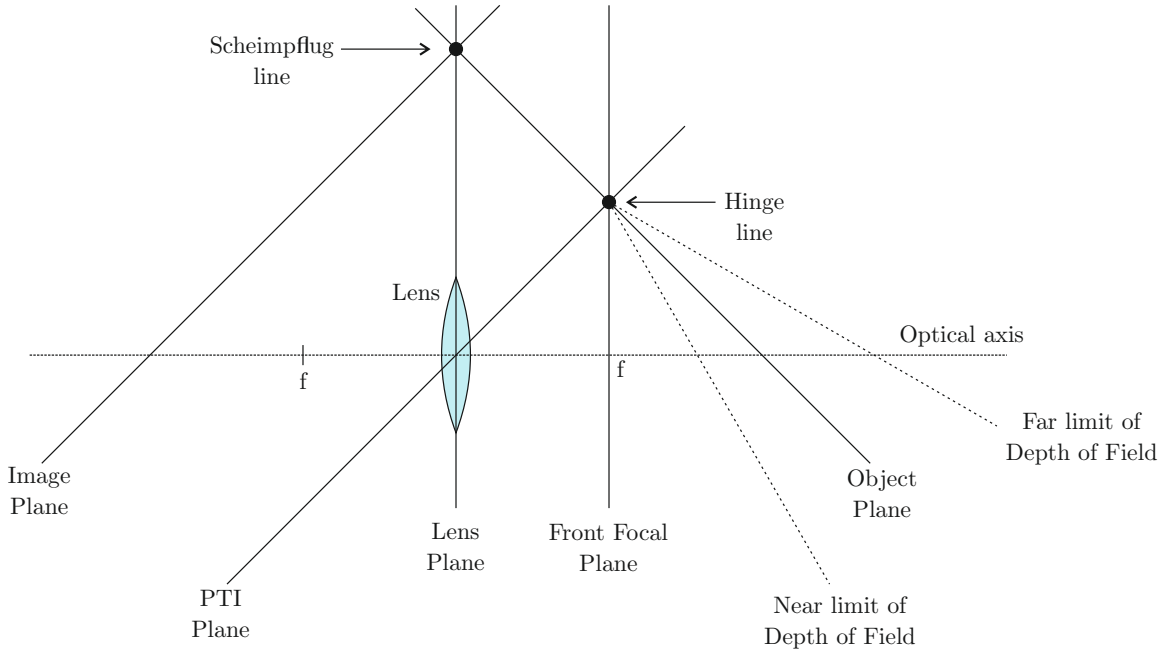


Figure 4.11: Figure showing the complete Scheimpflug solution with depth of field (bounded by the lines labelled 'near limit of depth of field' and 'far limit of depth of field').

4.4 Experimental design for characterisation

Having explained the concept of Scheimpflug imaging, this section explores how the approach could be characterised for a LITGS experiment. Figure 4.12 shows a simplified experimental layout. Two pump beams and a probe beam are crossed, at pre-determined angles, at the measurement point. As explained in Section 2.1, the region over which the pump beams cross (the 'interaction region') is where the thermal grating is established (in the presence of a suitable absorbing species), and the signal beam is produced by the scattering of the probe beam from this grating. Therefore, a signal can be generated from different locations within the interaction region by selectively supplying these locations with the absorbing species. To achieve this, nitrogen gas was passed through a seeder (which introduced the relevant absorbing species, as a vapour, into the gas flow), before being emitted through a needle (oriented vertically and set on a translation stage). This created a well-resolved jet of gas seeded with the required absorbing species, which enabled a LITGS signal to be created from *only* the location at which it flowed through the interaction region.

An imaging lens was used to image the signal beam, at the location at which it was

generated from the jet, onto a linear array of optical fibres. Each optical fibre led to an individual photomultiplier tube (PMT). Optical fibres were required because the relatively large housings of the PMT modules prohibited them from being placed close to each other. As the needle was displaced by the translation stage, the location of the generation of the signal beam was varied which meant that the imaged beam would travel along the array of fibres. For the application of Scheimpflug imaging, the object is the thermal grating (and therefore the object plane runs through the centre of the grating). Therefore the surface of the fibres should be set along the image plane.

A qualitative experiment was successfully conducted to verify the experimental design. The details are presented in Appendix A.

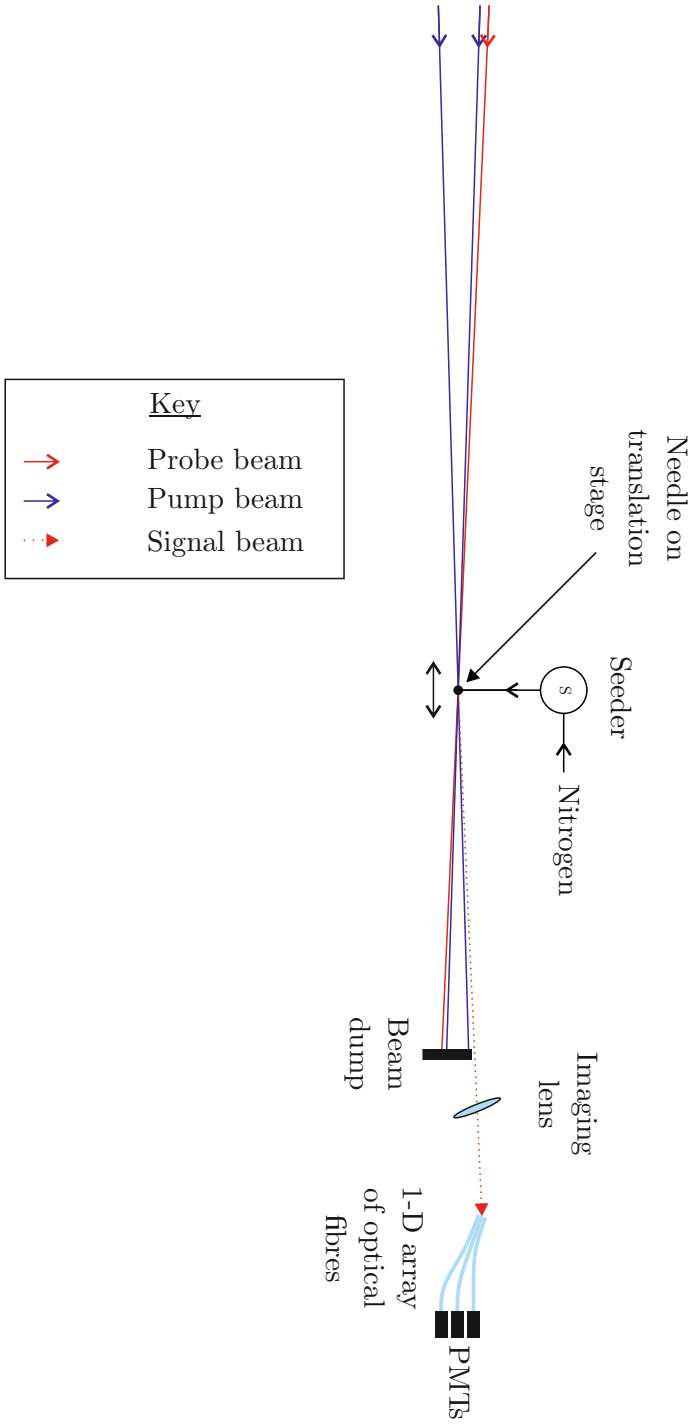


Figure 4.12: Plan view of the simplified experimental setup. Note that the needle emits a jet of nitrogen, seeded with an absorbing species, in the direction out of the paper. The laser beams pass through the jet.

4.5 Computational model

The theory behind Scheimpflug imaging introduces many experimental parameters, through the placement and angle of various planes, that can be optimised for any given setup. As these parameters are all interlinked and rely on the fundamental behaviour of optics as they are moved or rotated, it is difficult to predict what the optimal solution will be for a certain experiment. To aid with this, as well as to explore the effects of various changes to the experimental setup, a computational model was created using MATLAB[3]. Figure 4.13 gives an overview of how the model works. The next subsections explain each of the steps in more detail.

[3]The OptoMetrika Matlab library [96] was used for ray-tracing within the model. Note that this computational model therefore relies on the assumption that the propagation of light can be treated as a ray.

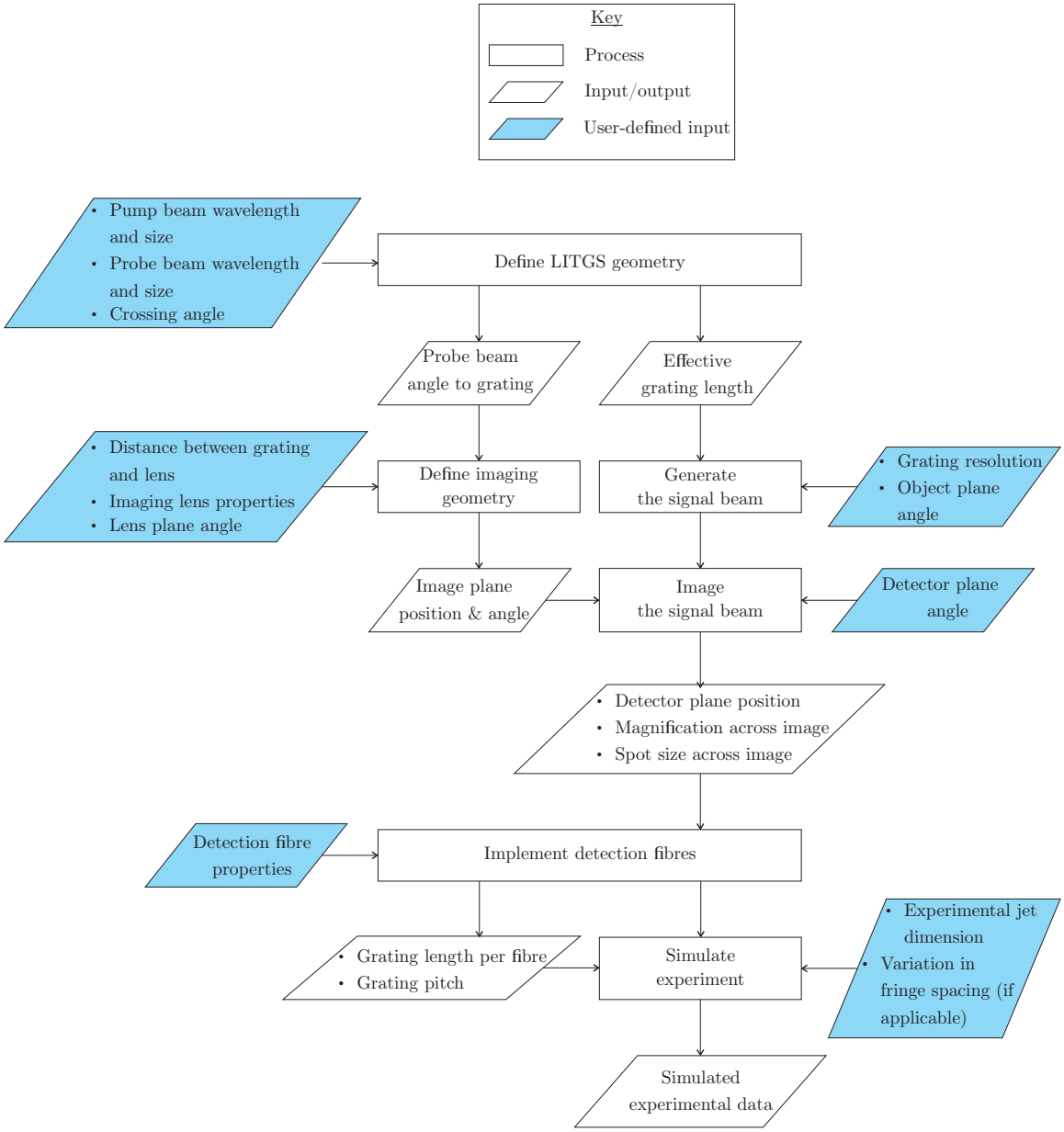


Figure 4.13: Flowchart showing the functionality of the computational model.

4.5.1 LITGS geometry

The first aspect to be modelled was the LITGS geometry being used for a given experiment. The program requires the user to input the wavelengths of the pump and probe lasers being used, their respective beam sizes, and the crossing angle for the pump beams. It then calculates the fringe spacing created by the interaction of the two pump beams, and the angle at which the probe beam must cross the pump beams (using Equation 2.2).

Next, the length and width of the grating are calculated by simple trigonometric equations. Rather than using the total length of the grating, the 'effective grating length' is used. This is defined as the length of the grating which interacts with the probe beam, and is demonstrated in Figure 4.14. As well as the length of the grating, the program calculates the angle at which the signal beam propagates away from the thermal grating (which is equal to the angle that the probe beam is incident on the grating, given by Equation 2.2).

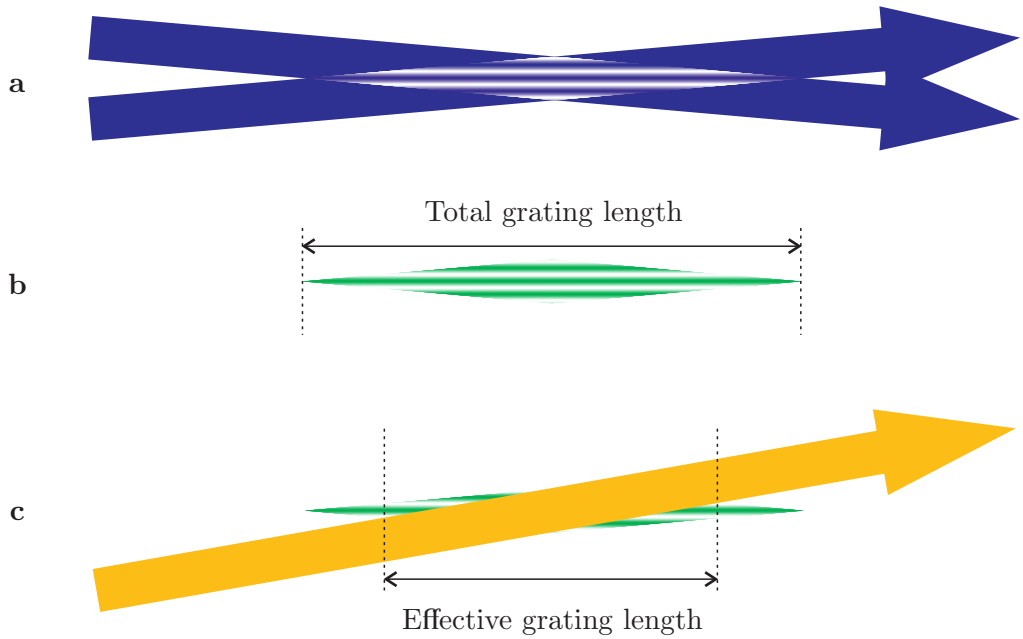


Figure 4.14: Diagram showing the formation of a LITGS grating, and the definition of the associated grating lengths:
a Two pump beams crossed over to form a fringe pattern.
b The fringe pattern leads to the formation of a thermal grating with an associated 'total grating length'.
c A probe beam is incident on the thermal grating. The length of interaction between the probe beam and the grating is defined as the 'effective grating length'.

4.5.2 Imaging geometry

The Scheimpflug imaging geometry was next to be modelled. As explained previously, the optical axis for this model is chosen to lie along the signal beam and the object plane is coincident with the thermal grating. The user is first required to give details about the imaging lens being used in the system (including the focal length, thickness and radii of curvature on both surfaces). Next, the distance between the object plane (i.e. the centre

of the thermal grating) and the imaging lens, along the optical axis, is required. The user can also state the lens' angular tilt (by default it will be perpendicular to the optical axis). The program uses the previously calculated angle of the object plane to the optical axis to determine the position and angle of the image plane for the experiment, obeying both the Scheimpflug and hinge rules.

4.5.3 Generating the signal beam

A LITGS signal beam is produced by the scattering of the probe beam from the thermal grating. This is modelled as a collection of rays produced from point sources along the object plane, spanning the effective length of the grating[4]. The spacing between the points is determined by the user. For simplicity, only three rays are modelled from each point source; one that propagates parallel to the optical axis (referred to as the 'middle ray') and two that propagate at the positive and negative divergence angles from the optical axis respectively (referred to as the 'divergent rays'). The divergence of the signal beam is assumed to be equal to the divergence of the probe beam that is being used in the experiment[5], and this value is also input by the user. This is illustrated in Figure 4.15.

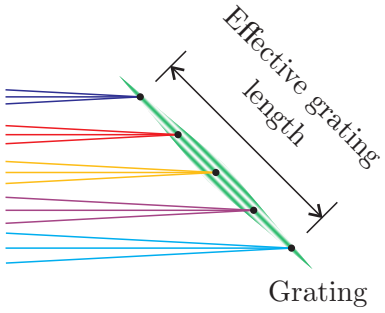


Figure 4.15: Diagrammatic representation of how the signal beam is modelled as being made up of a collection of rays (propagating to the left) from evenly-spaced point sources along the grating. Each point source is modelled to produce three rays to account for the divergence of the beam - a 'middle ray' and two 'divergent rays'.

[4]To reduce the complexity of the model, only point sources along a line through the centre of the grating were considered. As the width of a LIGS grating is typically an order of magnitude smaller than the length, contributions from across the grating could be neglected.

[5]This is a reasonable assumption since the scattering phenomenon can be thought of as a partial reflection of the probe beam by the thermal grating, and so the signal beam would display the same characteristics as the probe beam.

The model also allows the user to state the angle of the object plane. This refers to the angle of the plane, through the grating, along which the signal generation points are placed. Figure 4.15 illustrates this with five points placed on the object plane, along the length of the grating.

4.5.4 Imaging the signal beam

Next, the program models the propagation of each ray up to the first surface of the lens. It calculates the refraction that each ray will undergo as it enters and exits the lens, and then models the subsequent propagation. The user has the option to state a value for the angle of the detector plane. For perfect imaging this would be equal to the angle of the image plane; however practical limitations (such as the acceptance angle for optical fibres, which is explored further in Section 4.6.2.3) mean that a less-than-ideal angle may have to be used. The program places the detector plane, at the user-defined angle, at the theoretically correct distance (i.e. the same distance previously calculated for the image plane) from the back surface of the lens. This setup is shown in Figure 4.16.

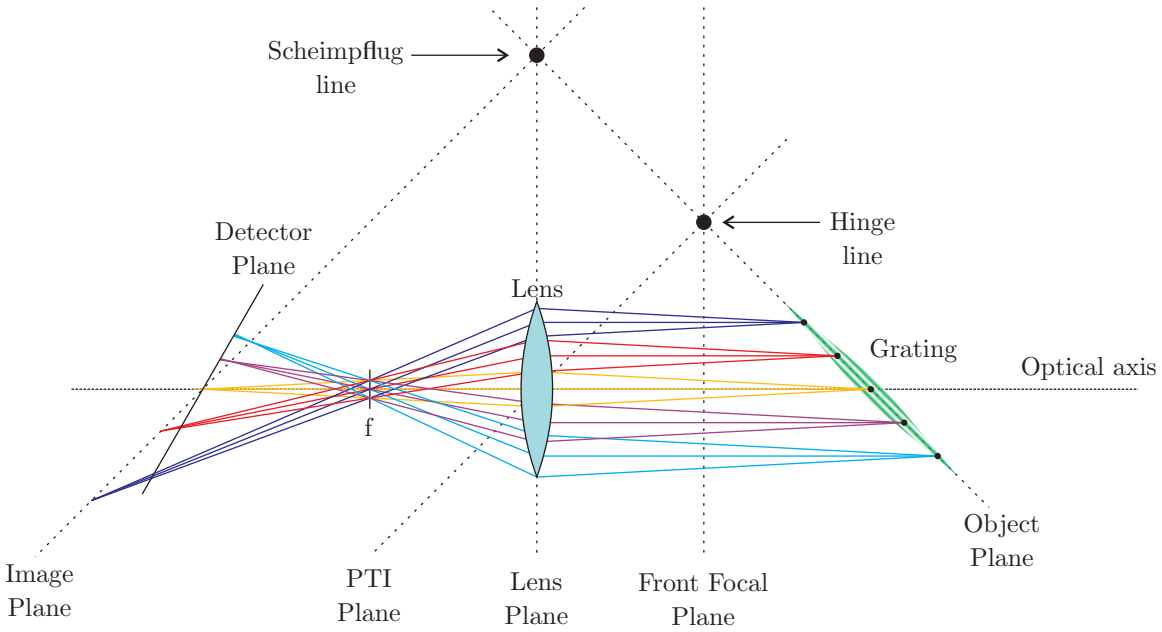


Figure 4.16: Imaging setup used by the computational model. Note that although the image plane shows the ideal imaging setup, the detector plane is orientated at a user-defined angle that meets practical requirements.

The program then calculates the position of every ray landing on the detector plane. Figure 4.17 shows what this may look like. The position data for every ray is used to derive two characteristic arrays for the system:

1. **Magnification** - By measuring the distance, along the detector plane, between every consecutive middle ray (referred to as 'spot distance' in Figure 4.17) and dividing the resulting array by the initial spacing of the point sources along the grating, we are able to model how the magnification varies along the detector plane.

2. **Spot size** - By measuring the distance, along the detector plane, between the divergent rays from each point source (as shown in Figure 4.17), we are able to model the blurriness of the image on the detector. This is a measure of how out-of-focus the detector plane is, as well as the the imperfections of the imaging lens - a perfect imaging system, with the detector plane coincident to the image plane, would result in a point image (and therefore a 'spot size' of 0mm).

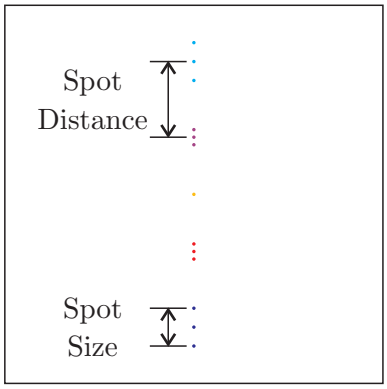


Figure 4.17: Example of how the rays land on the detector plane. The definitions of spot size and spot distance are shown.

The program then carries out the same procedure for a range of different positions of the detector plane (in steps of 1mm, centred about the position of the image plane). The position at which the mean spot size across the detector plane is smallest is considered the 'best focus'. This method enables the model to account for the practical effects of using a specific imaging lens rather than relying on an ideal position calculated using an equation based on a thin lens approximation.

4.5.5 Implementing the detection fibres

This section of the program allows the user to input the details (core size and cladding size) of each individual optical fibre that will be used to capture the signal beam. It also allows the user to state the number of fibres that will be used (if they wish to obtain simultaneous 1-D measurements). Using these inputs, the program is able to calculate the 'grating length per fibre' and 'grating pitch' for the system.

4.5.5.1 Grating length per fibre

The program is able to calculate a per-fibre spatial resolution called the 'grating length per fibre' (L_{gf}). This corresponds to the length along the LITGS grating from which the signal obtained by each fibre originates from. Another way to explain this property is that the LITGS grating is being divided into discrete sections of length (L_{gf}), with each fibre collecting a measurement from each section (and therefore temperature fluctuations within this length will not be resolvable). If the fibres (i.e. the detector plane) were placed along the image plane (so the signal beam was in focus on all the fibres), then L_{gf} would simply be calculated from the magnification of the system (M) and the core diameter of the fibre (d_{f}) by the following equation:

$$L_{\mathrm{gf}} = \frac{d_{\mathrm{f}}}{M} \tag{4.5}$$

However, in reality any given fibre is unlikely to be on the image plane, so the 'out of focus' blurring of the imaging system (and therefore 'broadening' of L_{gf}) should be accounted for. This is achieved by adding in a term for the spot size (d_{s}) as follows:

$$L_{\mathrm{gf}} = \frac{d_{\mathrm{f}} + d_{\mathrm{s}}}{M} \tag{4.6}$$

Figure 4.18 gives a visual explanation of Equation 4.6.

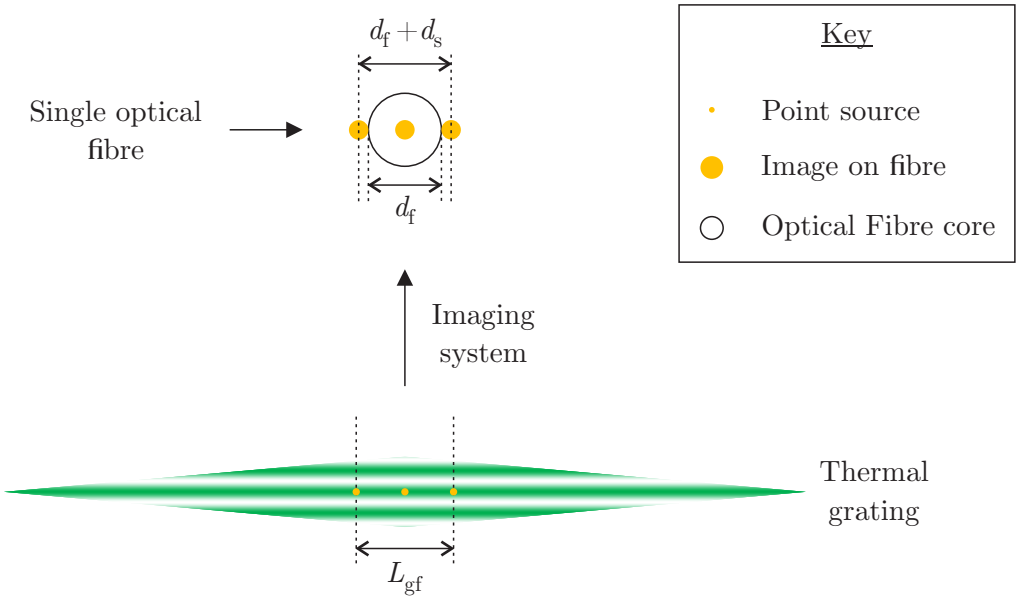


Figure 4.18: Illustration of concepts in establishing the grating length per fibre. Point sources on the grating undergo blurring and magnification effects through the imaging system before landing on the fibre array, leading to each fibre sensing a sub-element of the grating. Only one fibre from the detectionarray is displayed here.

4.5.5.2 Grating pitch

In an ideal imaging configuration where the detector receives an in-focus image of the grating, the rays originating from any point within the grating would land directly on a single fibre. However, due to blurring effects, this is not realistic. Instead, the rays produced from certain points within the grating will be imaged onto two different fibres at the same time. The more out-of-focus the detector plane is, the larger this overlapped region will be. The 'grating pitch' (P_g) of the system is a good way to quantify this effect. It is defined as the distance along the grating, between the centres of the regions captured by two consecutive fibres. This is demonstrated by in Figure 4.19.

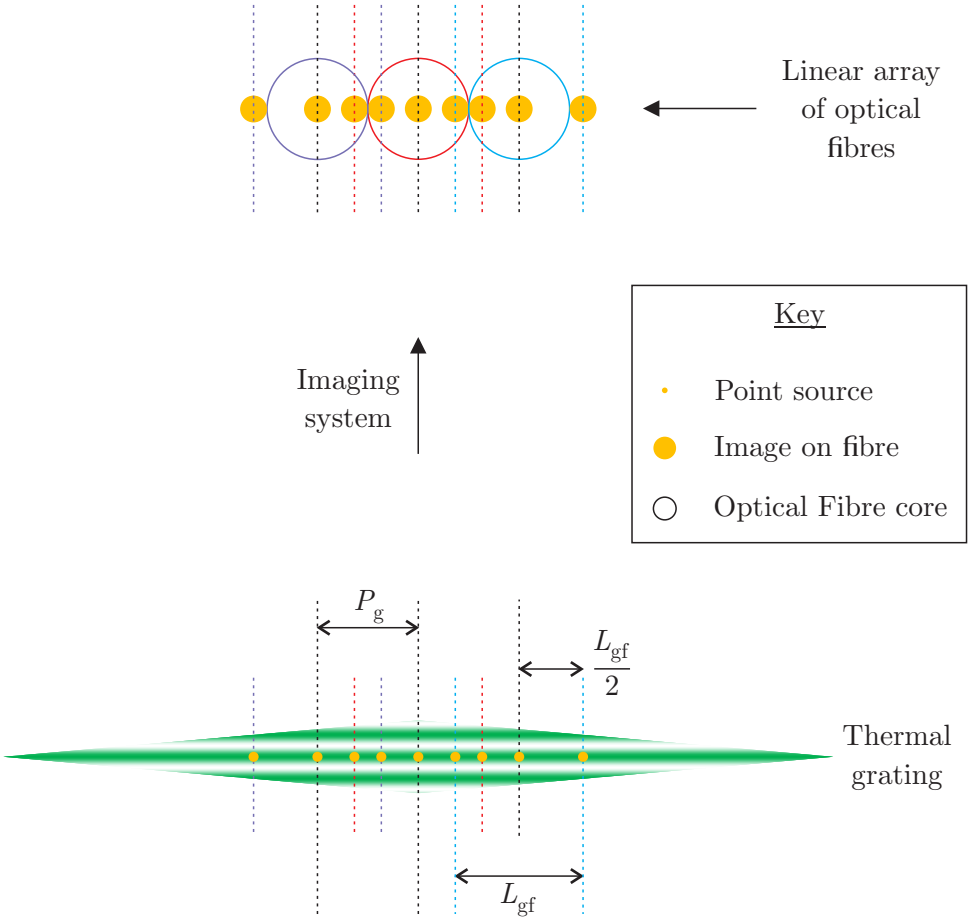


Figure 4.19: Explanation of the grating pitch (P_g). The coloured dotted lines on the grating signify the bounds of the region from which rays are collected by the correspondingly coloured optical fibre. The black dotted lines show the centres of the regions on the grating, and rays produced from these points would be imaged onto the centre of the corresponding fibres.

The grating pitch can be calculated by the following equation:

$$P_g = \frac{l_{cf}}{M} \tag{4.7}$$

where l_{cf} is the distance between the centres of two consecutive optical fibres.

The effect of accounting for the cladding around the optical fibres, or even spacing them out, is to increase the value of l_{cf} which results in an increase in grating pitch, P_g, while retaining the same grating length per fibre, L_{gf}.

4.5.6 Simulating the experiment

The final part of the code simulates the data expected from the experiment. This allows the model to first be experimentally validated, and then be used to characterise future experimental layouts. The experimental layout and methodology was described in Section 4.4. The first input required by the user is the diameter of the jet of nitrogen seeded with toluene that is to be used for the experiment. The user may also state the variation in fringe spacing along the grating, if there is one. The need for this is further described in Section 4.5.6.3. Using these inputs, the program is able to calculate the normalised intensity of the signal beam that falls on each detection fibre as the jet is translated along the length of the grating.

4.5.6.1 Simulating grating intensity variation

The first step of the simulation is to account for the variation in pump and probe beam intensities throughout the grating. This variation is due to the approximately Gaussian beam profiles, and will affect the intensity of the signal beam produced from different regions.

The grating strength throughout the interaction region is determined by the pump beam with the smallest intensity, since that is the value that limits the amplitude of modulation within the interference fringe pattern. The relative intensity of the grating (I_{grating}) throughout the interaction region is therefore calculated as

$$I_{\text{grating}} = \frac{I_1 + I_2 - |I_1 - I_2|}{2} \tag{4.8}$$

where I_i is the relative intensity of pump beam i, assuming an equal pulse energy and Gaussian profile for both beams given by

$$I_{\text{i}} = \exp\left[-2\left(\frac{r_i}{w_i}\right)^2\right] \tag{4.9}$$

where r_i is the radial distance from the central axis of pump beam i and w_i is the radius of the beam. Figure 4.20 shows an example intensity variation for a typical LIGS grating.

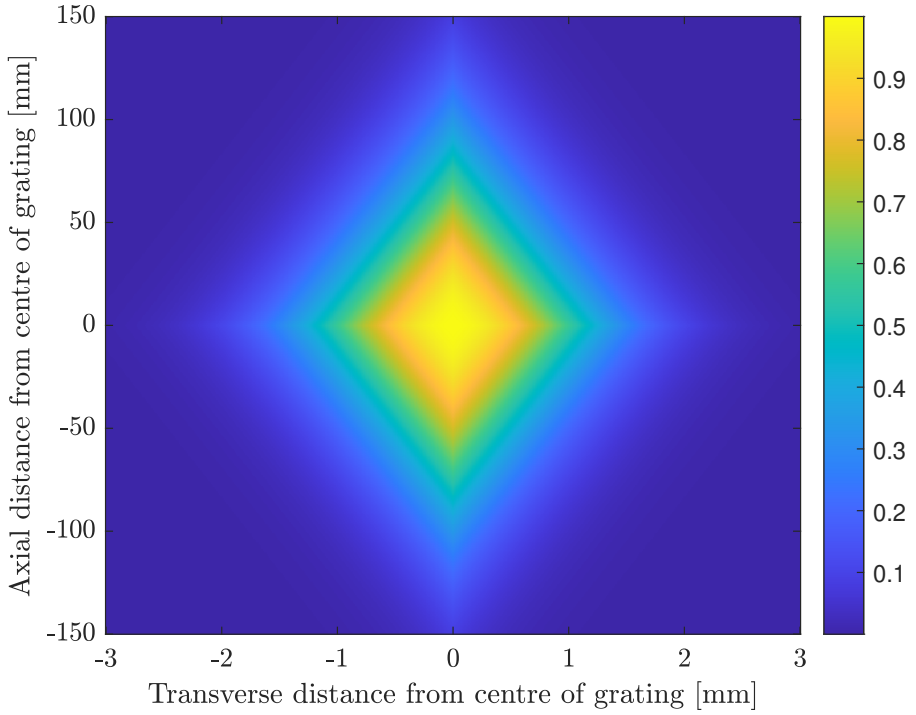


Figure 4.20: Relative grating intensity where the grating is produced by two pump beams, 3.8 mm in diameter, crossing at an angle of 1.6°. The beams are modelled as travelling up the page. Note that the x and y axes have different scales.

Next, the relative variation of the probe beam intensity within the interaction region is calculated by Equation 4.10 where r_{probe} is the radial distance from the central axis of the probe beam and w_{probe} is the radius of the probe beam:

$$I_{\text{probe}} = \exp\left[-2\left(\frac{r_{\text{probe}}}{w_{\text{probe}}}\right)^2\right] \tag{4.10}$$

Finally, the relative intensity of the signal beam ($I_{\text{signal beam}}$) generated from different points within the interaction region is calculated by Equation 4.11:

$$I_{\text{signal beam}} = I_{\text{probe}} I_{\text{grating}} \tag{4.11}$$

Figure 4.21 shows the results of an example simulation. It shows the effect of adding a probe beam to the grating displayed in Figure 4.20.

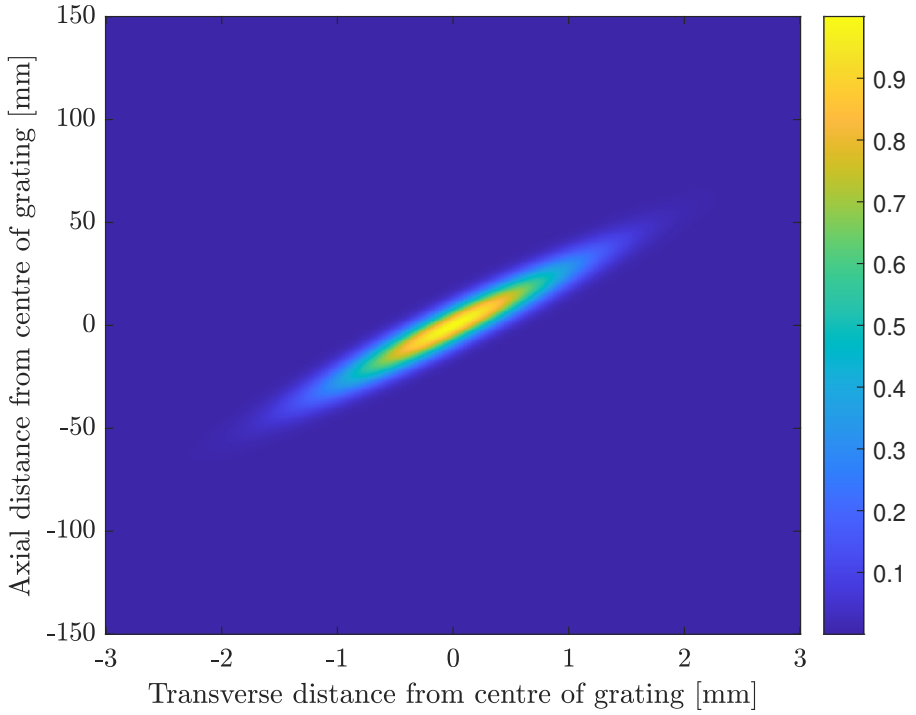


Figure 4.21: Relative signal beam intensity from an interaction region where pump beams (3.8 mm in diameter) are crossed over at 1.6° to produce the grating, and a probe beam (0.9 mm in diameter) crosses the centre of the grating at 2°. The beams are modelled as travelling up the page. Note that the x and y axes have different scales.

4.5.6.2 Simulating signal beam generation

As described in Section 4.5.4, the model described thus far is able to simulate a spot (the size of which depends on the amount of blur present in the imaging) which is created from a point source within the grating. However, the experimental validation of the technique requires a jet, which can't be modelled as a point source, to produce a signal beam. To account for the size of the jet, it was modelled as a line of point sources (spanning the diameter of the jet), parallel to the lens and image planes, that was then translated along the grating. Figure 4.22 illustrates the concept.

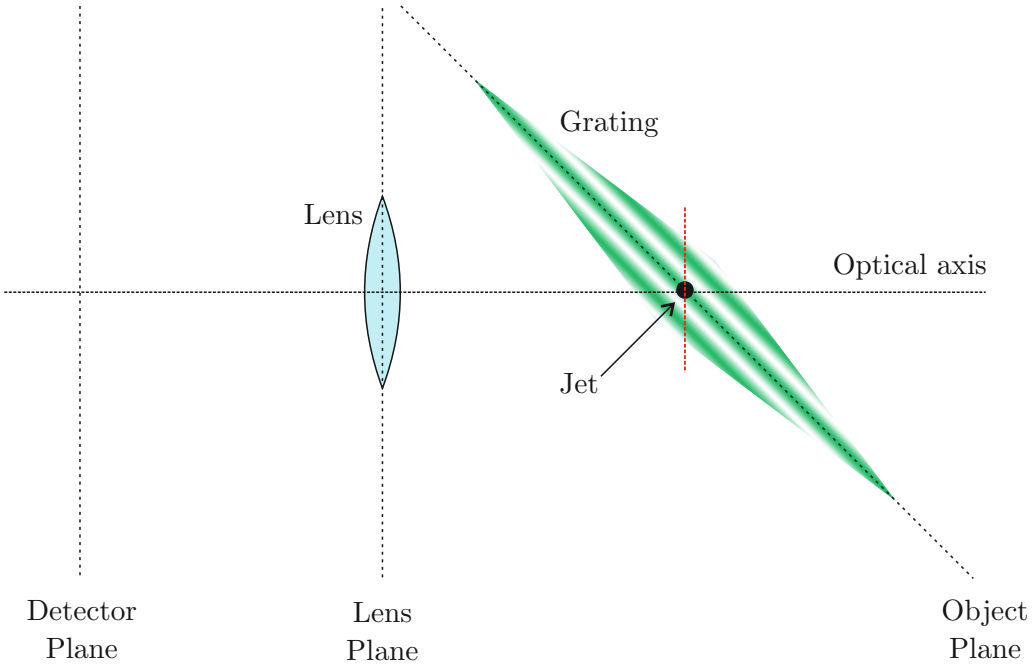


Figure 4.22: Diagram showing how the jet (black dot) is modelled as a line of point sources, along the dashed red line, which are then moved along the grating (and coincident to the object plane).

The plane through the jet, parallel to both the image and lens planes, was chosen because all the points along it would be equally blurred as it was translated along the grating. When the jet was at the centre of the grating, its one dimensional model (i.e. the generation of the signal beam) was imaged in perfect focus onto the detector plane. As it was moved along the grating, all the point sources experienced the same amount of blur, quantified by the variation in spot size.

It is important to note that modelling the jet as a one dimensional line of point sources is only acceptable for experiments where the jet size is small compared to the length of the grating (as was the case for the work presented in this thesis).

4.5.6.3 Simulating signal beam intensity variation

Section 4.5.6.1 explored how the Gaussian nature of the pump beams resulted in a variation in grating intensity throughout the interaction region. Another property of Gaussian beams is that they have curved wavefronts[6]. When beams with curved wavefronts are crossed over,

[6]The curvature of the wavefronts for practically-collimated beams is minimal, while for focused beams the curvature is weak at the focal point.

the resulting fringe spacing varies along the length of the grating. Figure 4.23**a** shows the consistently-spaced fringes formed by the superposition of flat wavefronts, while Figure 4.23**b** shows the variation in fringe spacing caused by curved wavefronts.

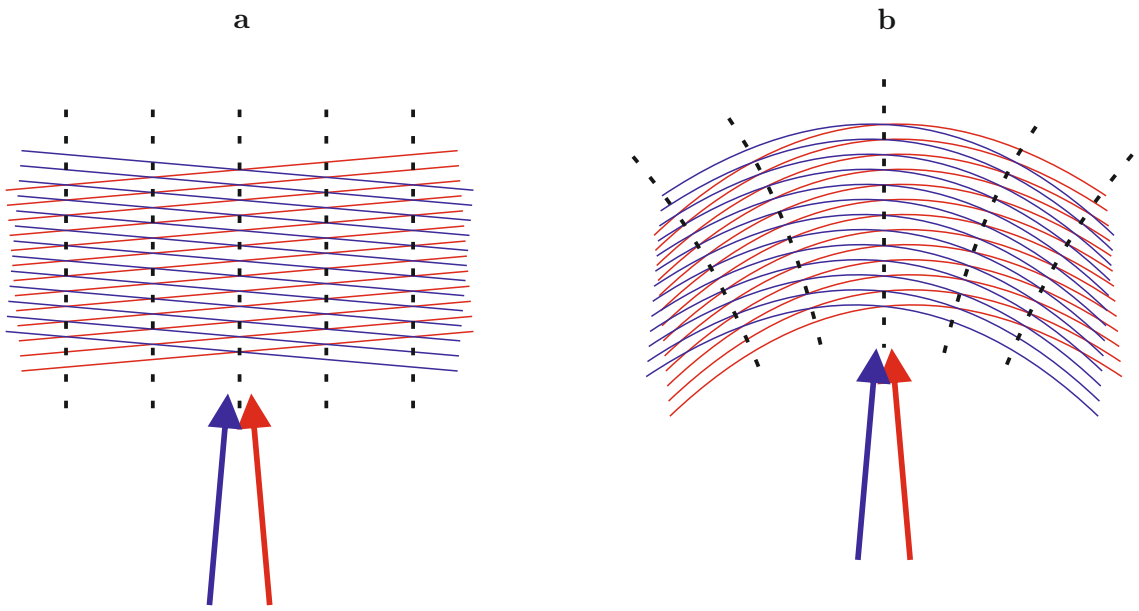


Figure 4.23: Diagrams illustrating the fringes, shown in dashed black lines, formed by the superposition of two beams, shown in red and blue. Figure **a** shows beams with flat wavefronts while Figure **b** shows beams with curved wavefronts.

As described in Section 2.1, the signal beam is produced by scattering the probe beam off the the grating when it is incident at the Bragg angle. Equation 2.2 shows that the calculated first order Bragg angle is dependent on the fringe spacing within the grating, and therefore a variation in fringe spacing will result in a change in the scattering efficiency of the grating. In order to estimate the sensitivity of scattering efficiency to fringe spacing, the LIGS grating was taken to behave similarly to a diffraction grating. The concept is described in Figure 4.24. Figure 4.24**a** shows how the probe beam scatters off the thermal grating, at the first order Bragg angle, to produce a signal beam. Figure 4.24**b** demonstrates how this process is modelled as a plane wave passing through a diffraction grating composed of slits which are separated by the same distance as the fringe spacing. The interference of light passing through each slit results in a variation in intensity along the plane parallel to the grating, known as a diffraction pattern. The relative intensity of the diffraction pattern

(I) as a function of the angle from the normal of the grating (θ) is calculated as

$$I(\theta) = \frac{\sin^2\left(\frac{\pi N d \tan\theta}{\lambda}\right)}{\sin^2\left(\frac{\pi d \tan\theta}{\lambda}\right)} \tag{4.12}$$

where N is the number of slits, d is the width of each slit and λ is the wavelength of the diffracted beam. As shown in Figure 4.24**b**, the diffraction pattern consists of peaks at certain angles from the normal to the grating. The first order peak, occurring at an angle of θ_1 from the normal to the grating, represents the signal beam of interest in LIGS.

To model the LIGS grating as a diffraction grating, the computational model uses Equation 4.12 to calculate the relative intensity of light being scattered into the signal beam. The number of slits is set to equal the calculated number of fringes in the simulated thermal grating, the width of the slits is equal to the fringe spacing and the wavelength of the diffracted beam is set to the same wavelength as the probe beam. The user-defined variation in fringe spacing, as a function of length along the grating, is then used to calculate how the scattering efficiency (which is equal to the relative intensity of the signal beam) varies along the grating.

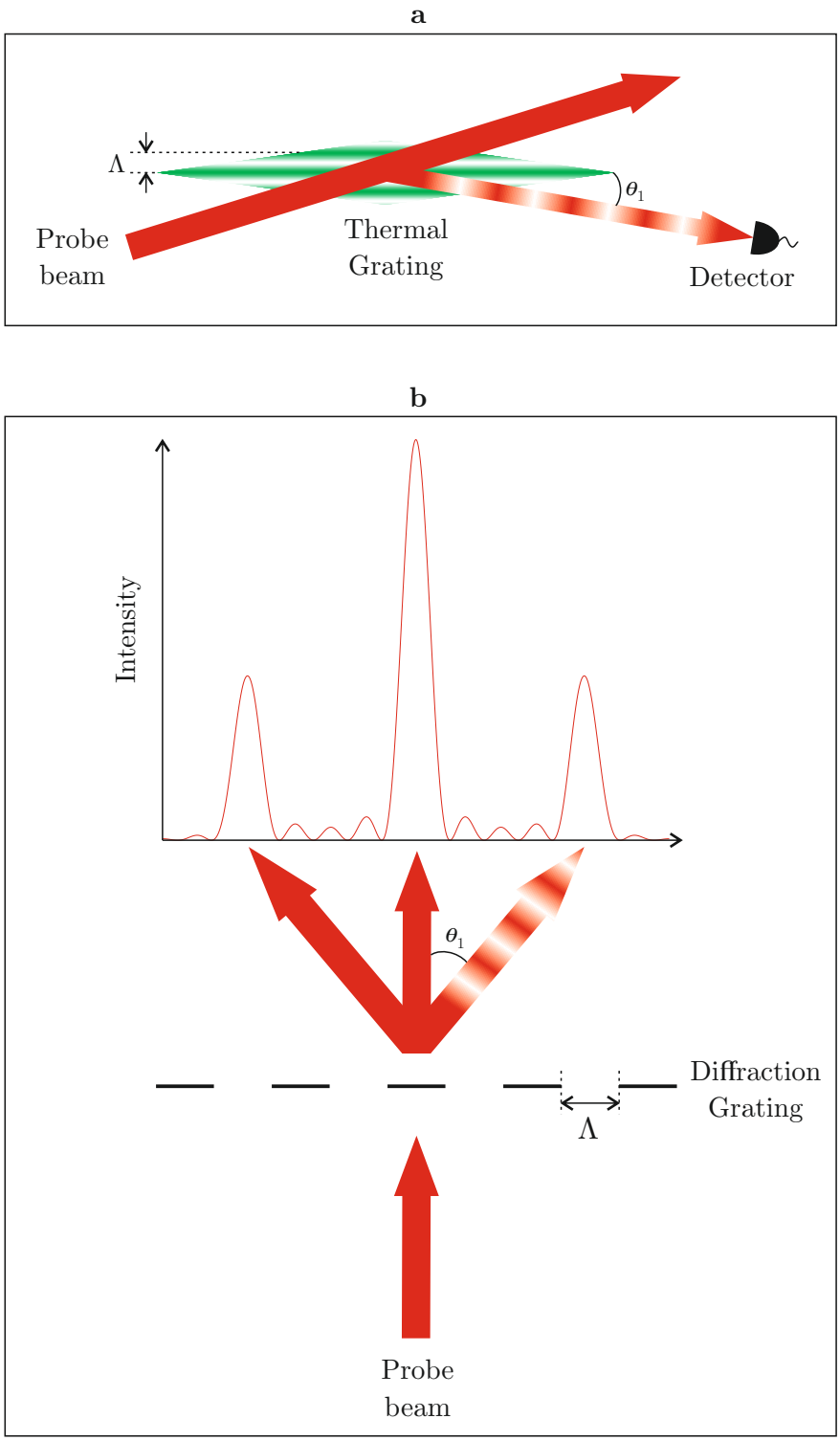


Figure 4.24: Figure **a** displays how the signal beam, collected by the detector, is generated from the scattering of the probe beam by the thermal grating (at the first order Bragg angle denoted by θ_1). The fringe spacing is defined by Λ. Figure **b** shows how the process was modelled as a plane wave passing through a diffraction grating.

4.5.6.4 Simulating signal beam detection

The final part of the program simulates the collection of the signal beam by the optical fibres. The program accounts for the circular cross-section of the optical fibres and allows the user to input a vertical offset; this enables the impact of having the optical fibres slightly vertically misaligned with the signal beam to be examined.

An example of the simulated data is shown in Figure 4.25. The graph shows the normalised strength of the LITGS signal received by each optical fibre as the jet is moved along the grating. As the signal beam moves onto each fibre, the intensity of the LITGS signal, referred to at the 'signal strength', received by that fibre increases. This continues up to a maximum (when the signal beam is directly in the centre of the fibre), and then the strength begins to decrease as the beam moves off the fibre and onto the next one. Note that the grating length per fibre (L_{gf}) and grating pitch can be calculated, for each fibre, from the graph.

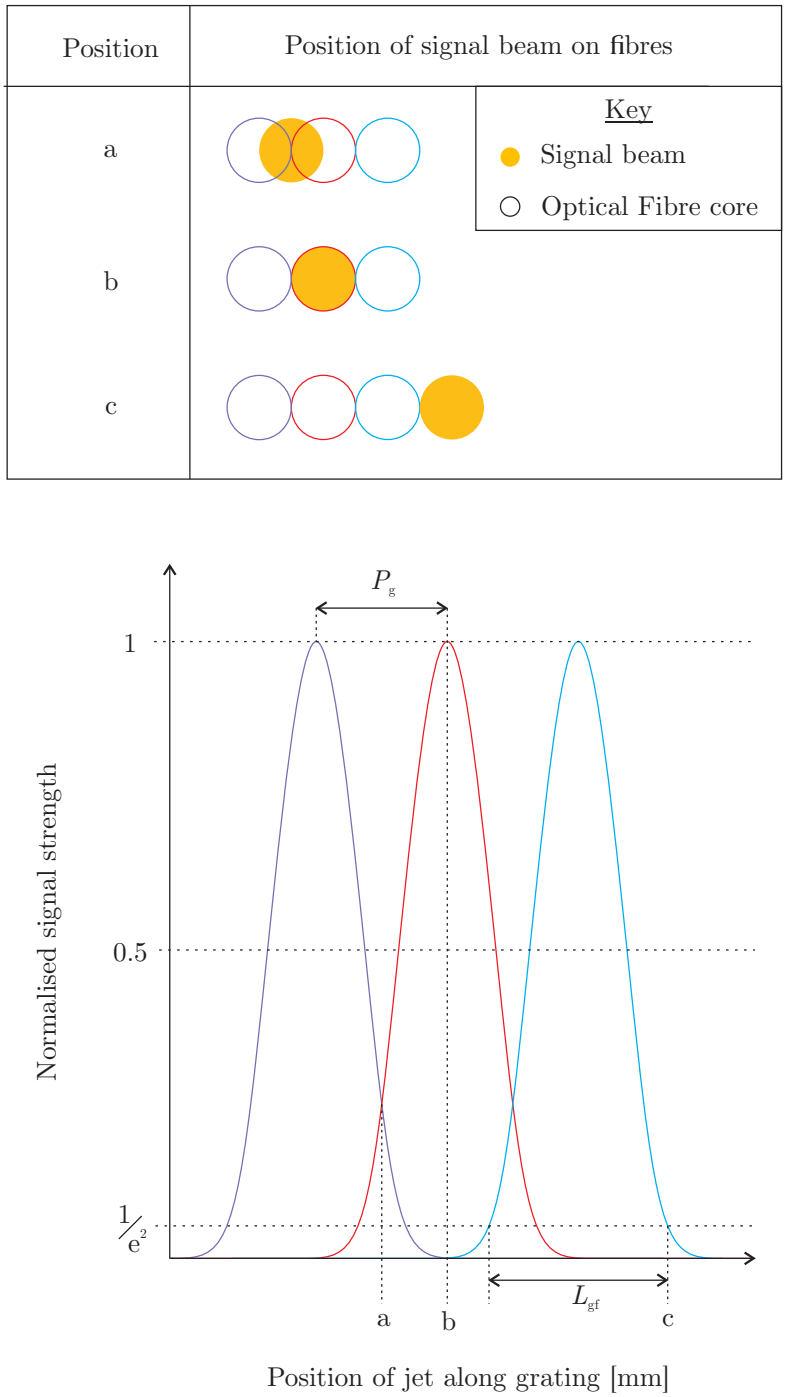


Figure 4.25: Example output of the the computational model. The table shows a physical depiction of the signal beam landing on the face of the optical fibres. The three positions shown correspond to those labelled on the graph showing the simulated data. Note that the colour of the graph corresponds to the signal being received by the optical fibre shown with the same colour. The grating length per fibre (L_{gf}) and grating pitch (P_g) are also shown.

4.6 Parametric investigation of spatial resolution

The computational model was used to investigate how the variation of the following experimental parameters within the setup would affect the spatial resolution of the technique:

1. Varying the angle of the detector plane.
2. Varying the angle of the lens plane.
3. Varying the distance between the grating and the imaging lens.

This section explores these effects, and how each can be optimised to increase the spatial resolution.

As explained in Section 4.5.5, the spatial resolution of the system is defined by two different parameters; namely the 'grating length per fibre' and the 'grating pitch'. The 'grating length per fibre' is affected by both the magnification and focus of the system, and is therefore a good intrinsic measure of the geometric and optical setup. The 'grating pitch' is dependent on the size and spacing of the optical fibres used for signal detection, and the magnification of the system; it is therefore only a measure of the geometric setup of the experiment[7]. Therefore, when considering the effect of varying experimental parameters on the spatial resolution of the system, it is the 'grating length per fibre' that will be optimised. By studying the form of Equation 4.6, it is clear that the goal to achieving a high spatial resolution (i.e. small grating length per fibre) is to aim for a large magnification together with a small spot size.

For the following investigations, the computational model used the inputs shown in Table 4.1 unless otherwise stated. The imaging lens was modelled as a bi-convex spherical lens manufactured by Thorlabs[8]. The jet producing the signal beam was also considered to be infinitesimally small, so that it was modelled as a point source.

[7]Note that the 'grating pitch' is only applicable for when multi-point measurements are being taken.
[8]Part number LB1199.

Simulation process	Property	Value
LITGS geometry	Pump beam wavelength	266 nm
	Pump beam size	3.8 mm
	Probe beam wavelength	671 nm
	Probe beam size	0.9 mm
	Pump & probe beam profiles	Top-hat
	Crossing angle	1.6°
Imaging geometry	Distance between grating and lens	420 mm
	Imaging lens focal length	200 mm
	Lens plane angle	90° to optical axis
Signal beam generation	Grating resolution	0.1 mm
	Object plane angle	0° to grating axis
	Fringe spacing variation	None
Imaging signal beam	Detector plane angle	90° to optical axis
Detection fibres	Optical fibre core diameter	1mm

Table 4.1: Input parameters used for the computational model. The 'grating axis' refers to the longitudinal axis through the centre of the grating.

4.6.1 Varying the angle of the detector plane

The first parameter to be systematically varied is the angle between the detector plane and the optical axis. As defined in Section 4.3, the symbol γ is used, in units of degrees.

4.6.1.1 Detector plane coincident to image plane

The image plane for the setup detailed in Table 4.1 is angled at 2° to the optical axis (γ=2°). Figure 4.26 shows how the spot size varies along the detector plane when it is placed coincident to the image plane. Theoretically, the spot size should be 0 along the entire detector plane as the image should be fully in focus. The oscillations shown in the figure are due to numerical errors in the computational model; however the general trend of a non-zero spot size is clear. This is because practical lenses induce aberrations that reduce

the sharpness of the image. The obtainable resolution for the system (using a standard, off-the shelf imaging lens) is still very good relative to the core diameters (minimum of 400 µm) of the optical fibres that were used in the validation experiments detailed in Chapter 5.

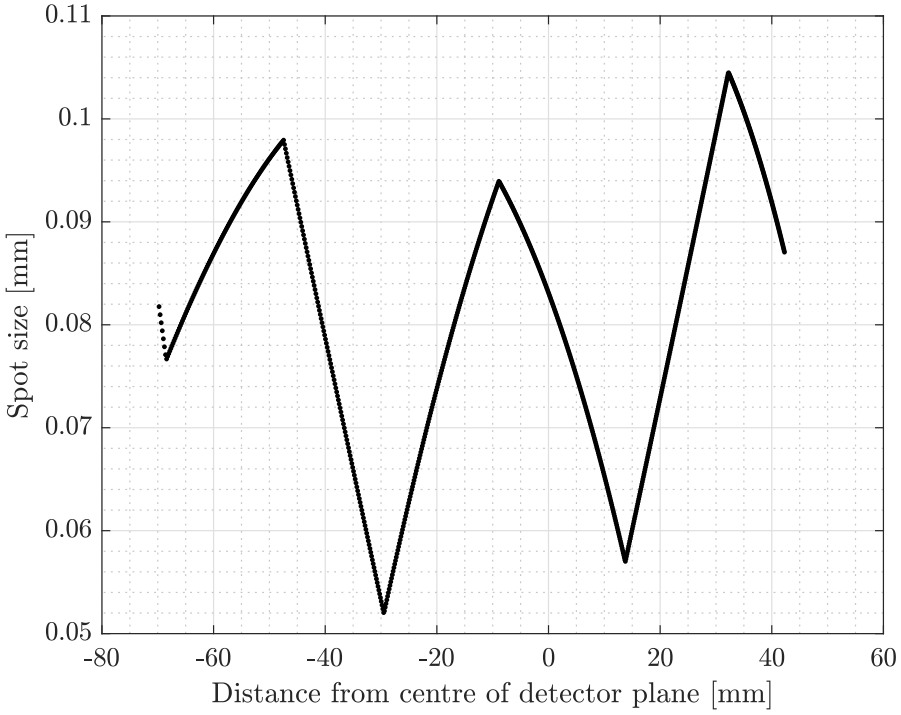


Figure 4.26: Results from computational model showing the variation of spot size along the detector plane.

If the object, lens and image planes were all parallel, a constant magnification (M) would be expected along the detector plane, given by the equation

$$M = -\frac{v}{u} \tag{4.13}$$

where u is the distance of the object from the lens and v is the distance of the image from the lens. Instead, in this situation the magnification varies along the plane resulting in a distorted image. This can be inferred by considering the layout of the imaging setup, as shown in Figure 4.27. The distance between an object placed at a and the lens plane is larger than the same distance for an object placed at b. However, the distance between the lens plane and a$'$ is smaller than for b$'$. Therefore, according to Equation 4.13, the

magnification of b will be larger than a.

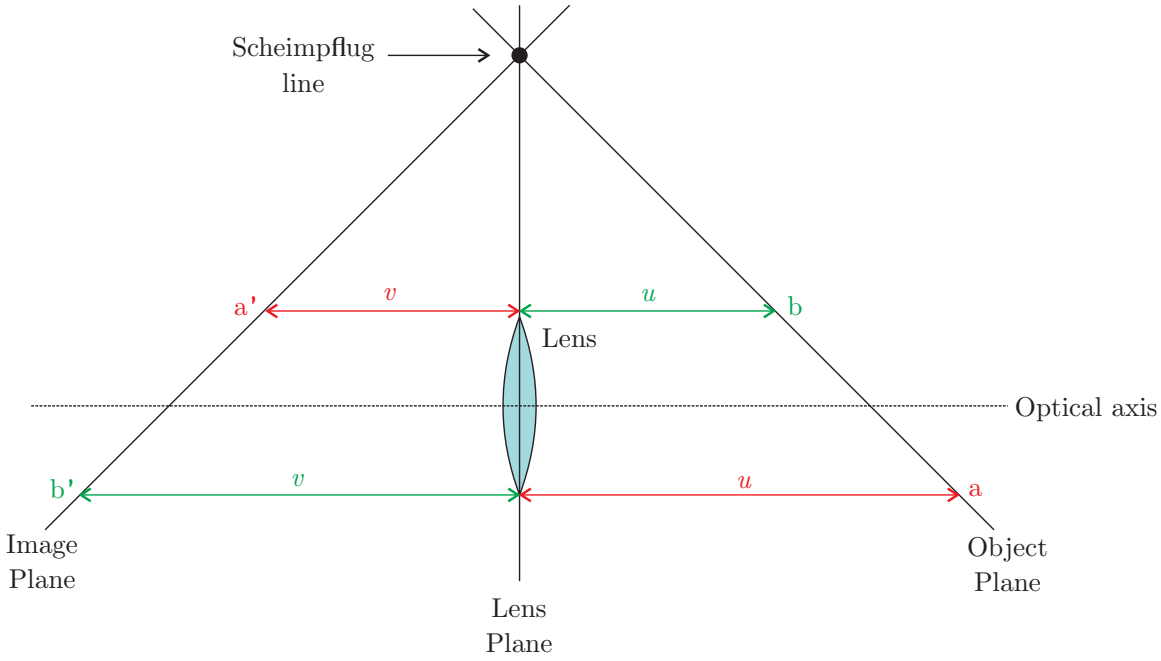


Figure 4.27: Imaging layout for the computational model. The variables u and v designate the distances between the object and image planes, respectively, from the lens plane. The colours represent which point on the object plane gets imaged to which point on the image plane.

This expected variation in magnification is seen in Figure 4.28. It also shows that the image length is not symmetrical about the centre of the detector plane. This is due to the distortion caused by the variation in magnification. Where there is a greater magnification, the image is stretched out across the detector plane. In this case the two ends of the grating are imaged to $+43\,\text{mm}$ and $-72\,\text{mm}$.

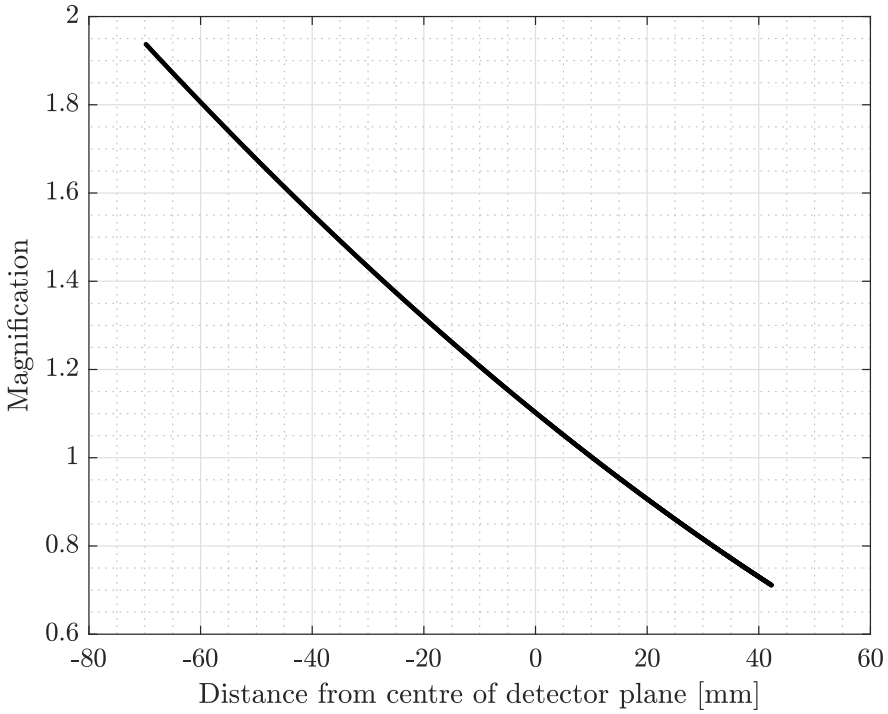


Figure 4.28: Results from computational model showing the variation of magnification along the detector plane.

Finally, Figure 4.29 shows how the spatial resolution of the system, given by the grating length per fibre, varies over the detector plane[9]. Although the entire image of the grating is similarly in focus along the detector plane, the change in magnification causes the spatial resolution to vary, with best resolution at $-72\,\text{mm}$. This is conceptually sound, since a larger magnification would allow a fixed-size fibre to 'see' a smaller area. Furthermore, this is to be expected from the mathematical form of Equation 4.6.

[9]Note that the oscillations are an artefact of the numerical errors shown in Figure 4.26.

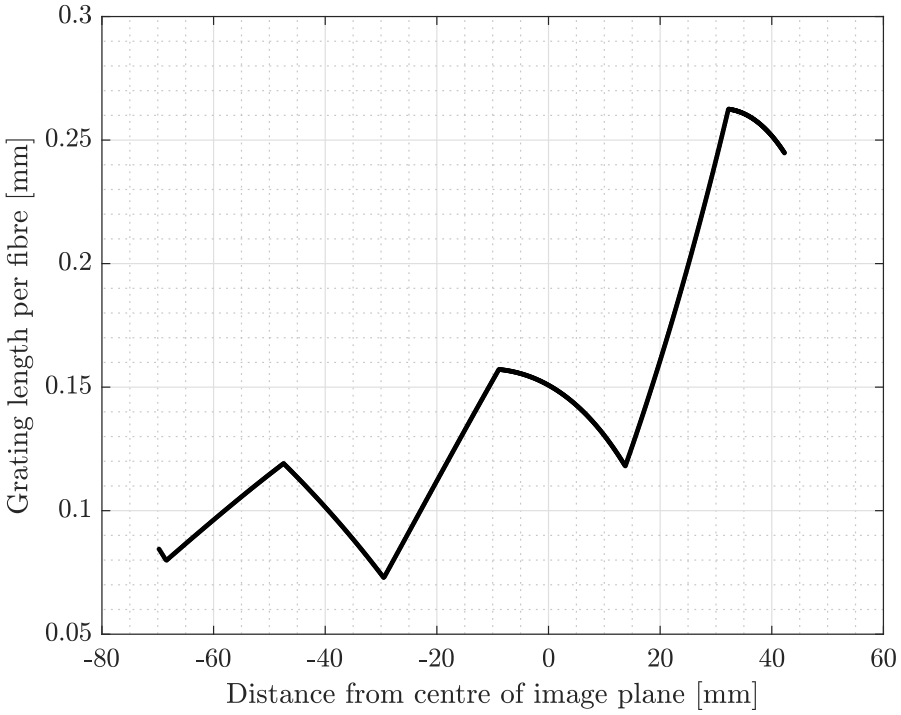


Figure 4.29: Results from computational model showing the variation of the grating length per fibre (L_{gf}) along the detector plane.

4.6.1.2 Rotating the detector plane about the optical axis

As explained in Section 4.6.1.1, the image plane for this model has a value of γ=2°. Figure 4.30 shows how the spot size, magnification and grating length per fibre (L_{gf}) vary for different values of γ, across the detector plane.

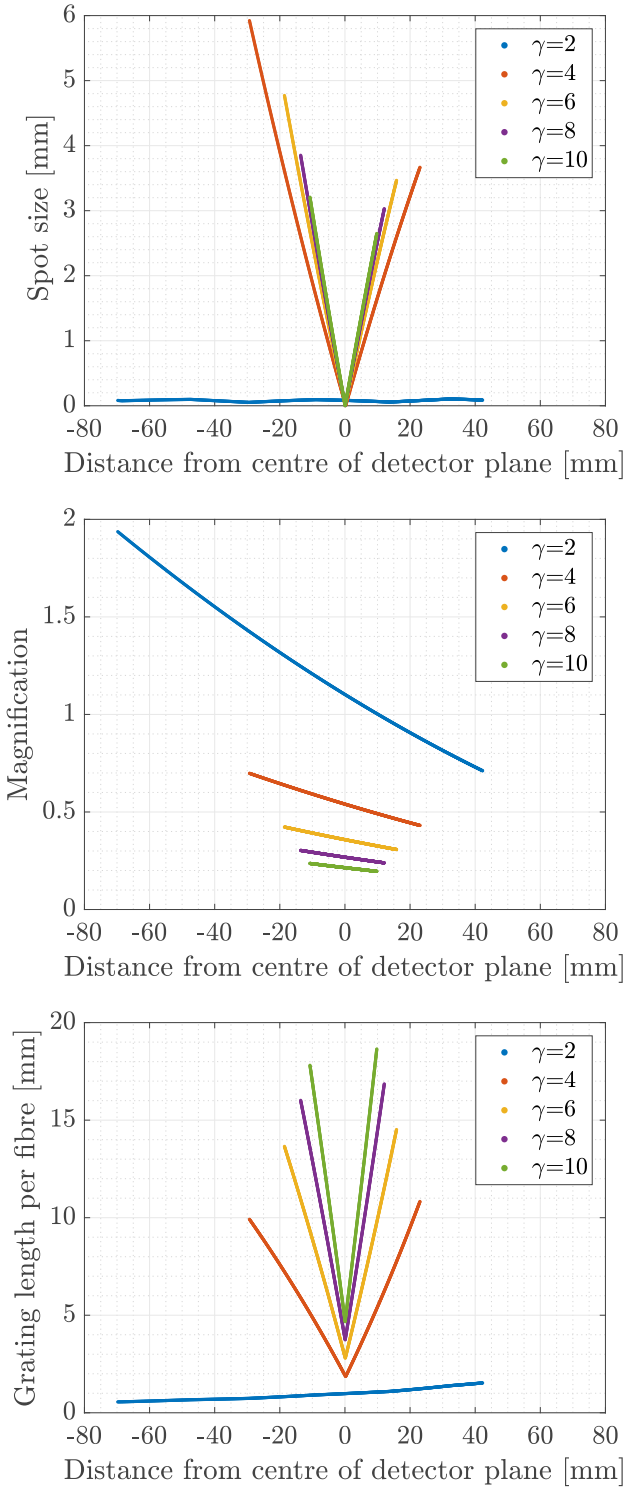


Figure 4.30: Results from computational model showing the variation of the spot size, magnification and grating length per fibre (L_{gf}), along the detector plane, for different angles of the detector plane. Note that γ is the angle, in degrees, between the detector plane and the optical axis.

The first trend to note is that as γ is increased, the shape of the graph of spot size along the detector plane changes to a 'V-shape'. The detector plane is being rotated about its centre, and so that region always remains in focus while the extremes of the image are increasingly out-of-focus as the plane is rotated. The higher the value of γ, the more out-of-focus the image is and this is shown by the increase in spot size at a given point along the detector plane. The magnification along the detector plane decreases as the angle of the detector plane is increased. This trend is caused by the geometry of the setup as explained in Figure 4.31.

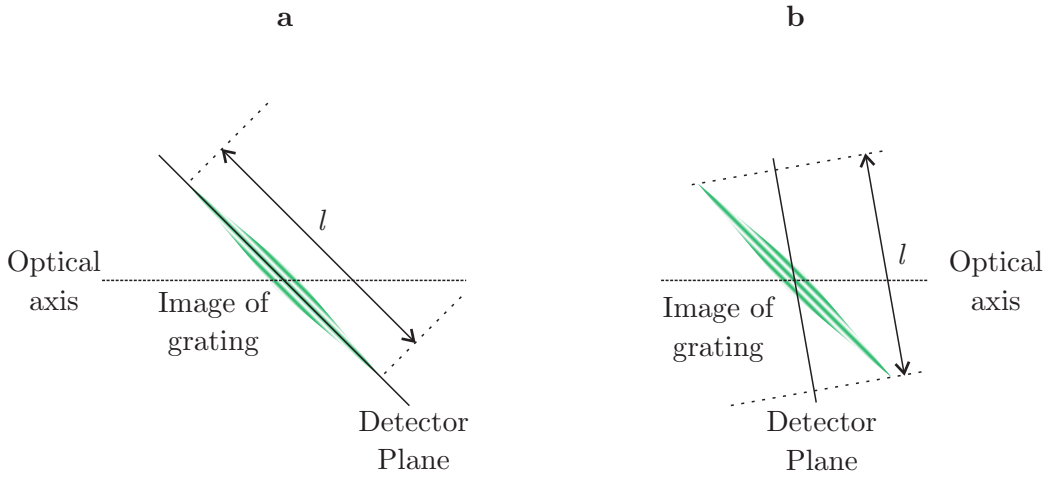


Figure 4.31: Two diagrams showing the same image of the grating (in green). The detector plane is at different angles in both pictures; γ, the angle between the detector plane and optical axis, is greater in diagram **b**. The length of the image along the detector plane, l, is shown to be greater in diagram **a** than it is in diagram **b**.

The average gradient of the magnification variation curves shown in Figure 4.30 also decreases as γ is increased. This can also be explained by the geometry of the experiment — as the angle of the detector plane is rotated to be closer to parallel to the lens plane, the relative distances of different points along the detector plane from the lens plane become similar. This concept was explained in Figure 4.27, and it leads to a decrease in the difference of magnification along the detector plane.

The grating length per fibre is shown to be best at the centre of the detector plane, and then increase with distance from the detector plane. This mirrors the variation of the spot size along the detector plane, and is therefore a result of the variation in focus along the

detector plane. As γ is increased, the length of the image of the grating along the detector plane decreases due to the overall decrease in magnification.

As expected from the definition of L_{gf} in Equation 4.6, these results show that the means of achieving a high spatial resolution is to aim for a large magnification together with a small spot size. This is evident from the shape of the L_{gf} curve following that of the spot size. At the centre of the detector plane, where spot sizes are similar, the effect of the magnification on L_{gf} is noticed (the larger the value of γ, the smaller the magnification and hence a lower L_{gf} is achieved).

Figure 4.32 shows the continuation of these trends as γ is further increased to the limit of 90°(at which point the detector plane is perpendicular to the optical axis). However, the impact of increasing γ on both the spot size and the magnification diminishes as γ increases. As expected, this trend is also reflected in the variation of the grating length per fibre. This means that angling the detector plane to be closer to the ideal image plane angle has an increasingly beneficial effect on the spatial resolution of the system.

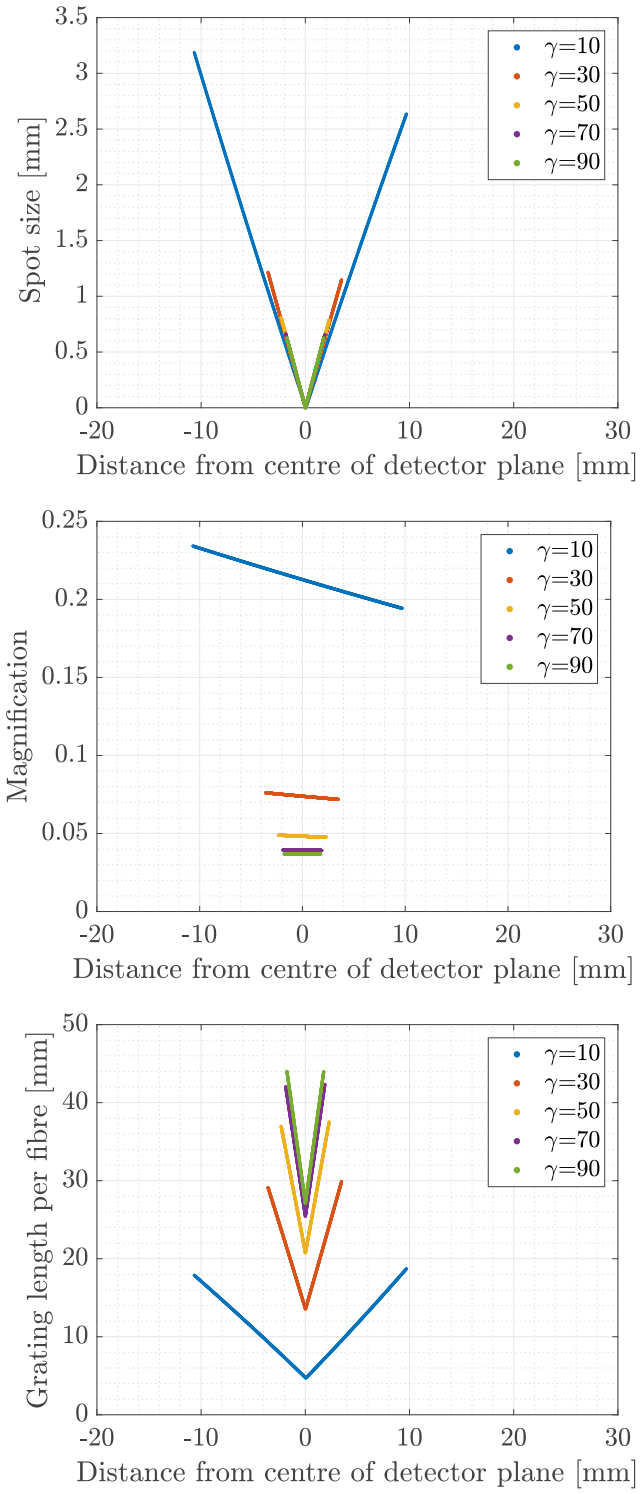


Figure 4.32: Results from computational model showing the variation of the spot size, magnification and grating length per fibre (L_{gf}), along the detector plane, for different angles of the detector plane. Note that γ is the angle, in degrees, between the detector plane and the optical axis.

4.6.2 Varying the angle of the lens plane

Another experimental variable within the imaging setup is the angle of the lens plane. In order to obey the Scheimpflug and hinge rules, angling the lens plane also requires the angle of the image plane to change. As defined in Section 4.3, the symbol Δ is used to describe the angle, in degrees, between the lens plane and the plane that is perpendicular to the optical axis.

4.6.2.1 Detector plane coincident to expected image plane

The first case to be considered was the effect of the angle of the lens plane on the spatial resolution of the system when the detector plane was adjusted to always be coincident to the image plane (and therefore in perfect focus). Table 4.2 shows how the angle of the image plane was expected to vary for different values of Δ, as calculated using Equation 4.4. Figure 4.33 shows the resulting graphs.

Lens tilt angle (Δ) [°]	Calculated angle of image plane (γ) [°]
0	2.0
10	2.0
20	2.1
30	2.1
40	2.2
50	2.2

Table 4.2: Effect of lens tilt, given as the angle of the lens plane (Δ), on the angle of the image plane (γ). Note that the distance between the grating and the lens (u) is 400 mm.

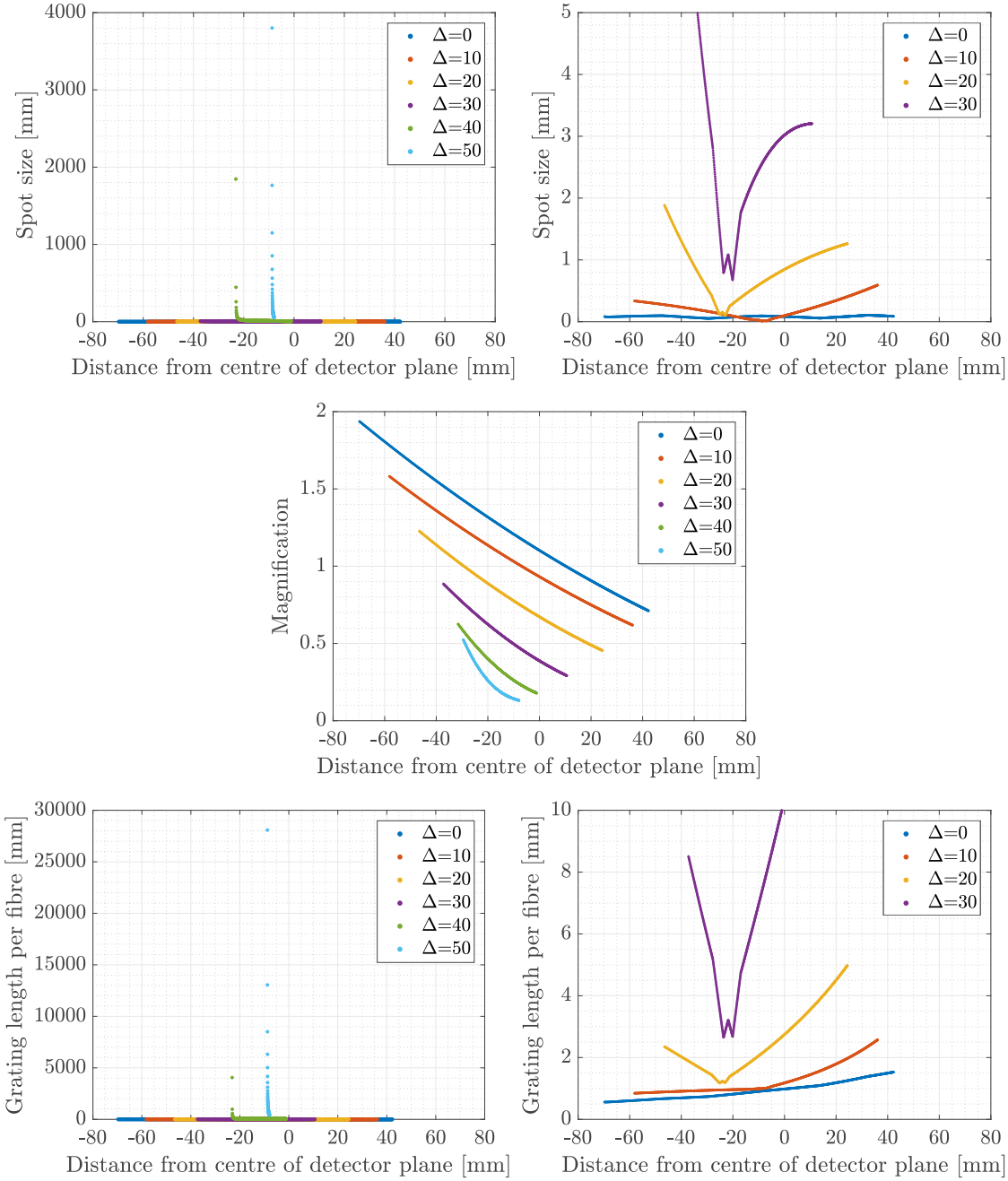


Figure 4.33: Results from computational model showing the variation of the spot size, magnification and grating length per fibre (L_{gf}), along the detector plane, for different angles of tilt of the lens plane (Δ). Note that Δ is the angle, in degrees, between the detector plane and the perpendicular to the optical axis. Also note that the additional graphs of spot size and L_{gf}, shown on the right, are the same as the graphs on the left but with a different scale on the y-axis.

The results from Figure 4.33 show that the spot size increases as the lens is tilted more, while the magnification decreases. Tilting the lens therefore results in a worse value of grating length per fibre. Since the detector plane was always angled to be coincident to the calculated image plane, these results are surprising - it would be expected that the images should always be in focus, and so the spot sizes should remain fairly small. However, another trend was noticed that helps to explain this decrease in focus as the lens is tilted. Table 4.3 shows how the distance (v) of the image plane from the centre of the lens, measured along the optical axis, varies as the lens is tilted.

Lens tilt (Δ) [°]	Image distance (v) [mm]
0	420
10	387
20	302
30	206
40	124
50	64

Table 4.3: Effect of lens tilt, given as the angle of the lens plane (Δ), on the distance (v), along the optical axis, of the image plane from the centre of the lens.

Since this distance is determined by the thin lens equation, as displayed by Equation 4.1, it is clear that this must be caused by a change in the focal length of the lens. The lens being modelled has a focal length of 200 mm when placed perpendicular to the optical axis, but this is not necessarily true for when it is tilted. As the lens is tilted, the centre of the image is also displaced from the optical plane. As this changes the distance between the image and the centre of the lens, the thin lens equation can not be used to calculate the exact focal length of the tilted lens. Instead, the computational model was used to determine the optimal angle of the detector plane (γ), and distance between the detector plane and lens plane (v), to produce a focused image. Table 4.4 shows the results. It also displays the focal length of the tilted lens, which is calculated by using the modelled value of γ in Equations 4.2, 4.2 and 4.4.

Lens tilt Δ [°]	Image distance v [mm]	Detector plane angle γ [°]	Calculated focal length f [mm]
0	420	1.9	205
10	387	2.0	203
20	305	2.4	186
30	212	3.1	163
40	133	3.8	145
50	77	4.0	145

Table 4.4: Optimal distance (v) and angle (γ) of the detector plane, and therefore also the image plane, for different angles of tilt of the lens plane (Δ). Note that the distance between the grating and the lens (u) is 400 mm. The calculated focal length for the tilted lens is also given.

It is apparent that tilting the lens has the effect of reducing its focal length. Merklinger [93] suggests that tilting a lens will increase its focal length. This is because in a 'standard' imaging system, objects that are further away from the optical axis (but still on the object plane) are brought to a focus further from the optical axis (but still on the image plane), meaning the effective focal length for these oblique rays is longer than that for rays perpendicular to the lens. However, this theory does not account for the curvature of field associated with real lenses. As shown in Figure 4.34, the curvature of field means that objects that are imaged at an angle to the lens plane have a reduced distance between the lens and the image (v). It follows from Equation 4.1 that the lens has a reduced focal length for these objects.

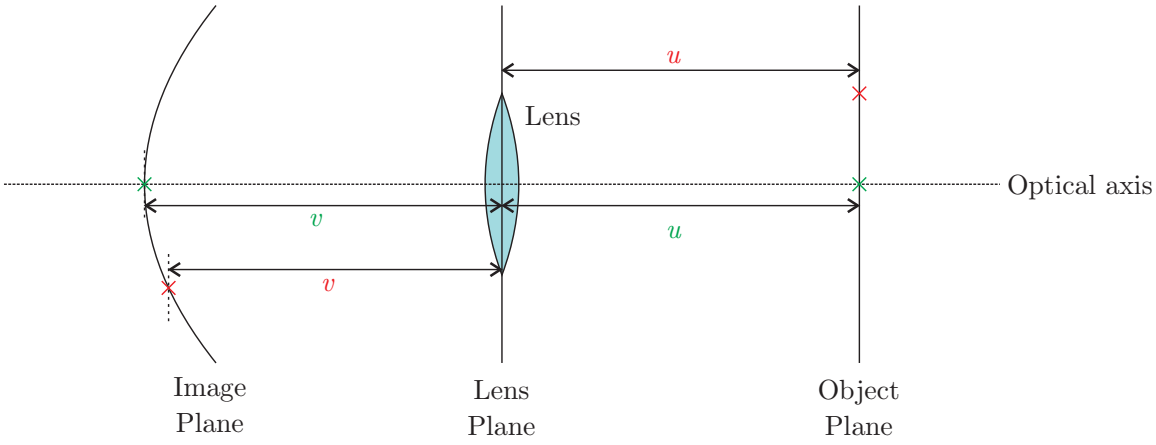


Figure 4.34: The red and green crosses on the object plane get imaged onto the red and green crosses on the image plane respectively. Although the distance between the objects and the lens (u) are the same for both, the distance between the image and the lens (v) is smaller for the red cross due to the curvature of field exhibited by the lens.

4.6.2.2 Detector plane coincident to adjusted image plane

Having accounted for the effect of lens tilt on the focal length of the lens, the computational model was employed to investigate the effect of lens tilt on the spot size, magnification and grating length per fibre when the detector plane was placed along the recalculated image plane. Figure 4.35 shows the results.

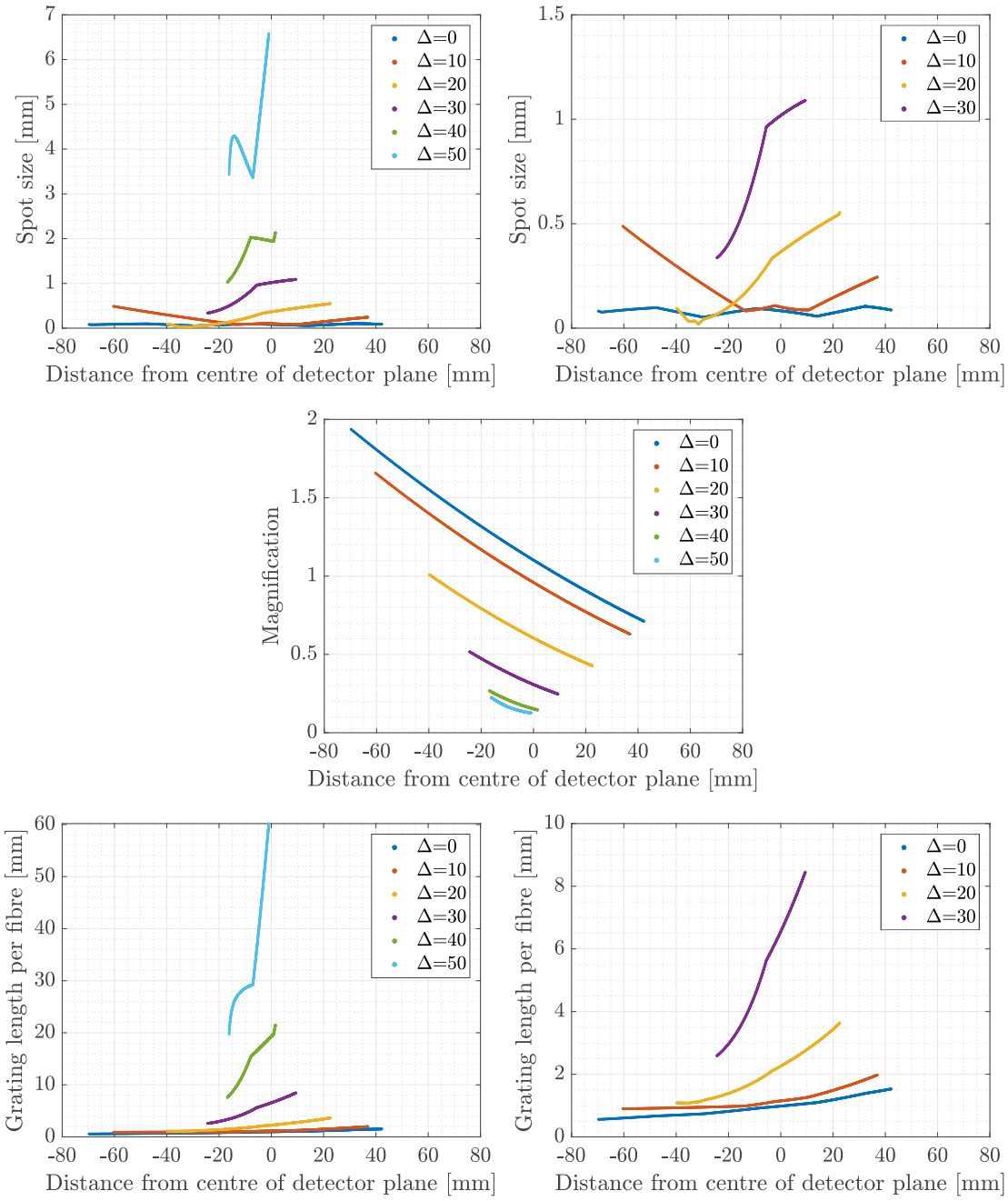


Figure 4.35: Results from computational model showing the variation of the spot size, magnification and grating length per fibre (L_{gf}), along the detector plane, for different angles of tilt of the lens plane (Δ) when the angle of the detector plane (γ) has been optimised. Note that Δ is the angle, in degrees, between the detector plane and the perpendicular to the optical axis. Also note that the additional graphs of spot size and L_{gf}, shown on the right, are the same as the graphs on the left but with a different scale on the y-axis.

Even though the detector plane is now along the ideal image plane for each value of Δ, the average spot size across the detector plane increases with lens tilt. This is because the lens used in this model is designed for imaging applications where the lens is perpendicular to the optical axis. The magnification of the imaging system decreases as the lens is tilted further. This can be attributed to a combination of the focal length of the lens decreasing, as well as the detector plane angle increasing. The trends in spot size and magnification result in the grating length per fibre increasing (worsening) as the lens plane angle is increased. These results show that when the detector plane can be placed along the image plane, it is preferable to keep the lens perpendicular to the optical axis.

4.6.2.3 Detector plane not coincident with image plane

Photomultiplier tubes (PMTs) are used as the detectors for LITGS signals due to their high sensitivity and short rise times. For the proposed technique presented here a 1-D array of detectors is required. As explained in Section 4.4, an array of optical fibres has to be used to achieve this, with each fibre leading to a separate PMT. The detector plane will therefore be drawn along the surfaces of an array of optical fibres. The investigation for angling the lens plane thus far has assumed that this detector plane can be placed coincident to the image plane. Unfortunately, this will rarely be the case for LITGS experiments. The angle at which the signal beam scatters off the thermal grating is usually only a few degrees, meaning that the image plane will also be angled by only a few degrees to the optical axis. However optical fibres, which are proposed for signal collection, can only accept light that deviates from being perpendicular to their surface by a small angle. This is because the light entering the fibre has undergo total internal reflection as it hits the boundary between the core and the cladding; if it doesn't meet this criteria, the light will travel through the cladding and exit the fibre. This concept is shown in Figure 4.36. The acceptance angle is generally only around 20°, meaning that the fibres can only be angled a minimum of 70° from the incoming light rays[10]. The value of γ, which is the angle of the detector plane to the optical axis, is therefore limited to a minimum of 70°.

[10]For example, the FT1000UMT optical fibres from Thorlabs, whaic were used for one experiment described in Chapter 5, have an acceptance angle of 23°.

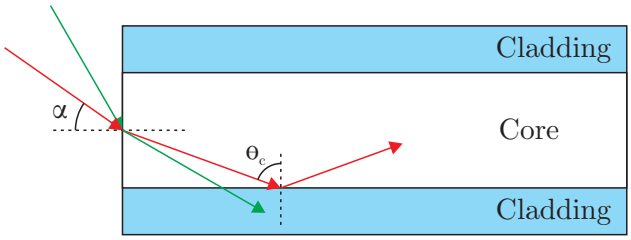


Figure 4.36: Optical fibres are made of two different materials - the core and the cladding. Light entering the fibre within the 'acceptance angle', denoted by α, will undergo total internal reflection at the material boundary, and thus propagate down the fibre. Light that enters at an angle greater than α, as represented by the green ray, will pass through the boundary and exit the fibre.

As discussed in Section 4.6.1.2, increasing the detector plane angle (γ) away from the angle of the image plane results in poorer spatial resolution of the system . However, the results in Table 4.4 show that increasing the angle at which the lens is tilted (Δ) has the effect of increasing the angle of the ideal image plane. Therefore, when the detector plane is placed at an angle that is larger than the ideal image plane, tilting the lens will have two competing effects:

1. The angle of the image plane will increase, decreasing the difference between the relative angles of the image and detector planes. This means that the detector plane is now more in-focus, and therefore should result in an improvement in spatial resolution.

2. The effect of tilting the lens leads to a poorer spatial resolution, even when the detector plane is placed along the ideal image plane. This is due to the combination of the design of the lens and the decrease in focal length.

To investigate the overall effect of lens tilt, the computational model was used again. Figure 4.37 shows how the spot size, magnification and grating length per fibre are affected by tilting the lens while the detector plane is fixed at an angle of 70° to the optical axis. As the lens tilt is increased, the variation of spot size across the detector becomes less uniform. As explained in Section 4.6.2.2, this is due to the field curvature of the lens and therefore shows that the decrease in spatial resolution as the lens is tilted is the dominant mechanism. This is verified by observing the effect of lens tilt on the grating length per fibre, where the best spatial resolution is achieved with the lens perpendicular to the optical axis.

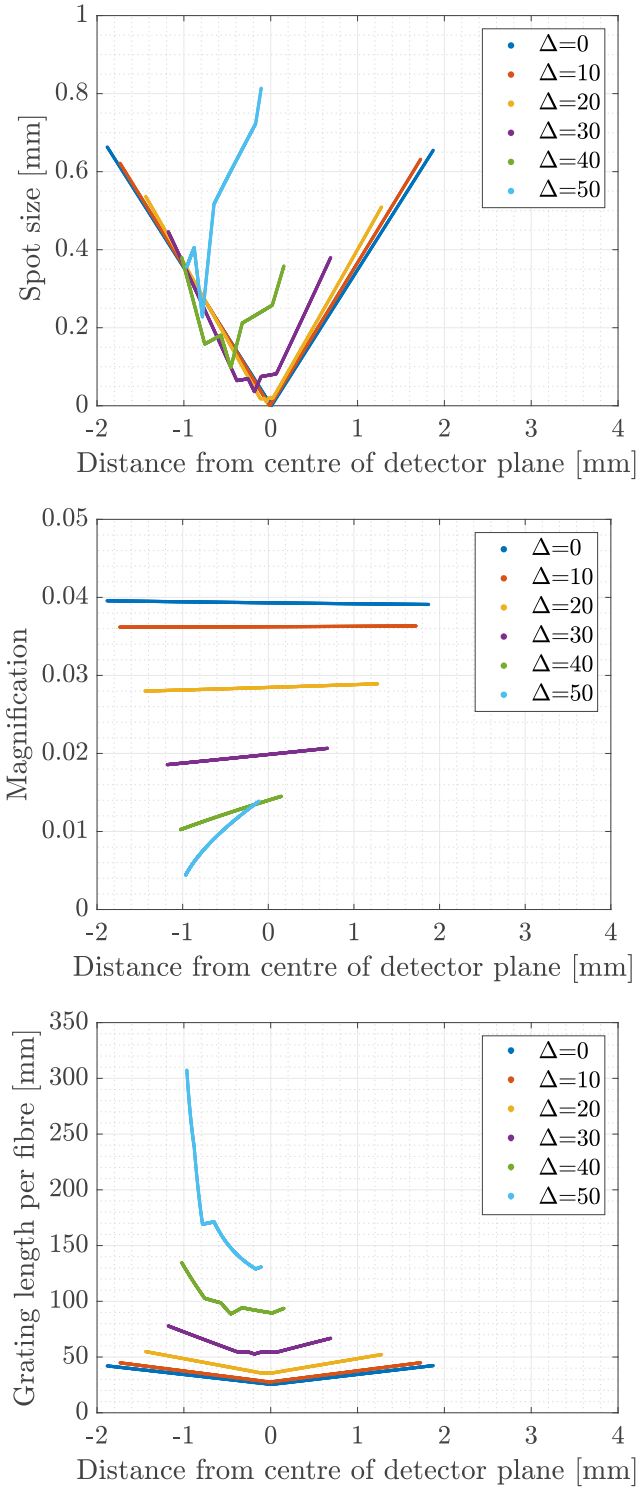


Figure 4.37: Results from computational model showing the variation of the spot size, magnification and grating length per fibre (L_{gf}), along the detector plane, for different angles of tilt of the lens plane (Δ) when the angle of the detector plane (γ) is set at 70° from the optical axis. Note that Δ is the angle, in degrees, between the detector plane and the perpendicular to the optical axis.

4.6.3 Varying the distance between the grating and the imaging lens

The final experimental parameter to be investigated was the distance (u), along the optical axis, between the object plane (along which the grating lies) and the lens. If the object, lens and image planes were parallel, then varying this distance would have the effect of changing the distance (v) between the lens and the image plane as shown by Equation 4.1, as well as altering the magnification of the system as calculated by Equation 4.13. However, since the planes are all angled, this variation will also affect the angle of the image plane (γ).

4.6.3.1 Detector plane coincident to image plane

First, the computational model was used to investigate the effect of changing the distance u while keeping the detector plane coincident to the image plane (and therefore in focus). Table 4.5 shows how the distance v and angle γ were found to vary with u.

Object distance u [mm]	Image distance v [mm]	Detector plane angle γ [°]
300	648	0.9
400	420	1.9
500	347	2.9
600	311	3.9

Table 4.5: Optimal distance (v) and angle (γ) of the detector plane (when it is placed along the image plane) as the distance between the grating and the lens (u) is varied.

Figure 4.38 shows how the spot size, magnification and grating length per fibre are affected by varying the distance u. The detector plane was adjusted to remain coincident to the image plane (and therefore the image is always in focus). The results show that the spot size is fairly constant for all values of u, which was expected since the image is always in focus. Table 4.5 shows that as u is increased, v decreases. By considering Equation 4.13, the magnification of the system is therefore expected to decrease as u is increased; this is verified by the results. Finally, the grating length per fibre is shown to decrease as u increases, which is also expected since a larger magnification improves the spatial resolution.

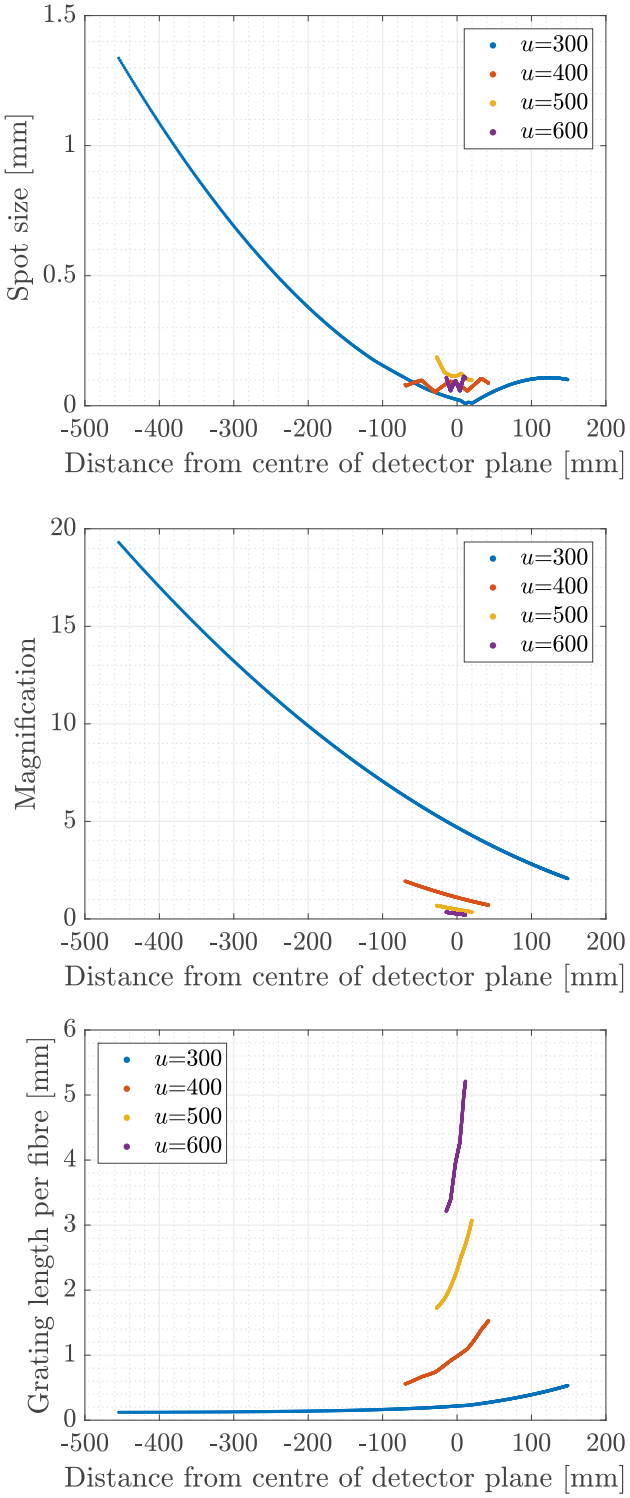


Figure 4.38: Results from computational model showing the variation of the spot size, magnification and grating length per fibre (L_{gf}), along the detector plane, for different values of u (which is the distance between the object and lens planes) when the angle of the detector plane to the optical axis (γ) has been optimised. Note that Δ is the angle, in degrees, between the detector plane and the perpendicular to the optical axis.

4.6.3.2 Detector plane not coincident with image plane

As explained in Section 4.6.2.3, it is unlikely that the detector plane will be coincident to the image plane for a LITGS application. Therefore, it is important to consider the effect of varying u when the detector plane is set at an angle γ=70°. Again, as was the case with varying the lens plane tilt (Δ), there are two contradicting trends:

1. The results shown in Figure 4.38 suggest that increasing u will decrease the magnification of the system, and therefore the spatial resolution will also worsen.

2. Table 4.5 shows that increasing u has the effect of increasing the angle of the image plane. This means that the detector plane, when placed at an angle of γ=70°, will be more in focus for higher values of u, leading to smaller spot sizes and improved spatial resolution.

Figure 4.39 shows the results, obtained from the computational model, of varying u while γ=70°. It is clear that as u is increased, the decrease in magnification outweighs the improvement in focus and therefore a smaller value of u is beneficial for the spatial resolution of the system.

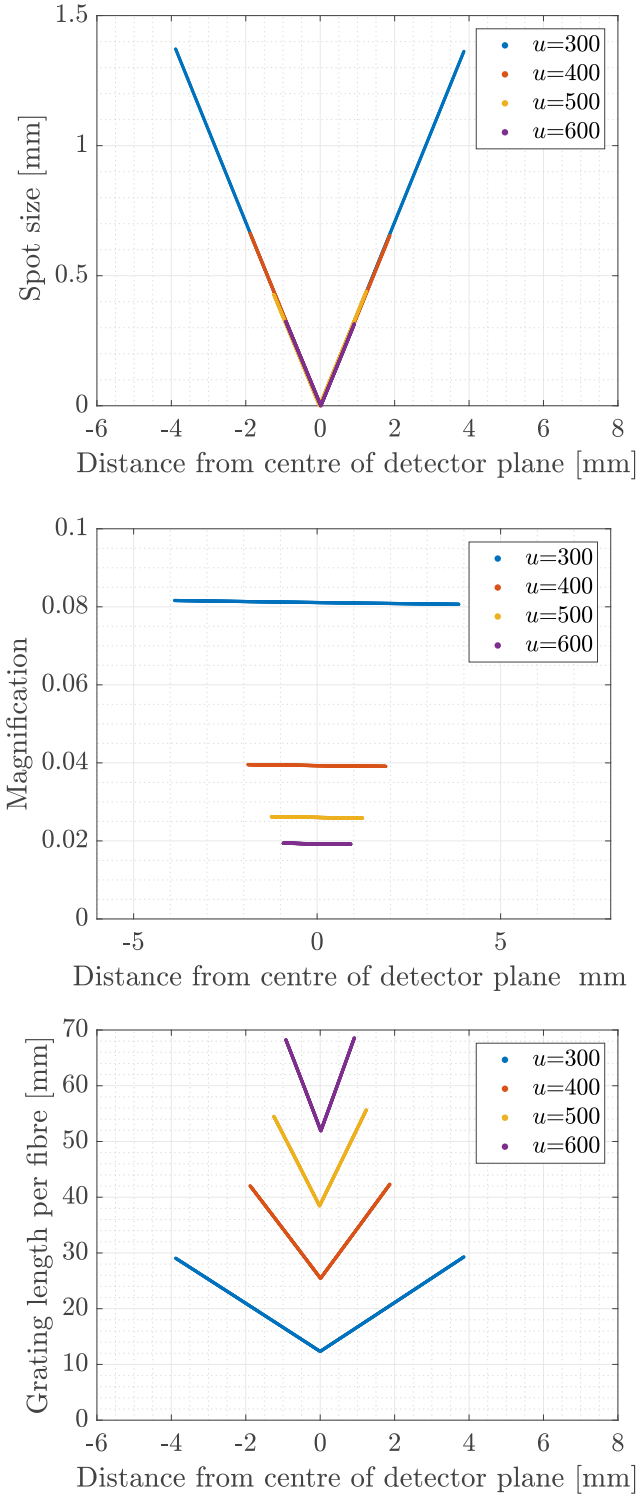


Figure 4.39: Results from computational model showing the variation of the spot size, magnification and grating length per fibre (L_{gf}), along the detector plane, for different values of u (which is the distance between the object and lens planes) when the angle of the detector plane (γ) is set at 70° from the optical axis. Note that Δ is the angle, in degrees, between the detector plane and the perpendicular to the optical axis.

4.7 Summary

This chapter introduced the inherently poor spatial resolution in the axial direction as one of the major drawbacks of the LIGS technique when compared to CARS. A solution to this problem, which would also enable the collection of 1-D LIGS measurements in the axial direction, was proposed. The concept involved dividing the signal beam into spatially-resolved 'sub-signals', and imaging each one onto a one dimensional array of optical fibres (with each fibre leading to an individual detector). However, due to the angle at which the signal beam propagates away from the grating, a 'standard' imaging setup would not suffice. The concept of Scheimpflug imaging was therefore introduced. An experiment was designed to characterise this novel approach.

However, before conducting the experiment, a ray-tracing computational model was developed that would enable a thorough parametric investigation of the technique. The capability to simulate the characterisation experiment was added to the model as a means to validate it. Assumptions included in the model were that all beams are Gaussian and that the divergence of the signal beam is equal to that of the probe beam. A variation in fringe spacing along the grating, as a result of the Gaussian nature of the beams, was also accounted for. This was done by modelling the LIGS grating as a diffraction grating which enabled the characterisation of how the signal beam intensity varies along the grating. The signal beam was also modelled to be generated from a 1-D line along the grating.

Two different measures of the spatial resolution were defined. The 'grating length per fibre', L_{gf}, refers to the length along the grating that each fibre (and therefore detector) receives a LIGS signal from. The 'grating pitch', P_{g}, is the distance along the grating between the centres of the regions captured by two consecutive fibres.

Finally, a parametric investigation of the technique was conducted. For this study, the effect on L_{gf} was considered since that is the per-fibre spatial resolution. Three experimental parameters that affect the imaging of the signal beam onto a detector were considered. The first parameter to be varied was the tilt of the detector plane. The conclusion was that the highest spatial resolution was achieved by placing the detector plane coincident to the image plane. Under this condition, the entire image is focused on the detector. However,

as discussed in Section 4.6.2.3, this would usually not be possible for a LIGS experiment due to the limitation of a relatively small acceptance angle for optical fibres.

A possible solution to this problem was to tilt the lens. In order to obey the Scheimpflug and hinge rules, this would result in an increase in the angle of the image plane so that the image on the detector plane was more in-focus. However, the results showed that tilting the lens also had the unwanted effect of reducing its focal length, which is detrimental to the magnification and thus the spatial resolution of the system.

The final parameter tested was the distance (u) between the centre of the object plane and the lens. The results showed that reducing the distance, and therefore increasing the magnification of the system, led to an increase in the spatial resolution.

Based on these findings, the design of a LITGS experiment using this imaging system should always try to minimise the distance between the grating and the imaging lens to achieve a higher spatial resolution. The detector plane should then be angled to be as close as possible to the image plane; the further that the plane is angled, the larger the incremental gain in resolution achieved by the adjustment. Access to a specialised imaging lens that has a low curvature of field may warrant tilting the lens to improve the resolution; however this is not the case for a simple lens.

5 Axially-resolved LIGS: Experimental validation

Chapter 4 introduced a novel technique to obtain spatially-resolved LIGS measurements in the axial direction. An experiment to characterise the approach was described in Section 4.4. A computational model was also developed and used to conduct a parametric investigation of the technique. The model included the capability to simulate the results of the characterisation experiment.

This chapter details the experiments that were conducted to explore this novel approach. The results are then compared to simulations from the computational model in order to validate it. Finally, multiple spatially-resolved LIGS temperature measurements in the axial direction are presented.

5.1 Experimental setup

The general experimental layout and methodology employed for this study were described in Section 4.4. This section describes the configuration and equipment used in more detail.

Figure 5.1 shows the complete experimental setup. A continuous wave DPSS laser[1] was used to produce the probe beam at a wavelength of 671 nm, while a pulsed Nd:YAG laser[2] (operating at 10 Hz) was used to generate a pump beam at a wavelength of 266 nm. A beam splitter was employed to divide the beam into two identical pump beams, which were then directed by mirrors to cross at 1.6°. A compensator plate was added to one beam path to account for the difference in path lengths between both pump beams.

A Pellin–Broca prism was placed at the output of the Nd:YAG laser to remove any residual 532 nm light. The beam was elliptical in shape, with the major axis being vertical, and so an image rotation prism was used to rotate the beam to have a horizontal major axis. This ensured that the pump beams interacted over a longer length, creating a long grating that could be probed by the nitrogen jet.

[1] A MLL-FN-671 model from CNI.
[2] A Minilite II model from Continuum.

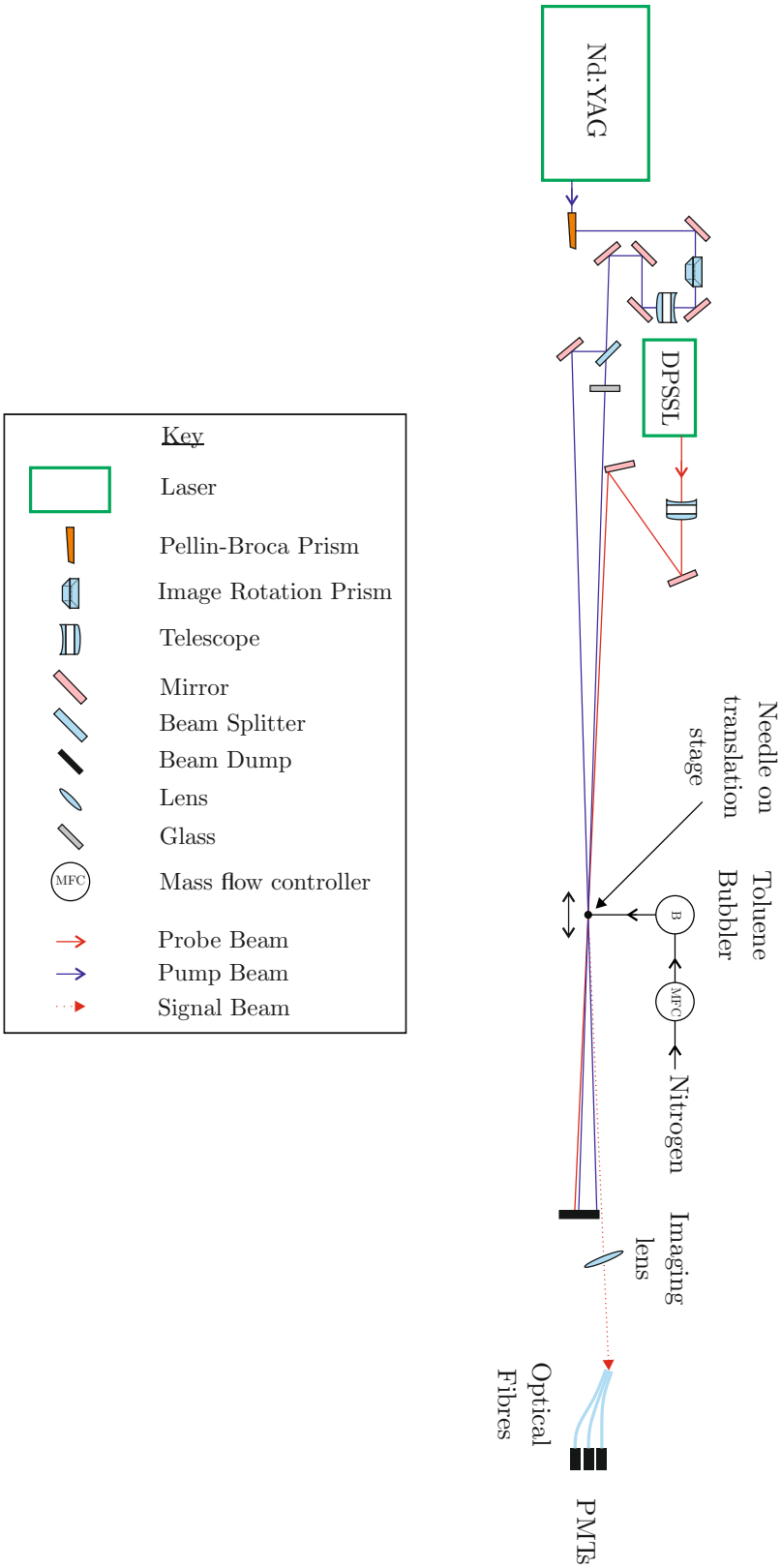


Figure 5.1: Bird's-eye view of the experimental setup using optical fibres. Note that the needle emits a jet of nitrogen saturated with toluene in the direction out of the paper, and the laser beams pass through the jet.

No crossing lens was used in the setup, and so a combination of one negative and one positive focal length lens (put together to create a telescope) were used to collimate both the pump and probe beams. Figure 5.2 shows the profiles, measured at the middle of the interaction region, of one pump beam and the probe beam respectively. Using a e^{-2} definition for beam size, the beam width was measured to be 3.8 mm for the pump beam and 0.9 mm for the probe beam.

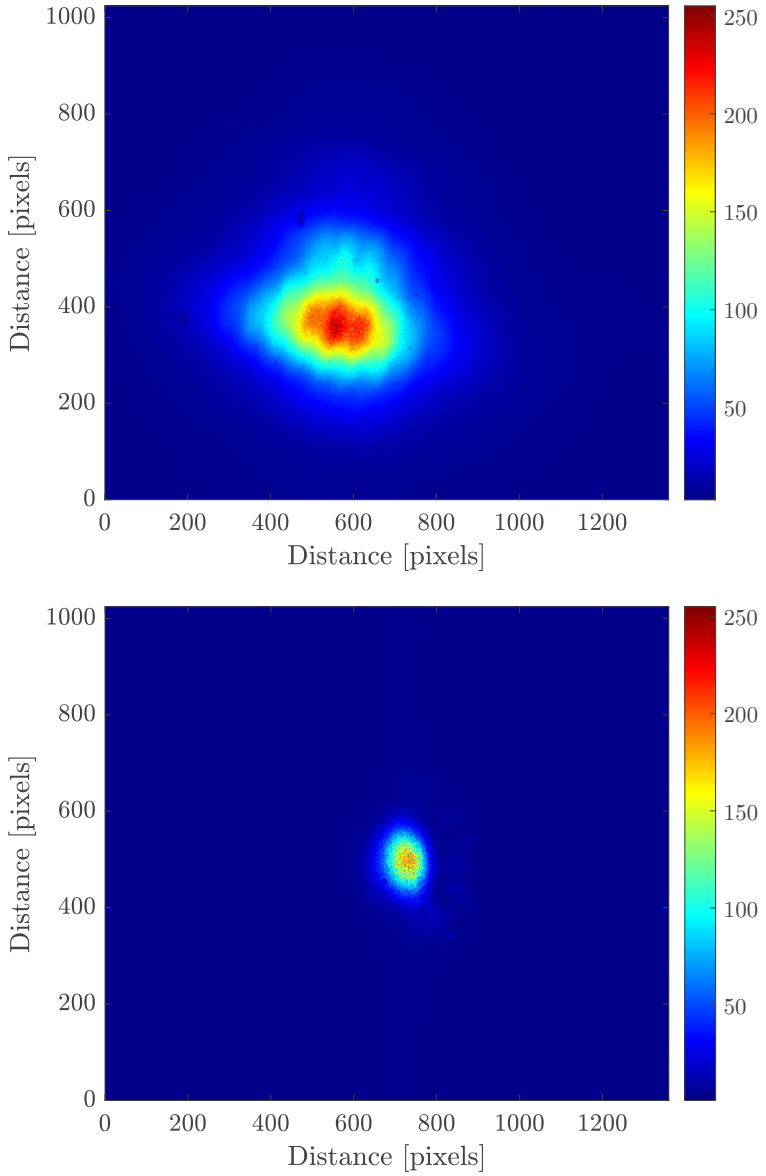


Figure 5.2: Beam profiles of one pump beam (top) and the probe beam (bottom) at the middle of the interaction region. Note that the pixel size is 6.4 µm x 6.4 µm. The colourbar represents the pixel intensity.

As the pump beams used for this experiment had a wavelength of 266 nm, toluene was chosen to be the absorbing species. A bubbler was used to seed the nitrogen gas with toluene vapour. A thin-walled stainless steel tube with an outer diameter of 1 mm was used as the needle to emit the jet of nitrogen saturated with toluene vapour. A mass flow controller[3] regulated the flow to be constant at 0.1 slpm. The needle was set on a motorised translation stage to allow it to be translated along the grating. Figure 5.3 shows a Laser-Induced Fluorescence (LIF) image taken of the jet (where the UV pump beams were used to induce fluorescence from toluene molecules). The image was captured using an intensified camera[4], and the jet was measured to be 0.67 mm in diameter.

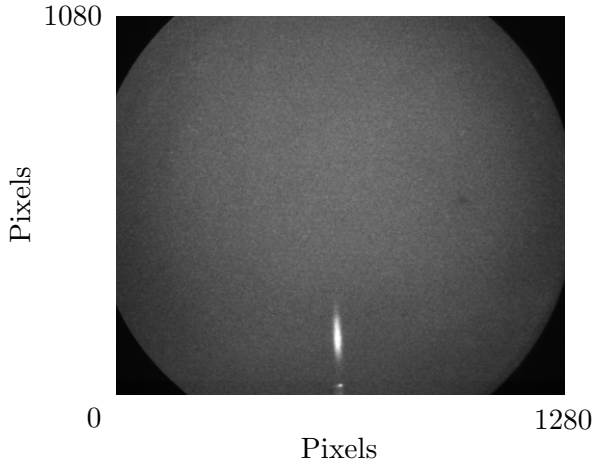


Figure 5.3: LIF image taken of the jet of nitrogen seeded with toluene vapour. The tip of the needle emitting the flow can be seen at the bottom. The jet was shown to be steady over multiple images.

Following the analysis of grating strength variation within the interaction region of the pump and probe beams presented in Section 4.5.6.1, it was decided that the translation stage for the needle would be aligned with the probe beam. This ensured that the needle travelled along the longest available length of the signal-generating part of the grating.

To image the signal beam onto the detector, a 200 mm focal length camera lens[5] was used. This focal length was chosen as the specific lens would provide a better image quality compared to a standard bi-convex lens.

[3]HFC-202 model from Teledyne Hastings Instruments.
[4]An iStar sCMOS model by Andor.
[5]A Serrac lens from Dallmeyer.

The distance between the grating and the imaging lens (u) was set to be 400 mm. The study presented in Section 4.6.3 showed that this distance should be minimised to obtain the best possible spatial resolution of the system. However, in the experimental setup used, the imaging lens could not be moved any closer to the grating due to the small difference in angle between the pump, probe and signal beams. In order to be able to safely dump the pump and probe beams while allowing the signal beam to continue, all the beams had to travel down the optical table for at least 400 mm to allow them to deviate from each other.

Usually, the signal beam in a LITGS experiment would be collected by one photomultiplier tube (PMT). As explained in Section 4.6.2.3, a linear array of optical fibres, each leading to an individual PMT[6], was used to collect the signal beam for this experiment. Two different experiments, using different linear arrays of optical fibres, were conducted.

Both experiments employed an array of 3 off-the-shelf optical fibres with a numerical aperture of 0.39 (i.e. a maximum acceptance angle of 23°). For the first experiment, the fibres[7] each had a core diameter of 1 mm. They were chosen as the mounted array, shown in Figure 5.4**a**, was already available from previous work done by Willman and Ewart [91]. For the second experiment, optical fibres[8] with a core diameter of 400 µm were used. A suitable mount for these smaller fibres, shown in Figure 5.4**b**, was designed and 3-D printed.

An oscilloscope[9] was used to record the signals from all three PMTs.

a **b**

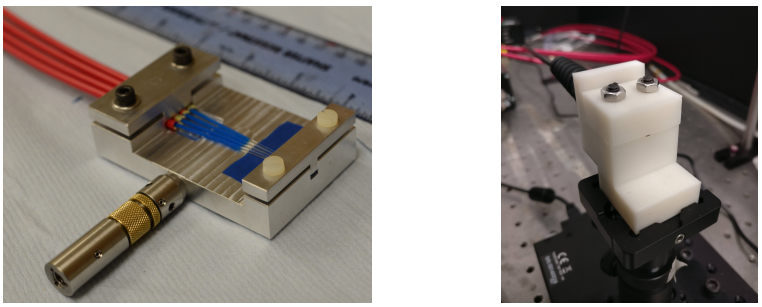


Figure 5.4: Figure **a** shows the 'large' fibre array, while Figure **b** shows the 'small' fibre array. In both figures the fibres (with red sheaths), seen entering the 'back' of the mount, are clamped in place with their faces visible at the 'front'.

[6]Two Hamamatsu H10721-20 PMT modules (stated rise time of 0.57 ns and sensitivity of 150 A/mW), and one Hamamatsu H6780-20 PMT module (stated rise time of 0.78 ns and sensitivity of 39 A/mW).
[7]FT1000UMT fibres from Thorlabs.
[8]FT400EMT fibres from Thorlabs.
[9]PicoScope 6402A from Pico Technology (5 Gs/s sampling rate and 250 MHz bandwidth).

5.2 Characterisation of fringe spacing variation

Section 4.5.6.3 introduced how the Gaussian nature of the pump beams can lead to a variation in fringe spacing along the grating which must be accounted for within the computational model. Although lenses were used to collimate the pump beams, as described in Section 5.1, the long distance over which the grating was formed (due to the large beam widths used for this experiment) meant that the fringe spacing needed to be characterised experimentally. To do this, the experiment detailed in Section 5.1 was run twice with the array of 'large' optical fibres and the array of 'small' optical fibres respectively. The jet was moved in discrete steps of 1 mm along the grating, and at each step the LITGS signal from each optical fibre was recorded. The LITGS signals taken at each position, regardless of which fibre they were recorded by, were then analysed to obtain the frequency of oscillations. Figure 5.5 shows the variation in frequency along the grating for both experiments. A least-squares linear fit was used for both figures, and gradients of -0.023 and -0.034 were calculated for Figures 5.5**a** and 5.5**b** respectively.

As the same jet of nitrogen saturated with toluene was used throughout both experiments, the temperature and composition of the flow remained constant. Equation 2.3 could therefore be rearranged and simplified to show that

$$F = \frac{C}{\Lambda} \tag{5.1}$$

where C is a constant and the frequency (F) was only a function of the fringe spacing (Λ). Using this relationship, the variation in fringe spacing was calculated for both experiments by assuming the desired spacing of 9.5 µm at the centre of the grating. The change in fringe spacing, per millimetre along the grating, was found to be 0.006 µm and 0.009 µm for the large and small fibre experiments, respectively, which gives a mean variation of 0.0075 µm (or 0.08 %).

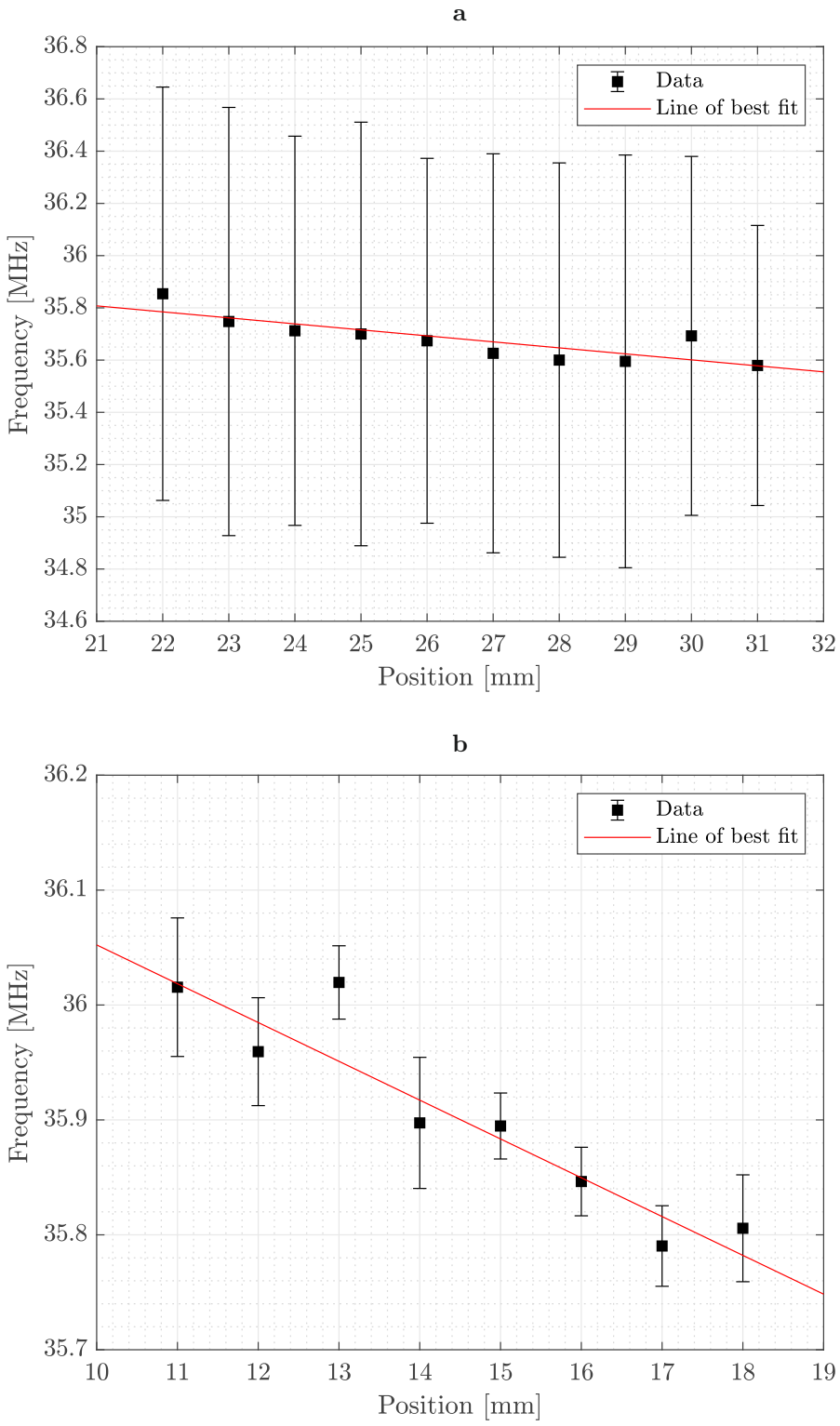


Figure 5.5: Frequency variation, along the grating, for the experiment with larger fibres (Figure **a**) and the smaller fibres (Figure **b**). The frequencies were measured in the region where the signal strength was strongest, so that the signal to noise ratio was high.

5.3 Computational model inputs

Table 5.1 shows the input parameters that were used for the computational model. The imaging lens was modelled as a bi-convex spherical lens manufactured by Thorlabs[10].

Simulation process	Property	Value
LITGS geometry	Pump beam wavelength	266 nm
	Pump beam size	3.8 mm
	Probe beam wavelength	671 nm
	Probe beam size	0.9 mm
	Pump & probe beam profiles	Gaussian
	Crossing angle	1.6°
Imaging geometry	Distance between grating and lens	400 mm
	Imaging lens focal length	200 mm
	Lens plane angle	90° to optical axis
Signal beam generation	Grating resolution	0.1 mm
	Object plane angle	2° to grating axis
Imaging signal beam	Detector plane angle	90° to optical axis
Detection fibres	Optical fibre core diameter	1 mm and 400 µm
Experimental data	Jet diameter	0.67 mm
	Variation in fringe spacing	0.0075 µm/mm

Table 5.1: Input parameters used for the computational model. The 'grating axis' refers to the longitudinal axis through the centre of the grating.

An important difference from the parameters that were used for the investigations presented in Section 4.6 is that the object plane was set to be 2° from the grating axis. This was to account for the motorised translation stage being aligned with the probe beam rather than the grating axis.

[10]Part number LB1199.

5.4 Signal beam size

This section describes an experiment to validate the spot size calculated by the computational model by comparing it to the experimentally measured signal beam size. To carry out the experiment, a camera was placed along the detector plane to image the signal beam.

5.4.1 Computational Results

As described in Section 4.5.6.2, the jet is modelled as a line of point sources spanning the length of the jet diameter. The collection of rays generated by these sources is the signal beam, and the variation in spot size (which affects each of these point sources equally) as the jet is moved along the grating is a measure of the induced blur. Figure 5.6 shows how the spot size and signal beam size were modelled to vary along the detector plane.

When the jet is at the centre of the grating, the spot size (blur) is minimised. As the jet was measured to be 0.67 mm in size (from the LIF image presented in Figure 5.3) and the magnification at the centre of the grating was calculated (by the model, for the plane along which the jet was modelled) to be 1.05, the signal beam size at this point was 704 µm.

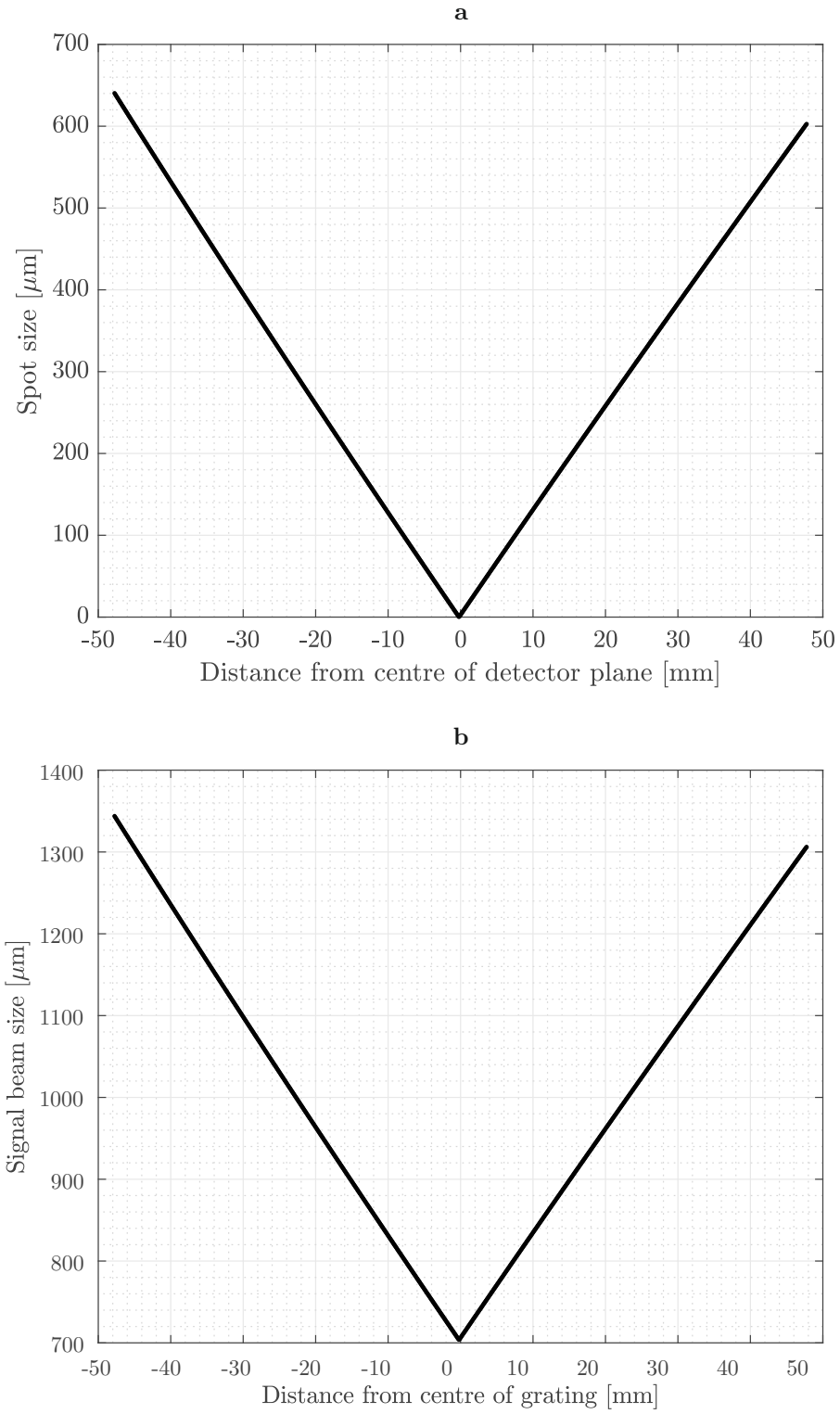


Figure 5.6: Results from the computational model of the experiment showing the variation of the spot size and signal beam size along the detector plane. For the spot size, the x-axis denotes the location of the point source along the grating. For the signal beam size, the x-axis denotes the location of the centre of the jet along the grating.

5.4.2 Experimental Results

Figure 5.7 shows the image of the signal beam captured by a camera[11] when it was placed along the detector plane. The image was taken with the jet positioned at the centre of the grating. Figure 5.7 also shows the average intensity variation along the image[12]. Using the method of least-squares to fit a Gaussian curve to the intensity variation, the beam size (using a e^{-2} definition) was calculated to be 727 µm.

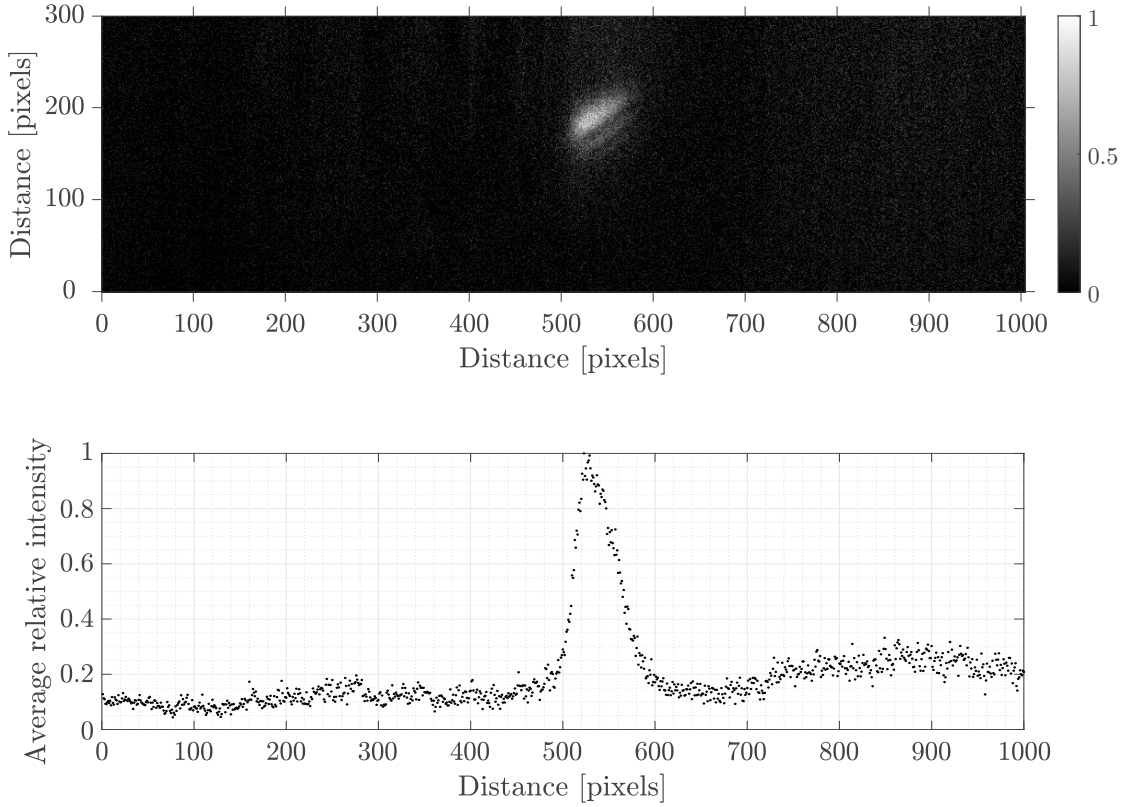


Figure 5.7: On top is an image of the signal beam (with the colourbar denoting relative intensity), and on the bottom is a graph showing the average relative intensity across the image. Note that the pixel size is 8 µm x 8 µm.

[11] A Luca-R EMCCD camera by Andor.

[12] Interestingly, there appear to be some fringes visible within the signal beam (with a relatively large spacing on the order of 100 µm), which could suggest the presence of two separate signal beams propagating at a slightly different angles. This could be possible due to the divergence of the probe beam and variation in fringe spacing along the grating.

5.4.3 Discussion

The signal beam size determined from the experiment was 727 µm while the computational model predicted it to be 704 µm. As explained in Section 4.5.6.2, the computational model assumes the jet to be a line of point sources, which produces a signal beam that is imaged in focus when the jet is at the centre of the grating. In reality, however, there will be some blurring caused by the circular nature of the jet that has not been accounted for by the model; this is expected to be minimal as the jet is only 0.67 mm in diameter, but does explain why the experimental signal beam is larger than predicted.

5.5 Magnification

The computational model is able to predict how the magnification varies across the detector plane. This section describes the experimental validation of this simulation. To carry out the experiment, a camera was placed along the detector plane to image the signal beam.

5.5.1 Computational Results

Figure 5.8 shows how the magnification is modelled to vary along the image plane. The magnification is virtually constant, with the slight curve resulting from lens aberrations.

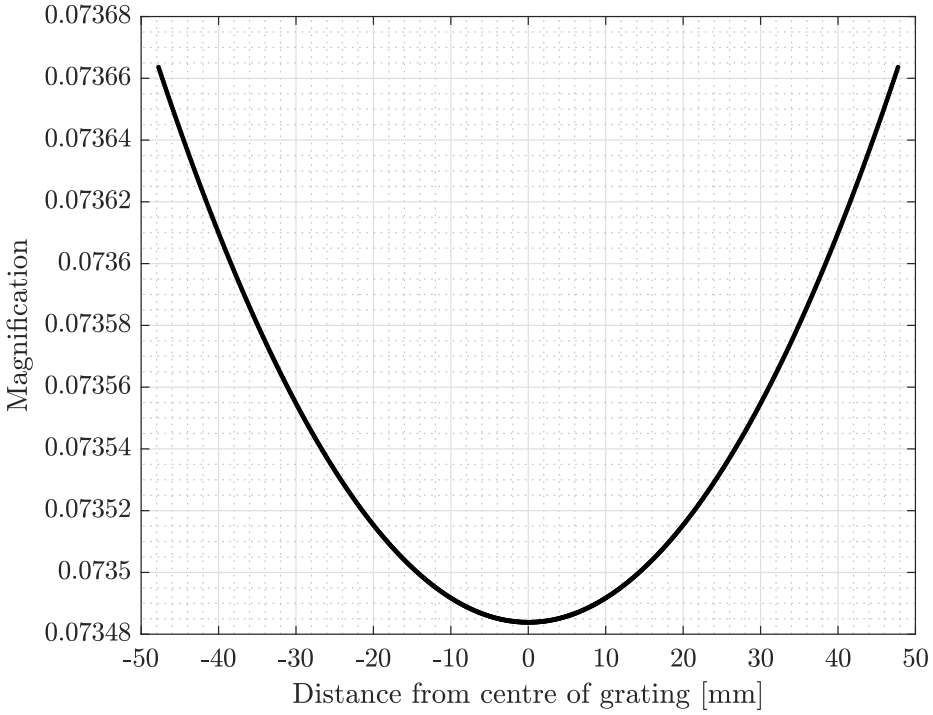


Figure 5.8: Results from the computational model of the experiment showing the variation magnification along the detector plane. The x-axis denotes the location of the point source along the grating.

5.5.2 Experimental Results

Figure 5.9 shows two images of the signal beam captured by a camera[13] which was placed along the detector plane. The first image was with the jet placed 2 mm before the centre of the grating, and the second image was with the jet 2 mm after the centre of grating. Figure 5.7 also shows the average intensity variation along both images. Using the method of least-squares to fit Gaussian curves to both intensity variations, the centre of the beam was calculated to have moved by 32 pixels. This shows a magnification of 0.064.

5.5.3 Discussion

The magnification derived from experimental results was 0.06 whereas the computational model predicted a value of 0.07. The value obtained experimentally is subject to error from the camera sensor not being perpendicular to the signal beam, as well as the respective

[13] A Luca-R EMCCD camera by Andor.

distances between the jet, lens and camera being different.

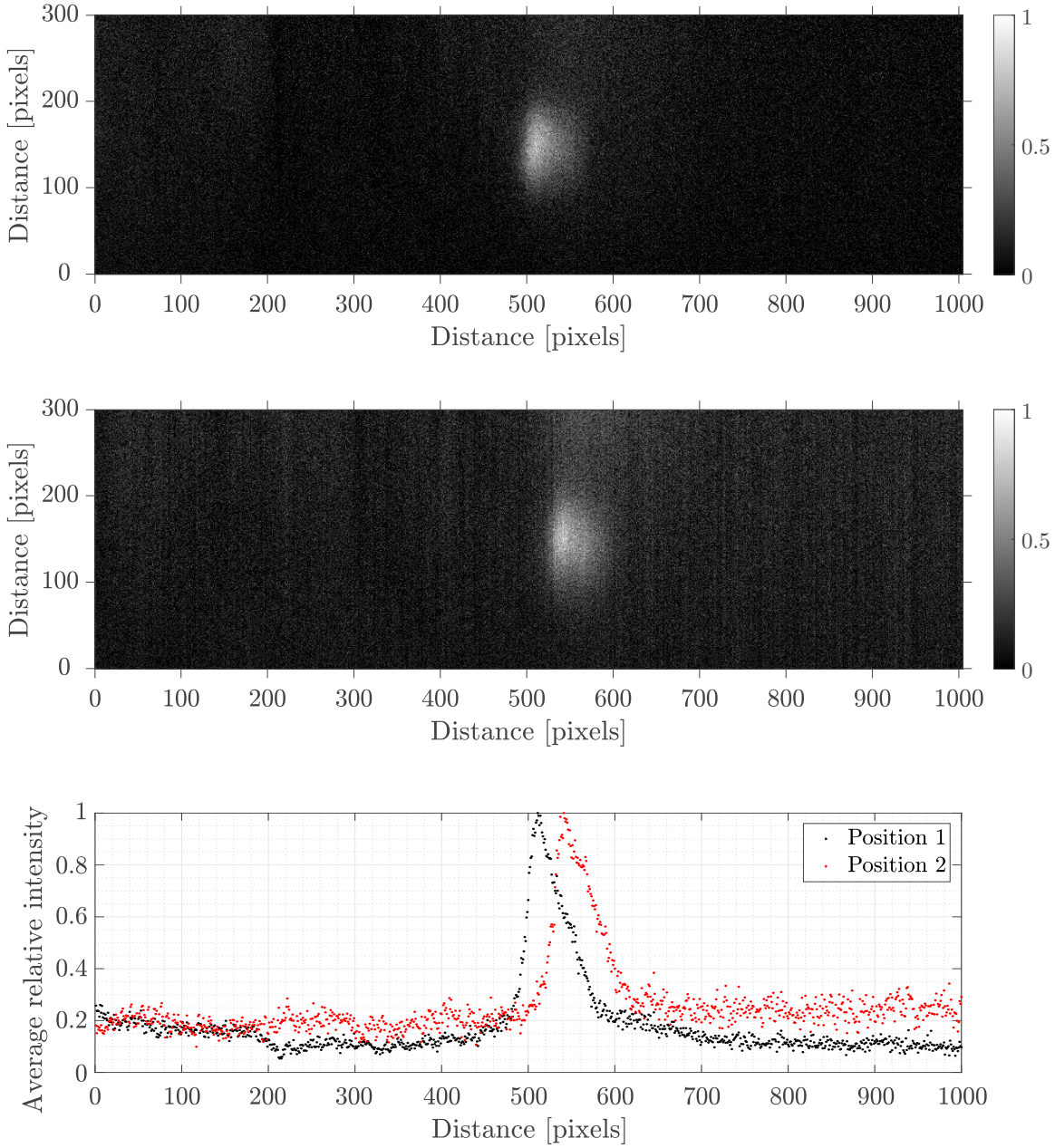


Figure 5.9: On top is an image of the signal beam at position 1, when the jet was 2 mm before the centre of the grating, and below it is an image of the signal beam at position 2 when the jet was 2 mm after the centre of the grating. The colourbar for both images represents relative intensity. On the bottom is a graph showing the average intensity along both images. Note that the pixel size is 8 µm x 8 µm.

5.6 Characterisation using 'large' optical fibres

For this experiment, the signal collection was performed by a linear array of three optical fibres, all with a core diameter of 1 mm and a total (core and cladding) diameter of 1.035 mm. The jet was moved in discrete steps along the grating, and at each step the signal from each optical fibre was recorded.

5.6.1 Computational Results

The computational model simulated the jet moving in discrete steps of 0.0.1 mm, and produced the simulated experimental data shown in Figure 5.10. The graph shows how the signal strength captured by each of the three optical fibres was expected to vary as the jet was moved along the grating. While Figure 5.10**a** shows the data for each fibre normalised to the maximum intensity seen by seen by any fibre, Figure 5.10**b** shows the data for each fibre normalised to the maximum intensity seen by the fibre itself. It is clear that the middle fibre receives the highest intensity signal, as is expected due to the variation of intensity of pump and probe beams throughout the grating.

The normalised signal intensity received by each fibre relative to the position of the jet along the grating, as presented in Figure 5.10**a**, can be fitted to Gaussian curves. A least-squares fit was used to retrieve the characteristics for each curve shown in Table 5.2.

Property	**Fibre 1**	**Fibre 2**	**Fibre 3**
Centre of curve along grating [mm]	60	48	36
Peak value relative to maximum	0.05	1.00	0.05
Width of curve [mm]	21.6	9.0	21.8
	(21.5, 21.7)	(9.0, 9.1)	(21.7, 22.0)

Table 5.2: Gaussian fit parameters for each optical fibre from modelled data. Note that the width of the curve is defined as the distance over which the normalised signal strength is greater than e^{-2}. The 95 % confidence intervals are denoted in brackets; however they are not stated if they are within the precision of the value.

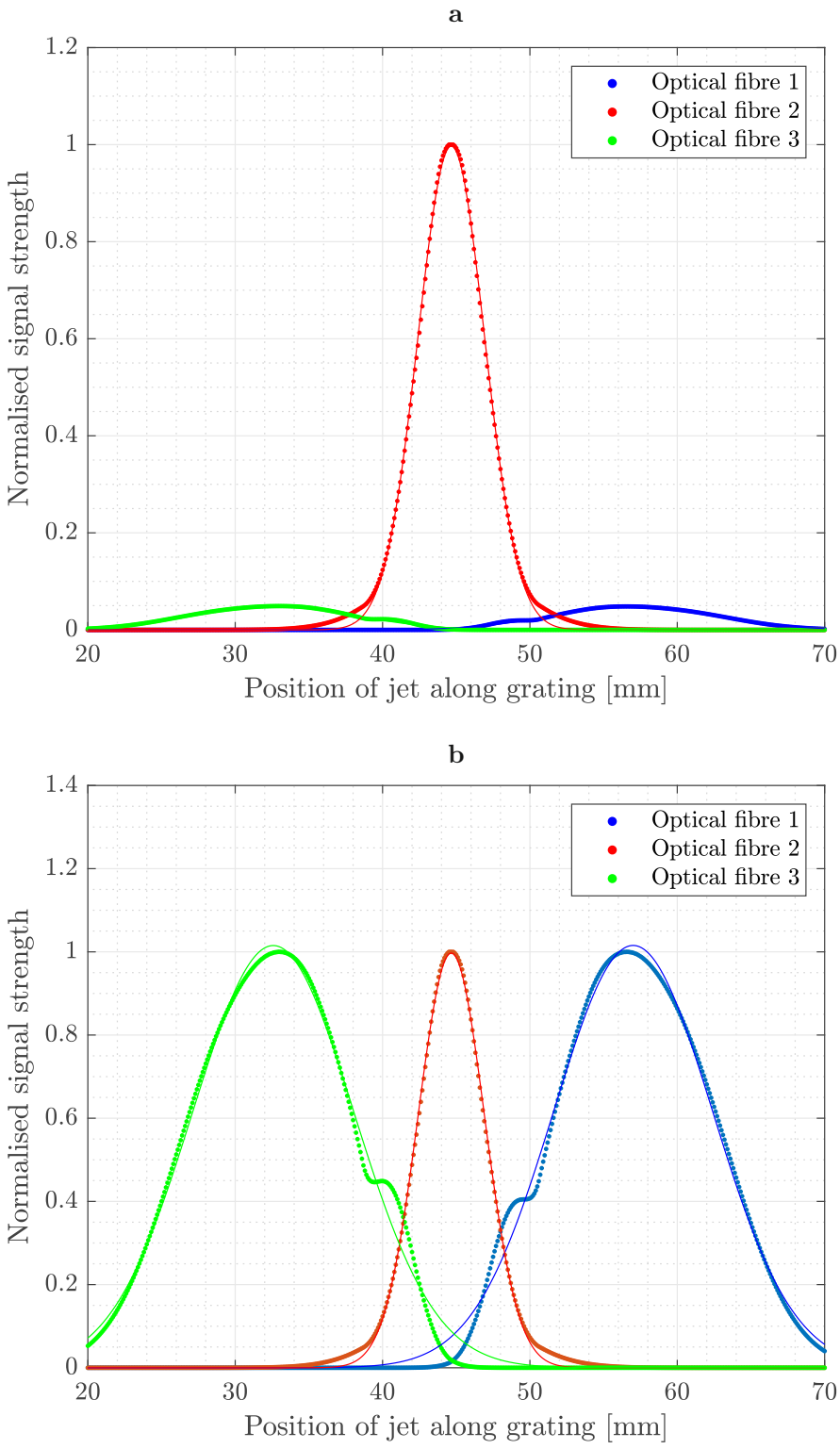


Figure 5.10: Experimental data simulated by the computational model, with a Gaussian fit applied to each curve. Figure **a** shows the data for each fibre normalised to the maximum intensity seen by any fibre (in this case optical fibre 2), while Figure **b** shows the data for each fibre normalised to the maximum intensity seen by the fibre itself.

5.6.2 Experimental results

Data from each optical fibre (one PMT per fibre) was recorded as the jet of saturated toluene vapour was moved along the grating in 1 mm increments. At each jet position, 100 signals were recorded. The 'strength' for each signal was calculated as the difference between the peak and mean baseline (to allow for background intensity variations during the experiment, and offset variations between different PMTs). The mean at each position was calculated, with the standard error for each dataset signifying the precision. The effect of gain on the different PMTs was also accounted for, so that the absolute signal strength from different fibres could be compared. A least-squares method was used to fit a Gaussian curve to the data for each optical fibre. The results are shown in Figure 5.11.

Table 5.3 shows the characteristics for each of the fitted Gaussian curves from Figure 5.11**a**.

Property	**Fibre 1**	**Fibre 2**	**Fibre 3**
Centre of curve along grating [mm]	39	27	13
Peak value relative to maximum	0.05	1.00	0.11
Width of curve [mm]	15.9	10.3	18.5
	(15.2, 16.5)	(10.2, 10.5)	(17.5, 19.6)

Table 5.3: Gaussian fit parameters for each optical fibre from experimental signal strength data. The width of the curve is defined as the distance over which the normalised signal strength is greater than e^{-2}. The 95 % confidence intervals are denoted in brackets; however they are not stated if they are within the precision of the value.

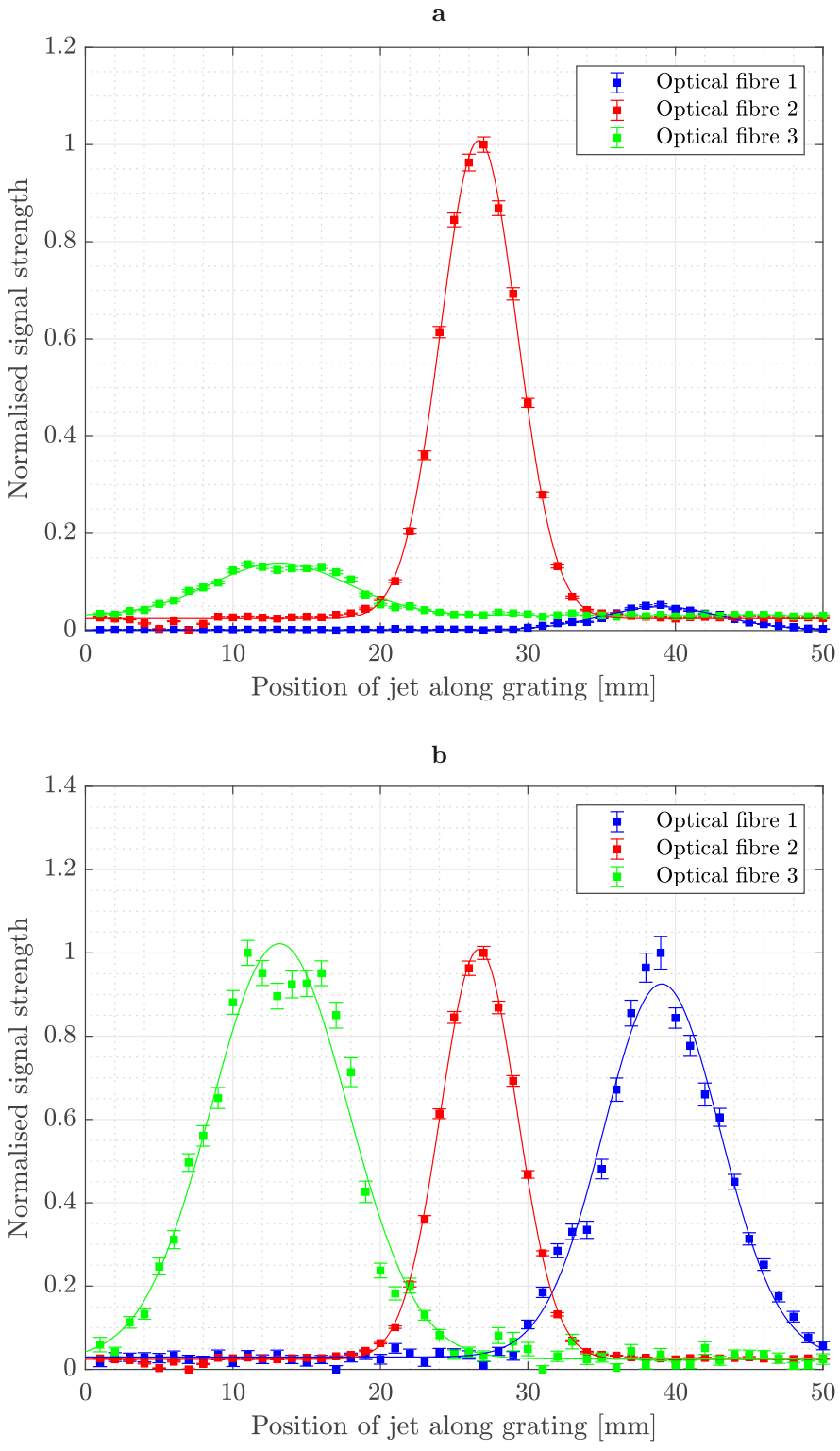


Figure 5.11: Experimental data showing the mean signal strength in each fibre as the jet was moved along the grating. Figure **a** shows the data for each fibre normalised to the maximum intensity seen by any fibre (in this case optical fibre 2), while Figure **b** shows the data for each fibre normalised to the maximum intensity seen by the fibre itself. The error bars show the standard error at each position, and the lines show the Gaussian fit.

5.6.3 Discussion

As explained in Section 4.5.6.4, the grating pitch (P_g) is derived by calculating the distances between peaks in Figures 5.10 and 5.11[14]. From Table 5.2, the mean grating pitch predicted by the computational simulation is 12 mm. The mean grating pitch calculated from the experimental data shown in Table 5.3 is 13 mm, but varies by ±1 mm. This difference suggests that the magnification is slowly varying along the image plane, which could happen experimentally if the detector plane is not truly perpendicular to the signal beam.

The model prediction and experimental data both showed that the maximum signal intensity collected by fibre 2 was higher than the maximum collected by the other fibres. This is quantified in Tables 5.2 and 5.3 as the peak value of the curve for each fibre relative to the maximum. This was expected because the grating is strongest in the centre (due to the Gaussian nature of the pump beams as explained in Section 4.5.6.1), and the fibre array was positioned such that the signal beam landing on the centre of fibre 2 would be produced by the jet when it was at the centre of the grating. Furthermore, the scattering efficiency was modelled to be highest at the centre of the grating (with the variation in fringe spacing causing it to decrease away from the centre). Unlike the simulation, however, the experimental data shows that the peak signal strength in fibre 3 should be higher than that of fibre 1. This asymmetry could be caused by experimental errors in positioning the three fibres which meant that the centre of fibre 2 may not have coincided perfectly with the signal produced by the centre of the grating. Additionally, the optimum fringe spacing may not have occurred at the centre of the grating, meaning that the signal intensity would be larger for one of the outer fibres than the other.

The grating length per fibre (L_{gf}) is calculated by measuring the width of the curves. Table 5.2 shows that the grating length per fibre for the three fibres was modelled to be 22 mm, 9 mm and 22 mm, respectively, while the experimental results displayed in Table 5.3 show the relative lengths to be 16 mm, 10 mm and 19 mm. The modelled data therefore predicts the trend of a better per-fibre spatial resolution for the central fibre compared to the outer ones. The experimental data again shows a larger difference between fibres 1 and

[14]Note that the absolute positions of the peaks were arbitrarily chosen for the simulations; it is only the distance between successive peaks that is of interest.

3, which is likely caused by the off-centre placement of the fibre array.

The modelled data shows a plateau on the left-side and right-side slopes of the curves for fibres 1 and 3, respectively. This artefact is also present in the experimental data. Upon closer inspection of the model, it was found that this is caused by the variation in scattering efficiency (due to the variation in fringe spacing along the grating). The ability of the computational model to predict this suggests that the assumption of a LIGS grating behaving similarly to a diffraction grating, as described in Section 4.5.6.3, is justified.

Overall, the trends predicted by the computational model agree well with experimental data. The absolute values of various parameters also show good agreement. The differences can be accounted for by expected experimental inaccuracies e.g. placement of the fibres at correct distances and angles.

5.7 Characterisation using 'small' optical fibres

For this experiment, the signal collection was achieved using an array of three identical optical fibres with a core diameter of 0.4 mm and a total (core and cladding) diameter of 0.425 mm. Once again, the jet was moved in discrete steps of 1 mm along the grating, and at each step the signal from each optical fibre was recorded.

5.7.1 Computational Results

Before conducting the experiment, the computational model was once again used to simulate the expected results. The model simulated the jet moving in discrete steps of 0.1 mm, and produced the results shown in Figure 5.12. The graph shows how the signal strength captured by each of the three optical fibres was expected to vary as the jet was moved along the grating. While Figure 5.12**a** shows the data for each fibre normalised to the maximum intensity seen by seen by any fibre, Figure 5.12**b** shows the data for each fibre normalised to the maximum intensity seen by the fibre itself.

The normalised signal intensity received by each fibre relative to the position of the jet along the grating, as presented in Figure 5.12**a**, is fitted to Gaussian curves. A least-squares fit was used to retrieve the characteristics for each curve shown in Table 5.4.

Property	**Fibre 1**	**Fibre 2**	**Fibre 3**
Centre of curve along grating [mm]	50	48	45
Peak value relative to maximum	0.3	1.0	0.3
Width of curve [mm]	8.3	7.1	8.2
	(8.2, 8.4)	(7.1, 7.2)	(8.1, 8.3)

Table 5.4: Gaussian fit parameters for each optical fibre from modelled data. Note that the width of the curve is defined as the distance over which the normalised signal strength is greater than e^{-2}. The 95 % confidence intervals are denoted in brackets; however they are not stated if they are within the precision of the value.

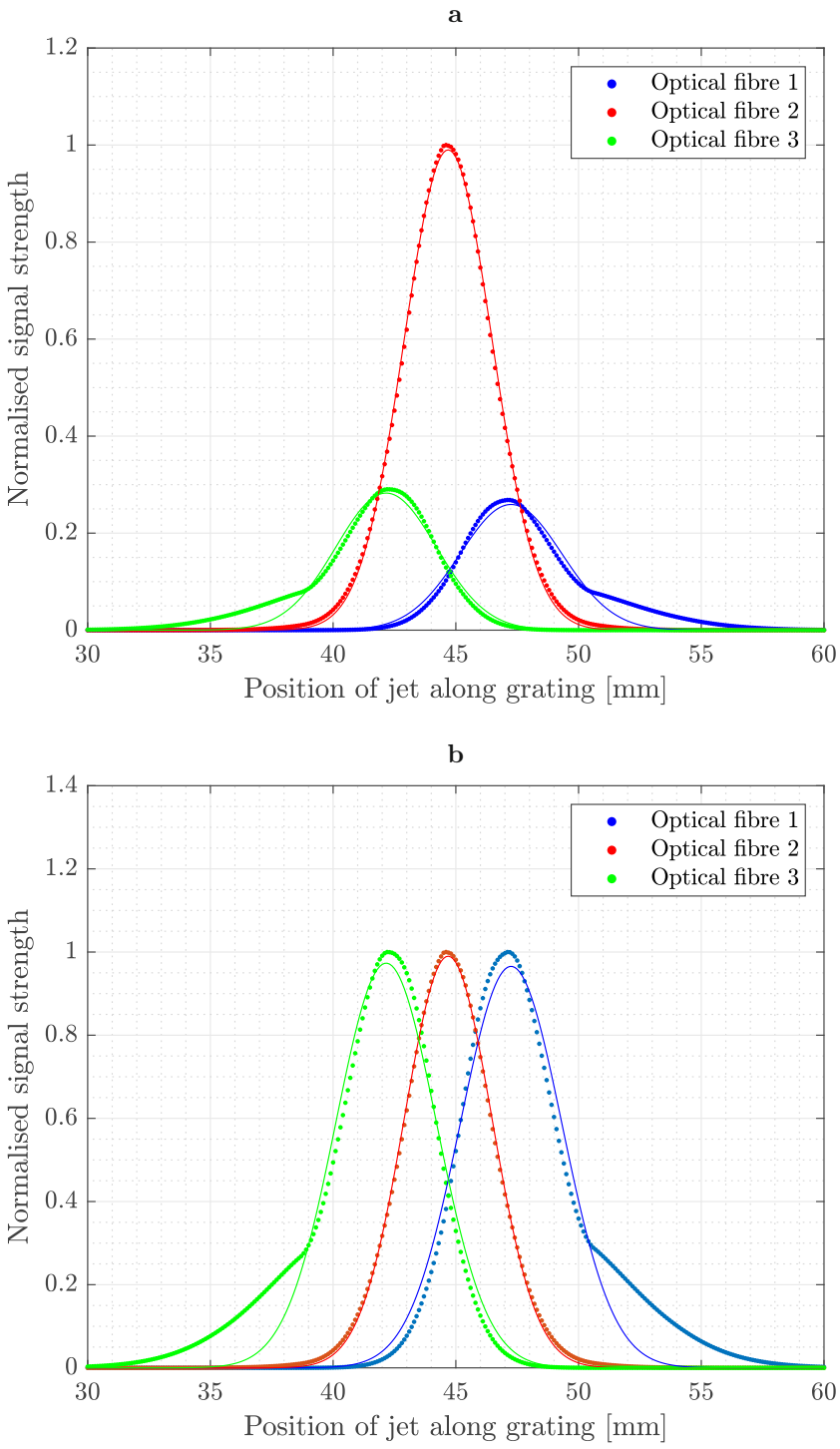


Figure 5.12: Experimental data simulated by the computational model, with a Gaussian fit applied to each curve. Figure **a** shows the data for each fibre normalised to the maximum intensity seen by any fibre (in this case optical fibre 2), while Figure **b** shows the data for each fibre normalised to the maximum intensity seen by the fibre itself.

5.7.2 Experimental results

Following the same methodology presented in Section 5.6.2, Figure 5.13 shows the experimental results from the smaller fibres.

Table 5.5 shows the characteristics for each of the fitted Gaussian curves from Figure 5.13**a**.

Property	**Fibre 1**	**Fibre 2**	**Fibre 3**
Centre of curve along grating [mm]	18	15	12
Peak value relative to maximum	0.2	1.0	0.4
Width of curve [mm]	8.1	9.0	9.8
	(7.1, 9.1)	(8.8, 9.1)	(8.7, 10.8)

Table 5.5: Gaussian fit parameters for each optical fibre from experimental signal strength data. The width of the curve is defined as the distance over which the normalised signal strength is greater than e^{-2}. The 95 % confidence intervals are denoted in brackets; however they are not stated if they are within the precision of the value.

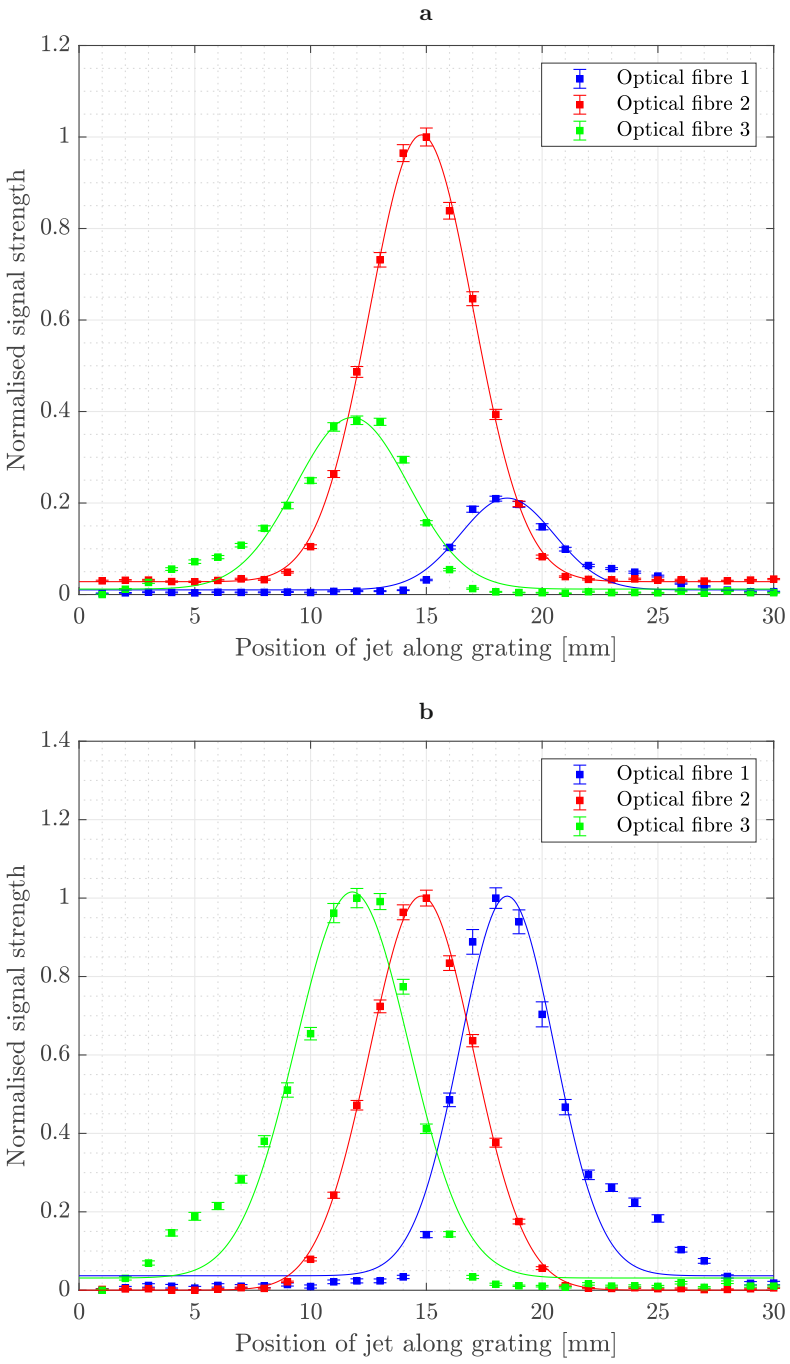


Figure 5.13: Experimental data showing the mean signal strength in each fibre as the jet was moved along the grating. Figure **a** shows the data for each fibre normalised to the maximum intensity seen by any fibre (in this case optical fibre 2), while Figure **b** shows the data for each fibre normalised to the maximum intensity seen by the fibre itself. The error bars show the standard error at each position, and the lines show the Gaussian fit.

5.7.3 Discussion

The grating pitch (P_g) is derived by calculating the distance between the peaks in the graph[15]. From Table 5.4, the average value of P_g as predicted by the computational simulation was 2.5 mm. The mean value calculated from the experimental data shown in Table 5.3 was 3 mm.

The peak signal intensities received by fibres 1 and 3, relative to fibre 2, are similar for the experimental results compared to the simulation (both show a mean of 0.3). However, the experimental data shows that fibre 3 received a higher peak signal intensity than fibre 1. This asymmetry was also reported in Section 5.6.3 for the experiment with the 'large' fibres, and is most probably caused by the placement of the fibre mounts (they were placed in the same position for both experiments).

The grating length per fibre (L_{gf}) is calculated by measuring the width of the curves. Table 5.4 shows that L_{gf} for the three fibres was modelled to be an average of 8 mm which is in good agreement with the experimental results displayed in Table 5.3 showing a mean of 9 mm. However, the modelled data predicted the central fibre (fibre 2) to have the lowest L_{gf} while the experimental data shows a minimum fibre 1. This is likely due to a combination of the fibres being placed slightly off-centre, as well as the optimum fringe spacing (which would result in the highest scattering efficiency) not being coincident with the centre of the grating. Furthermore, the shape of the curves for fibres 1 and 3 mean that the Gaussian fits have a larger uncertainty than for the central curve, and as the variations in widths are all small (within a total of 2 mm) they can also be attributed to fitting uncertainty.

The modelled data shows a widening on the right-side and left-side slopes of the curves for fibres 1 and 3. This observation is also present in the experimental data. As was the case for the artefacts discussed in Section 5.6.3, this was caused by the assumption in the model of the LIGS grating behaving as a diffraction grating.

The experimental results when using 'small' and 'large' fibres were also compared to evaluate the effect of optical fibre cores size on the per-fibre spatial resolution (L_{gf}). For the first experiment described in this work, using 'large' optical fibres, a L_{gf} of 10.3 mm was

[15]Note that the absolute positions of the peaks were arbitrarily chosen for the simulations; it is only the distance between successive peaks that is of interest.

achievable. Without changing the LITGS geometry, but replacing the optical fibres with 'small' ones, the spatial resolution was improved to 8.1 mm.

The use of linear arrays of fibres, rather than just single fibres, meant that the effect of optical fibre core size on P_g could also be considered. The array using 'large' optical fibres was capable of a mean P_g of 13 mm, while the array of smaller fibres achieved a mean P_g of 3 mm.

These results showed that when applying this novel approach, it is beneficial to minimise the core size of the optical fibres being used. However, they also demonstrated that the enhancement in P_g was larger than for L_{gf} — a 60 % reduction in fibre core size resulted in a 21 % decrease in L_{gf} compared to a 77 % decrease in P_g. This meant that for the case of 'smaller' fibres, the value of L_{gf} was greater than the value of P_g. The effect of this discrepancy was that the signal produced from certain regions along the grating would be captured by two different optical fibres. This is further explored in Section 5.8.

Finally, the work presented in this section and Section 5.6 has demonstrated a good level of agreement between the experimental and computational results. This validation enables the computational LIGS model to be used to predict the spatial resolution for different LIGS geometries, and can inform the future design of LIGS experiments.

5.8 Simultaneous axially-resolved LITGS temperature measurements

Having calibrated the experimental setup (using the 'small' fibres) to determine the achievable spatial resolution, the system was used to obtain simultaneous spatially-resolved LITGS temperature measurements.

5.8.1 Experimental setup

The setup shown in Figure 5.14 was employed. The equipment used was identical to that described in Section 5.1, with the only difference being the addition of two extra needles.

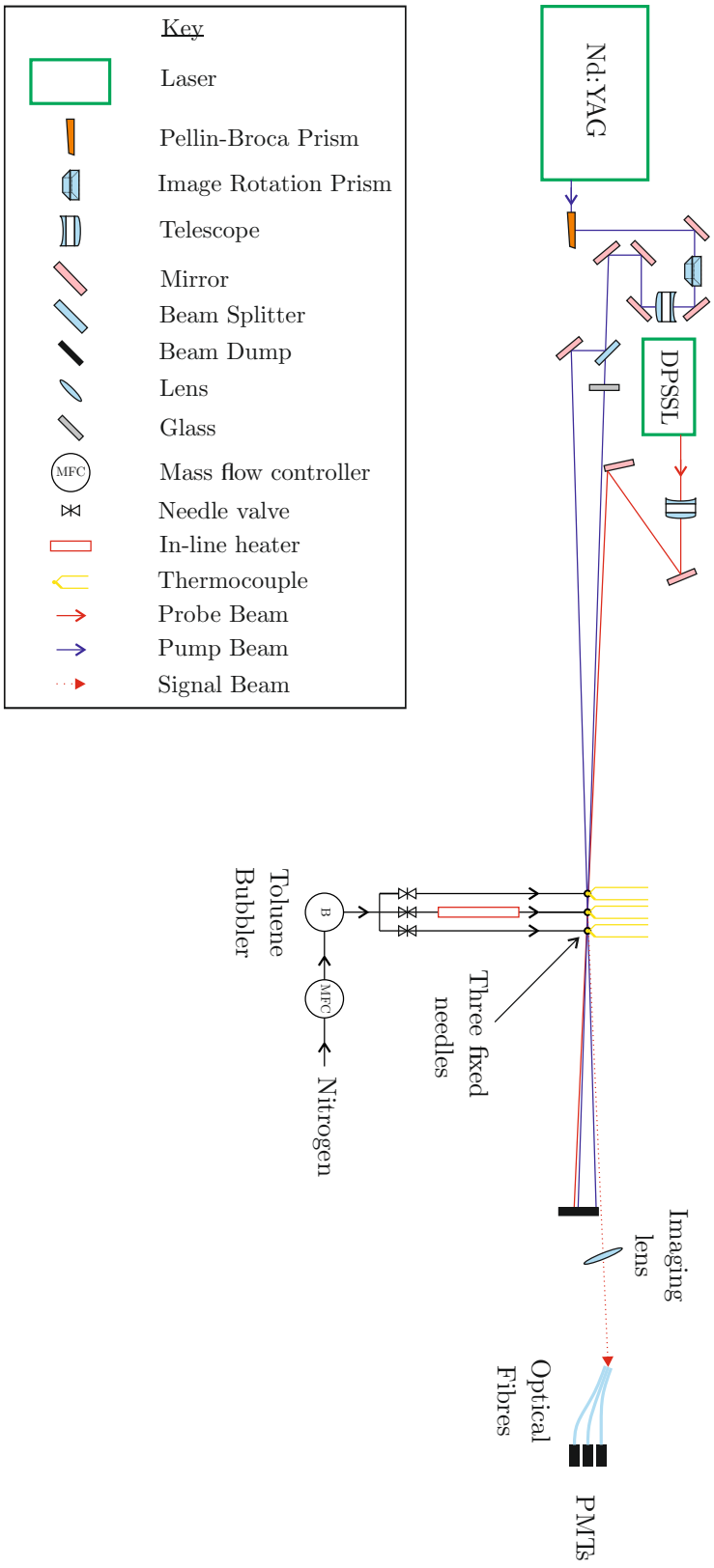


Figure 5.14: Bird's-eye view of the experimental setup using optical fibres. Note that the needles emit jets of nitrogen saturated with toluene in the direction normal to the paper. The jets pass through the laser beams and then interact with the thermocouples.

As the grating pitch for the experimental setup was found to be 3 mm (as described in Section 5.7), the three needles were placed at the same axial spacing along the grating. The size of the gas flow fittings required for the needles meant that all three needles could not be spaced 3 mm apart when placed next to each other. To account for this, the centre needle was rotated by 180° and suspended from above, while one of the outer needles was rotated by 45°. This configuration is shown in Figure 5.15.

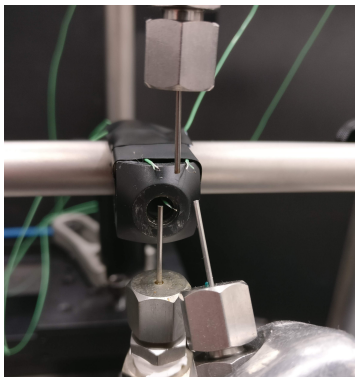


Figure 5.15: Mounting setup employed to enable the three needles to emit jets that were spaced 3 mm apart. The laser beams for LITGS measurements were directed from right to left, and passed through the gap between all three needles. Three exposed junction thermocouples (with green sheaths), each placed within the flow of the relevant jet, can also be seen.

Also seen in Figure 5.15 are the thermocouples that were placed in the three flows, after each flow had passed through the laser beams. They were introduced into the experimental setup to allow an independent temperature measurement of the flows, to compare to the LITGS measurements. Type K thermocouples with a 0.08 mm diameter wire were used. These were chosen as the junction would be small enough to be completely immersed in the flow (which had previously been measured to be 0.67 mm in diameter). One thermocouple was connected directly to a datalogger[16] which was capable of recording data at 1 Hz with an accuracy of ±1 °C. The other two thermocouples were manually wired up to amplifiers[17] with a stated accuracy of ±1 °C, which in turn were connected to a datalogger[18]. This configuration allowed for data logging at up to 1 kHz, but measurements were taken at 10 Hz to match the frequency at which the LITGS measurements were also taken.

[16] EasyLog EL-USB-TC-LCD product from Lascar Electronics.
[17] AD8495 K-type thermocouple amplifiers from Analog Devices.
[18] 'DrDAQ' from Pico Technology.

An in-line gas heater[19] was connected to the middle flow to enable the temperature of that flow to be increased while the others were kept constant. Needle valves allowed all three needles to be aligned into the setup by passing the gas through one needle at a time and optimising its position.

One of the Hamamatsu H6780-20 photomultiplier tube (PMT) modules developed a fault and had to be replaced by an older model for this experiment. The replacement device was a Hamamatsu R955 PMT.

The mass flow controller enabled a specified flow rate to be used for the experiment. By taking Laser-Induced Fluorescence (LIF) images[20] of the three jets under different flow rates, it was found that a higher flow rate led to unsteady jets. This is shown by the two images in Figure 5.16. The figure on the left shows the central jet when nitrogen was fed into the bubbler with a flow rate of 0.1 slpm (and the valves for the other needles were closed). The image on the right shows a LIF image of the same jet, but with a flow rate of nitrogen of 0.15 slpm. Comparing the two images, it is clear that when the flow rate is increased above a threshold level turbulence is introduced into the jet. Similar analyses for the other jets showed that a flow rate of nitrogen of 0.25 slpm, when all the valves were open, ensured that all three flows were laminar.

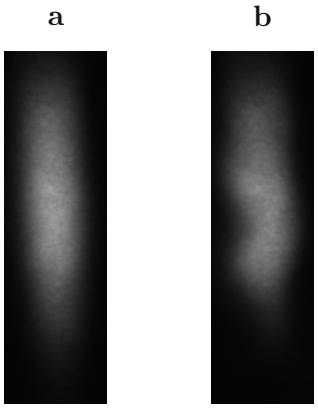


Figure 5.16: Laser Induced Fluorescence images of the flow emitted by the central needle. Image **a** shows an image of the jet, flowing from top to bottom, with a flow rate of 0.1 slpm of Nitrogen passed through the bubbler. Image **b** shows the same jet for a flow rate of 0.15 slpm.

[19] AHP-7562 model from Omega.
[20] Taken using an iStar sCMOS intensified camera by Andor.

5.8.2 Steady-state temperature measurements with the heater off

The experiment was first run with the in-line heater turned off, so that all flows were expected to be at room temperature. Data was acquired over 100 seconds (at a frequency of 10 Hz), and the LITGS signals were subsequently analysed to calculate the frequency of oscillations. Equation 2.3 shows how the temperature (T), in Kelvin, is calculated from the frequency of a LITGS signal. It can be simplified to

$$T = CF^2 \tag{5.2}$$

where F is the frequency of the LITGS signal and C is a proportionality coefficient defined as

$$C = \frac{\Lambda^2 M}{\gamma k_{\mathrm{B}}} \tag{5.3}$$

where Λ is the fringe spacing, M is the molar mass of the gas, γ is the heat capacity ratio for the gas, and k_{B} is the Boltzmann constant.

Since the fringe spacing used to obtain the LITGS measurements for each flow was assumed to be equal, and the chemical composition of each flow was also similar, a constant proportionality coefficient could be assumed for all three flows. To obtain this coefficient, the signals from each flow were first calibrated to their respective thermocouple temperatures to derive the proportionality coefficient for each set of LITGS signals. The mean of these three proportionality coefficients was then used to convert the frequency for each signal to a temperature. Figure 5.17 shows the results. The error bars for the thermocouples demonstrate the accuracy of the readings ($\pm 1\,^{\circ}\mathrm{C}$ as stated in Section 5.8.1), while the error bars for the LITGS measurements show the calculated standard error of the mean for the dataset. Presenting the data in this way allows an accuracy assessment of the LITGS data to be made by comparing the mean LITGS measurement for a flow with its respective thermocouple measurement. The precision of a LITGS measurement is demonstrated by the size of its error bar.

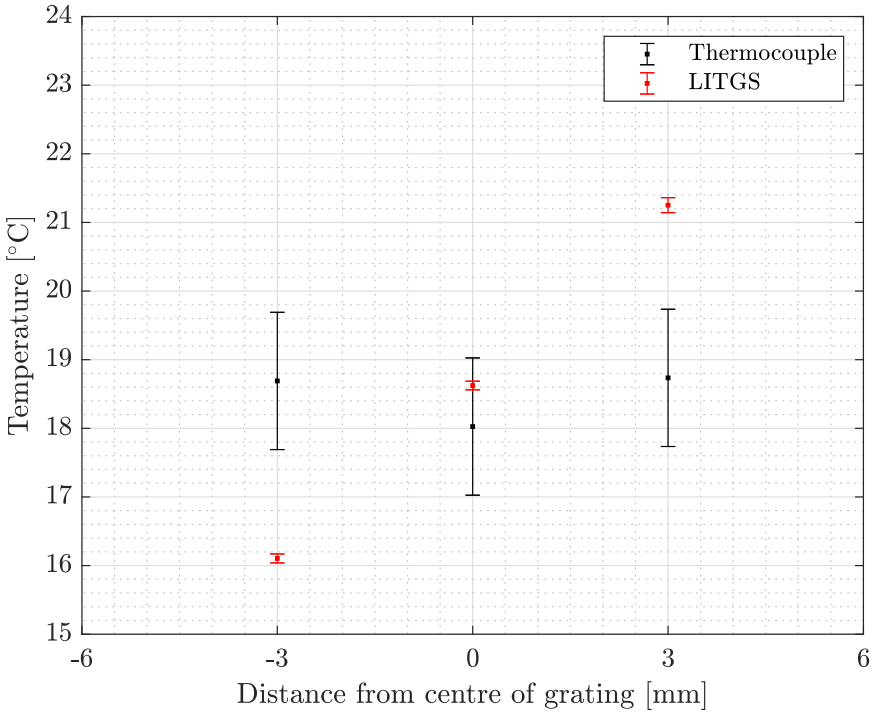


Figure 5.17: Thermocouple and LITGS temperature measurements of the three flows when the in-line heater was turned off.

The results show a good correlation between the LITGS and thermocouple measurements when averaged over all three flows. However, there is a difference in the mean LITGS temperatures for each of the three flows even though they are expected to be the same. This is because the fringe spacing was found to vary along the grating, as described in Section 5.2. Figure 5.18 shows the derived temperatures once the varying fringe spacing is accounted for.

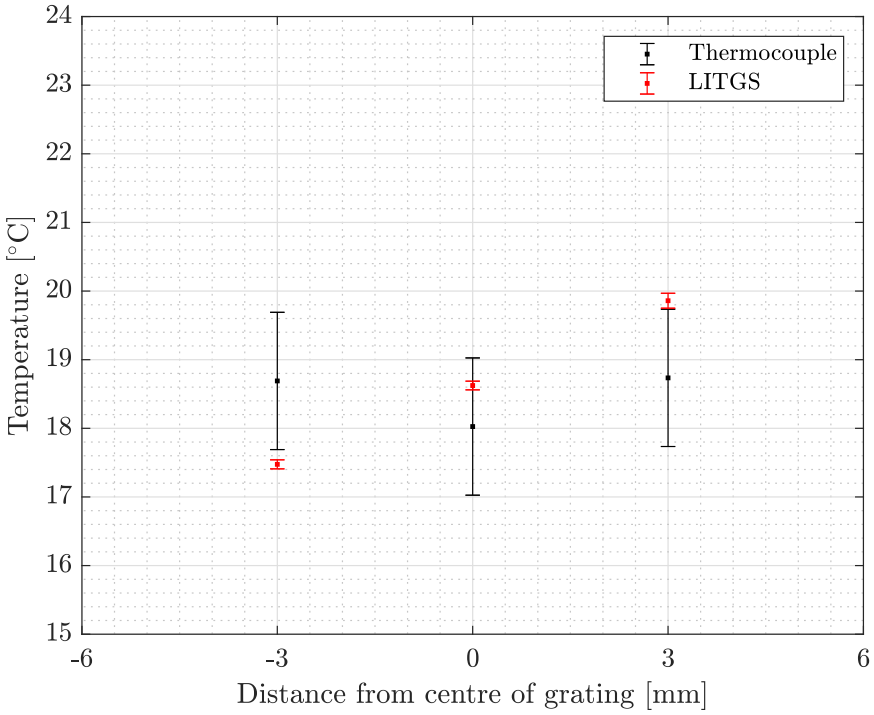


Figure 5.18: Thermocouple and LITGS temperature measurements of the three flows when the in-line heater was turned off. The LITGS temperature calculations have accounted for the varying fringe spacing.

The results also displayed an increase in the error bar size (and therefore loss of precision) for the LITGS signals taken at +3 mm from the centre of the grating. This discrepancy was caused by an increased shot-to-shot variation in frequency for these signals. The signals for this flow were being collected by the older PMT module (as mentioned in Section 5.8). Figure 5.19 shows an example of the signals obtained by the three PMT modules from one shot.

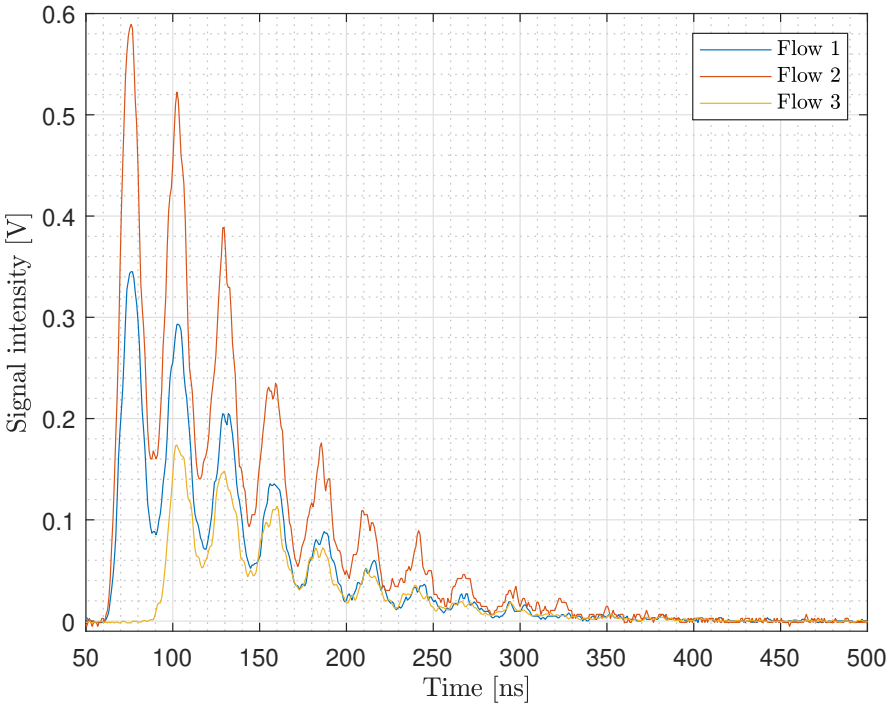


Figure 5.19: Example LITGS signals obtained for each flow during one shot. Flow 1 refers to the jet at +3 mm from the grating centre, flow 2 is the central jet and flow 3 is the jet at −3 mm from the grating centre.

The gold line, labelled as 'Flow 3', refers to the signal obtained by the replacement PMT module. It is clear that this signal has a reduced number of oscillations, and this trend was noticed on all the signals collected by the PMT module. To extract the frequency from each signal, the data analysis code employs on a Fast Fourier Transform (FFT) function on the signal. By having one less oscillation in every signal, the dominant frequency is less distinct, which results in a larger spread of calculated frequencies across the range of the dataset.

5.8.3 Steady-state temperature measurements with the heater on

The in-line heater was turned on and the external temperature of the heater was monitored to ensure that it settled to a steady-state temperature before the experiment was run. This enabled the central flow to be heated to a constant temperature while the two outer flows were maintained at room temperature. Data was again acquired over 100 seconds (at a

frequency of 10 Hz), and the LITGS signals were analysed to calculate the frequency of oscillations. Since the composition of the flows was similar to that used for the experiment with the heater turned off, the same mean proportionality coefficient used in Section 5.8.2 was employed to convert the frequency for each signal to a temperature. The variation in fringe spacing described in Section 5.2 was accounted for.

It was also noted that the LITGS measurements would include the outer regions of the flow where there was mixing between the hot nitrogen/toluene jet and cooler room air. On the other hand, the thermocouple had a junction diameter of about 0.2 mm, and was therefore only measuring the temperature in the centre of the jet. The effect of this mixing on the LITGS measurements therefore needed to be considered before comparing the results with the thermocouple measurements.

To characterise the mixing between room air and the nitrogen/toluene jet, Laser-Induced Fluorescence (LIF) images[21] of the heated central jet were captured. Figure 5.20**a** shows the averaged image of the flow. Figure 5.20**b** shows the intensity variation across the averaged LIF image after accounting for the background intensity.

[21] Obtained using an iStar sCMOS intensified camera from Andor.

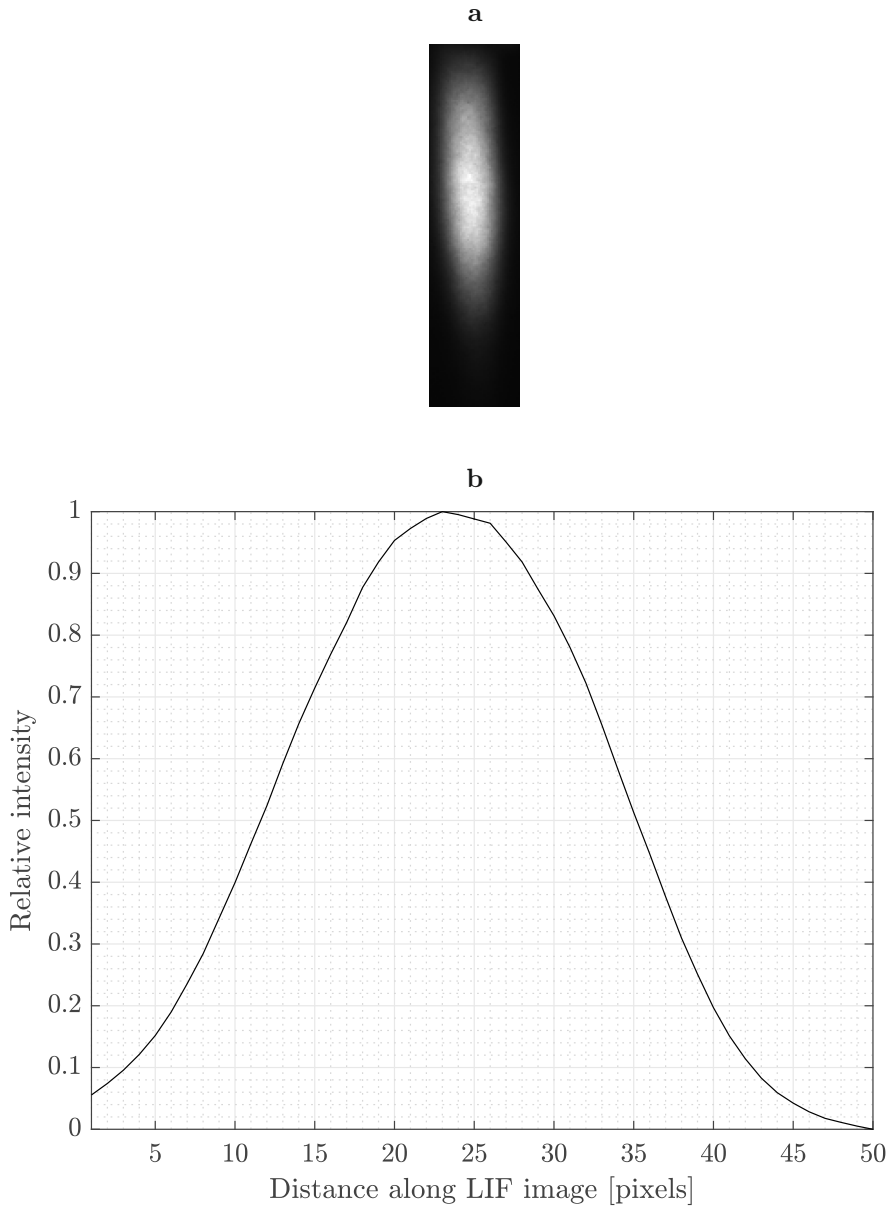


Figure 5.20: Image **a** shows an average Laser Induced Fluorescent image of the heated jet, flowing from top to bottom. Image **b** shows the intensity variation across Image **a**.

The intensity variation shown in Figure 5.20**b** is indicative of the variation in concentration of the hot nitrogen/toluene mixture across the jet. The average composition of the flow was calculated to be 65 % nitrogen/toluene and 35 % room air. The LITGS temperature measured for the central flow was the weighted mean, based on mixture fraction, between the hot nitrogen/toluene flow and ambient room air. Figure 5.21 shows the temperature measurements of each flow once this was accounted for. The error bars for the thermocou-

ple readings show the accuracy as stated in the documentation for the amplifiers, while the error bars of the LITGS measurements are the calculated standard error of the mean for the datasets (and therefore demonstrate the precision).

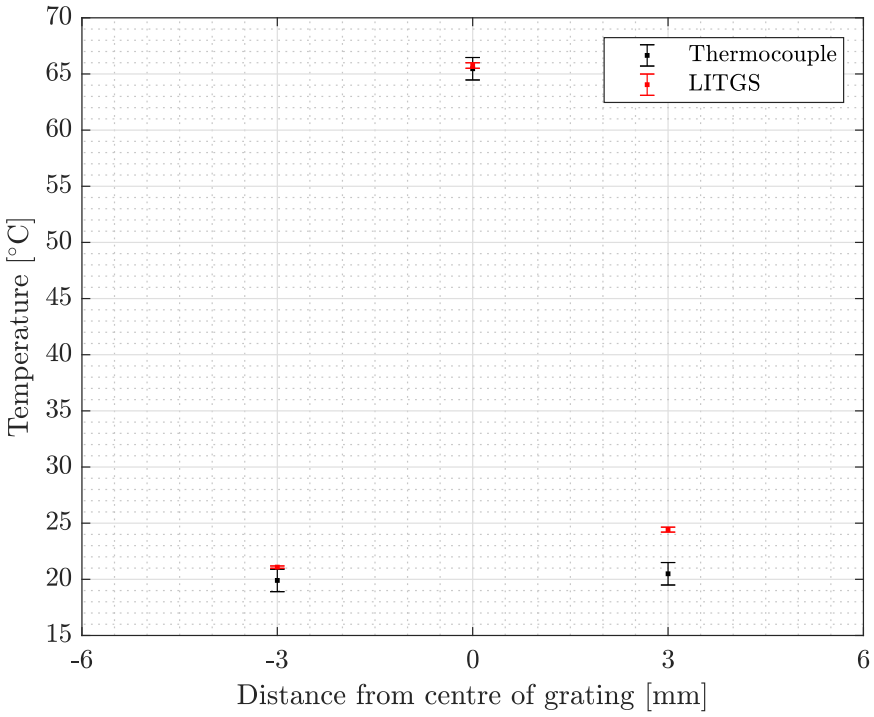


Figure 5.21: Thermocouple and LITGS temperature measurements of the three flows when the in-line heater was turned on and allowed to settle to a steady-state temperature. The LITGS measurements have been corrected to account for the effects of crosstalk and jet entrainment of room air.

The results displayed in Figure 5.21 demonstrate excellent agreement between the LITGS and thermocouple measurements for the central jet and the jet placed at -3 mm from the centre of the grating. However, the LITGS temperature measurement for the jet at $+3$ mm from the centre of the grating is significantly different to the thermocouple measurement. This suggests that the LITGS signal obtained by the optical fibre looking at the flow at $+3$ mm from the centre of the grating might be influenced by the signal generated by the heated flow at the centre of the grating. The extent to which signals from all three flows contribute to each other, hereon referred to as the 'crosstalk' between fibres, needed to be quantified. To do this, signals were collected on all three fibres with only one flow turned on. This was then repeated for each of the other two flows. A FFT routine was applied to

all the signals obtained across all three fibres, for each of the three flows. By studying the resultant power spectra of the signals, the magnitude of the contribution from each of the three flows to each optical fibre was determined. The power spectrum value at the LITGS frequency, referred to as the 'frequency power', collected on each fibre, for each flow, was normalised to the maximum frequency power collected by that fibre and the results are displayed in Figure 5.22.

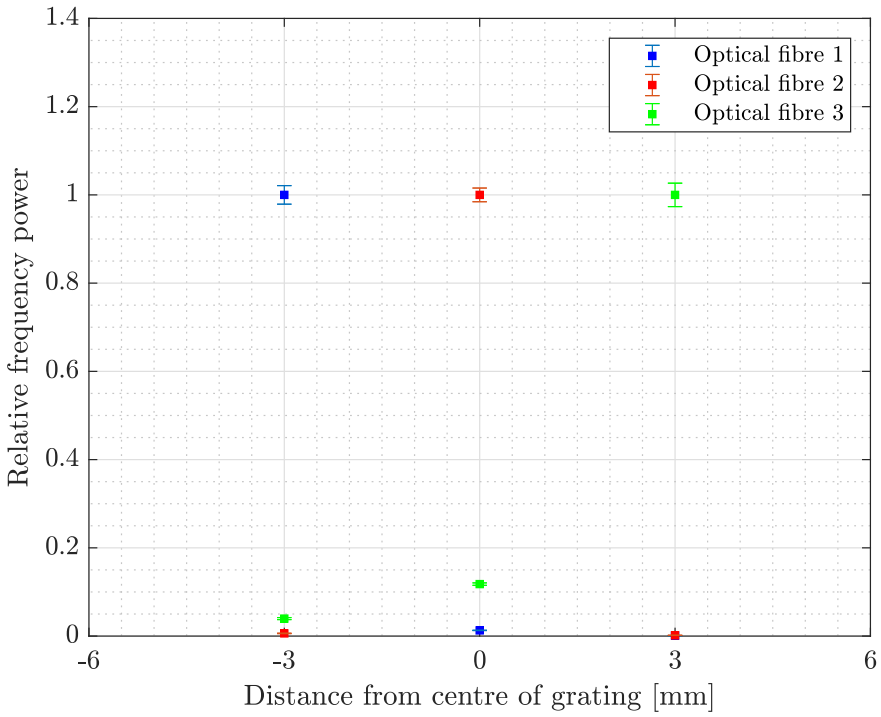


Figure 5.22: Relative frequency power captured by each optical fibre when only one flow was turned on. The x-axis shows the location of the flow that was turned on.

The results show that while optical fibres 1 and 2 received negligible amounts of crosstalk from the different jets, optical fibre 3 received significant crosstalk from the central jet. To account for this, the LITGS signal received by each fibre was assumed to be a weighted average of three signals (one from each jet). The relative contribution of each signal was determined by the results shown in Figure 5.22. The frequency derived from the LITGS signal received by each jet was similarly assumed to be a weighted average of the signal frequencies from each jet. This set up a system of three equations with three unknowns, which could be easily solved to extract the LITGS signal frequency (and therefore tempera-

ture) for each individual jet. Figure 5.23 shows how the LITGS temperature measurements correlate to the thermocouple measurements after accounting and correcting for crosstalk.

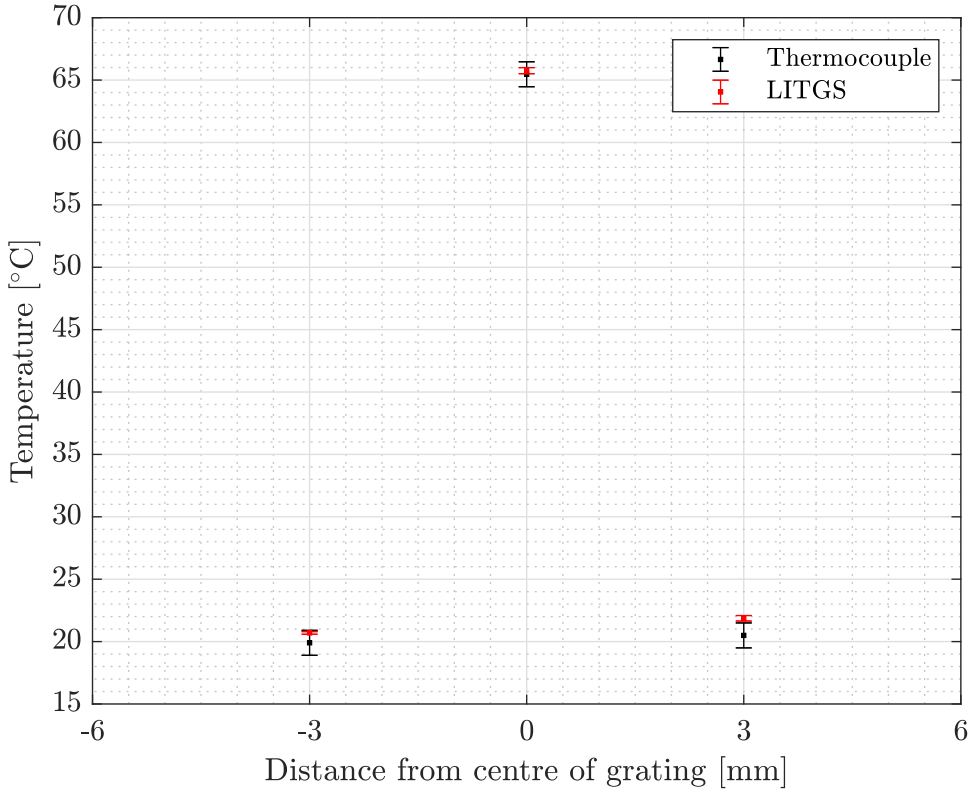


Figure 5.23: Thermocouple and LITGS temperature measurements of the three flows when the in-line heater was turned on and allowed to settle to a steady-state temperature. The LITGS measurements have been corrected to account for the effects of crosstalk.

The effect of 'crosstalk' was expected due to the jets being spaced at the 'grating pitch' (P_g) distance rather than the 'grating length per fibre' (L_{gf}). However, the results show that optical fibres 1 and 2 did not see the effects of crosstalk. This suggests that the definition used for the per-fibre spatial resolution as being the length of the grating over which 87 % of its signal originates (given by the e^{-2} limit to calculate the width of the curves presented in Section 5.7) is a conservative estimate, and in reality the spatial resolution could be better. However, further work is required to investigate what the practical limit should be. The reason why optical fibre 3 did see some crosstalk is likely due to the placement of the jets not being exactly 3 mm apart along the centre of the grating.

The results also show that when cross-talk is present, it can be accounted for. However, this has been demonstrated for a situation where each fibre sees one dominant temperature. In practical applications, this may not be the case if there are steep temperature gradients present and the spatial resolution of each fibre is not small enough to assume a single temperature for each signal. Therefore some further work would need to be conducted to investigate whether the this method could be applied in such cases.

5.8.4 Transient temperature measurements as the heater is turned on

Using the same experimental setup detailed in Section 5.8.1, the inline heater was switched on and transient temperature data was collected as the central flow heated up. Data was acquired over 800 seconds (at a frequency of 10 Hz), and the LITGS signals were analysed to calculate the frequency of oscillations. Since the composition of the flows was similar to that used for the experiment with the heater turned off, the same mean proportionality coefficient used in Section 5.8.2 was employed to convert the frequency for each signal to a temperature. The variation in fringe spacing described in Section 5.2 was accounted for. The effects of signal crosstalk and mixing of the hot flow with room air, both described in Section 5.8.3, were also considered. The results are displayed in Figure 5.24. The thermocouple data is displayed as line plots, and one error bar demonstrating the accuracy of the measurements is displayed on each plot. Error bars were not plotted for every data point to simplify the graph. The LITGS data was discretised into groups of 100 shots. Representative error bars for the LITGS data, showing the standard error of the mean as calculated from the steady state experiments from Sections 5.8.2 and 5.8.3, are shown on the first and last data points.

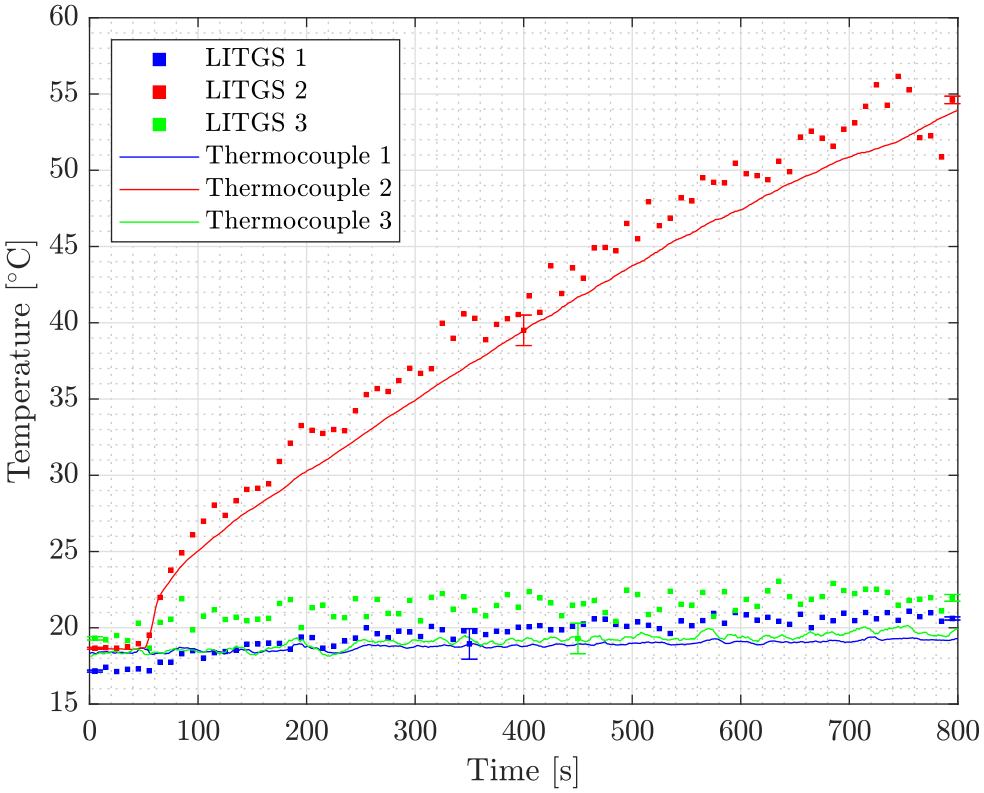


Figure 5.24: Thermocouple and LITGS temperature measurements of the three flows while the in-line heater was heating up.

The excellent correlation between LITGS and thermocouple measurements presented here show that the novel technique proposed in Chapter 4 can be used to obtain simultaneous, spatially-resolved 1-D LIGS temperature measurements. In the demonstrative experiments shown here, a spatial resolution of 6 mm was achieved and simultaneous multi-point measurements were obtained.

5.9 Summary

This chapter has presented experimental results that characterise the novel technique of spatially-resolved LIGS in the axial direction, and validate the computational model that was developed in Chapter 4.

The first experiment conducted to validate the model was to compare the experimentally-measured signal beam size to that predicted by the model. The modelled beam size (704 µm)

showed an excellent correlation to the measured beam size (727 µm), with the small discrepancy between the values expected due to the jet being modelled as being one dimensional.

Next, the modelled magnification at a point along the detector plane was practically justified. Once again, the results matched well (0.06 modelled compared to 0.07 measured) and the modelled magnification was within the tolerance of experimental error.

Two experiments were then conducted to validate the model over the length of the grating, and also to characterise the experimental setup being used. The signals were collected by a linear array of optical fibres in both cases; however the core sizes of the fibres used for the first experiment were 1 mm while for the second experiment they were 400 µm. The best per-fibre spatial resolution, in terms of grating length per fibre (L_{gf}), achievable by the larger fibres was 10.3 mm while this was improved to 8.1 mm for the smaller fibres. However, the mean values of L_{gf} across all three fibres was 14.9 mm for the larger fibres compared to 9.0 mm for the smaller fibres. These results show that reducing the fibre core size offers a marked improvement in per-fibre spatial resolution, particularly when using a linear array of fibres (as the resolution for each fibre in the array is more consistent for smaller fibres).

The experiments also showed a variation in grating pitch (P_{g}) related to fibre core size. The larger fibres exhibited a mean P_{g} value of 13 mm while the smaller fibres were capable of a mean P_{g} of 3 mm. The large (77 %) improvement in P_{g} due to a relatively small (60 %) reduction in fibre core size shows that when taking measurements using a linear array of fibres, the size of the fibres should be minimised.

When comparing the experimental results to those obtained from the computational model, it was found that the model was able to predict artefacts in the shapes of the various curves. This was found to be caused by the variation in fringe spacing along the grating, and thus validated the assumption that a LIGS grating could be modelled as a diffraction grating when considering the scattering efficiency. These results, as well as the generally excellent agreement between the simulated and experimental data, validate the model used and confirm that it can be implemented to characterise LITGS geometries and inform future design choices for the use of this technique.

Finally, two experiments were conducted to obtain simultaneous, axially-resolved LITGS

temperature measurements. The signals were collected by a linear array of optical fibres with a core size of 400 µm. Three jets, placed 3 mm apart along the grating, were used to produce the signals. The spacing was chosen to be equal to the grating pitch measured previously. The outer jets remained at room temperature, while the central jet was heated to a steady temperature of 65 °C. The concept of 'crosstalk' between the fibres, due to the grating length per fibre being larger than the grating pitch, was introduced and a method to account for it was applied. The LITGS temperature measurements, obtained simultaneously, were compared to thermocouple measurements and showed excellent agreement. Following this, the temperature of the central jet was varied between room temperature and 54 °C while measurements were taken. Again, the LITGS measurements for all three jets correlated well with the thermocouple measurements.

These results showed that applying the novel technique allowed simultaneous LITGS measurements to be obtained at 3 mm intervals. The central fibre, by not being affected by different temperatures at distances of ±3 mm from it, was shown to have a spatial resolution of 6 mm. This was better than expected, since the L_{gf} was measured to be 9 mm, and suggests that the definition of L_{gf} for a fibre as being the region from which 87 % of the its signal originated is conservative. This is an 86 % improvement in spatial resolution compared to the single measurement that would have previously been possible (over the entire 43 mm grating length). Furthermore, the results demonstrated the capability of simultaneously collecting multiple spatially-resolved point measurements. The potential of increasing the spatial resolution of multi-point measurements by introducing and accounting for cross-talk was demonstrated, but this method requires further work to determine its applicability for applications where there are steep temperature gradients present and the spatial resolution of each fibre is not small enough to assume a single temperature for each signal.

6 Development of a transportable LIGS system (PILOT)

This chapter first considers the motivations for a portable LIGS setup, and then describes the design, manufacture and characterisation of the PILOT (Portable In-line LIGS for Optical Thermometry) system. Finally, the successful deployment of PILOT is demonstrated.

6.1 Motivations

In Section 2.3, the relatively low cost and complexity of LIGS as an alternative optical diagnostic technique to CARS was highlighted. Its versatility in challenging environments and applications, and ability to probe various properties (predominantly temperature) in gases, liquids and solids was also presented. Furthermore, the potential use of electrostrictive gratings (LIEGS), which does not require the probed sample to be seeded with a resonant tracer species, was considered.

These substantial advantages enable the technique to be applied to a range of research and industrial facilities, as well as new applications that have not been able to use optical diagnostics due to the cost and complexity involved. However, despite its 'simplicity' relative to CARS, the use of a large, extremely precise experimental setup is a significant barrier to wider adoption of the technique. In order to make it more accessible, the Ewart group in Oxford built a transportable system which was used to obtain temperature measurements in a reciprocating compression machine as reported by Förster *et al.* [97]. However, this system was only capable of LIGS measurements at 10 Hz which does not offer sufficient temporal resolution for many transient events. Furthermore, the system was designed primarily for LITGS measurements (which require a tracer species), the procedure for alignment was cumbersome and the size of the system was still prohibitive for some applications.

It was therefore decided to design and build a LIGS system with improved temporal resolution, capable of both thermal and electrostrictive grating spectroscopy, that would be entirely self-contained and suited for a range of different applications.

6.2 Design and development

This section details the design process, from equipment selection and optical layout through to functionality considerations. The key features required for the system were:

- Laser energies (pump and probe) capable of tracer-free LIEGS measurements.
- Temporal resolution of at least 100Hz.
- Simple operation (including simplified alignment procedure).
- Minimal footprint and weight.

As with any practical undertaking, financial and time constraints also had to be considered.

6.2.1 Laser selection

The laser for the pump beams was the first component to be decided. To enable the capability of obtaining electrostrictive measurements, a laser with a high pulse energy (>50 mJ) was required. A Nd:YAG laser was selected, and it was decided to use the fundamental emission wavelength (1064 nm) since this would maximise the pulse energy. Furthermore, the photomultipler tubes (PMTs) used for signal detection are not sensitive to light at this wavelength which may substantially boost the signal-to-noise ratio of the system.

After surveying the market, the Quantel Merion C laser was chosen. This model provided a sufficient repetition rate (it is capable of 400 Hz) and pulse energy (up to 100 mJ) while meeting the budgetary constraints. This repetition rate provided more than an order of magnitude upgrade on the 10 Hz capability of the pre-existing portable system [97]. The laser also met environmental and mechanical requirements, ensuring that it would allow the system to be employed in a range of facilities. As well as being compact with a rack-mountable power supply, it could be used in any orientation and could be operated remotely. Internal closed-loop water-cooling and a 13 A BS1363 mains-ready power plug meant that no additional plumbing/wiring would be required on-site.

For the probe laser, it was decided to use a continuous wave laser emitting at 532 nm. This wavelength was chosen as it is well developed, leading to products that would have a

high power and good beam stability at a low cost. From a laser safety point of view, having the probe laser wavelength at a harmonic frequency of a Nd:YAG laser makes it easier to source safety equipment. The GLR-20 fibre laser from IPG Photonics was selected as it offered good beam quality[1] and power at a reasonable cost. The laser head was also very compact and did not require water cooling. The power supply was rack-mountable and could be fitted with a 13 A BS1363 plug for convenience.

A third laser was required to predict how the signal beam would propagate and therefore assist in aligning the detection optics. Since this laser was only required to aid with alignment during experimental setup, and would not be used for the actual LIGS measurements, there were no limiting requirements regarding the laser beam quality; simply that the beam was round in shape. To aid with laser safety considerations, a laser with a maximum power that was low enough for it to be classified as a Class 2 laser (i.e. less than 1 mW in the visible spectrum) was desirable. It also needed to be compact and emit at the same wavelength as the probe (and therefore the signal) beam. A Thorlabs collimated laser-diode-pumped DPSS Laser module (the CPS-532C2 model) which operates at 532 nm was chosen.

6.2.2 Laser integration

The next design step was to decide how to integrate the two lasers (producing the pump and probe beams) into the system. Various designs were considered with the aim of optimising the portability of the system. A multi-level layout, where the lasers would be fastened onto the underside of a breadboard with the optical components placed on top of it, was chosen to minimise the total footprint of the system. By using the same breadboard for mounting both lasers and the optical components, the footprint of the system was halved[2]. The underside would not require any adjustments after installation and so would be sealed off; all the optical components that a user might require access to would be on the top level.

For this approach, periscopes were used to guide the beams from the outputs of the lasers (on the bottom level) onto the optics (on the top level). The mirror at the top of the periscope was adjustable so that the beam directions and heights could be varied as

[1] Typical M^2 value of 1.05 and stated optical noise of 0.2 % up to 20 MHz.
[2] The total footprint is 460 mm x 310 mm.

required for the subsequent optics. The entire periscope was enclosed to contain the beams and ensure that no light was emitted perpendicular to the breadboard, that might otherwise pose a hazard.

6.2.3 Pump beam optical layout

Figure 6.1 shows the optical layout within the PILOT system. Following the exit from the periscope, the pump beam passes through an adjustable attenuator. This allows the energy of the pump beams to be varied without changing any settings on the laser, which ensures a consistent beam profile.

After the attenuator, the beam is incident on a (non-polarising) 50:50 beam splitter. The transmitted beam then reflects off a mirror onto the crossing lens. The mirror is held in a kinematic mount which, in combination with the aforementioned adjustable output from the periscope, allows the user complete adjustment over this beam direction. The reflected beam from the beam splitter bounces off two mirrors before also passing through the crossing lens. This layout was chosen to ensure that the distance travelled by both beams between the beam splitter and the crossing lens could be matched, thus ensuring the coherence required for a strong interference fringe pattern. The beam splitter, as well as both mirrors in the reflected beam path, were mounted in 2-axis adjustable mounts.

In order to precisely match the path lengths of both pump beams, the two mirrors in the reflected beam path were set on a translation stage. The characterisation of this adjustment is described further in Section 6.3.1, including an illustration of its impact on signal intensity. The extra path length added to the beam is referred to as the ‘delay line’.

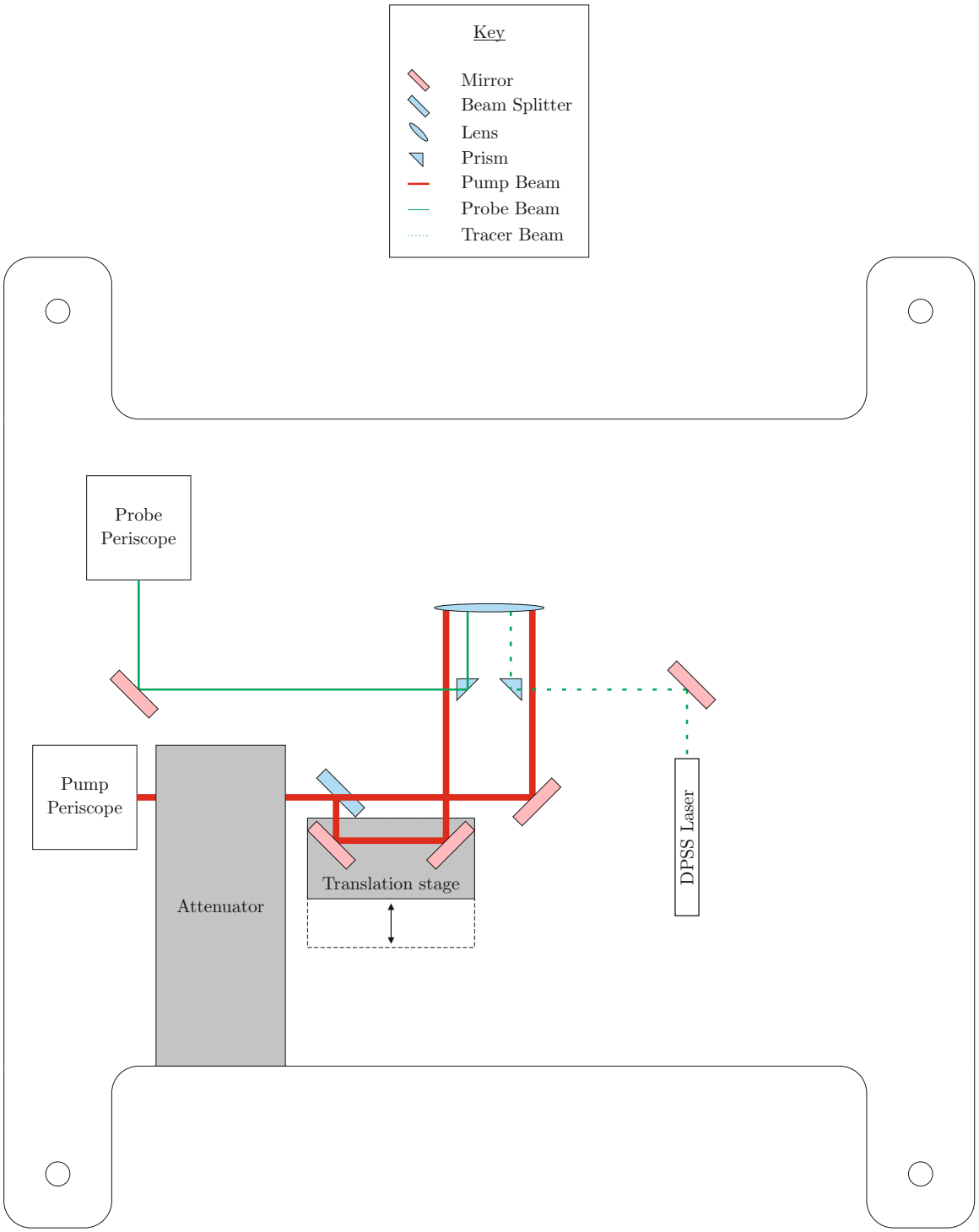


Figure 6.1: Schematic of the top deck of the PILOT system, showing the path of the pump, probe and signal tracing beams.

6.2.4 Probe and signal tracing beams optical layouts

Figure 6.1 also shows the optical layout within the PILOT system for the pump, probe and signal tracing beams. The probe beam is directed out of the periscope onto a mirror, and then reflected through a prism onto the crossing lens. The mirror is held in an adjustable mount to offer control over the beam direction, while the prism is held in a fixed mount. A fixed prism mount is used because the proximity of the probe beam to the pump beam mean that a kinematic mirror mount would obstruct the pump beam path. Furthermore, having an adjustable mount so close to the pump beam path was undesirable from a safety perspective.

The Thorlabs DPSS laser module (that was used to create the signal tracing beam) is mounted in an adjustable mount. The beam is directed onto a mirror held in a kinematic mount, followed by a fixed prism for the same reasons outlined for the probe beam path.

6.2.5 Alignment optics

As explained in Section 2.1, a LIGS experiment requires the two pump beams to cross over at a specified crossing angle, and the probe beam to cross over at the calculated probe beam angle. The PILOT system achieves this by using a lens, referred to as the crossing lens. The pump and probe beams are all perpendicularly incident on the lens, and so the lens will cross all three beams at a distance equal to its focal length. Since the focal length of the crossing lens can be set by using different lenses, and the distance between the incident beams can be adjusted using the mirrors in the respective beam paths, this design enables the system to be used for numerous LIGS geometries as required by the user. The default configuration for the system is to use a 750 mm focal length crossing lens with a 3° crossing angle for the pump beams.

Once a certain geometry has been chosen, the beams need to be aligned accordingly. A design specification for this system was to incorporate internal alignment capability. This was desirable because it would allow for quick and easy alignment on-site without the need for an extensive optical reconfiguration. To achieve this, the layout shown in Figure 6.2 was employed. A prism on a magnetic mount was installed after the crossing lens. This prism

could then reflect the pump, probe and signal tracing beams successively onto two other prisms, and finally onto a detector. By setting the distance of the detector from the crossing lens to be equal to the focal length of the lens, it could be used to ensure that all four beams were overlapped at the correct point. Setting the first prism on a magnetic mount meant that it could be removed and replaced in exactly the same position at any time, thereby enabling the option of a rapid alignment check *in situ* during an experiment. To ensure that no beams were emitted out of the PILOT system during alignment, a mounting bracket for a beam dump was added after the prism.

The decision on what detector to use at the end of the alignment path was subject to certain constraints. A detector that would be able to detect the pump beams (at a wavelength of 1064 nm) as well as the probe and signal tracing beams (at a wavelength of 532 nm) was required. The detector also needed to be compact and cost-effective, and offer a video feed showing the beam alignment in real time. For these reasons the Raspberry Pi NoIR Camera V2 module was chosen. This infrared camera module met all the requirements, and only needed a (compact and cheap) Raspberry Pi computer to interface with. A camera mount that allowed the camera position to be adjusted in all directions was designed and manufactured.

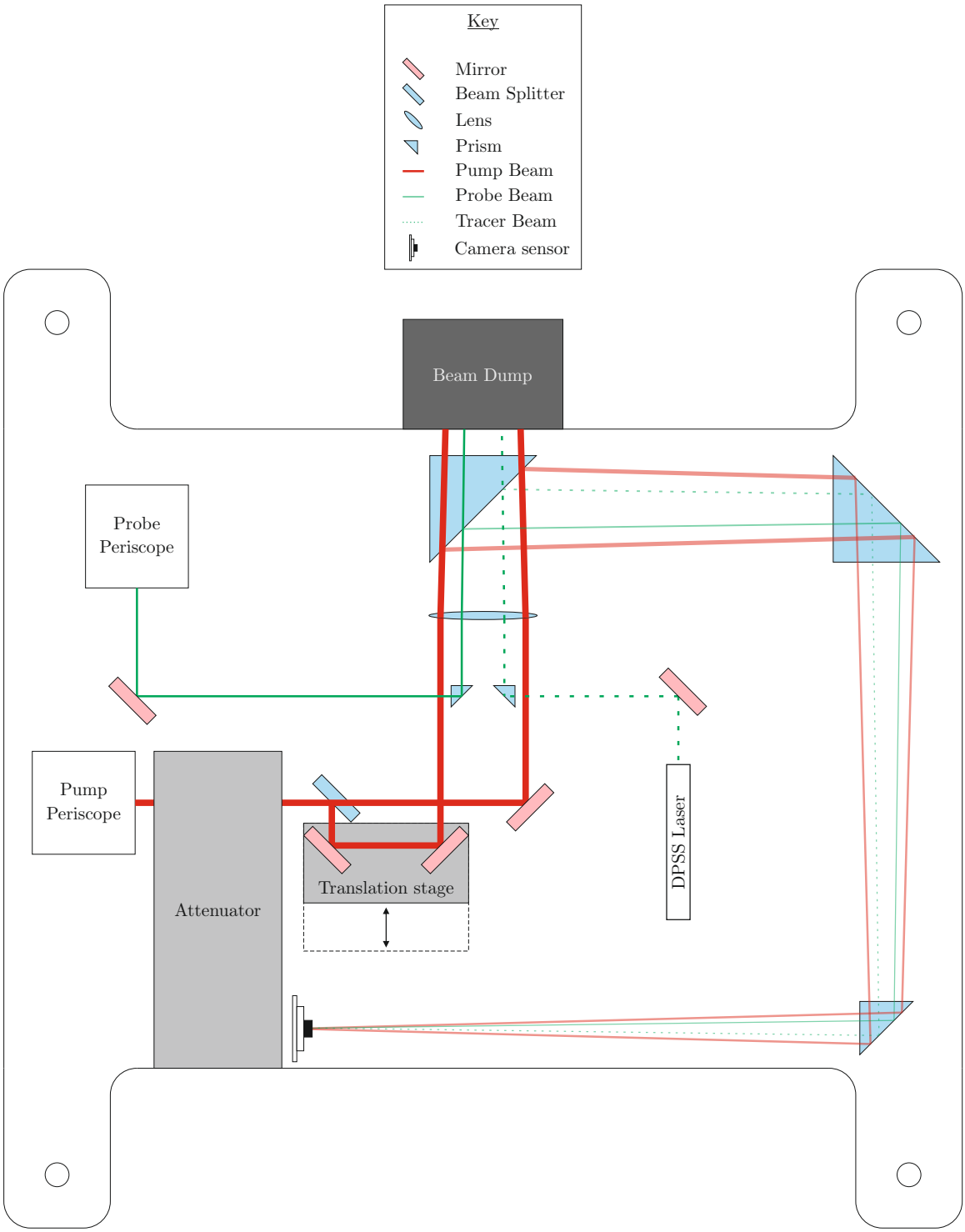


Figure 6.2: Schematic of the top deck of the PILOT system, showing the path of the pump, probe and signal tracing beams during internal alignment.

6.2.6 Mechanical considerations and peripherals

As mentioned in Section 6.2.5, a Raspberry Pi computer was required to interface with the Raspberry Pi NoIR camera for beam alignment. The camera was connected to the Raspberry Pi by a ribbon cable, and so the computer had to also be installed on the breadboard. To save space, it was installed in the bottom level alongside the pump and probe lasers. An HDMI cable connected the Raspberry Pi to a display screen and a wireless keyboard and mouse were used to control it. Having the Raspberry Pi computer on board was also beneficial as it could be used as the power source for the Thorlabs DPSS laser module (which was used to create the signal tracing beam for alignment purposes).

Mounting holes were drilled into the breadboard that the optics and laser heads were bolted on to, so that the system could be installed onto a frame in any orientation depending on the application. To ensure laser safety while minimising wight and maximising portability, anodised aluminium was used to enclosed the entire system. Rubber trim was used to seal gaps between the metal plates. The lid of the system could be unfastened and lifted to provide easy access to the optical components that required adjustment during the aligning process.

The only connections leading out of the PILOT system were the water and electrical connections from the pulsed laser head to its controller, the optical fibre from the probe laser head to its controller, and an electrical connection and HDMI cable from the Raspberry Pi. The laser umbilicals were 3 m long. A supporting rig, referred to as 'Co-PILOT', was constructed to hold the laser controllers in a rack-mount configuration. Wheels and mechanically-lowered feet allowed the rig to be easily manoeuvred into place and stabilised during operation. The design of Co-PILOT also allowed the PILOT system to be mounted on top for transportation. As the rig could be stabilised with the feet lowered down, the PILOT system could even be used while mounted on Co-PILOT. All the accessories and tools required for full operation of the system could be stored on or in Co-PILOT.

A fused multi-point extension lead on Co-PILOT meant that only one electrical socket was required to run the entire system. The only other external connection required for the system was an interlock socket to comply with laser safety procedures.

6.3 Optimising and characterising the PILOT system

Having designed and built the PILOT system, a set of experiments were conducted to optimise and characterise the system. First, the importance of phase-matching the two pump beams was reviewed by adjusting the delay line translation stage. Following that, the relative effects of pump beam energy and probe beam power on the LIEGS signal were investigated. Finally, temperature measurements, taken in air, were compared to thermocouple readings to characterise the performance of the PILOT system.

6.3.1 Delay line

As described in Section 6.2.3, an adjustable delay line was incorporated into the path of one of the pump beams. This enabled the path length to be optimised to ensure coherence between both pump beams at the crossing point. The adjustment was achieved by moving the manual translation stage that both turning mirrors were placed on.

6.3.1.1 Experimental setup

To conduct this experiment, a standard LIGS setup was employed as shown in Figure 6.3. The default PILOT geometry (750 mm crossing lens, 3° crossing angle for the pump beams) was used. After their interaction at the crossing point, the residual pump and probe beams were directed into a beam dump while a prism was used to direct the signal beam onto a mirror. The mirror turned the beam onto a lens, which focused it into an optical fibre. The fibre led to a photomultiplier tube (PMT)[3] which output the signal onto an oscilloscope[4].

[4]The PMT module used was a H10721-20 model from Hamamatsu.
[4]The oscilloscope used for this experiment was a Picoscope 6402 model by Pico Technology.

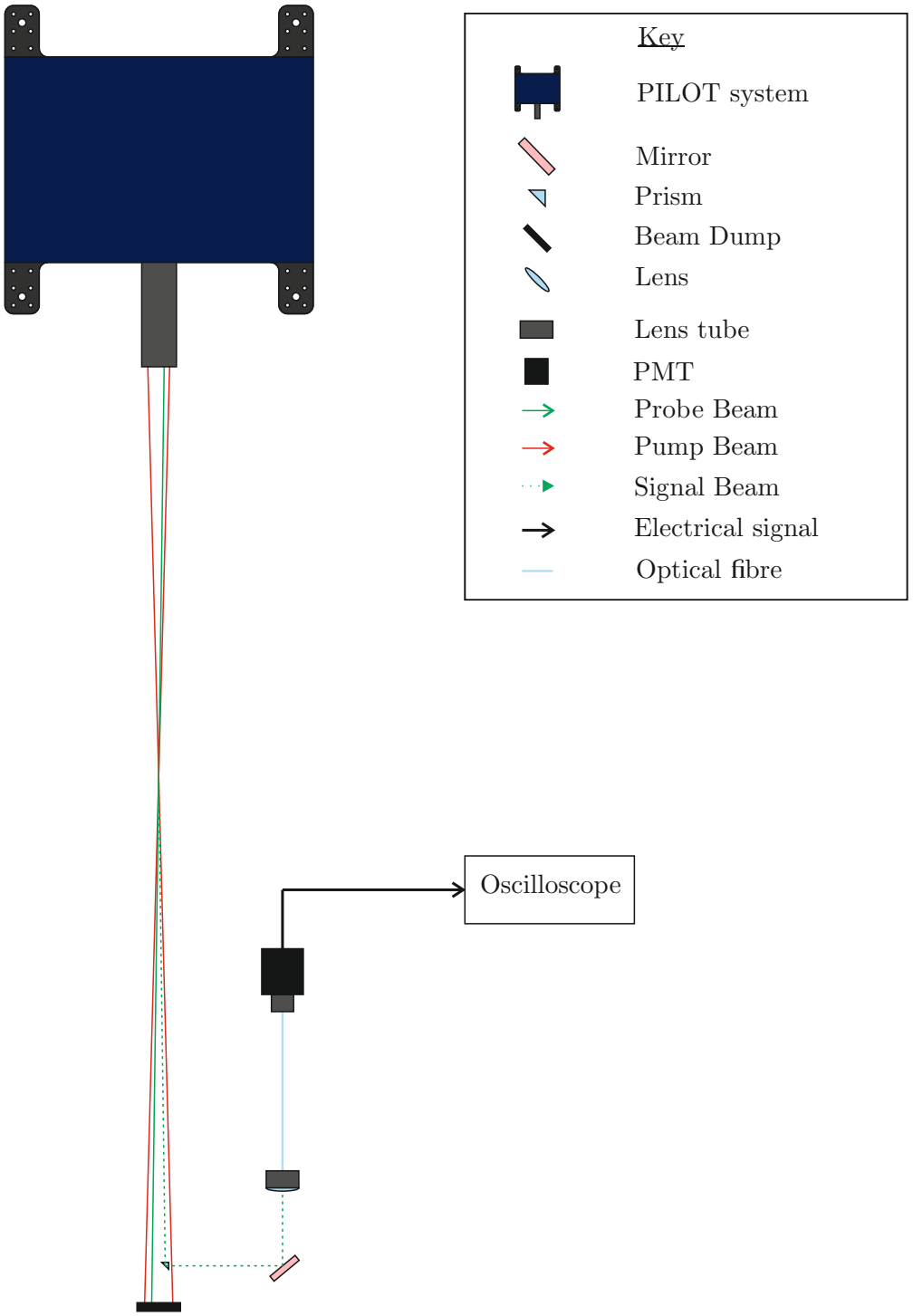


Figure 6.3: Plan view of the experimental setup used to optimise the delay line within the PILOT system.

6.3.1.2 Results and discussion

The PILOT system was run at 400 Hz, with the continuous wave probe laser at 2 W. The probe laser was operated at this reduced power (compared to its 20 W maximum) to ensure that the photomultiplier response would remain linear. The turning mirrors were translated in steps of 1 mm (which resulted in a total variation of 2 mm in the beam path length). The beam alignment was re-optimised after each movement, and data was collected over 0.25 seconds. Figure 6.4 shows the mean LIGS signal intensity achieved at each position, with the error bars showing 1 standard deviation of the data from the mean. The data shows a good correlation with a Gaussian fit, which is consistent with the findings reported by Stampanoni-Panariello *et al.* [98]. The e^{-2} width of the Gaussian fit was 7.5 mm. This finding shows that a misalignment of the position of the mirrors by only ~3 mm either side of the optimal position would result in a 50 % decrease in signal intensity, and highlights the significant advantage that this positional flexibility provides for the PILOT system.

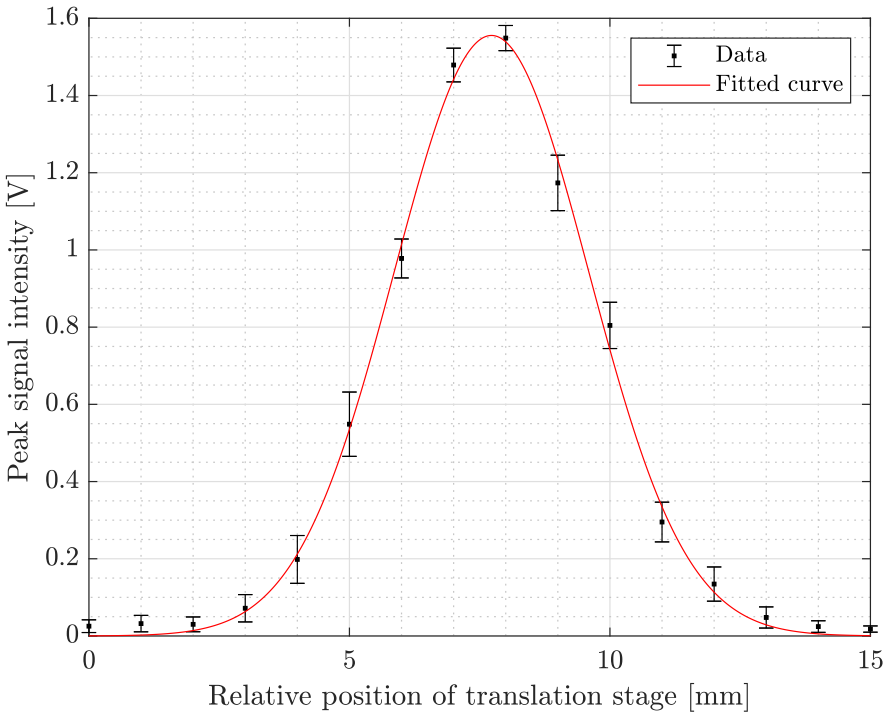


Figure 6.4: Variation of LIEGS signal strength as the delay line translation stage is moved. Each point is the mean of 100 data points, and the error bars signify 1 standard deviation from the mean. The red line shows a least-squares Gaussian fit.

6.3.2 Scaling probe/pump beam power/energy

Some applications of the PILOT system might require either the probe beam power, or the pump beam energies, to be reduced. Therefore, the next experiment conducted to characterise the PILOT system was to observe the effect, on the LIGS signal intensity, of varying these parameters.

6.3.2.1 Experimental setup

The experimental layout for both experiments is shown in Figure 6.5. The default PILOT geometry (750 mm crossing lens, 3° crossing angle for the pump beams) was employed, and the same photomultiplier tube module and oscilloscope detailed in Section 6.3.1.1 were used.

First, the PILOT system was run with a constant pump beam energy and the probe beam was directed onto a power meter[5]. The system was run at 400 Hz, and 10 data points were collected as the probe power was varied between setpoints of 0.5 W and 9 W. In order to remain within the linear regime of the photomultiplier tube, the probe power was not increased further. As there was a loss of power within the PILOT system due to the beam interaction with the optics, the actual power incident on the LIGS grating was measured for each step using the power meter (rather than relying on the setpoint values).

Next, a different (due to damage threshold considerations) power meter[6] was placed in the path of one of the pump beams. The probe beam was kept at a constant power, and the attenuator module within the PILOT system was used to increase the pump beam energy. Due to the damage threshold of the power meter, the system was run at 10 Hz and an absorptive neutral density filter had to be placed in front of the meter. The attenuation of the filter for the 1064 nm pump beam was calibrated beforehand so that it could be accounted for when analysing the results. The pump beam energy was also measured after the grating, so that any losses within the PILOT system were accounted for.

For both experiments, LIGS signals were collected over 1 second at each discrete power/energy setting.

[5] A UP19K-15S-VR-D0 thermopile model from Gentec.
[6] A model S470C thermopile power meter from Thorlabs.

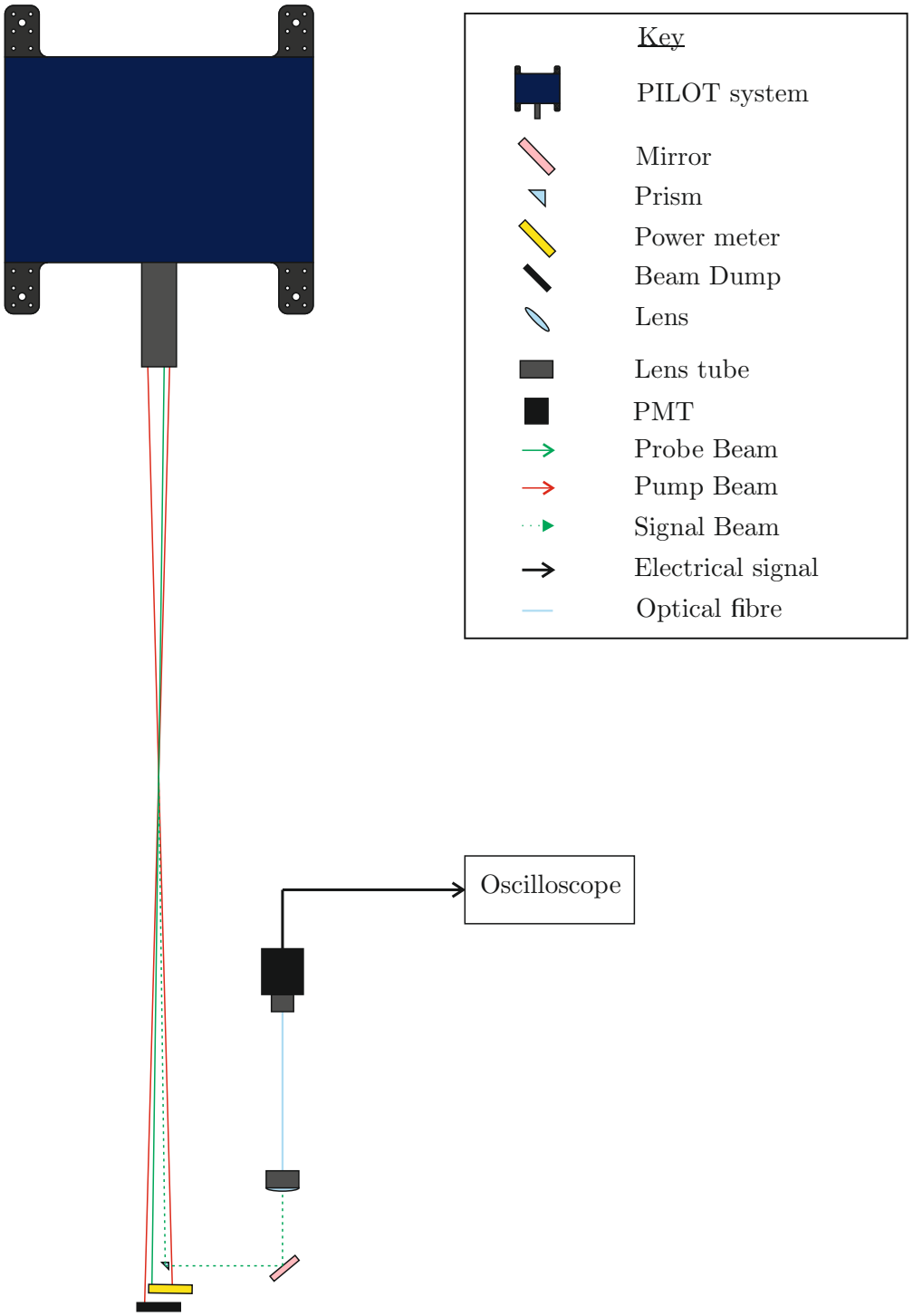


Figure 6.5: Plan view of the experimental setup used to characterise the effect of varying the probe/pump beam power/energy.

6.3.2.2 Results and discussion

Figure 6.6 shows the mean signal intensity for the LIEGS signals collected at different probe powers (and constant pump beam energies). The data is presented with error bars displaying 1 standard deviation of the data from the mean. The results show a linear trend, which is to be expected as an increase in probe power results in a proportional increase in the light scattered off the grating to form the signal beam.

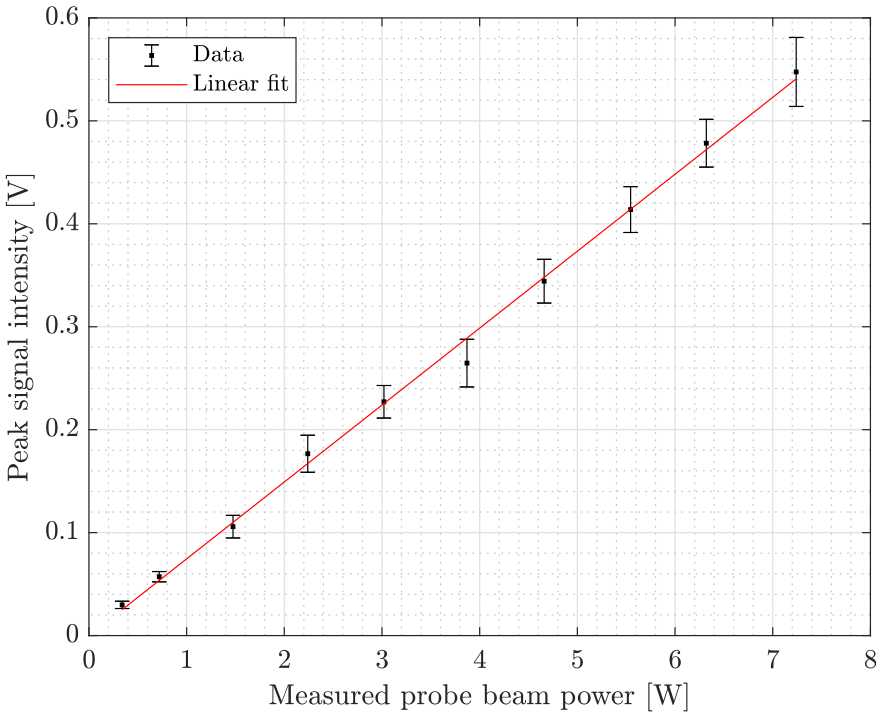


Figure 6.6: Variation of LIEGS signal strength as the probe power was increased. Each point is the mean of 400 data points, and the error bars signify 1 standard deviation from the mean. The red line shows a least-squares linear fit.

Figure 6.7 shows the mean signal intensity for the LIGS signals collected at each pump energy, with the error bars displaying 1 standard deviation of the data from the mean. A least-squares quadratic fit has been applied to the data, which shows that the signal beam intensity (S) increased as a function of the pump beam energy (E) squared:

$$S \propto E^2 \tag{6.1}$$

The R-squared value, which is a measure of the strength of the correlation, was 99.7 %. This is in agreement with the theory derived by Stampanoni-Panariello *et al.* [16], who showed that the diffraction efficiency of the grating (which they denote as η) is proportional to the squared pump energy.

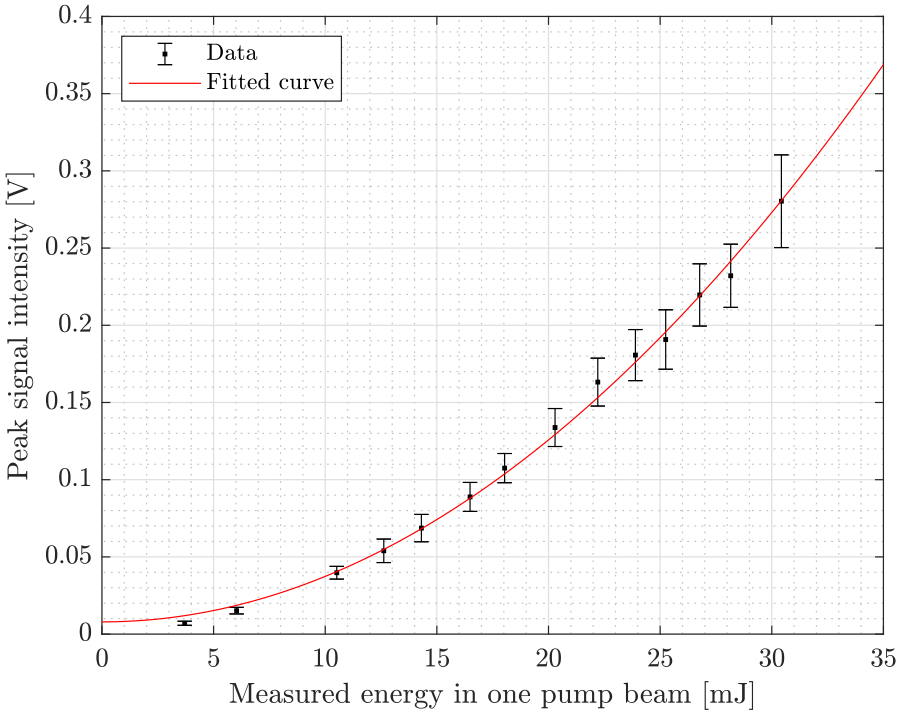


Figure 6.7: Variation of mean LIGS signal strength as the pump energy was increased. Each point is the mean of 400 data points, and the error bars signify 1 standard deviation from the mean. The red line shows a least-squares fit.

The results show that, as expected, both probe power and pump beam energy should be maximised to obtain strong LIEGS signals[7]. However the signal intensity only scales linearly with probe beam power while it scales quadratically with pump beam energy, and so maximising pump beam energy should be prioritised if possible.

6.3.3 Spatial resolution

The spatial resolution of LIGS is determined by the geometry and size of the pump and probe beams that intersect to create the signal beam. The use of a crossing lens in the

[7]Note that there would be a limit at which high beam irradiance would lead to gas breakdown.

default PILOT configuration (using a 750 mm crossing lens and a 3° crossing angle for the pump beams) meant that the beams were focused at the crossing point. An experiment was designed to measure the spatial resolution of the system in this configuration, and the results were compared to the modelled spatial resolution.

6.3.3.1 Experimental setup

To measure the spatial resolution of the system, an experiment was devised where a jet of gas that doesn't create a LIEGS signal could be translated through the grating. The variation in signal intensity for different positions of the jet could then be used to measure the size of the grating.

The experimental setup, shown in Figure 6.8, enabled PILOT to obtain LIEGS measurements in air. The LIEGS signal beam, produced at the crossing point of the pump and probe beams, was collected by a photomultiplier tube (PMT) and recorded by an oscilloscope[8]. In order to measure the spatial resolution of the system, a needle fixed to a 2-axis translation stage was placed just below the crossing point of all three beams. The needle was connected to a helium gas line via a mass flow controller[9]. Helium was chosen as it produces a negligible LIEGS signal compared to air and is inert.

[8]The same PMT and oscilloscope that were used for the experiment described in Section 6.3.1.1.
[9]HFC-202 model from Teledyne Hastings Instruments.

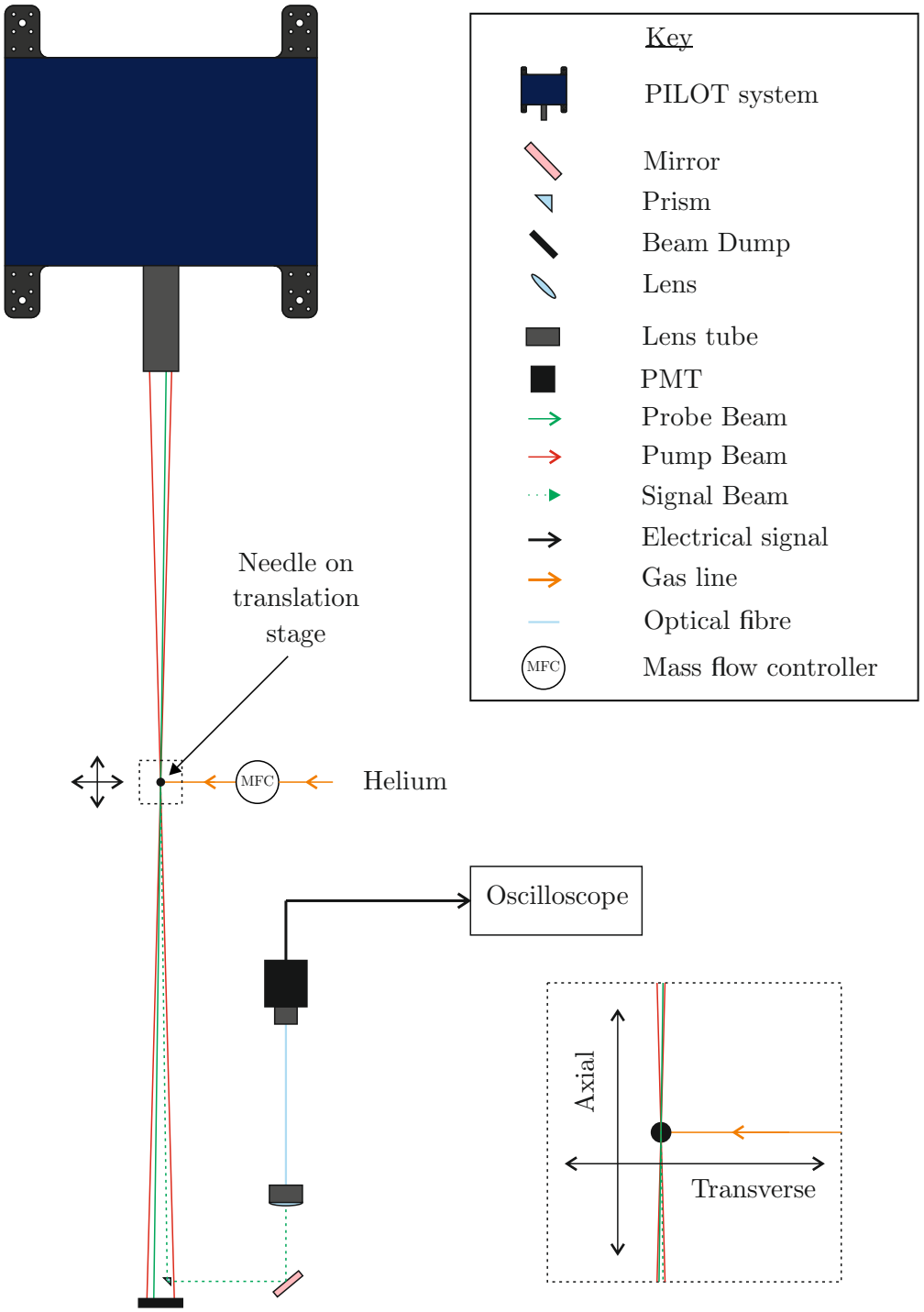


Figure 6.8: Plan view of the experimental setup to measure the spatial resolution of the PILOT system. The inset image, on the bottom right, shows a magnified view of the needle and defines the directions in which it is translated.

Before running the experiment, the size of the helium jet was characterised. The phenomenon of Rayleigh scattering, which is the elastic scattering of light by molecules of gas, was employed for this purpose. The scattering efficiency of air is about 100 times larger than that of helium [99]. To illuminate the helium jet, the probe beam was converted into a light sheet by using a cylindrical lens. A camera[10] was used to image the jet. Figure 6.9 shows the image captured by the camera. The diameter of the helium jet, using a e^{-2} definition, was measured[11] to be 1.9 mm. The mass flow rate used for the jet was 0.15 slpm.

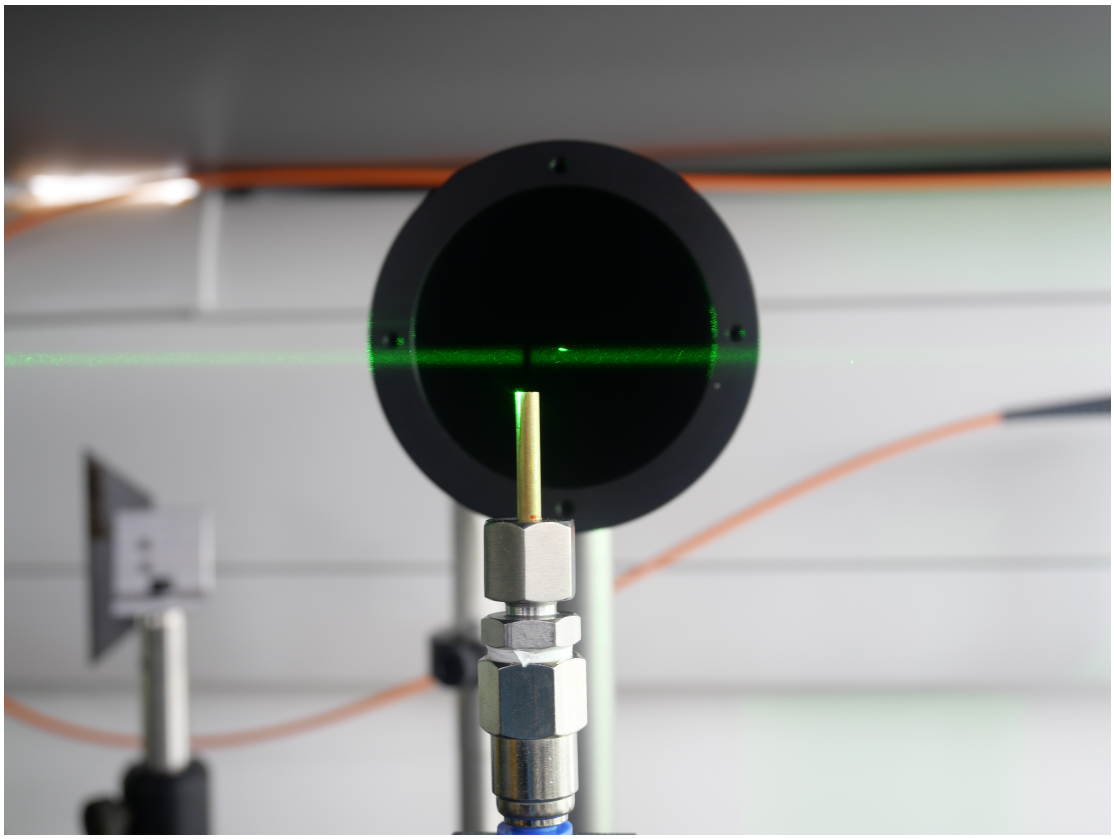


Figure 6.9: Image showing the Rayleigh scattering of the probe sheet from air. Note the gap in the laser sheet which corresponds to the helium jet being emitted from the brass needle.

[10] LUMIX DC-GX9 model from Panasonic.
[11] The RAW sensor data was used for this analysis.

6.3.3.2 Results and discussion

During the experiment, the needle was translated over a distance of 17 mm, in steps of 0.2 mm, in the axial direction (along the grating). At each axial position, the needle was also moved in the transverse direction (across the grating), over a distance of 4.5 mm, in steps of 0.2 mm (a coarser spacing of 0.5 mm was used for the four furthest positions from the grating centre). At each position, data was collected for 1 second at 400 Hz.

The mean signal intensity was defined for each position and a moving average of 21 data points was used to smooth the data in both directions. Figure 6.10 shows the results.

As expected, the signal intensity drops when the helium jet is within the grating (since it has the effect of partially 'blocking' the signal beam generation). However, the results show that the jet also caused a reduction in signal intensity when it was positioned before and after the grating. This can be attributed to the interference of the jet with the probe and signal beams respectively, as it would have caused some beam steering.

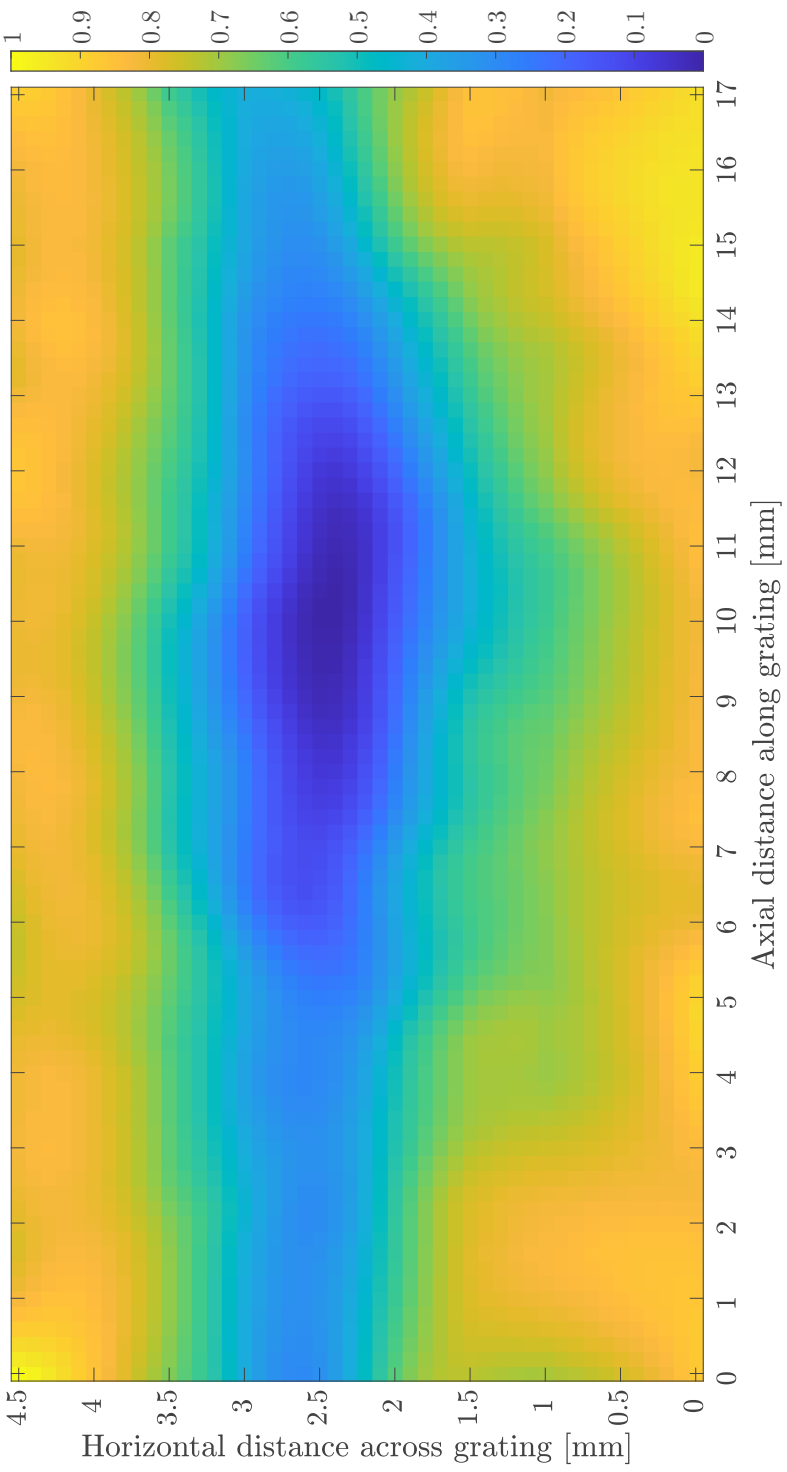


Figure 6.10: Mean LIEGS signal intensity at each position characterised in the experiment. As the figure is presented here, the PILOT system was positioned below these positions, and the beams were travelling up the page. Note that the data has been smoothed as described in the text.

To quantify the length and width of the LIEGS grating, a normalised mean from the data presented in Figure 6.10 was calculated in both directions. A Gaussian curve was fitted to both data sets, and the results are shown in Figure 6.11. After accounting for the size of the helium jet, the length and width (using a e^{-2} definition) of the grating were calculated to be 11.2 ± 1.2 mm and 0.88 ± 0.16 mm respectively, with the upper and lower limits representing the 95 % confidence bounds of the Gaussian fit.

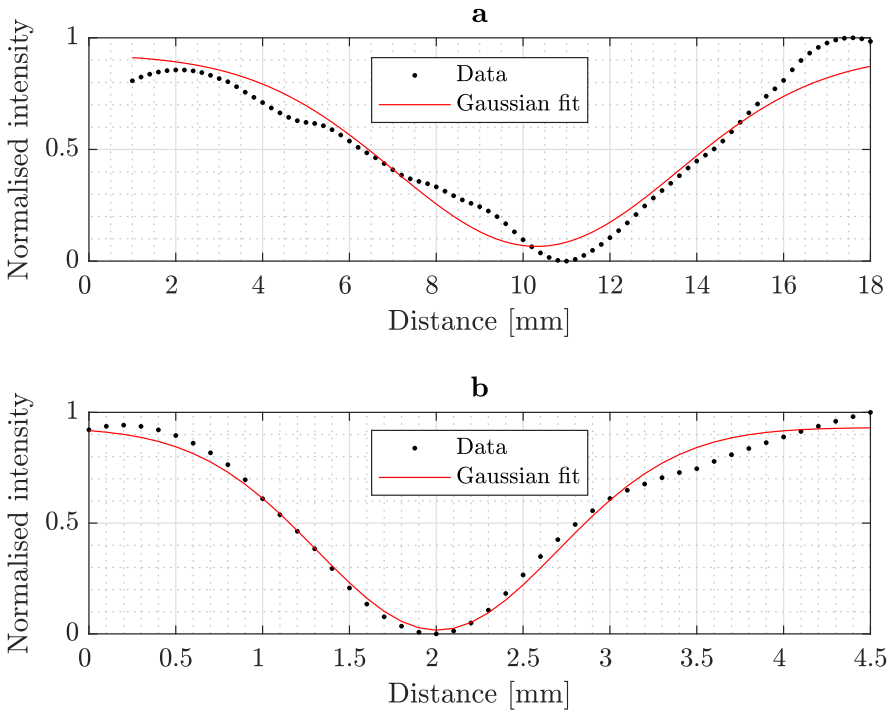


Figure 6.11: Graphs showing the normalised mean signal intensity along the grating (Figure **a**) and across it (Figure **b**).

To validate these measurements, the computational model described in Section 4.5.1 was used. This model calculates the theoretical length and width of the interaction region between pump and probe beams. It also accounts for the Gaussian nature of the beams. Using this model, it was found that an interaction width (using e^{-2} definition) of ~0.8 mm would require all the beams to be ~3 mm in diameter, and would also result in a length of ~40 mm. However, the probe beam was measured to be 0.5 mm in diameter using a beam profiler[12]. A reason for the larger measured value of the width of the interaction region could be that a relatively large measurement device (helium jet of 1.8 mm diameter)

was being used to measure a small dimension (∼0.5 mm). This means that relatively small inaccuracies in the helium jet characterisation (e.g. jet diameter or angle of orientation) would have a large effect on the measurement. On the other hand, the length of the grating, which is much larger than the diameter of the helium jet, would not be greatly affected by these inaccuracies and so the measurement is more likely to be accurate. Using the computational model again, it was found that pump beams with 0.8 mm diameters (which is a reasonable value based on experience) would produce an 11 mm long grating. Therefore the PILOT system has been characterised to have an axial spatial resolution of 11.2 mm and a transverse spatial resolution of less than 0.88 mm.

6.3.4 Temperature measurement comparison with thermocouples

The PILOT system is capable of obtaining temperature measurements at 400 Hz, which equates to a measurement every 2.5 ms. This enables temperature measurements of quickly varying phenomena, which would be otherwise difficult to characterise. This section first presents an experiment that was conducted to compare steady-state room temperature measurements of the PILOT system to those obtained by two standard K-type thermocouples with different junction sizes. A second experiment was then run to compare the time response of the PILOT system and the two thermocouples to a temperature impulse.

6.3.4.1 Experimental setup

The same experimental setup, shown in Figure 6.12, was used for both experiments. The default PILOT geometry (750 mm crossing lens, 3° crossing angle for the pump beams) was employed. Two exposed junction K-type thermocouples with junction diameters of 1 mm and 0.65 mm, respectively, were placed above and below the thermal grating. A heat gun was angled towards the grating to influence the gas temperature. Data for both thermocouples was collected at 400 Hz by a data logger[13], and the LIEGS signals were collected by a photmultiplier tube (PMT)[14] and recorded using an oscilloscope [15]. A pulse generator[16]

[12] A Thorlabs CCD Camera Beam Profiler was used.
[13] A DrDAQ data logger by Pico Technology was used.
[14] The PMT module used was a H10721-20 model from Hamamatsu.
[15] A Wavesurfer 3074 oscilloscope from Teledyne LeCroy was used.

was employed to provide a synchronising pulse to the data logger and oscilloscope.

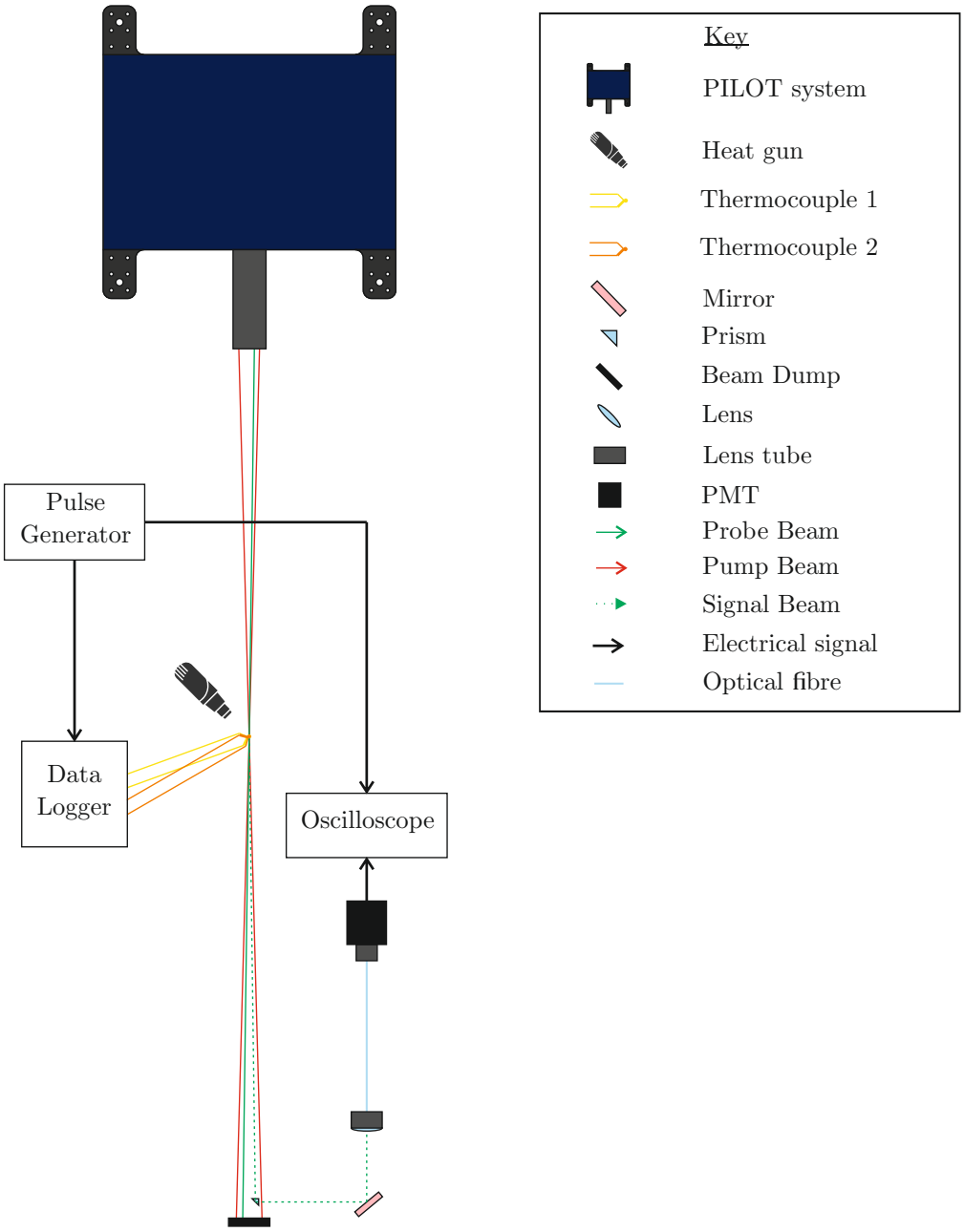


Figure 6.12: Plan view of the experimental setup to compare temperature measurements by the PILOT system and two thermocouples. A heat gun was used to vary the temperature.

[16]The TGP110 model from Aim & Thurlby Thandar Instruments was used.

6.3.4.2 Steady-state temperature measurement

First, data was collected with the heat gun turned off, meaning that the air was at room temperature. Data was collected for 1 second at 400 Hz. Figure 6.13 displays the mean temperatures measured by each measurement device/technique. The error bars on the the thermocouple measurements (±1 °C) is the stated error of the amplifiers that were used[17]. The error bar on the LIEGS measurement shows the standard deviation from the mean for the dataset. By displaying the results in this way, the accuracy of LIEGS temperature measurements using the PILOT system can be determined by comparing it to the thermocouple measurements and error bars, while the single-shot precision of the LIEGS measurement can be inferred from the error bar on the LIEGS measurement.

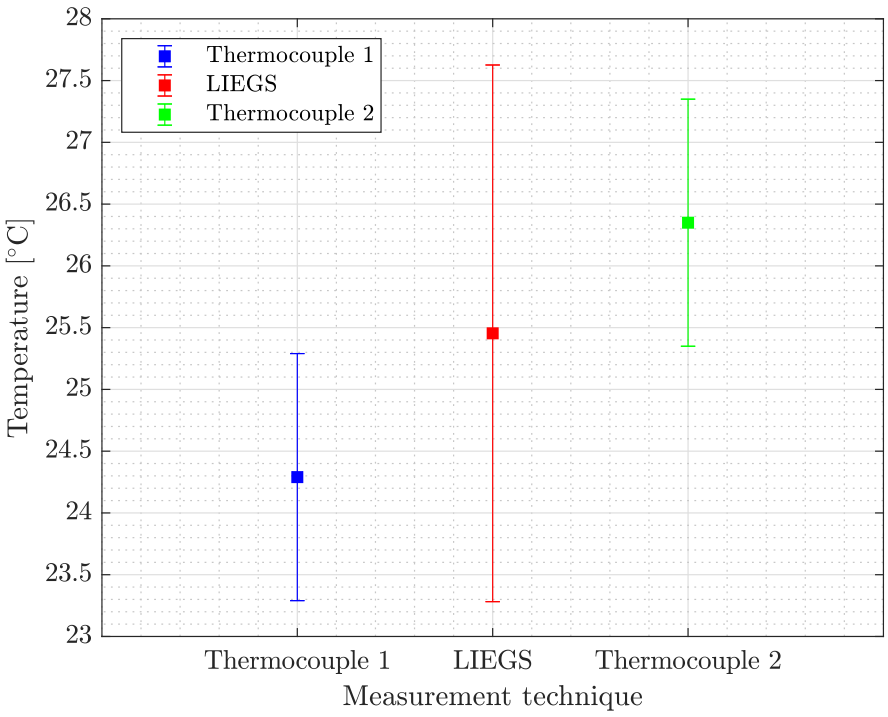


Figure 6.13: Steady-state thermocouple and LIEGS temperature measurements at room temperature and pressure.

The data shows LIEGS temperature measurements, taken at room temperature and pressure, from the PILOT system are within the stated accuracy of the two K-type thermocouples used for this experiment. This suggests a LIEGS accuracy of better than 0.37 %.

[17] AD8495 K-type thermocouple amplifiers from Analog Devices.

The single shot precision of the PILOT system at room temperature and pressure is $\pm 0.7\,\%$.

6.3.4.3 Impulse temperature measurements

The time response of an exposed junction K-type thermocouple is dependent on the size of the junction [100–103]. This characteristic limits the temporal resolution for temperature measurements made by a thermocouple. To compare the time response of two thermocouples with different junction diameters (1 mm and 0.65 mm) with the PILOT system, the setup described in Section 6.3.4.1 was used. The heat gun was turned on and allowed to reach a steady temperature. Data collection was then started (for the thermocouples and LIEGS), and a synchronising pulse was sent to the data loggers and the oscilloscope. The heat gun was suddenly switched off to provide a temperature impulse which was measured by all three devices. Figure 6.14 shows the LIEGS temperature measurements obtained by the PILOT system. Since the LIEGS measurements are instantaneous, the dashed line showing when the temperature changed by 50 % can be used as the time at which the heat gun was switched off. Note that the large variations in temperature before the heat gun was switched on are due to the localised temperature fluctuations caused by the heat gun.

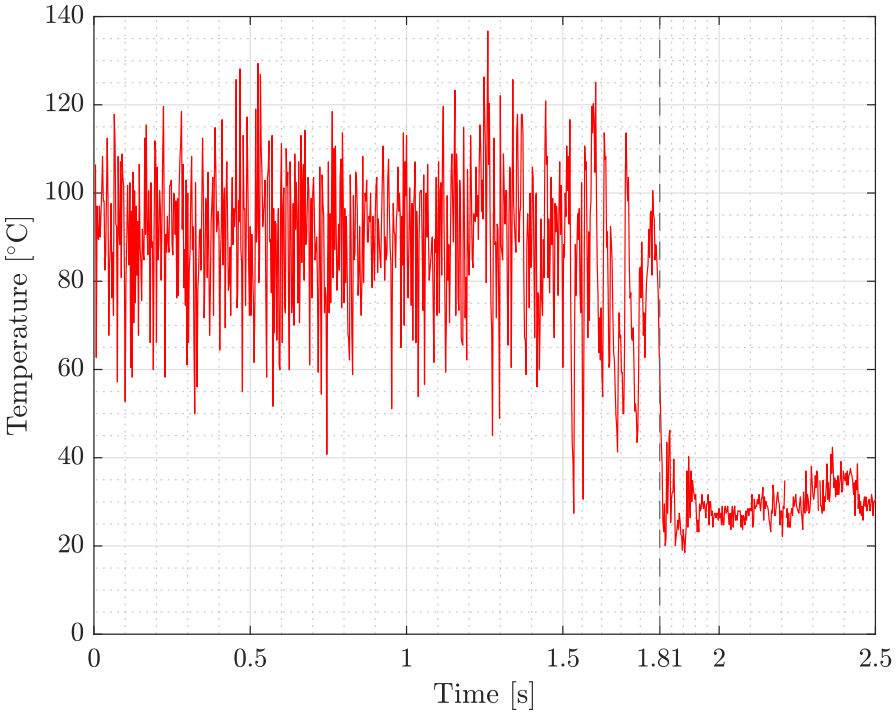


Figure 6.14: LIEGS temperature measurements as the heat gun was switched off. The dashed line shows the time at which the temperature fell by 50 % of its total change.

Figure 6.15 shows the temperature recorded by the two thermocouples. The time constant of a thermocouple is defined as the time required for the thermocouple to reach 63.2 % of an instantaneous temperature change. The blue and green dashed lines show when this occured for each thermocouple. The respective time constants for thermocouple 1 (with a junction diameter of 1 mm) and thermocouple 2 (with a junction diameter of0.65 mm) were 16.2 s and 13.6 s, respectively.

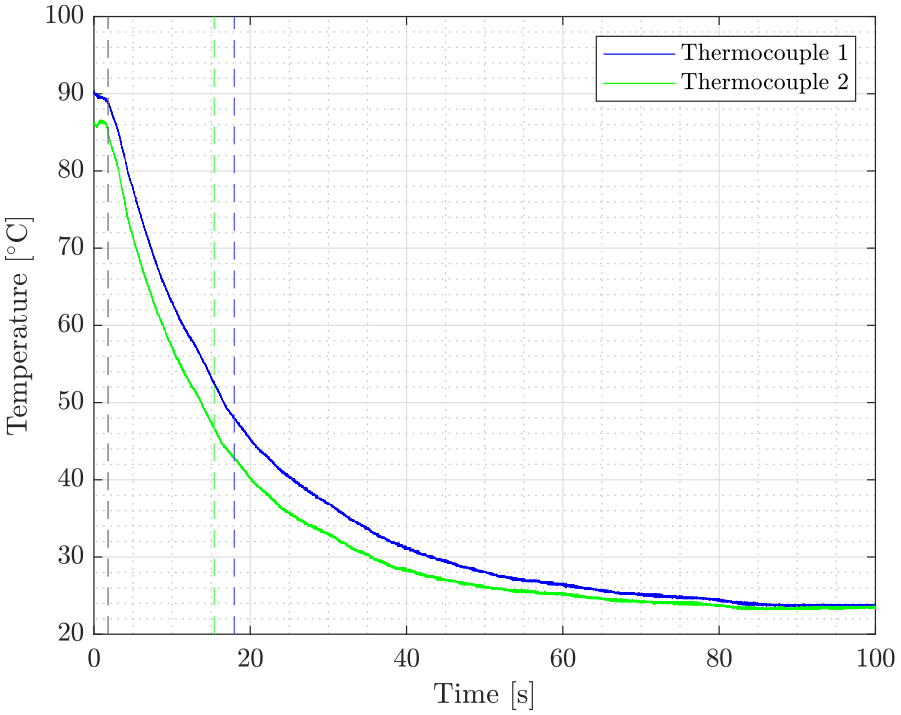


Figure 6.15: Temperature recorded by both thermocouples as the heat gun was switched off. Thermocouple 1 had a junction diameter of 1 mm while thermocouple 2 had a junction diameter of 0.65 mm. The black dashed line shows when the heat gun was switched off. The blue and green dashed lines show the times when the respective thermocouple temperatures fell by 63.2 % of the total temperature drop.

Using a simple lumped capacitance model for the thermocouple junction [104], the time constant τ is defined as

$$\tau = \frac{\rho V c_p}{h A_\mathrm{s}} \tag{6.2}$$

where ρ and c_p are the density and heat capacity of the sensor, V and A_s are the volume and surface area of the junction and h is the heat transfer coefficient.

By modelling the sensor junction as a spherical bead, Equation 6.2 can be simplified to

$$\tau \propto r \tag{6.3}$$

where r is the radius of the sensor junction.

By applying Equation 6.3 to the two thermocouples used in this experiment, the time

constant for thermocouple 2 relative to that of thermocouple 1 is calculated to be 0.65. The measured relative time constant was 0.8. The discrepancy between both values is due to the assumptions made in the simple heat transfer model, but the trend of a faster response for a smaller sensor is clear.

Using the time constant obtained for thermocouple 1, and the relationship shown in Equation 6.3, it was predicted that a thermocouple with a bead size of 0.14 µm would have a time constant equal to the time period between measurements taken by PILOT. Realistically, however, to take measurements at 400 Hz the thermocouple bead size would have to be even smaller since the relationship shown in Equation 6.3 has been proved to be a conservative estimate (and the time constant is defined as the time for the thermocouple to reach only 63.2 % of the total temperature change). Such a small bead size is of course impractical which highlights the advantage of the high repetition rate of the PILOT system.

6.4 Practical and environmental considerations

Having optimised and characterised the PILOT system, there was a requirement to investigate the different applications where it might be employed, and how practical constraints might affect its performance. First, the effect of the high-energy pump beams on optical windows (which are present in many practical applications) was considered. Next, the performance of the PILOT system in scattering environments was characterised and the impact of different detectors was investigated. Finally, the application of the PILOT system for LIEGS measurements in different gases was studied.

6.4.1 Window damage thresholds

Many research applications for optical diagnostic techniques involve otherwise enclosed chambers fitted with windows [105–110]. The damage threshold of the windows thus becomes relevant.

The damage threshold for highly transmitting materials, when using a continuous wave laser, is linked to the absorption of the laser energy by the material leading to thermal damage. On the other hand, damage by pulsed lasers (with a pulse duration of the order

of nanoseconds) is caused by the dielectric breakdown of the material, where electrons are stripped from the lattice [111]. The high energy and short pulse duration (100 mJ over 5 ns) of the Nd:YAG laser used in the PILOT system means that window damage will be caused by the dielectric breakdown caused by the pulsed laser[18].

The damage threshold in this regime for a transmitting material is dependent on the wavelength [112, 113] and pulse duration [114–116] of the laser. However, since this work was only concerned with the PILOT system, these factors weren't varied. Another important consideration is the surface finish of the window. The presence of defects such as scratches and cracks on the surface lower the damage threshold of the material by causing a localised increase in electric field strength [117]. Furthermore, defects can also be absorbing inclusions which create thermal stresses on the surface leading to damage [117, 118]. Window manufacturers often specify the quality of the surface with a 'scratch/dig' ratio, where the number assigned to the 'scratch' specification is the width of scratches on the surface and the 'dig' number refers to the diameter of any craters on the surface. The purpose of this experiment was to characterise the surface damage threshold for some common materials used for windows at research facilities, and compare how the surface finish impacted the damage threshold.

6.4.1.1 Experimental setup

It was decided to test windows made of borosilicate, fused silica and sapphire. These materials were chosen as they are common. Three different surface finishes and one window with an anti-reflection coating were also tested.

To conduct this experiment the setup shown in Figure 6.16 was used.

[18] It was known, from experience, that the 20 W continuous wave probe laser employed in the PILOT system did not exceed the damage threshold for commonly used windows.

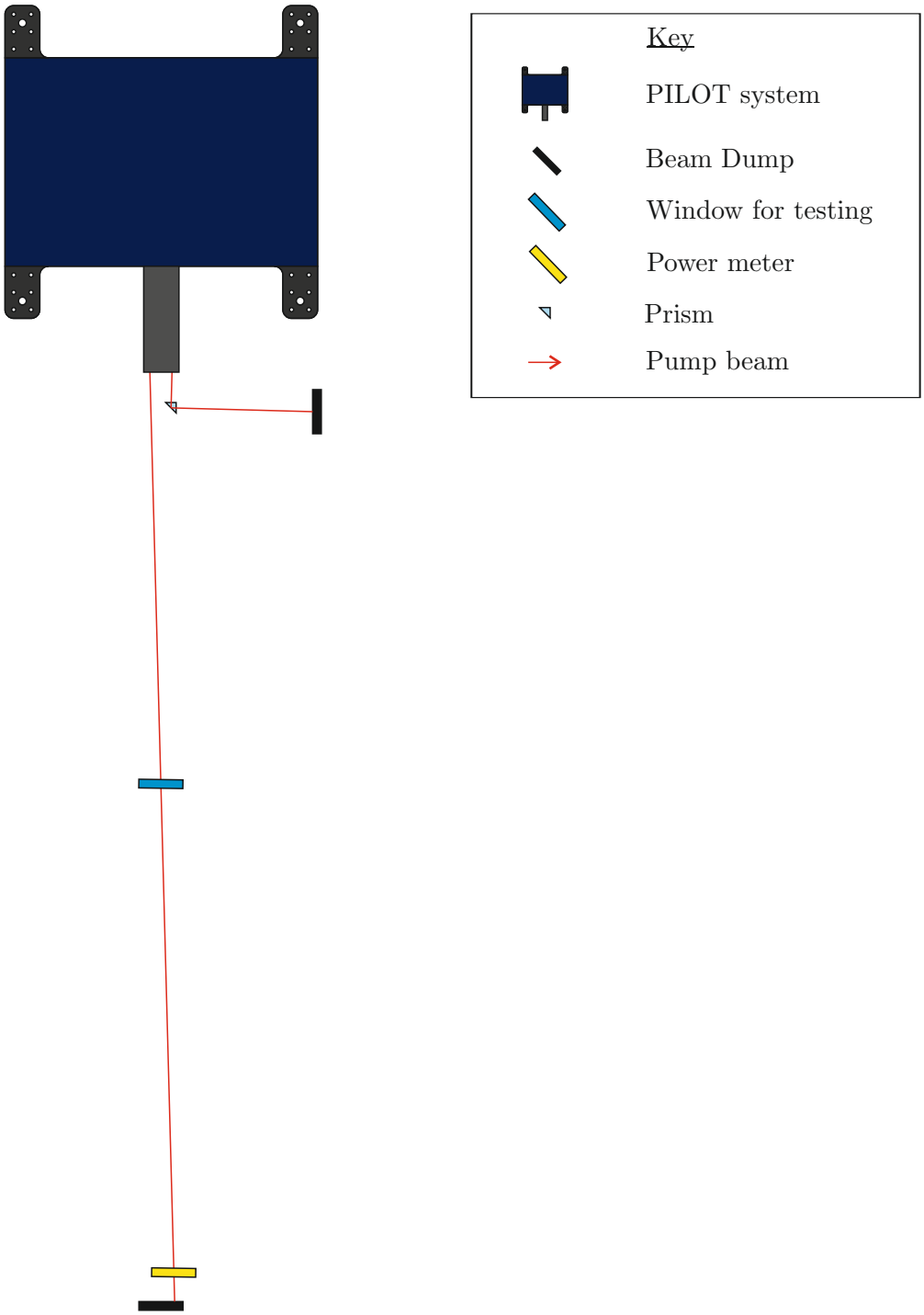


Figure 6.16: Plan view of the experimental setup to measure the damage threshold of various windows when subjected to the pump beam from the PILOT system.

One of the pump beams was blocked off, and the other was directed down the optical table into a beam dump. Due to the crossing lens within the PILOT system, the beam was focused. Sample windows could then be placed near the focal point of the beam. A beam profiler[19] was used to characterise the size and shape of the beam at this point. Figure 6.17 shows the image obtained. The beam diameter, using a Gaussian fit and e^{-2} definition, was measured to be 665 µm.

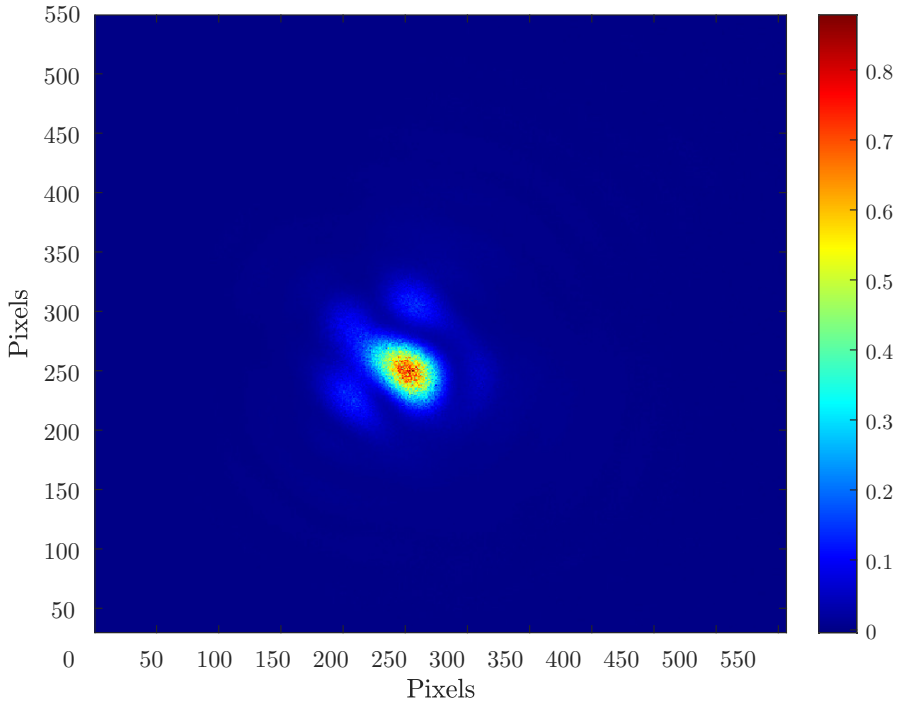


Figure 6.17: Image showing the beam profile of the pump beam at the testing point. The colourbar shows relative intensity, and the pixel size is 6.45 µm x 6.45 µm.

After placing the sample window, held in a rotation mount, at the test location, the attenuator in PILOT was used to slowly increase the energy of the beam until the window fractured. At this point, the window was removed and a power meter[20] was placed in front of the beam dump to measure the beam energy. An absorptive neutral density filter had to be used with the power meter due to its low damage threshold, and the filter's attenuation was characterised so that the beam energy could be calculated. Using the beam profile shown in Figure 6.17, the maximum energy fluence in the beam was calculated as the damage

[19] A Thorlabs CCD Camera Beam Profiler was used.
[20] A Thorlabs S470C thermopile power meter was used.

threshold for that sample point. The window was then rotated and the test was repeated 4 more times before switching to a different sample.

6.4.1.2 Results

The first comparison carried out was between different surface finishes for borosilicate glass. Figure 6.18 shows the results, where each data point is the mean of 5 different test points within the sample window. There is a clear fall in damage threshold as the quality of surface finish is reduced, which is in line with expectations based on literature. The reduction in damage threshold as the surface quality is reduced from a 20/10 scratch/dig specification to 60/40 was quantified to be 27 %, and clearly larger than experimental repeatability.

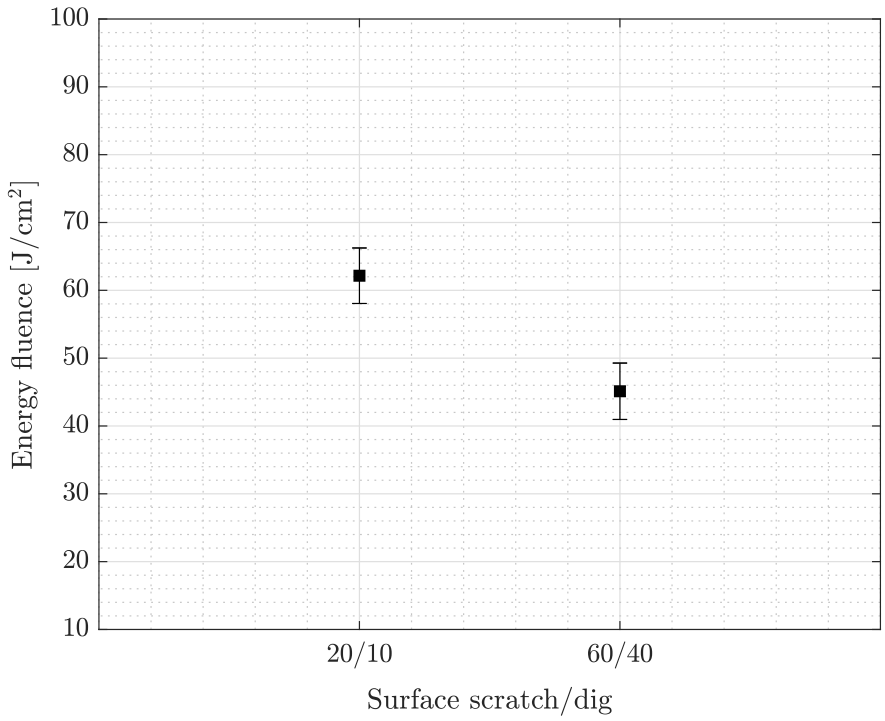


Figure 6.18: Damage thresholds for borosilicate glass with different surface finishes. The error bars show the standard deviation from 5 different sample points.

Next, different surface finishes were compared for fused silica windows and the results are displayed in Figure 6.19. Similarly to the borosilicate glass results, there was a 23 % fall in damage threshold as the surface finish quality was lowered. However, it should be noted that the lower quality surface finish in this case was a 40/20 scratch/dig specification

compared to the 60/40 specification for the borosilicate glass sample. This suggests that the quality of surface finish has a larger effect on damage threshold for fused silica when compared to its effect on borosilicate. A sample window with an anti-reflection (AR) coating for visible (VIS) and near-infrared (NIR) wavelengths was also tested. The addition of the coating was shown to substantially lower the damage threshold of the window by 59 %.

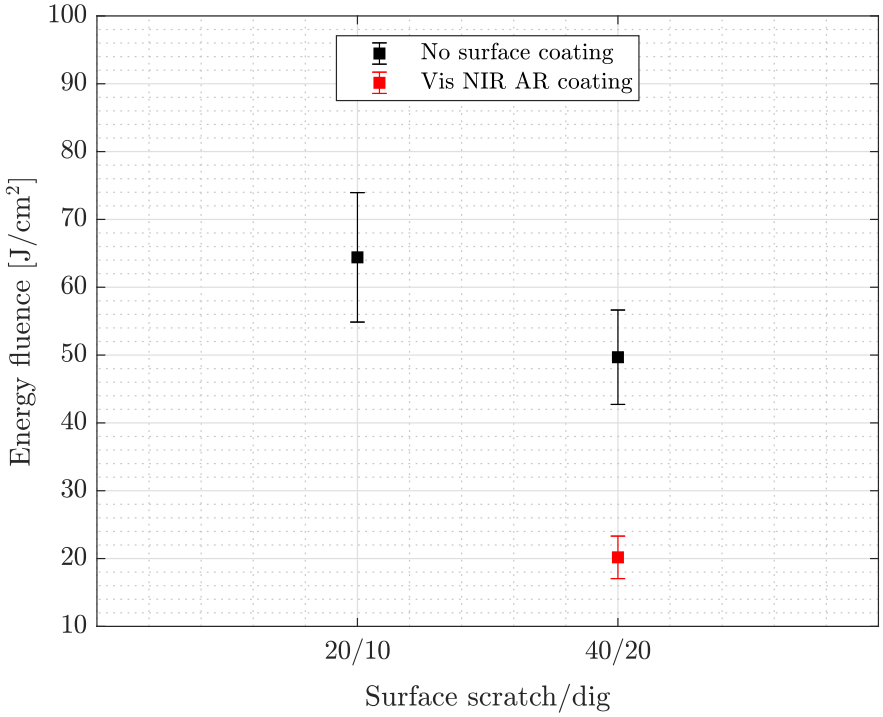


Figure 6.19: Damage thresholds for fused silica with different surface finishes. The error bars show the standard deviation from 5 different sample points. The VIS NIR AR coating refers to a window with an anti-reflection coating suitable for wavelengths in the visible and near-infrared spectrum.

Finally, results for the three different materials were compared as shown in Figure 6.20. Due to practical constraints, two different surface qualities had to be used; comparisons should therefore be made between samples with the same surface quality. The results show that fused silica and borosilicate have a similar damage threshold while sapphire has a substantially lower threshold. However, sapphire was the most repeatable (the window fractured with the same energy fluence for each test) while fused silica was the most variable.

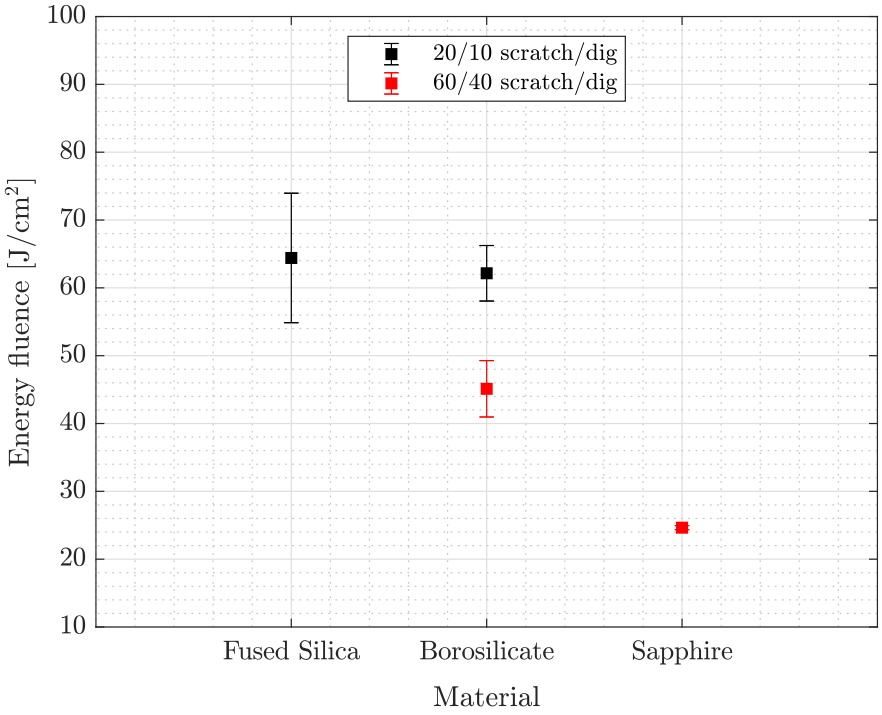


Figure 6.20: Damage thresholds for fused silica, borosilicate and sapphire. Two different surface finishes, specified by their scratch/dig specifications, were used. The error bars show the standard deviation from 5 different sample points.

6.4.1.3 Discussion

The results showed that windows made of fused silica and borosilicate offered the highest damage thresholds, while the sapphire window had a substantially lower threshold. The surface quality was also found to have a large effect on the damage threshold of the fused silica and borosilicate windows. This effect was more pronounced for fused silica than it was for borosilicate. Finally, adding an anti-reflection coating to the surface was shown to substantially lower the damage threshold of the window.

Another observation that was made during the experimental campaign was the effect of dust particles near the surface of the window. It was observed that sometimes the damage on the window surface was propagated by the destruction of a dust particle either near or on the surface of the window. This observation suggests that care should be taken when using windows in applications where particles will be close to the window surfaces and that dirty surfaces should be avoided.

6.4.2 Measurements in scattering environments

One of the main advantages of the LIGS technique is that its temperature measurement relies on recovering the frequency of oscillations of the signal beam rather than examining the signal intensity. This characteristic makes the technique particularly attractive in 'dirty' or absorbing environments when an intensity measurement would be subject to large sources of error. However, this aspect of LIGS also necessitates the use of a detector that can capture a signal that oscillates at a high frequency (usually of the order of 10 MHz) and is also very weak in intensity. Given these constraints, the most common detector used is a photomultiplier tube (PMT) [29, 38, 97].

A PMT operates by first making use of the photoelectric effect to convert incoming photons into electrons. These 'primary' electrons are then accelerated through the tube, towards a series of dynodes. Upon contacting each dynode, more electrons are emitted which leads to a multiplication of electrons through the tube. Finally, the electrons are captured by an anode, which generates a current that can be measured on an oscilloscope. This method of operation is ideal for LIGS applications where the PMT is able to respond quickly to the oscillating signal beam and is capable of amplifying the signal beam to be captured by an oscilloscope. However, a problem arises in the presence of a scattering environment. In this case, particles can continuously scatter light from the probe beam onto the PMT. This can push the PMT into operating in a non-linear response regime. This is due to two different effects [119]:

1. Photocathode bleaching where the continous high level of photons hitting the photocathode depletes its 'reserve' of electrons before the LIGS signal beam arrives, meaning that it is then unable to respond to the signal.

2. Space charge build up at the last few dynodes which leads to electrons being repelled from the dynodes and therefore reducing the gain of the PMT.

Many potential applications for the PILOT system involve the presence of scattering particles in the measurement region[21]. This section details an experiment that was conducted to characterise the response of the research group's typical PMT module[22] to a LIGS signal generated in a scattering environment. Three alternative detectors were also tested to see whether they might offer a better performance in such environments.

6.4.2.1 Experimental setup

The main considerations in choosing the alternative detectors were their suitability for a LIGS experiment (rise time, sensitivity and gain), cost and availability. With these factors in mind, the three alternative detectors chosen were:

1. **Amplified photodetector** - Si amplified photodetector from Menlo Systems (model number FPD610-FS-VIS). The detector was a PIN diode (i.e. a diode that consists of an undoped 'intrinsic' semiconductor region sandwiched by n-type and p-type semiconductor regions) with a reverse bias voltage applied across it. When photons are incident on the 'intrinsic' region, electron-hole pairs are formed which then travel under the influence of the reverse bias voltage to produce an electric signal. This signal is then amplified.

2. **Avalanche photodetector** - High-speed avalanche photodetector from Menlo Systems (model number APD210). This detector is also based on a PIN diode. However, the reverse bias voltage is extremely high which causes the free electrons (created by the incident photons) to be accelerated through the 'intrinsic' region resulting in collisions that 'free' more electrons. This process, known as avalanche breakdown, results in an internally amplified electrical signal.

3. **Gated PMT** - Time-gated photomultiplier module from Hamamatsu (model number H11526-20-NF). This is just like the typical PMT, but with the voltage to the dynodes normally 'switched off' to achieve a very low gain (quantified as a high extinction

[21] Due to the coherence of the signal beam, compared to the incoherence of the scatter, the amount of scattered light incident on the detector can be limited by maximising the signal beam path and using irises. However, this is not enough for highly scattering environments.
[22] The PMT module used was the H10721-20 model from Hamamatsu.

ratio). A gating circuit allows the user to 'switch on' the gain for the PMT for a specified period of time, meaning that the gain of the detector can be high for the duration of the LIGS signal only.

In order to test the response of each detector to a scattering environment, the experimental setup shown in Figure 6.21 was used.

The default PILOT geometry (750 mm crossing lens, 3° crossing angle for the pump beams) was employed. The signal tracing beam, emitted by the DPSS Laser module described in Section 6.2.1, was used to simulate continuous wave scatter incident on the detectors. The intensity of the beam was varied by placing different neutral density filters in front of the beam within the PILOT system. The attenuation provided by each filter was characterised before the experiment. Removable mirrors were used to change which detector the signal (and signal tracing beam) were incident on. To change between the two PMT modules, the optical fibre was coupled accordingly. A four-channel oscilloscope[23] was used to record the signals from each detector.

The PMT and avalanche photodiode detectors had variable gains which were set to the middle of their range. The gated PMT also had a variable gain, and this was set to match that of the PMT. The amplified photodiode had a fixed gain.

[23]Wavesurfer 3074 model from Teledyne LeCroy.

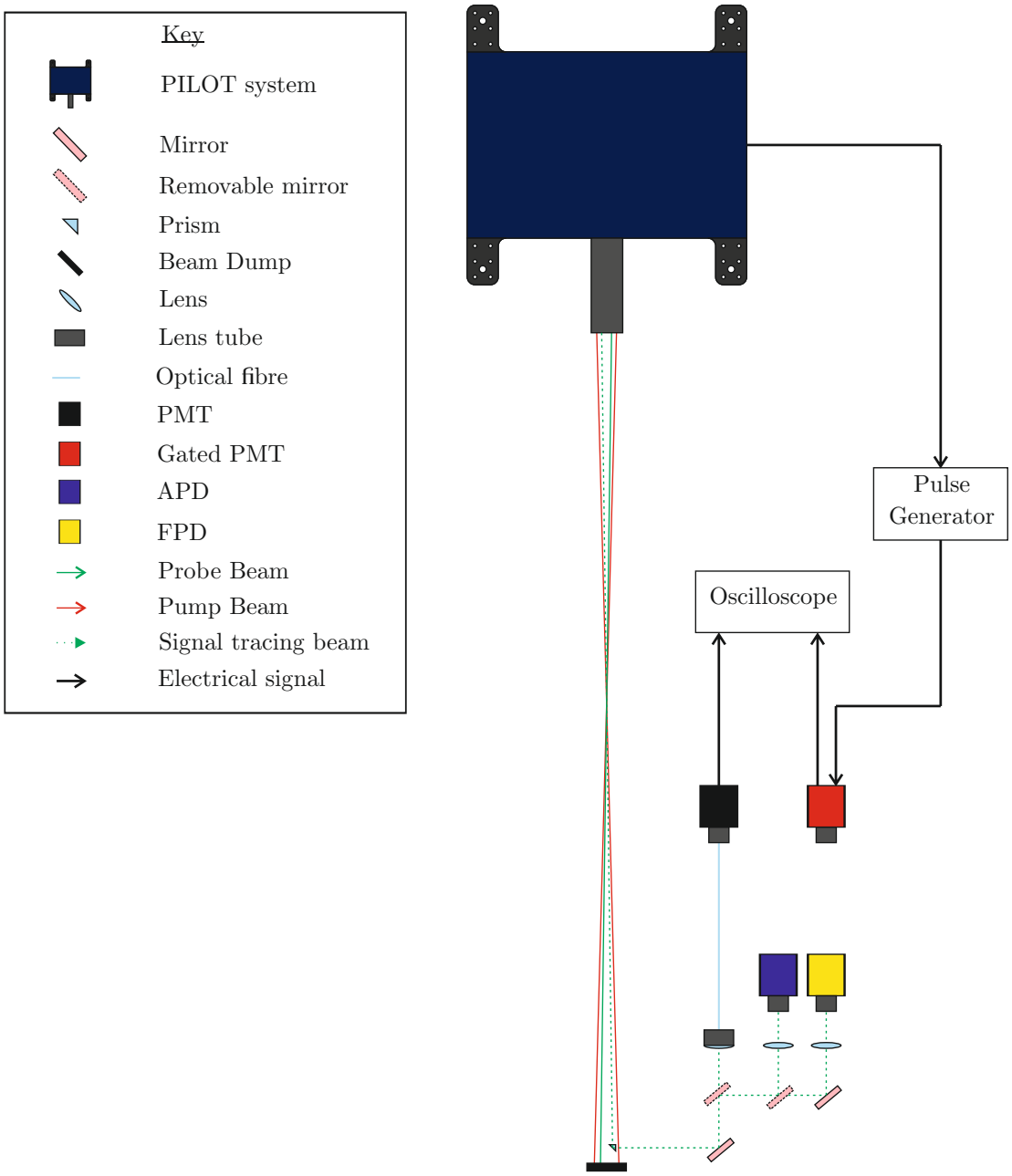


Figure 6.21: Plan view of the experimental setup used to characterise the effect of scatter on different detectors. Note that the APD and FPD detectors refer to the avalanche and amplified photodetectors respectively.

6.4.2.2 Results

Due to practical constraints, the PMT was first compared to the avalanche and amplified photodetectors. The comparison experiment between the PMT and the gated PMT was performed at a later date, after re-aligning the entire system.

First, the detectors were set up as shown in Figure 6.21 and the PILOT system was run to check that a LIGS signal could be captured by all three detectors. The system was run at 400 Hz over 0.25 seconds, and the average signal captured by each detector over this period is shown in Figure 6.22. The results show that the PMT offers the best signal-to-noise ratio of all three detectors, while the avalanche photodiode offers the worst ratio due to its low peak signal intensity. The avalanche photodiode also displays an undershoot where the minimum signal strength falls below the baseline. However this does not affect the frequency of oscillations from which the temperature is derived, and so the detector is still suitable for LIGS temperature measurements. The average signal for the gated PMT is not displayed here because it is identical to that of the standard PMT.

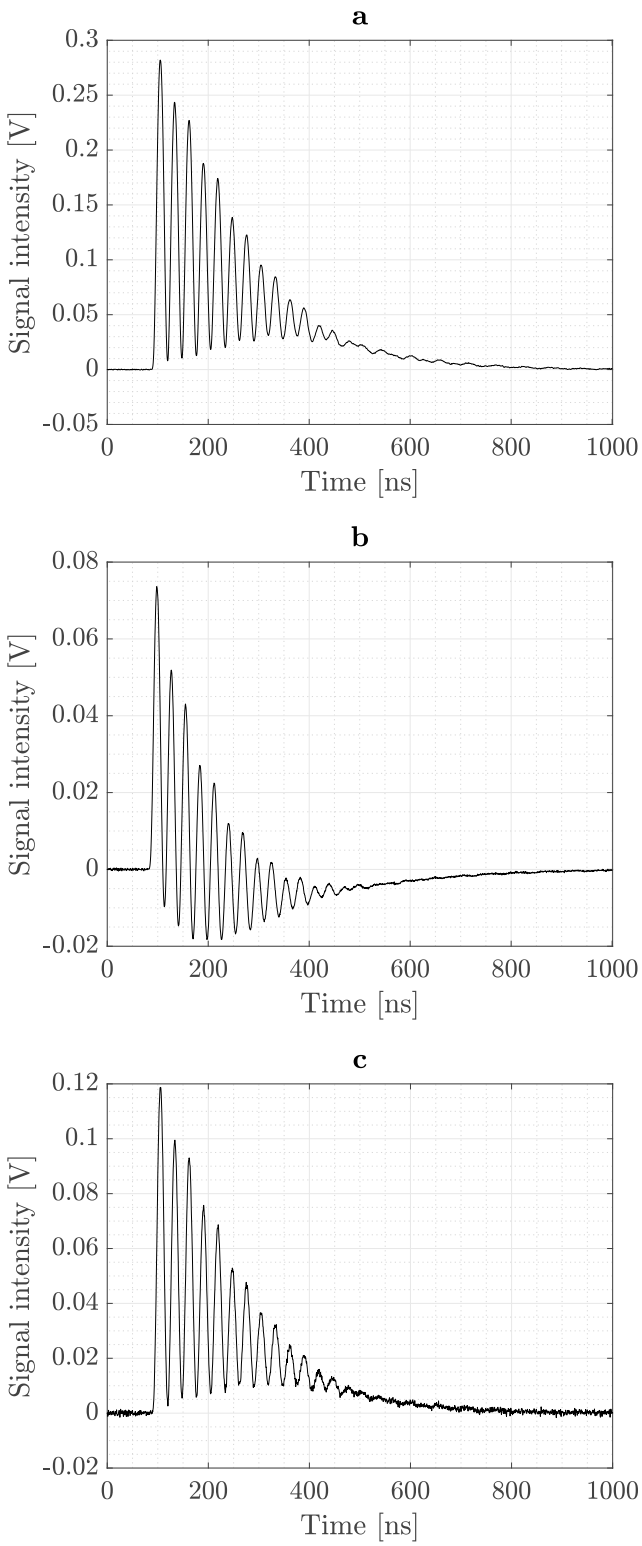


Figure 6.22: Mean LIEGS signal captured by each detector over 100 shots. Signals **a**, **b** and **c** were captured by the standard PMT, avalanche photodiode and amplified photodiode respectively. Each signal was post-processed to remove any zero offset.

Next, data was collected by each detector for a range of different simulated scatter powers (i.e. different values of neutral density placed in front of the signal tracing beam) at 400 Hz for 0.25 seconds. Figure 6.23 displays the results for the PMT. Although the maximum optical power was measured to be 0.7 mW, the results are displayed as a function of *relative* background optical power because the alignment of the beams meant that some of the signal tracer beam may not have been incident on the detector face. Figure 6.23 shows that the mean signal strength (defined as the relative peak intensity of the captured LIGS signal) decreases rapidly as background optical power is increased. As expected, this correlates with a loss of accuracy and precision in the derived frequency of oscillations in the signal.

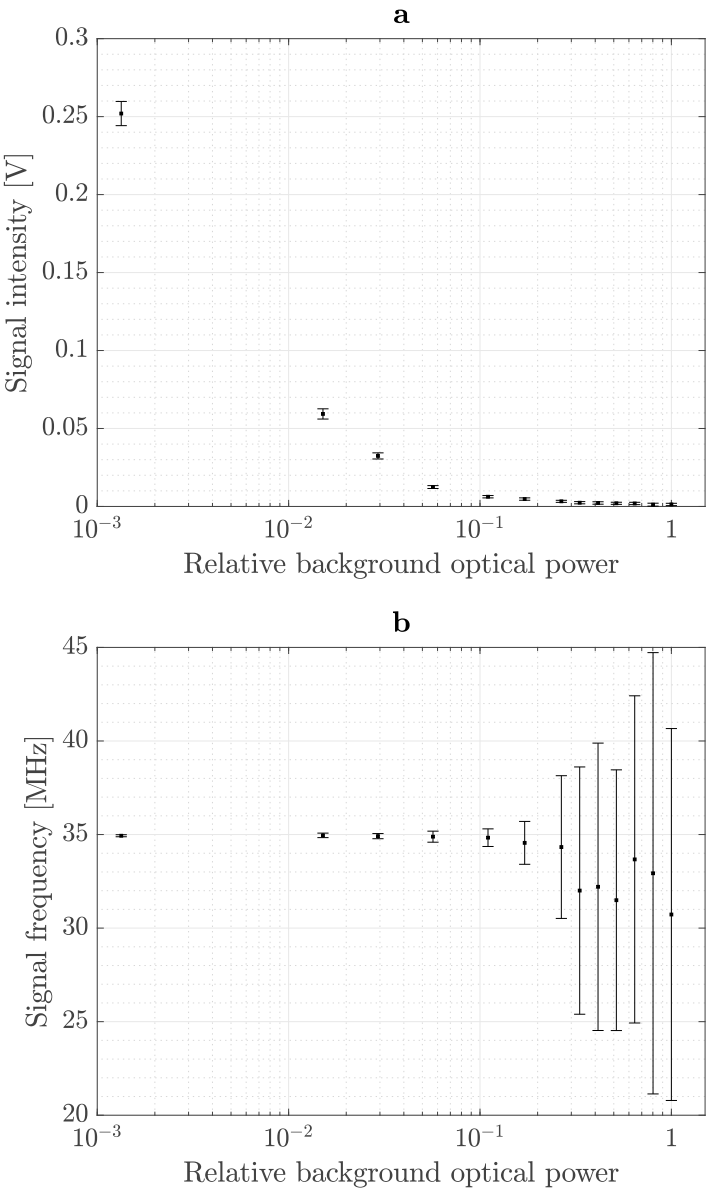


Figure 6.23: Variation in mean LIGS signal strength and mean calculated frequency for signals collected by the PMT as background optical power was increased. The error bars signify one standard deviation of the data from the mean.

Figure 6.24 shows the results for signals captured by the avalanche photodiode. The mean signal strength decreases as the background optical power is increased in a similar way to the PMT, albeit at a slower rate. However, even at the maximum incident background optical power, an accurate frequency of oscillations was obtainable from the the signals. As expected, there was a loss in the single shot precision of the frequency as the signal strength decreased.

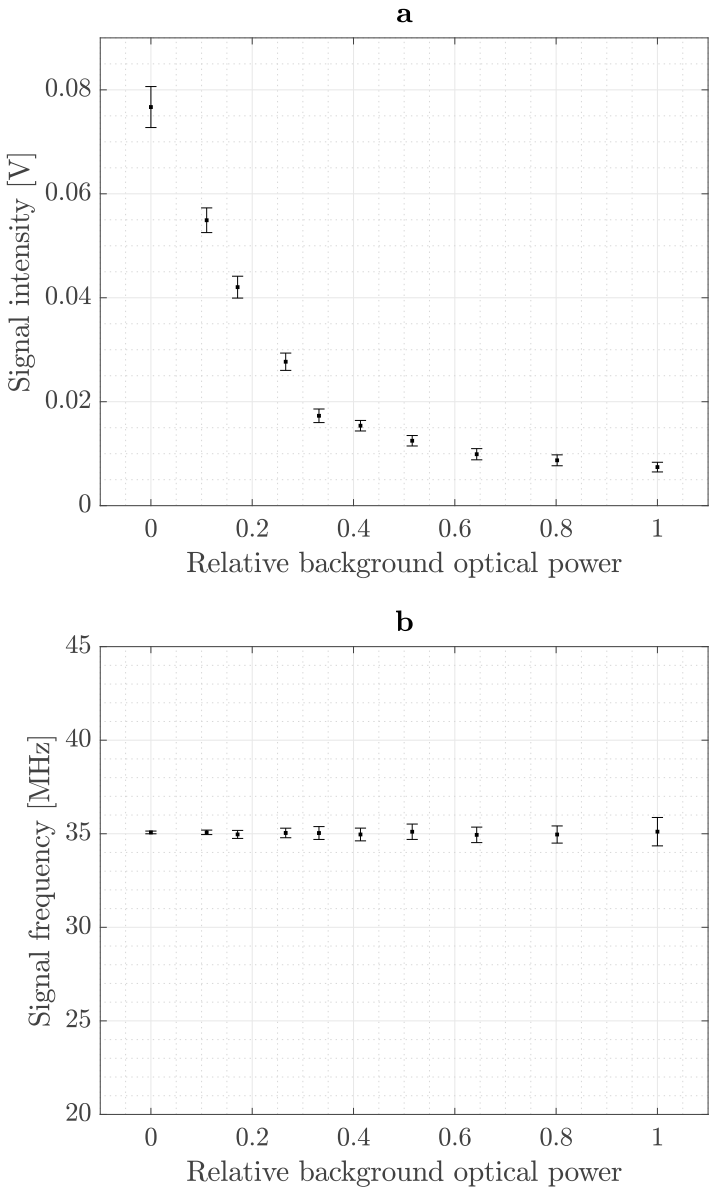


Figure 6.24: Variation in mean LIGS signal strength and mean calculated frequency for signals collected by the avalanche photodiode as background optical power was increased. The error bars signify one standard deviation of the data from the mean.

Figure 6.25 shows the results for signals captured by the amplified photodiode. Unlike the other two detectors, the mean signal strength remains fairly constant at first as the background optical power is increased. During this regime, the derived frequency of oscillations also shows good accuracy and precision. However, above a threshold of relative background optical power of 0.8 the signal strength does diminish rapidly and the accuracy and precision of the derived frequency of oscillations deteriorates accordingly. A closer look at the signals shows that as the background optical power was increased, the baseline of the LIGS signals also increased. Figure 6.26 displays this observation. A linear fit has been applied to the first 8 data points, and shows that the final data point deviates from this trend. This can be attributed to the detector being saturated by the background optical power at this stage.

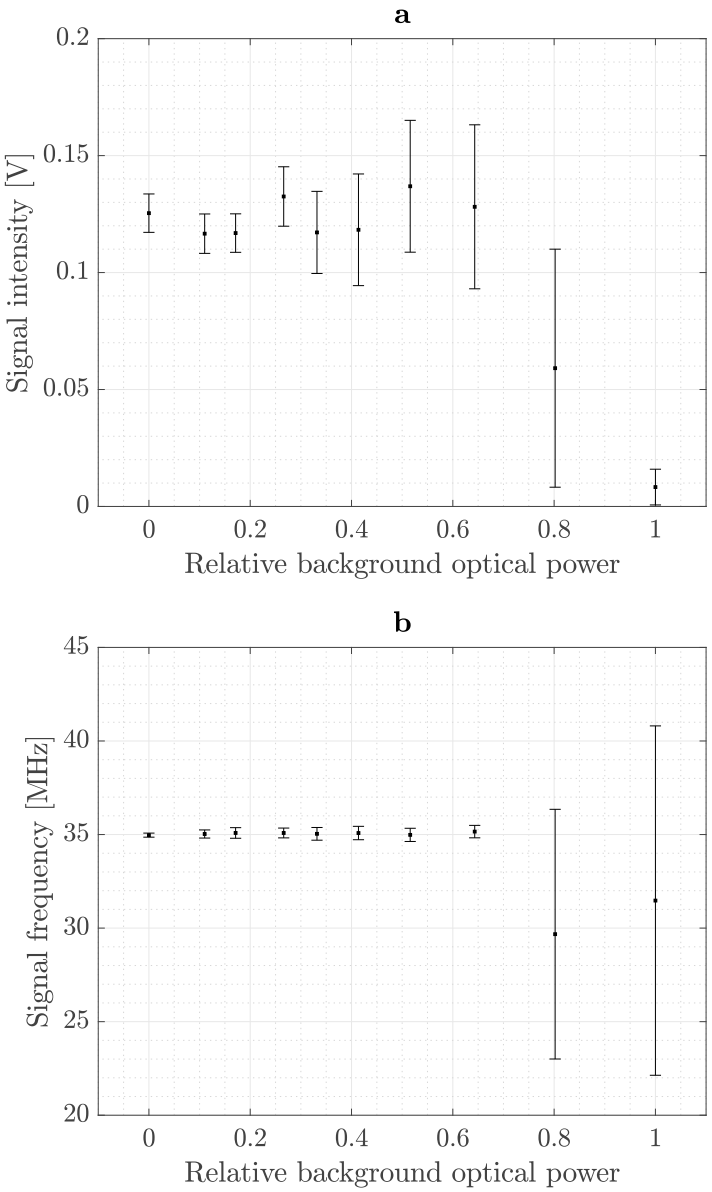


Figure 6.25: Variation in mean LIGS signal strength and mean calculated frequency for signals collected by the amplified photodiode as background optical power was increased. The error bars signify one standard deviation of the data from the mean.

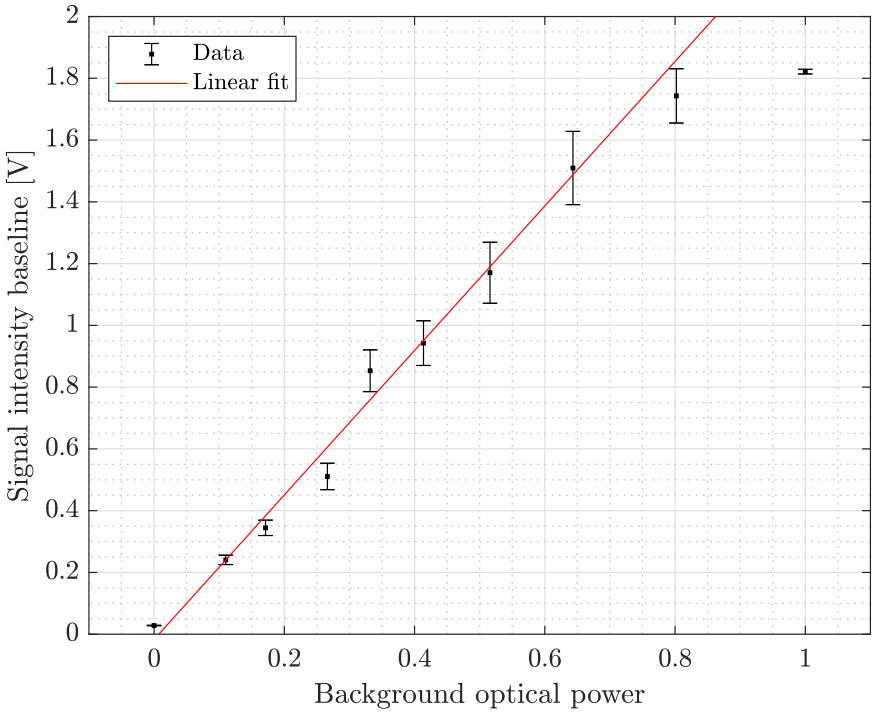


Figure 6.26: Variation in mean LIGS signal baseline for signals collected by the amplified photodiode as background optical power was increased. The error bars signify one standard deviation of the data from the mean. A least-squares linear fit has been applied to the first 8 data points.

Finally, a comparison was also made between the standard PMT and the gated PMT. The gate width was set to 1.2 µs so that it captured the entire LIGS signal. Figure 6.27 shows the results. The gain in the gated PMT had been set to give the same signal strength as the standard PMT when there was no background optical power. The results therefore show that the gated PMT retained a strong signal for a longer time than the standard PMT. However, it then quickly deteriorated in a similar fashion to that of the standard PMT. For both detectors, the accuracy and precision of the derived frequency of oscillations became unusable above a relative background optical power of about 0.1.

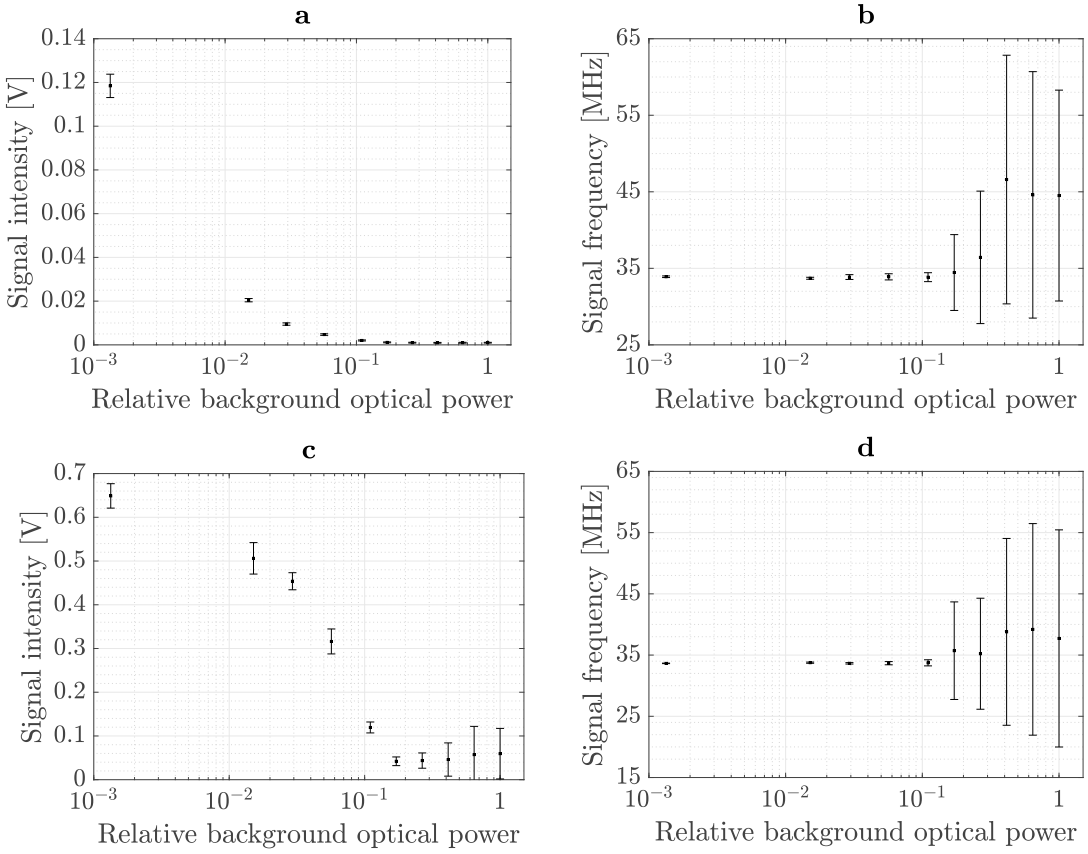


Figure 6.27: Variation in LIGS signal strength (Figures **a** and **c**) and calculated frequency (Figures **b** and **d**) for signals collected by the standard PMT (Figures **a** and **b**) and gated PMT (Figures **c** and **d**) as background optical power was increased. The error bars signify one standard deviation of the data from the mean.

6.4.2.3 Discussion

This section detailed an experiment that was carried out to see how the performance of three alternative detectors would compare to a typical photomultiplier module capturing LIGS signals in scattering environments. A scattering environment was simulated by using a continuous wave beam directed at the detectors with varying power.

At very low background optical powers, the standard and gated photomultiplier tubes outperformed the amplified and avalanche photodiodes by providing much stronger LIGS signals. However, the performance of both quickly deteriorated as the background optical power was increased. The gated PMT performed better than the standard PMT while both were still able to pick up a LIGS signal, but both lost this ability at similar background optical powers. The better initial performance can be attributed to the gated PMT reducing

the build-up of space charge (as described at the beginning of Section 6.4.2) when the gate is not 'on'. However, the decrease in signal strength at higher background optical powers is due to photocathode bleaching, which continues to occur even when the gate is 'off', hence why it didn't offer an increase in performance at these levels.

The amplified photodiode displayed a marked improvement in performance at higher background optical powers when compared to the standard PMT. Its performance deteriorated at a background optical power that was about 5 times higher than the PMT. Furthermore, it showed a linear increase in the signal baseline level up until this point, which could be useful to quantify the amount of scatter present in a given application. The deviation of the baseline response of the detector from a linear trend coincided with the background optical power at which it was unable to capture the LIGS signals, which suggests that saturation effects are the limiting factor.

Finally, the avalanche photodiode showed the best performance of all the detectors. Even at the maximum background optical power, it was still able to capture the LIGS signal. However, the signal shape is different to that of the other detectors. Although this didn't affect the oscillation frequency that is required for a temperature measurement, it would need to be investigated further if attempting to derive other gas properties (such as pressure) from the signal.

6.4.3 Characterising different gases for use with LIEGS

As explained in Section 2.1, the primary advantage of using the electrostrictive LIGS technique compared to thermal LIGS is the 'tracer-free' characteristic. The LIEGS technique relies on the ability of the large electric field generated by the pump beams to polarise whichever gas is present in the measurement region. The polarised molecules are then subject to an electrostrictive force, which results in the release of acoustic waves across the region and the subsequent formation of an oscillating density grating. From this description, it follows that the polarisability of a gas (i.e. its tendency to acquire an electric dipole moment when subjected to an external electric field) will play a part in the strength of the resultant grating. The molecular mass of the gas will also affect the strength of the grating as a larger electrostrictive force will be required to move a heavier polarised molecule.

This section presents an experiment that was conducted to explore the effect of the polarisability and molecular mass of a gas on the strength of a LIEGS grating.

6.4.3.1 Experimental setup

A standard LIGS arrangement, employing the default PILOT geometry (750 mm crossing lens, 3° crossing angle for the pump beams), was used as shown in Figure 6.28[24]. A gas cell with optical access on either side was placed in the beam paths such that the crossing region was contained within the cell. This cell could then be filled with different gases, each with their own characteristic polarisability and molecular mass, at atmospheric pressure. The PILOT system was then run to collect LIGS signals for each gas.

The gases chosen for this experiment are listed in Table 6.1. They were chosen due to their variation in polarisability and molecular mass, as well as ease of access.

Gas	**Polarisability** [$\mathbf{Å^3}$]	**Molecular mass** [**g/mol**]
Nitrogen	1.710	28.0
Oxygen	1.562	32.0
Argon	1.664	39.9
Carbon dioxide	2.507	44.0
Krypton	2.498	83.8
Methane	2.448	16.0
Sulphur hexafluoride	4.490	146.1

Table 6.1: Polarisability [120] and molecular masses [121] for the gases characterised using the PILOT system.

[24] A Wavesurfer 3074 oscilloscope from Teledyne LeCroy and a H10721-20 PMT module from Hamamatsu were used.

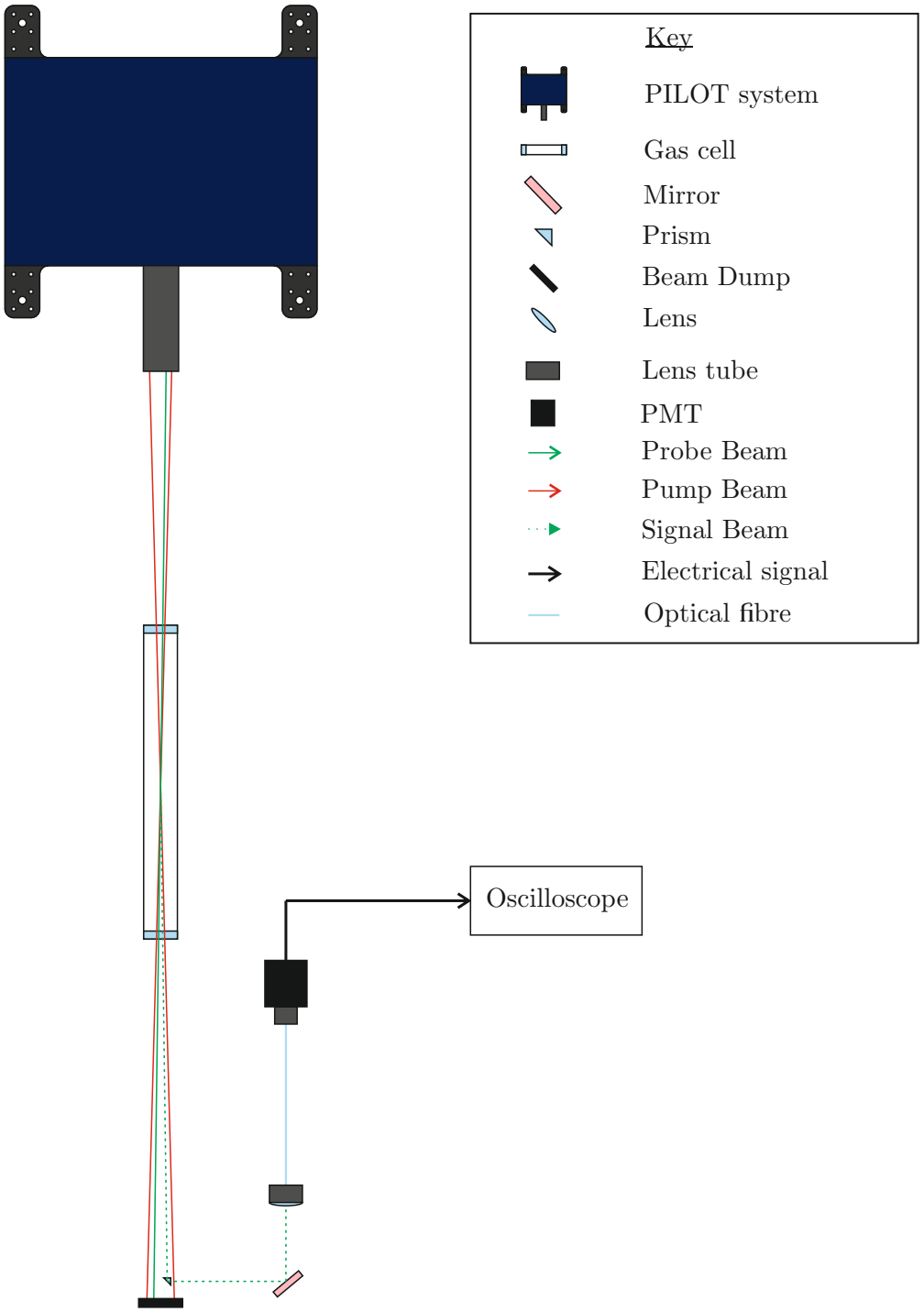


Figure 6.28: Plan view of the experimental setup to characterise the suitability of different gases for LIEGS.

6.4.3.2 Results

For these experiments, the PILOT system was run at 10 Hz and data was acquired for 10 seconds. Figures 6.29**a** and **b** show the data collected. Three sets of data were acquired for each gas, and the results presented show the mean over all three. Since the experiments were run over a number days, three calibration data sets were taken each day (in air at atmospheric pressure) so that variations in signal intensity due to optical misalignment and environmental changes could be accounted for when comparing the signals for different gases. To ensure that the intensity of the LITGS signals collected for each gas were within the linear regime of the photomultiplier tube, the power of the probe laser was raised or lowered as required. The results shown in 6.29**a** and **b** have therefore been corrected for changes in the experimental setup over time and also for the different powers used in the probe beam. The data in Figure 6.29**b** supports the theory that gases with a higher polarisability will form a stronger LIEGS grating resulting in an increased signal intensity. For gases with a similar polarisability (for example methane, carbon dioxide and krypton), Figure 6.29**a** shows that a larger molecular mass would result in a decreased LIEGS signal intensity. The molecular mass and polarisability values for air were calculated to be the weighted mean of nitrogen and oxygen (in an 80:20 ratio). The comparison with argon (which has a similar polarisability) in Figures 6.29**a** and **b** shows that air follows the same trend as seen for the other gases. This suggests that calculating the molecular mass and polarisability of a gas mixture as a weighted mean of its constituents (based on molar composition) is valid.

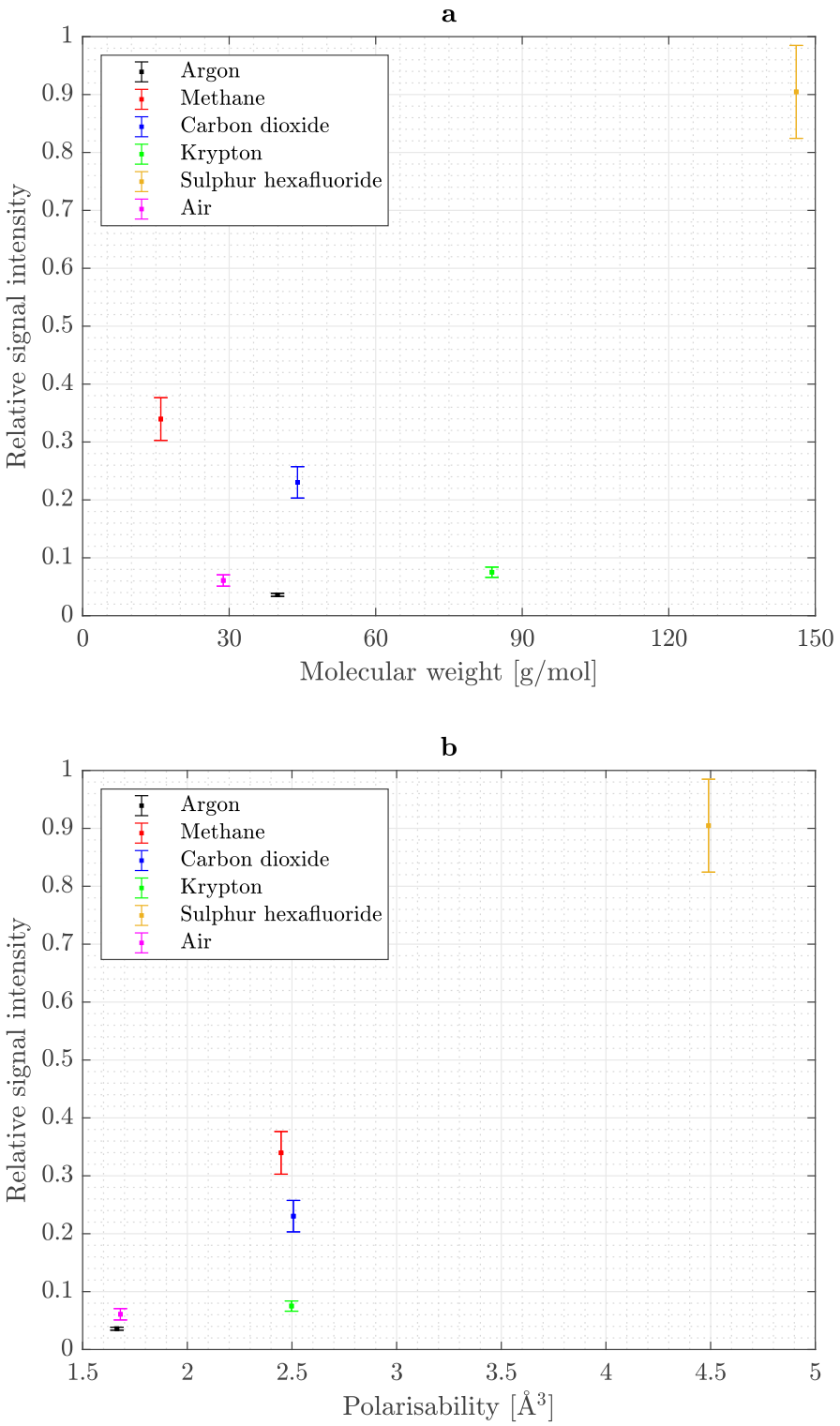


Figure 6.29: Mean peak LIGS signal intensities in different gases. The results have been corrected for changes over time and probe power. The error bars signify one standard deviation from the mean of the data.

The data was further analysed to characterise the relative importance of polarisability and molecular mass to the expected strength of a LIEGS signal. Using a simple least-squares fitting function, the relationship between signal strength (I_{signal}), polarisability (P) and molecular mass (M) was found to be

$$I_{\text{signal}} \propto \frac{P^{3.4}}{M} \tag{6.4}$$

Figure 6.30 shows the experimental data in relation to the applied fit. The R-squared value for the goodness of fit was 99 %.

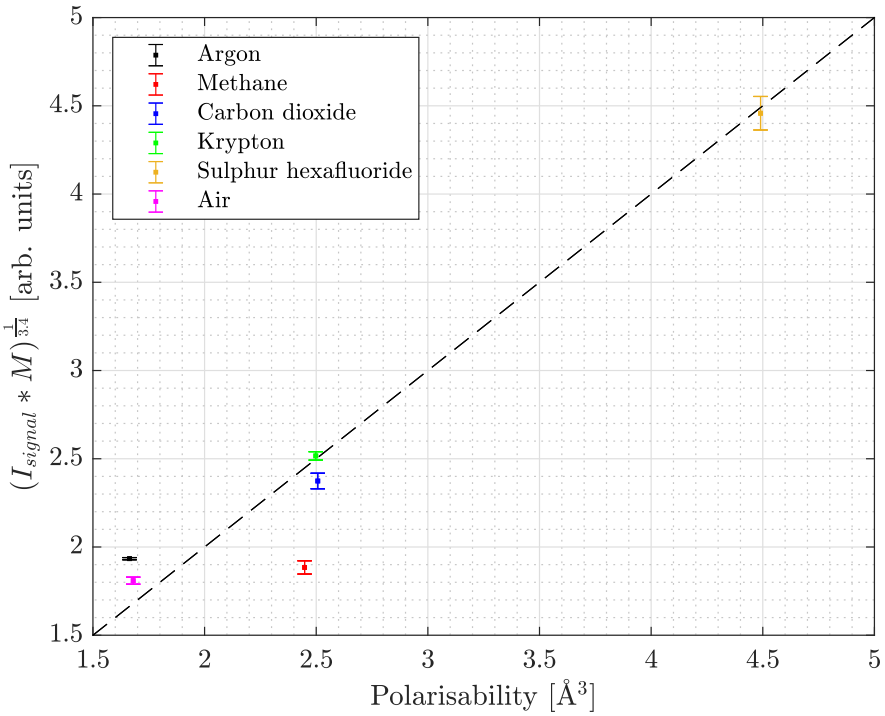


Figure 6.30: Graph showing the relationship between signal strength (I_{signal}), polarisability (P) and molecular mass (M) as shown by Equation 6.4. The dashed line shows an equal fit.

The results show that, as expected, the LIEGS signal intensity is maximised in gases with a high polarisability and low molecular mass. However, the polarisability of the gas has a much more significant impact on signal intensity than the molecular mass. This could be due to the high pulse energies in the pump beams, which mean that there is a large electrostrictive force available to move the gas molecules (and hence the mass of the

molecules is *relatively* unimportant). Instead, the limiting factor becomes the ability of the pump beams to polarise the molecules in the first place, hence the larger dependence on the polarisability of the gas.

6.5 Applying PILOT in research facilities

The primary objective for this work was to design, build and characterise a portable LIGS system that could be easily deployed to measure gas properties in a range of different applications. This section shows how the system was successfully used in a research setting, and briefly discusses some future applications.

6.5.1 Imperial College London wind tunnel

The PILOT system was deployed for tracer-free temperature measurements in the '10 x 5' wind tunnel, which is owned and operated by the Department of Aeronautics at Imperial College London. The study was undertaken as part of a larger research project investigating the use and development of so-called 'transpiration cooling' (where a cool gas is passed through a porous wall to manage heat flux into the wall) for applications in hypersonics and gas turbines. The wind tunnel was fitted with an 'effusion plate' through which gas at a sub-atmospheric temperature was delivered into the main air flow. This simulated the previously mentioned transpiration cooling applications but operated at length and time scales more amenable to investigation. The geometry was also better suited to CFD modelling enabling validation of the latter.

Particle Image Velocimetry (PIV) measurements had already been used to quantify the momentum transfer properties of the boundary layer near the effusion plate [122]. PILOT was required to learn more about the cooling film and thermal boundary layer produced by the effusion panel, without using thermocouples that would otherwise perturb the flow. The frequency associated with the large scale motion of the flow was modelled to be about 50 Hz, which further necessitated the use of PILOT (capable of measurements at 400 Hz).

6.5.1.1 Experimental setup

The PILOT system was fitted with a 0.75 m focal length crossing lens, meaning that the measurement point was located <0.75 m away from the output face of the system. In order to collect the signal beam before it became overly divergent, the detection optics could be situated up to 1.5 m behind the measurement point. Since the wind tunnel was 3m wide, both the PILOT system and the detection optics would need to be mounted within the tunnel. However, a practical requirement was to minimise the presence of bluff bodies within the tunnel so that the flow wasn't affected. To account for this, a lens tube was installed at the output of the PILOT system (and the crossing lens was held at the end of the tube). This allowed the PILOT system to be mounted outside the tunnel, with only the lens tube protruding into the test section. The detection optics were integrated onto a rail for ease of mounting, and were positioned far enough away from the measurement point to not disturb the flow. Figure 6.31 shows the view from within the tunnel. During testing, fairings were constructed and added to the lens tube and detection rail to streamline them.

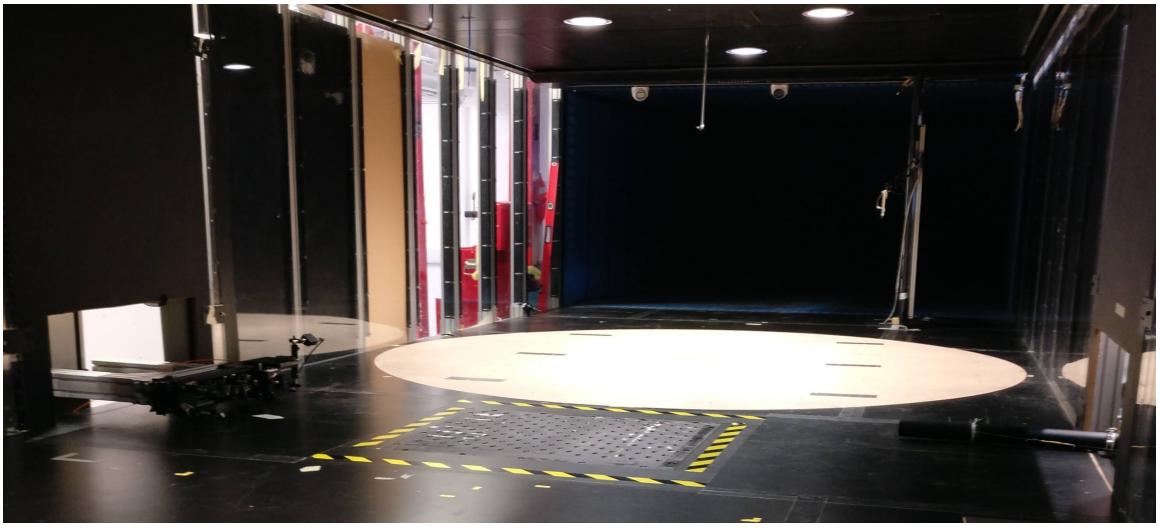


Figure 6.31: PILOT system at the wind tunnel facility in Imperial College London. The lens tube fitted to PILOT can be seen protruding into the wind tunnel from the right, while the detection optics, integrated onto a rail, are seen on the left. The effusion plate can also be seen on the floor of the tunnel within the yellow striped tape.

This application also necessitated the measurement point to be translated in all three directions within the wind tunnel. To achieve this, the PILOT system was mounted onto a 3-axis motorised translation stage as seen in Figure 6.32.

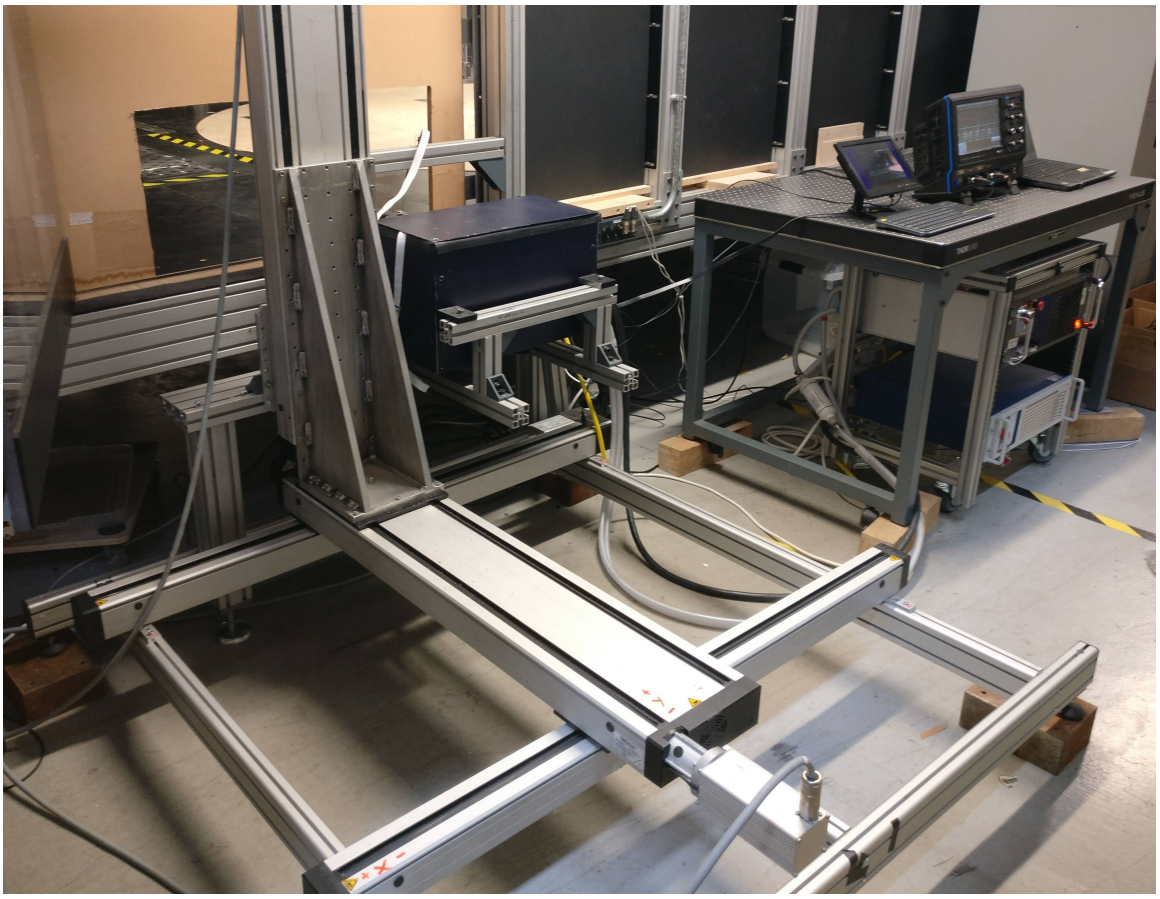


Figure 6.32: The PILOT system, in blue, can be seen mounted on a 3-axis motorised translation stage and pointing into the wind tunnel. The laser power supplies, mounted in the Co-PILOT trolley, are positioned under the optical table in the background. The oscilloscope and laptop required to control the system are positioned on the optical table.

The detection rail was also mounted on a 3-axis translation stage on the other side of the tunnel as shown in Figure 6.33.

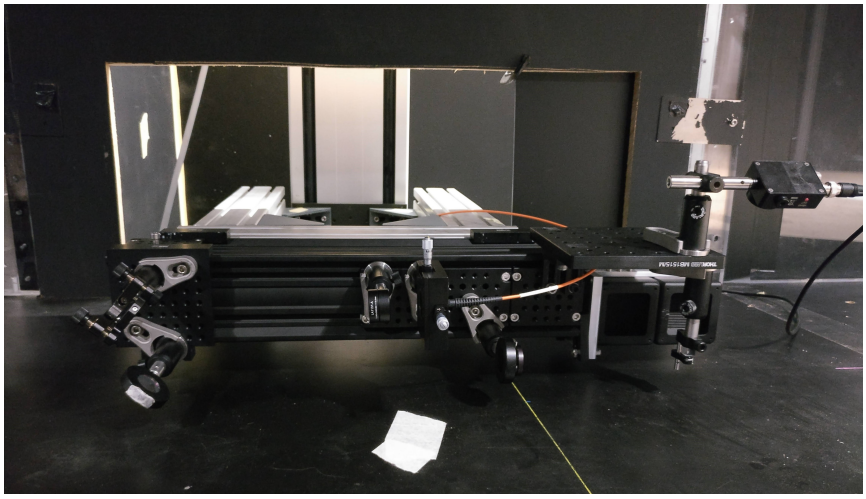


Figure 6.33: Detection optics for the PILOT system integrated onto a rail, which was mounted onto a 3-axis motorised translation stage (the stage is seen in the background of the photo).

A camera, connected to the Raspberry Pi computer that is built into the PILOT system, was installed onto the PILOT mounting frame. This allowed the user to monitor the system during operation. Due to the design of the system, the user is able to operate it entirely remotely through one computer. However, for this application where remote operation was not necessary, the system was controlled from a table next to the tunnel. Figure 6.34 shows the setup used.

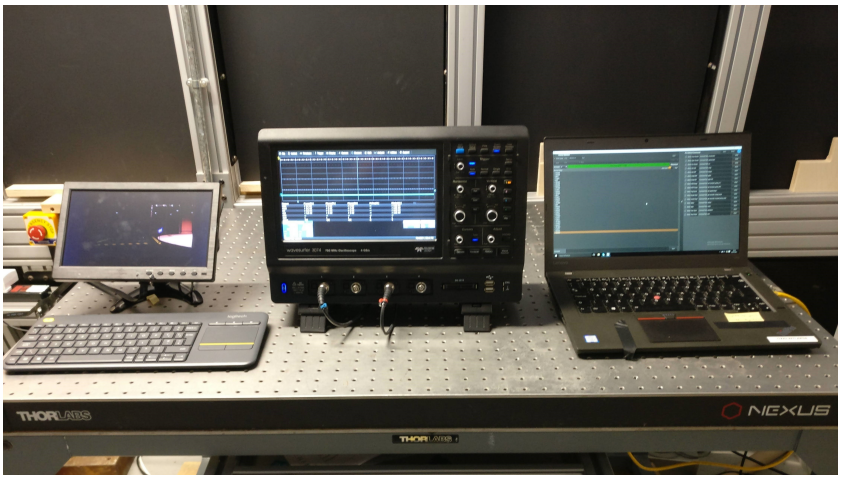


Figure 6.34: Control room for PILOT. On the left is a screen showing a live video feed of the tunnel as seen from the camera mounted on PILOT. In the centre is the oscilloscope used for data collection, and on the right is a laptop to control the lasers.

6.5.1.2 Results

The purpose of this section was to demonstrate the application of the PILOT system in a research facility, and as such a detailed analysis of the findings from the experiment are beyond the scope of this thesis. Instead, the successful application of the PILOT system is presented. The system was first internally aligned, and then run in the wind tunnel. Figure 6.35 shows the PILOT system during operation.

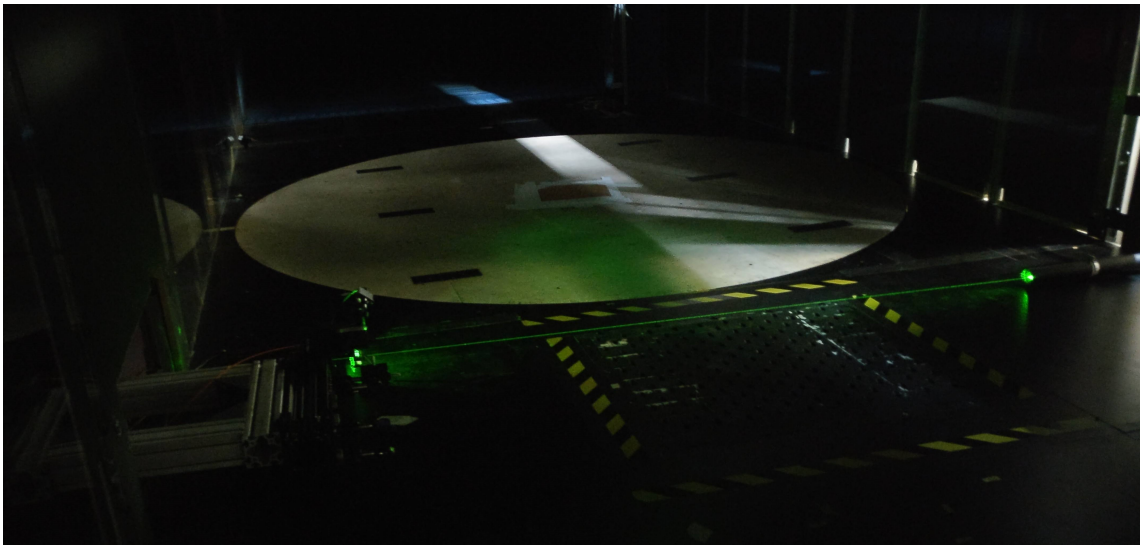


Figure 6.35: PILOT system during operation at the wind tunnel facility in Imperial College London. The lens tube from the system can be seen protruding into the wind tunnel from the right, while the detection optics, integrated onto a rail, are seen on the left. The green beam is the probe laser, which is visible due to Rayleigh scattering from the air. The effusion plate can also be seen on the floor of the tunnel within the yellow striped tape.

Data at each experimental position was collected at 400 Hz over 1 second. Figure 6.36 shows the mean normalised signal obtained at one position.

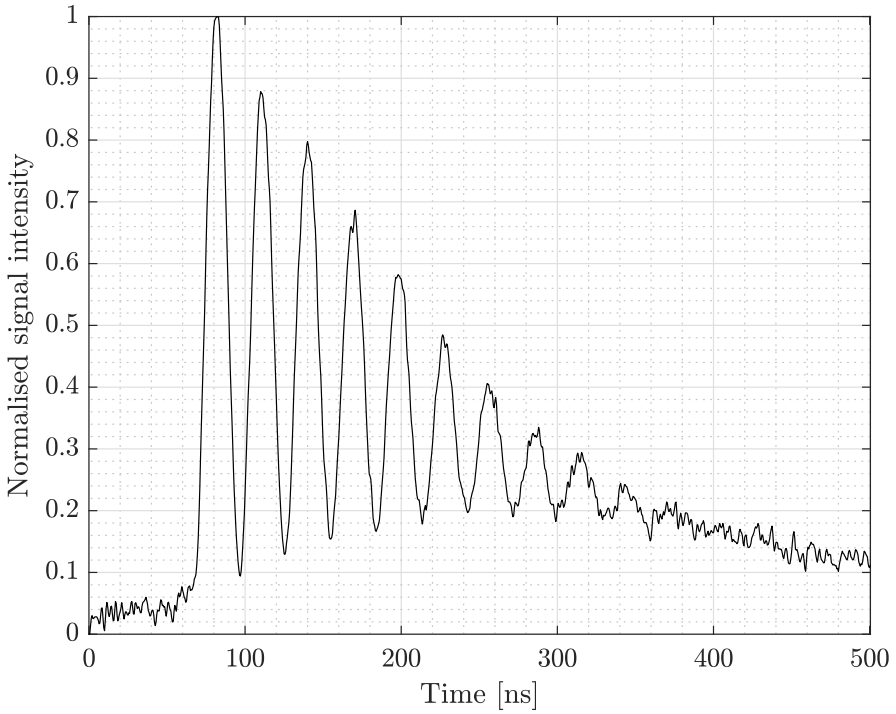


Figure 6.36: Mean LIEGS signal obtained over 400 shots from the PILOT system operating at 400 Hz in the wind tunnel facility at Imperial College London.

6.5.2 Future applications

A substantial advantage for the LIGS technique over similar optical diagnostic techniques, such as CARS, is that it is relatively inexpensive and robust. In order to capitalise on this, the PILOT system was designed to be easily used in a range of facilities and applications. This versatility also makes the system attractive for new applications where cost, space and optical expertise might have been barriers. To characterise performance in new applications, Section 6.4 also considered the use of the system in different environments. Two future applications that are immediately attractive based on this work are:

1. The characterisation of how the system could be used in applications which have optical access through windows, carried out in Section 6.4.1, opens up the potential use of the system in facilities such as the Gas Turbine Research Facility at Cardiff University [123]. Here, the use of LIGS to characterise combustion systems and validate

computational models is of high interest[25].

2. The use of LIGS in scattering environments, considered in Section 6.4.2, is particularly relevant to the characterisation of sprays where droplets are sources of scatter.

6.6 Summary

This chapter described the design and manufacture of a transportable system, known as PILOT, which is capable of obtaining tracer-free LIEGS measurements at a rate of 400 Hz. In addition to its mobility, a novel feature of the system is its capability for internal alignment, which greatly simplifies the application of LIGS in practical facilities. The system also includes a translation stage to adjust the length of the delay line, which allows the phase difference between both pump beams to be minimised. An experiment was carried out to quantify the effect of this adjustment, and the results showed that a misalignment of 3 mm would result in a 50 % decrease in signal intensity.

The PILOT system also includes the capability to scale the energy of the pump beams and power of the probe beam. An experiment was conducted to investigate the impact of both on the LIEGS signal intensity. As expected, it was found that the signal intensity scaled linearly with probe beam power, but displayed a quadratic growth with respect to pump beam energy.

The focused beam geometry employed by the PILOT system allows for the spatial resolution of the system to be minimised due to the small size of the beams at the measurement point. An experiment to characterise this resolution showed that the system is capable of an axial (along the grating) resolution of 11 mm and a transverse (across the grating) resolution of less than 0.9 mm.

LIEGS temperature measurements in room air, taken using the PILOT system at 400 Hz, were compared to measurements taken by two K-type thermocouples (with bead sizes of 1 mm and 0.65 mm). The results showed that PILOT is capable of an accuracy of 0.37 % and a single shot precision of ±0.7 %. The time constants for both thermocouples were characterised (by using a heat gun to provide a temperature difference), and it was cal-

[25] When running at high pressures, however, beam steering effects may be significant [17].

culated that an impractical bead size of less than 0.14 µm would be required for a K-type thermocouple to collect measurements at the same rate as the PILOT system (400 Hz).

The application of the system in different facilities and environments was also investigated. First, the damage thresholds of windows made of different materials and surface finishes was compared. It was found that fused silica and borosilicate windows had a higher damage threshold than sapphire. A higher quality surface finish was shown to increase the damage threshold of a window, while the application of an AR coating reduced it. A qualitative observation made during the experiment was that the presence of dust particles on/near the window surface was correlated to a lowered damage threshold. Therefore, in order to be able to use the PILOT system with a maximised pump beam energy (which, as stated earlier, has a large effect on the signal intensity), windows made of fused silica or borosilicate (with high quality surface finishes and no coatings) should be used.

The application of the system in scattering environments was also considered. It was found that although photomultiplier tubes (PMTs) are an excellent detector choice in non-scattering environments, their performance rapidly degrades with increasing background scatter. Amplified and avalanche photodectors both offer inferior sensitivity compared to PMTs in non-scattering environments, but show promise in scattering environments. The amplified photodetector showed an increase in its baseline signal level as the intensity of background scatter was increased, which could be exploited to characterise the amount of scatter present in an environment. However, the avalanche photodetector displayed the best capability at the maximum intensity of background light used for the experiment, and so this is the recommended detector for such applications.

The final investigation experiment characterised the relative intensity of the signal produced from LIEGS measurements in different gases. In particular, the correlation between the polarisability of a gas, its molecular weight and the signal intensity was explored. It was found that an increase in the polarisability of a gas resulted in a roughly cubic relative increase in signal intensity, while an increase in molecular mass resulted in a linear decrease in signal intensity. These findings can be used to predict the performance of the PILOT system in different gases, and inform gas selection when appropriate.

Finally, the practical application of the PILOT system in a research facility was demon-

strated. PILOT was used to collect non-invasive temperature measurements in a tracer-free air flow at Imperial College London's '10 x 5' wind tunnel facility. The high temporal resolution of the measurements (collected at 400 Hz) was important to characterise the flow field, and the portability of the system allowed it to be mounted on translation stages and collect measurements at different points of interest.

7 Conclusions

This chapter summarises the work presented in this thesis, and draws conclusions from the findings.

7.1 Temporally-Resolved Biacetyl LITGS

This work discovered a new LITGS tracer species highly suited to high repetition rate measurements and demonstrated its application in the study of thermoacoustic instability.

The use of biacetyl as an absorbing species for LITGS (using the third harmonic of a Nd:YAG laser at 355 nm), referred to as 'biacetyl LITGS', has been demonstrated for the first time. This enables the practical use of accessible high-repetition rate lasers to obtain LITGS measurements with a high temporal resolution. As biacetyl is already a commonly used tracer species for other optical diagnostic techniques, these findings also permit the use of LITGS alongside other techniques for practical applications.

First, the presence of biacetyl vapour in trace quantities was shown to have a negligible effect on gas temperature due to 'beam heating', which enables its use as a tracer for accurate temperature measurements. Characterisation experiments, conducted using a steady jet, showed that the variation in gas composition due to the presence of biacetyl vapour did have an impact on the measured LITGS signal frequency. Therefore, the concentration of biacetyl vapour in the gas needs to be quantified for accurate LITGS measurements. LITGS temperature measurements taken in the jet, as it was heated, showed a good correlation with temperature measurements obtained using a thermocouple. Isothermal measurements of the speed of sound (derived from the LITGS signal frequencies), taken in different bulk gases, were shown to agree well with theoretical predictions. These variations in signal frequency for different gases enabled the evaluation of species concentration. This was demonstrated by obtaining LITGS concentration measurements, at a temporal resolution of 1 kHz, of argon, carbon dioxide and helium when pulses of each gas were introduced into the bulk flow of the jet.

The biacetyl LITGS technique was then applied to the Cambridge University Engineer-

ing Department's 'Entropy Generator'. It was used to characterise the passage of entropy spots (packets of heated air) and composition spots (packets of a different gas) along a duct. Measurements were taken at 5 different positions along the duct, and collected at 500 Hz. The LITGS temperature measurements of the passage of the entropy spots showed a good correlation with data collected previously using thermocouples. The results from the experiment using composition spots revealed the effects of dispersion as the packets of gas travelled along the duct, and showed this to be more pronounced with lighter gases.

7.2 Axially-Resolved LIGS

The work presented in Chapters 4 and 5 introduced, modelled and experimentally-validated a novel method to obtain simultaneous spatially-resolved LIGS measurements in the axial direction. This work is the first time axially-resolved LIGS has been reported. It is also the first time that 1-D LIGS along the axial direction has been demonstrated. Significantly, the only change in this novel approach, compared to a usual LIGS experiment, is a variation in the detection optics which means that the technique retains its key advantage of accessibility thanks to its relatively low cost and complexity.

The technique of 'axially-resolved LIGS' is based on the concept of dividing the LIGS signal beam into 'sub-signals' which originate from discrete regions along the axial axis of the grating, and then imaging each sub-signal onto an individual detector. The application of concepts from Scheimpflug imaging was discussed, and a computational model was developed to simulate the technique. A method to experimentally validate the model and practically characterise an experimental LIGS setup was devised, and the capability to simulate the results of the characterisation experiments (which would allow for comparison and validation) was incorporated into the model. The model also accounted for variations in scattering efficiency, due to differences in the fringe spacing along the grating, by assuming the LITGS grating to behave as a diffraction grating. Two important variables were introduced to describe the spatial resolution of an experiment employing this technique. The 'grating length per fibre' (L_{gf}) is a measure of the length of the grating that each optical fibre (and therefore each detector) receives a LIGS signal from. This is therefore a measure

of the inherent spatial resolution of each measurement collected using the technique. The 'grating pitch' (P_g) is the distance along the grating between the centres of the regions captured by two consecutive fibres. P_g is only relevant when using a linear array of optical fibres to simultaneously collect measurements along a line.

A parametric investigation of the technique to optimise L_{gf} was conducted using the model. This was required because practical limitations meant that an ideal Scheimpflug imaging setup could not be used for LIGS measurements. The results of this study showed that the distance between the grating and the imaging lens should be minimised to achieve the best spatial resolution. The tilt of the detector plane should also be as similar as practically possible to the tilt of the image plane (determined by the imaging setup). Finally, tilting the imaging lens would be beneficial to the achievable spatial resolution of the system; however this was shown to only be applicable if using a lens with a low curvature of field which is not the case for simple lenses.

The first two experiments to validate the model compared the predicted signal beam size and magnification (at the centre of the grating), produced from a jet, with experimental measurements. Both experimental results showed excellent agreement with the model, and so two characterisation experiments were conducted to validate the model over the length of the grating. The experiments would also allow the spatial resolution, in terms of L_{gf} and P_g, to be experimentally characterised. Both experiments were run in the same way, with the only difference being the core size of the optical fibres used to collect the LITGS signals (1 mm for the first experiment, compared to 400 µm for the second one). The results of both experiments were in good agreement with simulated results produced by the model, which validates it as a valuable tool to inform the future design of experiments to use the technique in practical applications. It was also found that using smaller optical fibres improved the spatial resolution of the technique. With the small fibres, the mean L_{gf} (a linear array of three fibres was used) for the setup was found to be 9.0 mm while the mean P_g was 3 mm.

Finally, two experiments were conducted to obtain LITGS temperature measurements using the same experimental setup. First a heated jet, constant in temperature, was flanked on either side (in the axial direction) by jets at ambient temperature. The spacing between each jet was 3 mm, which was equal to the previously measured P_g of the setup. Because the

L_{gf} of the setup was larger than P_g, the effect of 'crosstalk' was considered. This arose from the overlap in the regions along the grating that each optical fibre received a signal from; in the reported experiment, it meant that one outer optical fibre received a signal contribution from the central (heated) jet. Once this was accounted for, the LITGS temperature measurements demonstrated an excellent correlation with thermocouple measurements. These findings showed that the central optical fibre was able to achieve a spatial resolution of 6 mm despite an L_{gf} of 9 mm. This suggests that the definition of L_{gf} for a fibre as being the region from which 87 % of the its signal originated is conservative. The results also demonstrated that despite the inherent spatial resolution of each fibre being defined by L_{gf}, temperature variations on smaller scales may be resolved by using a linear array of fibres with a smaller value of P_g. However, the method still needs to be validated for applications where there are steep temperature gradients present and the spatial resolution of each fibre is not small enough to assume a single temperature for each signal.

For the second experiment, single-shot LITGS measurements were obtained at a rate of 10 Hz as the temperature of the central jet was increased from ambient to 54 °C. The results showed a good fit with thermocouple measurements, and demonstrated the successful application of the technique to simultaneously collect 3 spatially-resolved temperatures. The axial resolution of the measurements was 6 mm, compared to the a standard LITGS setup which would have collected one temperature measurement over the entire length of the grating (43 mm for this setup). This amounts to an 86 % improvement in spatial resolution as well as a three-fold increase in the number of single-shot measurements obtained.

7.3 Development of PILOT system

The design, manufacture, characterisation and application of a unique transportable LIGS system (PILOT) was presented in Chapter 6. The system is capable of collecting tracer-free LIGS measurements at a rate of 400 Hz. In addition to its mobility, it features an internal alignment mechanism that simplifies the deployment of the system in practical applications. PILOT therefore greatly enhances the accessibility of the LIGS technique for industrial and research applications. Characterisation work for the system also provided valuable insight

into LIGS signal detection and a novel systematic investigation of LIEGS signal generation in different gases.

The optical layout within PILOT included an adjustable (via a translation stage) delay line to ensure phase-matched pump beams for different geometries. An experiment was conducted to identify the optimal position for the translation stage for the system's default optical configuration (using a 750 mm crossing lens and a 3° crossing angle for the pump beams). The results of the experiment showed that a misalignment of only 3 mm would result in a 50 % drop in signal intensity, which highlights the value of this feature. The effect of varying the pump beam energies and probe power were also explored, and it was found that maximising both was beneficial for the signal intensity. While the increase in signal intensity due to probe beam power was linear, the effect due to pump beam energy was quadratic. These findings are useful to predict the performance of PILOT in applications where either beam power/energy are practically limited. The spatial resolution of PILOT, when using its default optical configuration, was found to be 11 mm in the axial direction and less than 0.9 mm in the transverse direction.

Following these experiments, temperature measurements were taken by PILOT in room air and compared to the temperature reported by two different K-type thermocouples. The precision of the system was found to be ±0.7 % and the accuracy was comparable to the stated accuracy of the thermocouples, which was 0.37 %. The PILOT system was also used to characterise the time response of the thermocouples. It was calculated that an exposed junction K-type thermocouple would need to have an impractical bead size of less than 0.14 µm to be able to collect temperature measurements at the same rate (400 Hz) as the PILOT system.

Next the application of the PILOT system in different facilities and environments was investigated. First, practical applications that would require the beams to pass through windows were considered. It was found that the high pulse energies of the pump beams could cause window damage, which would necessitate a reduction in their pulse energies. As explained previously, this would cause an undesirable decrease in signal intensity. Experimental results showed that fused silica and borosilicate windows had a higher damage threshold compared to sapphire windows. A higher surface quality was also beneficial, while

anti-reflection coatings and the presence of dust particles on the surface both reduced the damage threshold. Following this, experiments were conducted to characterise the performance of PILOT in the presence of background light (to simulate its use in scattering environments). Since the problem encountered by scatter is centred around the detection of the LIGS signal, four different detectors were trialled. It was found that for non-scattering environments a photomultiplier tube offered the best signal-to-noise ratio. However, for high levels of simulated scatter an avalanche photodetector performed best. The choice of detector to use for an application should therefore be informed by the expected level of scatter. The final characterisation experiment was a study of the performance of the system for measurements in different gases. In particular, the effects on LIEGS signal intensity of the polarisability and molecular mass of a gas were explored. It was found that an increase in the polarisability of a gas resulted in a roughly cubic relative increase in signal intensity, while an increase in molecular mass resulted in a linear decrease in signal intensity. These findings can be used to predict the performance of the PILOT system in different gases, and inform gas selection when applicable.

Finally, the successful deployment of the PILOT system in a research facility was demonstrated. PILOT was used to collect non-invasive temperature measurements in a tracer-free air flow at Imperial College London's '10 x 5' wind tunnel facility. Its portability allowed it to be mounted on translation stages to enable data collection at different points. This work confirmed the potential of the PILOT system to enable LIGS measurements in previously inaccessible facilities and applications.

8 Future Prospects

Chapter 3 presented the successful characterisation and demonstration of the the use of biacetyl as a suitable tracer species for temporally-resolved LITGS. Biacetyl was selected due to its absorption at 355 nm which enabled the use of high-repetition rate lasers, as well as its history as a commonly-used tracer species for optical diagnostics. In particular, it has been used extensively for Planar Laser Induced Fluorescence (PLIF) measurements. The work presented in this thesis therefore enables the future application of biacetyl LITGS as an *in situ* calibration technique for temporally-resolved PLIF measurements.

Chapter 4 introduced the concept of axially-resolved LIGS and described the development of a computational model to simulate it. This aspect of the model was then employed to perform a parametric investigation to improve the achievable spatial resolution of the technique. For this, the imaging lens was modelled as a standard off-the-shelf lens. It was noted that the field of curvature of this lens model limited the improvement in spatial resolution gained by tilting the lens. A future improvement would be to model a multi-element camera lens which has improved field curvature to see whether that would allow the use of a tilted lens to improve spatial resolution.

An assumption made in the model was to only consider the signal beam generated from point sources in a line along the grating. The accuracy of the model could therefore be enhanced by simulating the signal beam as being generated from points throughout the grating. This would have the effect of introducing some more out-of-focus contributions to the signal received by each fibre. The impact of this is expected to be minimal due to the typically small width of a LIGS grating, but it would be useful to quantify it.

Another aspect of the model was the capability to simulate the characterisation experiment. This is an invaluable feature of the model as it allows it to be experimentally validated and used to inform the design of future experiments. The model allows the user to input a variation in fringe spacing along the grating (due to the Gaussian nature of the beams). It then models the LIGS grating as a diffraction grating in order to characterise the variation in scattering efficiency along the grating (due to the changing fringe spacing). Although this model is a suitable approximation, a thorough investigation of the effect of

fringe spacing on scattering efficiency for a LIGS grating would be a worthwhile endeavour.

Chapter 5 described the methodology of the characterisation experiments and presented the results. These showed that the per-fibre spatial resolution (referred to as the 'grating length per fibre', L_{gf}) was larger than the grating pitch, P_{g}. During the analysis of the data, it was shown that accounting for the 'crosstalk' between the optical fibres (where the magnitude of crosstalk was measured via a calibration experiment) enabled the resolution of temperature fluctuations at a spatial resolution of P_{g} rather than L_{gf}. Since the value of P_{g} is determined by the core size of the optical fibres being used, the extent to which the spatial resolution can be improved by using smaller fibres should be explored.

Another way to improve the spatial resolution of the technique, as shown during the parametric investigation, is to tilt the detector plane. Tilting the detector plane improves the spatial resolution at an increasing rate, until the best resolution is achieved when the detector plane is at the same angle as the image plane. Practically, however, the angle of the detector plane is limited by the acceptance angle of the optical fibres. One way to overcome this limitation would be to angle-polish the fibre end-faces. This could enable an order-of-magnitude improvement in the spatial resolution of the technique.

Chapter 6 described the design, development, characterisation and application of a transportable LIGS system (PILOT). The system, capable of tracer-free LIEGS measurements at 400 Hz, was characterised to have an axial spatial resolution of 11 mm when using its default configuration. However, the spatial resolution in the transverse direction was difficult to measure. An improvement to the measurement of its spatial resolution would be to use a jet containing a suitable absorbing species to create a thermal grating, similar to the toluene vapour used for the experiments detailed in Chapter 5.

Given the relatively poor axial spatial resolution of the PILOT system in the axial direction (11 mm), the application of the axially-resolved LIGS method would be of benefit to the system. Furthermore, it would mean that the beams would no longer need to be focused at the measurement point which may help reduce concerns of window damage in certain applications.

A couple of potential future applications for the PILOT system have already been identified in Section 6.5.2.

Bibliography

[1] Morris R Cohen and Ernest Nagel. *Introduction to logic and scientific method*. Allied Publishers Private Limited, New Delhi, 1936.

[2] Tuan Vo-Dinh. *Biomedical photonics handbook: biomedical diagnostics*. CRC press, 2014.

[3] Irving P Herman. *Optical diagnostics for thin film processing*. Elsevier, 1996.

[4] A. C. Eckbreth. *Laser diagnostics for combustion temperature and species*, volume 3. CRC Press, 1996.

[5] Paris Agreement. Paris agreement. In *Report of the Conference of the Parties to the United Nations Framework Convention on Climate Change (21st Session, 2015: Paris). Retrived December*, volume 4, page 2017. HeinOnline, 2015.

[6] S Basu, MW Renfro, and BM Cetegen. Spatially resolved optical measurements of water partial pressure and temperature in a pem fuel cell under dynamic operating conditions. *Journal of Power Sources*, 162(1):286–293, 2006.

[7] JP Bonnet, D Gresillon, and JP Taran. Nonintrusive measurements for high-speed, supersonic, and hypersonic flows. *Annual review of fluid mechanics*, 30(1):231–273, 1998.

[8] Simone Mancin, Claudio Zilio, Alberto Cavallini, and Luisa Rossetto. Pressure drop during air flow in aluminum foams. *International Journal of Heat and Mass Transfer*, 53(15-16):3121–3130, 2010.

[9] JD Posner, CR Buchanan, and D_ Dunn-Rankin. Measurement and prediction of indoor air flow in a model room. *Energy and buildings*, 35(5):515–526, 2003.

[10] Todd D Fansler and Scott E Parrish. Spray measurement technology: a review. *Measurement Science and Technology*, 26(1):012002, 2014.

[11] Blane Scott, Christopher Willman, Ben Williams, Paul Ewart, Richard Stone, and David Richardson. In-cylinder temperature measurements using laser induced grating spectroscopy and two-colour plif. *SAE International Journal of Engines*, 10(4):2191–2201, 2017.

[12] A-L Sahlberg, A Luers, C Willman, BAO Williams, and P Ewart. Pressure measurement in combusting and non-combusting gases using laser-induced grating spectroscopy. *Applied Physics B*, 125(3):1–12, 2019.

[13] Michael S Brown, Peter A DeBarber, Eric B Cummings, and Hans G Hornung. Trace species concentration and temperature measurements at high pressure using laser-induced grating spectroscopy. In *Optical Techniques in Fluid, Thermal, and Combustion Flow*, volume 2546, pages 519–529. International Society for Optics and Photonics, 1995.

[14] Stefan Schlamp, Eric B Cummings, and Thomas H Sobota. Laser-induced thermal-acoustic velocimetry with heterodyne detection. *Optics letters*, 25(4):224–226, 2000.

[15] B. A. O. Williams. *Quantitative laser diagnostics for combustion.* PhD thesis, University of Oxford, 2009.

[16] A Stampanoni-Panariello, DN Kozlov, PP Radi, and B Hemmerling. Gas phase diagnostics by laser-induced gratings i. theory. *Applied Physics B*, 81(1):101–111, 2005.

[17] Francesca De Domenico, Thibault F Guiberti, Simone Hochgreb, William L Roberts, and Gaetano Magnotti. Temperature and water measurements in flames using 1064 nm laser-induced grating spectroscopy (ligs). *Combustion and Flame*, 205:336–344, 2019.

[18] DW Pohl, SE Schwarz, and V Irniger. Forced rayleigh scattering. *Physical Review Letters*, 31(1):32, 1973.

[19] H Eichler, G Salje, and H Stahl. Thermal diffusion measurements using spatially

periodic temperature distributions induced by laser light. *Journal of Applied Physics*, 44(12):5383–5388, 1973.

[20] HJ Eichler, Ch Hartig, and J Knof. Laser induced gratings in cds. *physica status solidi (a)*, 45(2):433–438, 1978.

[21] DR Dean and RJ Collins. Transient phase gratings in zno induced by two-photon absorption. *Journal of Applied Physics*, 44(12):5455–5457, 1973.

[22] H Hervet, W Urbach, and F Rondelez. Mass diffusion measurements in liquid crystals by a novel optical method. *The Journal of Chemical Physics*, 68(6):2725–2729, 1978.

[23] Dieter W Pohl and V Irniger. Observation of second sound in naf by means of light scattering. *Physical Review Letters*, 36(9):480, 1976.

[24] Keith A Nelson and MD Fayer. Laser induced phonons: A probe of intermolecular interactions in molecular solids. *The Journal of Chemical Physics*, 72(9):5202–5218, 1980.

[25] Keith A Nelson, DR Lutz, MD Fayer, and Larry Madison. Laser-induced phonon spectroscopy. optical generation of ultrasonic waves and investigation of electronic excited-state interactions in solids. *Physical Review B*, 24(6):3261, 1981.

[26] Keith A Nelson, RJ Dwayne Miller, DR Lutz, and MD Fayer. Optical generation of tunable ultrasonic waves. *Journal of Applied Physics*, 53(2):1144–1149, 1982.

[27] RJ Dwayne Miller, Roger Casalegno, Keith A Nelson, and MD Fayer. Laser-induced ultrasonics: A daynamic holographic approach to the measurement of weak absorptions, optoelastic constants acoustic attenuation. *Chemical Physics*, 72(3):371–379, 1982.

[28] Mark Anthony Buntine. *Application of ion imaging and laser-induced gratings to chemical dynamics*. PhD thesis, Stanford University, 1992.

[29] EB Cummings. Laser-induced thermal acoustics: simple accurate gas measurements. *Optics letters*, 19(17):1361–1363, 1994.

[30] Thomas J Butenhoff and Eric A Rohlfing. Laser-induced gratings in free jets. i. spectroscopy of predissociating no2. *The Journal of chemical physics*, 98(7):5460–5468, 1993.

[31] B Hemmerling, R Bombach, and W Hubschmid. Laser-induced gratings in oxygen excited via the b $^1\sum_g^+$ (v'= 0) state. *Chemical physics letters*, 256(1-2):71–76, 1996.

[32] B Hemmerling and DN Kozlov. Collisional relaxation of singlet $o_2(b^1\sum^+{}_g)$ in neat gas investigated by laser-induced grating technique. *Chemical physics*, 291(3):213–242, 2003.

[33] B Hemmerling, DN Kozlov, OM Stel'makh, and B Attal-Trétout. Diagnostics of water-containing gas mixtures using thermal laser-induced gratings. *Chemical physics*, 320 (2-3):103–117, 2006.

[34] Thomas Seeger, Johannes Kiefer, Markus C Weikl, Alfred Leipertz, and Dimitrii N Kozlov. Time-resolved measurement of the local equivalence ratio in a gaseous propane injection process using laser-induced gratings. *Optics express*, 14(26):12994–13000, 2006.

[35] B Roshani, A Flügel, I Schmitz, DN Kozlov, T Seeger, L Zigan, J Kiefer, and A Leipertz. Simultaneous measurements of fuel vapor concentration and temperature in a flash-boiling propane jet using laser-induced gratings. *Journal of Raman Spectroscopy*, 44(10):1356–1362, 2013.

[36] DJW Walker, RB Williams, and P Ewart. Thermal grating velocimetry. *Optics letters*, 23(16):1316–1318, 1998.

[37] Roger C Hart, R Jeffrey Balla, and GC Herring. Simultaneous velocimetry and thermometry of air by use of nonresonant heterodyned laser-induced thermal acoustics. *Applied Optics*, 40(6):965–968, 2001.

[38] R Stevens and P Ewart. Single-shot measurement of temperature and pressure using laser-induced thermal gratings with a long probe pulse. *Applied Physics B*, 78(1): 111–117, 2004.

[39] Robert Stevens and Paul Ewart. Simultaneous single-shot measurement of temperature and pressure along a one-dimensional line by use of laser-induced thermal grating spectroscopy. *Optics letters*, 31(8):1055–1057, 2006.

[40] Christopher Willman, Laurent M Le Page, Paul Ewart, and Benjamin AO Williams. Pressure measurement in gas flows using laser-induced grating lifetime. *Applied Optics*, 60(15):C131–C141, 2021.

[41] Michael S Brown and William L Roberts. Single-point thermometry in high-pressure, sooting, premixed combustion environments. *Journal of Propulsion and Power*, 15 (1):119–127, 1999.

[42] A Stampanoni-Panariello, B Hemmerling, and W Hubschmid. Temperature measurements in gases using laser-induced electrostrictive gratings. *Applied Physics B: Lasers & Optics*, 67(1), 1998.

[43] Annika Hell, Felix Förster, Eduard Rosenko, and Bernhard Weigand. Experiments in chemically reacting subsonic flames and heated supersonic flows using laser-induced thermal acoustics (lita). In *16th Int Symp on Applications of Laser Techniques to Fluid Mechanics, Lisbon, Portugal*, pages 1–11, 2012.

[44] H Latzel, A Dreizler, T Dreier, J Heinze, M Dillmann, W Stricker, GM Lloyd, and P Ewart. Thermal grating and broadband degenerate four-wave mixing spectroscopy of oh in high-pressure flames. *Applied Physics B*, 67(5):667–673, 1998.

[45] Peter F Barker, Jay H Grinstead, and Richard B Miles. Single-pulse temperature measurement in supersonic air flow with predissociated laser-induced thermal gratings. *Optics communications*, 168(1-4):177–182, 1999.

[46] B Hemmerling, DN Kozlov, and A Stampanoni-Panariello. Temperature and flow-velocity measurements by use of laser-induced electrostrictive gratings. *Optics letters*, 25(18):1340–1342, 2000.

[47] S Schlamp, T Rosgen, DN Kozlov, C Rakut, P Kasal, and J Von Wolfersdorf. Tran-

sient grating spectroscopy in a hot turbulent compressible free jet. *Journal of propulsion and power*, 21(6):1008–1018, 2005.

[48] Mark G Allen. Diode laser absorption sensors for gas-dynamic and combustion flows. *Measurement Science and technology*, 9(4):545, 1998.

[49] X Liu, JB Jeffries, RK Hanson, KM Hinckley, and MA Woodmansee. Development of a tunable diode laser sensor for measurements of gas turbine exhaust temperature. *Applied Physics B*, 82(3):469–478, 2006.

[50] M. G. Allen. Diode laser absorption sensors for gas-dynamic and combustion flows. *Measurement Science and Technology*, 9(4):545, 1998.

[51] D. F. Davidson, A. Y. Chang, M. D. DiRosa, and R. K. Hanson. Continuous wave laser absorption techniques for gasdynamic measurements in supersonic flows. *Applied optics*, 30(18):2598–2608, 1991.

[52] J. Kiefer and P. Ewart. Laser diagnostics and minor species detection in combustion using resonant four-wave mixing. *Progress in Energy and Combustion Science*, 37(5): 525–564, 2011.

[53] T. Kamimoto, Y. Deguchi, and Y. Kiyota. High temperature field application of two dimensional temperature measurement technology using ct tunable diode laser absorption spectroscopy. *Flow Measurement and Instrumentation*, 46:51–57, 2015.

[54] Wieland Koban, Jon D Koch, Ronald K Hanson, and Christof Schulz. Absorption and fluorescence of toluene vapor at elevated temperatures. *Physical chemistry chemical physics*, 6(11):2940–2945, 2004.

[55] K. Kohse-Höinghaus. Laser techniques for the quantitative detection of reactive intermediates in combustion systems. *Progress in Energy and Combustion Science*, 20 (3):203–279, 1994.

[56] Daniel Hofmann and Alfred Leipert. Temperature field measurements in a sooting flame by filtered rayleigh scattering (frs). In *Symposium (International) on Combustion*, volume 26, pages 945–950. Elsevier, 1996.

[57] Ulrich Doll, Guido Stockhausen, and Christian Willert. Pressure, temperature, and three-component velocity fields by filtered rayleigh scattering velocimetry. *Opt. Lett.*, 42(19):3773–3776, Oct 2017. doi: 10.1364/OL.42.003773. URL http://ol.osa.org/abstract.cfm?URI=ol-42-19-3773.

[58] D. Hoffman, K-U Münch, and A. Leipertz. Two-dimensional temperature determination in sooting flames by filtered rayleigh scattering. *Optics letters*, 21(7):525–527, 1996.

[59] A. Mielke, K. Elam, and C. Sung. Rayleigh scattering diagnostic for measurement of temperature, velocity, and density fluctuation spectra. In *44th AIAA Aerospace Sciences Meeting and Exhibit*, pages 9–12, 2006.

[60] Sean P Kearney, Robert W Schefer, Steven J Beresh, and Thomas W Grasser. Temperature imaging in nonpremixed flames by joint filtered rayleigh and raman scattering. *Applied optics*, 44(9):1548–1558, 2005.

[61] Paul M Danehy, Phillip H Paul, and Roger L Farrow. Thermal-grating contributions to degenerate four-wave mixing in nitric oxide. *JOSA B*, 12(9):1564–1576, 1995.

[62] P Ewart and M Kaczmarek. Two-dimensional mapping of temperature in a flame by degenerate four-wave mixing in oh. *Applied optics*, 30(27):3996–3999, 1991.

[63] P Ewart and P Snowdon. Multiplex degenerate four-wave mixing in a flame. *Optics letters*, 15(23):1403–1405, 1990.

[64] Katharina Kohse-Höinghaus. Laser techniques for the quantitative detection of reactive intermediates in combustion systems. *Progress in Energy and Combustion Science*, 20(3):203–279, 1994.

[65] Thomas Dreier and David J Rakestraw. Measurement of oh rotational temperatures in a flame using degenerate four-wave mixing. *Optics letters*, 15(1):72–74, 1990.

[66] P Ewart. Temperature measurement by uv-degenerate four wave mixing. *Berichte der Bunsengesellschaft für physikalische Chemie*, 97(12):1625–1629, 1993.

[67] IP Jefferies, AJ Yates, and P Ewart. Temperature measurement by multiplex degenerate four wave mixing. In *Coherent Raman Spectroscopy: Applications And New Developments-Proceedings Of The Xi European Cars Workshop*, page 129. World Scientific, 1993.

[68] B Yip, PM Danehy, and RK Hanson. Degenerate four-wave mixing temperature measurements in a flame. *Optics letters*, 17(10):751–753, 1992.

[69] R. Stevens and P. Ewart. Single-shot measurement of temperature and pressure using laser-induced thermal gratings with a long probe pulse. *Applied Physics B*, 78(1): 111–117, 2004.

[70] Sean P Kearney, Kraig Frederickson, and Thomas W Grasser. Dual-pump coherent anti-stokes raman scattering thermometry in a sooting turbulent pool fire. *Proceedings of the Combustion Institute*, 32(1):871–878, 2009.

[71] Thomas Seeger and Alfred Leipertz. Experimental comparison of single-shot broadband vibrational and dual-broadband pure rotational coherent anti-stokes raman scattering in hot air. *Applied optics*, 35(15):2665–2671, 1996.

[72] Joseph D Miller, Mikhail N Slipchenko, Terrence R Meyer, Hans U Stauffer, and James R Gord. Hybrid femtosecond/picosecond coherent anti-stokes raman scattering for high-speed gas-phase thermometry. *Optics letters*, 35(14):2430–2432, 2010.

[73] Joseph D Miller, Sukesh Roy, Mikhail N Slipchenko, James R Gord, and Terrence R Meyer. Single-shot gas-phase thermometry using pure-rotational hybrid femtosecond/picosecond coherent anti-stokes raman scattering. *Optics Express*, 19(16):15627–15640, 2011.

[74] Claresta N Dennis, Carson D Slabaugh, Isaac G Boxx, Wolfgang Meier, and Robert P Lucht. Chirped probe pulse femtosecond coherent anti-stokes raman scattering thermometry at 5 khz in a gas turbine model combustor. *Proceedings of the Combustion Institute*, 35(3):3731–3738, 2015.

[75] Michael Scherman, Joanna Barros, Rosa Santagata, Elodie Lin, Philippe Nicolas, Jean Pierre Faleni, Axel Vincent-Randonnier, Pascal Cherubini, Florestan Guichard, Ajmal Mohamed, et al. 1-khz hybrid femtosecond/picosecond coherent anti-stokes raman scattering thermometry of turbulent combustion in a representative aeronautical test rig. *Journal of Raman Spectroscopy*, 2021.

[76] Felix J Förster, Cyril Crua, Martin Davy, and Paul Ewart. Time-resolved gas thermometry by laser-induced grating spectroscopy with a high-repetition rate laser system. *Experiments in Fluids*, 58(7):1–8, 2017.

[77] Alexis Bohlin, Brian D Patterson, and Christopher J Kliewer. Communication: Simplified two-beam rotational cars signal generation demonstrated in 1d. *The Journal of chemical physics*, 138(8):081102, 2013.

[78] S. Roy, J. R. Gord, and A. K. Patnaik. Recent advances in coherent anti-stokes raman scattering spectroscopy: Fundamental developments and applications in reacting flows. *Progress in Energy and Combustion Science*, 36(2):280–306, 2010.

[79] A. Bohlin and C. J. Kliewer. Two-beam ultrabroadband coherent anti-stokes raman spectroscopy for high resolution gas-phase multiplex imaging. *Applied Physics Letters*, 104(3):031107, 2014.

[80] A. Bohlin, B. D. Patterson, and C. J. Kliewer. Communication: Simplified two-beam rotational cars signal generation demonstrated in 1d. *The Journal of Chemical Physics*, 138(8):081102, 2013. doi: 10.1063/1.4793556.

[81] Brian Thurow, Naibo Jiang, and Walter Lempert. Review of ultra-high repetition rate laser diagnostics for fluid dynamic measurements. *Measurement Science and Technology*, 24(1):012002, 2012.

[82] Stanley V Dawson and Marc B Schenker. Health effects of inhalation of ambient concentrations of nitrogen dioxide. *American Review of Respiratory Disease*, 120(2): 281–292, 1979.

[83] Francesca De Domenico, Thibault F Guiberti, Simone Hochgreb, William L Roberts, and Gaetano Magnotti. Tracer-free laser-induced grating spectroscopy using a pulse burst laser at 100 khz. *Optics express*, 27(22):31217–31224, 2019.

[84] Christof Schulz and Volker Sick. Tracer-lif diagnostics: quantitative measurement of fuel concentration, temperature and fuel/air ratio in practical combustion systems. *Progress in energy and combustion science*, 31(1):75–121, 2005.

[85] James D Smith and Volker Sick. Crank-angle resolved imaging of biacetyl laser-induced fluorescence in an optical internal combustion engine. *Applied Physics B*, 81 (5):579–584, 2005.

[86] Stephanie Clark and Carl K Winter. Diacetyl in foods: a review of safety and sensory characteristics. *Comprehensive Reviews in Food Science and Food Safety*, 14(5):634–643, 2015.

[87] A. Horowitz, R. Meller, and G. Moortgat. The uv-vis absorption cross sections of the α-dicarbonyl compounds: pyruvic acid, biacetyl and glyoxal. *Journal of Photochemistry and Photobiology A: Chemistry*, 146(1):19–27, 2001. doi: http://dx.doi.org/10.1016/S1010-6030(01)00601-3. [Accessed: 16th August 2017].

[88] M. O'Neil (ed.). *The Merck Index - An Encyclopedia of Chemicals, Drugs, and Biologicals*. The Royal Society of Chemistry, Cambridge, UK, 15th edition, 2013. p. 537.

[89] Francesca De Domenico, Priyav Shah, Steven M Lowe, Luming Fan, Paul Ewart, Benjamin AO Williams, and Simone Hochgreb. High frequency measurement of temperature and composition spots with litgs. *Journal of Engineering for Gas Turbines and Power*, 141(3), 2019.

[90] Francesca De Domenico, Erwan O Rolland, and Simone Hochgreb. Detection of direct and indirect noise generated by synthetic hot spots in a duct. *Journal of Sound and Vibration*, 394:220–236, 2017.

[91] Christopher Willman and Paul Ewart. Multipoint temperature measurements in gas flows using 1-d laser-induced grating scattering. *Experiments in Fluids*, 57(12):1–9, 2016.

[92] Theodor Scheimpflug. Improved method and apparatus for the systematic alteration or distortion of plane pictures and images by means of lenses and mirrors for photography and for other purposes. GB1196 (patent), 1904.

[93] Harold M Merklinger. *Focusing the view camera*. Seaboard Printing Limited, 2006. Available from: http://www.trenholm.org/hmmerk/FVC161.pdf [Accessed 1st May 2019].

[94] Harold M Merklinger. Scheimpflug's patent. *Photo Techniques*, 17(6):56, 1996.

[95] Harold M Merklinger. The scheimpflug principle—part iv. *Shutterbug Magazine*, 23, 1993.

[96] Alexander Schultze and Yury Petrov. *OptoMetrika -Optical ray tracer for MATLAB*, 02 2021. DOI: 10.13140/RG.2.2.10027.98081/1.

[97] Felix Förster, C Crua, Martin Davy, and Paul Ewart. Temperature measurements under diesel engine conditions using laser induced grating spectroscopy. *Combustion and Flame*, 199:249–257, 2019.

[98] A Stampanoni-Panariello, B Hemmerling, and W Hubschmid. Electrostrictive generation of nonresonant gratings in the gas phase by multimode lasers. *Physical Review A*, 51(1):655, 1995.

[99] F O'YOUNG and RW Bilger. Measurement of scalar dissipation in premixed flames. *Combustion science and technology*, 113(1):393–411, 1996.

[100] N Papaioannou, F Leach, and M Davy. Effect of thermocouple size on the measurement of exhaust gas temperature in internal combustion engines. In *International Powertrains, Fuels & Lubricants Meeting*, SAE Technical Papers, page Article: 1765. SAE International, 2018.

[101] Kenneth Kar, Stephen Roberts, Richard Stone, Martin Oldfield, and Boyd French. Instantaneous exhaust temperature measurements using thermocouple compensation techniques. *SAE Transactions*, 113:652–673, 2004. ISSN 0096736X, 25771531. URL http://www.jstor.org/stable/44740790.

[102] M. Tagawa and Y. Ohta. Two-thermocouple probe for fluctuating temperature measurement in combustion—rational estimation of mean and fluctuating time constants. *Combustion and Flame*, 109(4):549–560, 1997. ISSN 0010-2180. doi: https://doi.org/10.1016/S0010-2180(97)00044-8. URL https://www.sciencedirect.com/science/article/pii/S0010218097000448.

[103] Kenneth Kar, Akshya K Swain, and Robert Raine. Identification of time-varying time constants of thermocouple sensors and its application to temperature measurement. *Journal of dynamic systems, measurement, and control*, 131(1), 2009.

[104] Kambiz Farahmand and Jonathan W Kaufman. Experimental measurement of fine thermocouple response time in air. *Experimental heat transfer*, 14(2):107–118, 2001.

[105] Sheridan C Johnston, CW Robinson, W Smith Rorke, JR Smith, and PO Witze. Application of laser diagnostics to an injected engine. *SAE Transactions*, pages 353–370, 1979.

[106] Mark PB Musculus. Multiple simultaneous optical diagnostic imaging of early-injection low-temperature combustion in a heavy-duty diesel engine. *SAE Transactions*, pages 83–110, 2006.

[107] Ben Williams, Megan Edwards, Richard Stone, John Williams, and Paul Ewart. High precision in-cylinder gas thermometry using laser induced gratings: quantitative measurement of evaporative cooling with gasoline/alcohol blends in a gdi optical engine. *Combustion and Flame*, 161(1):270–279, 2014.

[108] Haifeng Liu, Chia-fon Lee, Ming Huo, and Mingfa Yao. Comparison of ethanol and butanol as additives in soybean biodiesel using a constant volume combustion chamber. *Energy & fuels*, 25(4):1837–1846, 2011.

[109] Matthew McGilvray, Luke J Doherty, Andrew J Neely, Robert Pearce, and Peter Ireland. The oxford high density tunnel. In *20th AIAA International Space Planes and Hypersonic Systems and Technologies Conference*, page 3548, 2015.

[110] Naibo Jiang, Matthew Webster, Walter R Lempert, Joseph D Miller, Terrence R Meyer, Christopher B Ivey, and Paul M Danehy. Mhz-rate nitric oxide planar laser-induced fluorescence imaging in a mach 10 hypersonic wind tunnel. *Applied optics*, 50(4):A20–A28, 2011.

[111] Roger M Wood. *Laser-induced damage of optical materials [electronic resource]*. Series in optics and optoelectronics. Institute of Physics, Bristol, 2003. ISBN 9781420034059 (electronic bk.).

[112] CWo Carr, HB Radousky, and SG Demos. Wavelength dependence of laser-induced damage: determining the damage initiation mechanisms. *Physical Review Letters*, 91 (12):127402, 2003.

[113] Kunio Yoshida, Nobuhiro Umemura, Nobu Kuzuu, Hidetsugu Yoshida, Tomosumi Kamimura, and Takatomo Sasaki. Wavelength dependence of laser-induced damage in fused silica and fused quartz. In *Laser-Induced Damage in Optical Materials: 1997*, volume 3244, pages 164–175. International Society for Optics and Photonics, 1998.

[114] ES Bliss. Pulse duration dependence of laser damage mechanisms. *Opto-electronics*, 3(2):99–108, 1971.

[115] RM Wood. Laser induced damage thresholds and laser safety levels. do the units of measurement matter? *Optics & Laser Technology*, 29(8):517–522, 1998.

[116] D Du, X Liu, G Korn, J Squier, and G Mourou. Laser-induced breakdown by impact ionization in sio2 with pulse widths from 7 ns to 150 fs. *Applied physics letters*, 64 (23):3071–3073, 1994.

[117] N. Bloembergen. Role of cracks, pores, and absorbing inclusions on laser induced damage threshold at surfaces of transparent dielectrics. *Appl. Opt.*, 12(4):661–664,

Apr 1973. doi: 10.1364/AO.12.000661. URL http://ao.osa.org/abstract.cfm?URI=ao-12-4-661.

[118] RW Hopper and Donald R Uhlmann. Mechanism of inclusion damage in laser glass. *Journal of applied physics*, 41(10):4023–4037, 1970.

[119] Christoph Knappe, Johannes Lindén, F Abou Nada, Mattias Richter, and Marcus Aldén. Investigation and compensation of the nonlinear response in photomultiplier tubes for quantitative single-shot measurements. *Review of Scientific Instruments*, 83 (3):034901, 2012.

[120] Russell Johnson. Nist 101. computational chemistry comparison and benchmark database, 1999. URL http://cccbdb.nist.gov/. [Accessed: 01/09/2021].

[121] National Institute of Standards and Technology (U.S.). Nist chemistry webbook, 1997. URL https://purl.fdlp.gov/GPO/LPS87332. [Accessed: 01/09/2021].

[122] Jeremy Basley, Kevin Gouder, and Jonathan F Morrison. Turbulent boundary layer injected with low blowing ratio effusion film. In *APS Division of Fluid Dynamics Meeting Abstracts*, pages P40–005, 2019.

[123] Nicholas Syred, Stephen M Morris, PJ Bowen, Agustin Valera-Medina, and Richard Marsh. Preliminary results from a high pressure optical gas turbine combustor model with 3d viewing capability. In *53rd AIAA Aerospace Sciences Meeting*, page 1655, 2015.

A Validation of axially-resolved LITGS experimental design

The section describes a qualitative experiment that was undertaken to validate the experimental setup, described in Chapter 4.4, to characterise axially-resolved LITGS.

Figure A.1 shows the experimental layout. A Nd:YAG laser[1] and a beam splitter were used to create two identical pump beams, with a compensator plate added to one beam path to account for the difference in path length. A crossing lens was employed to cross the beams over at the desired crossing angle θ_x, while a lens further 'upstream' ensured that the beams would be collimated after the crossing lens (the pair of lenses acted as a telescope). A DPSS laser[2] was used to produce the probe beam, which was also passed through a lens before the crossing lens to ensure a collimated beam.

As the pump beams used for this experiment had a wavelength of 266 nm, toluene was chosen to be the absorbing species. A bubbler was used to seed the nitrogen gas with toluene vapour. The seeded nitrogen was then emitted, as a jet, out of a needle (with an inner diameter of 0.5 mm) was oriented vertically and set on a translation stage so that it could be moved axially along the grating.

An imaging lens[3] was used to image the signal beam, at the location at which it was generated from the jet, onto a camera. As the needle was moved along the translation stage, the camera was used to view the signal beam and experimentally confirm that the beam could be divided into 'sub signal' beams which each originated from different regions within the grating. As the camera would need to be sensitive enough to see the weak signal beam, an Andor Luca-R EMCCD camera was used.

[1] Minilite II model from Continuum.
[2] MLL-FN-671 model by CNI.
[3] A Serrac lens from Dallmeyer with 200 mm focal length.

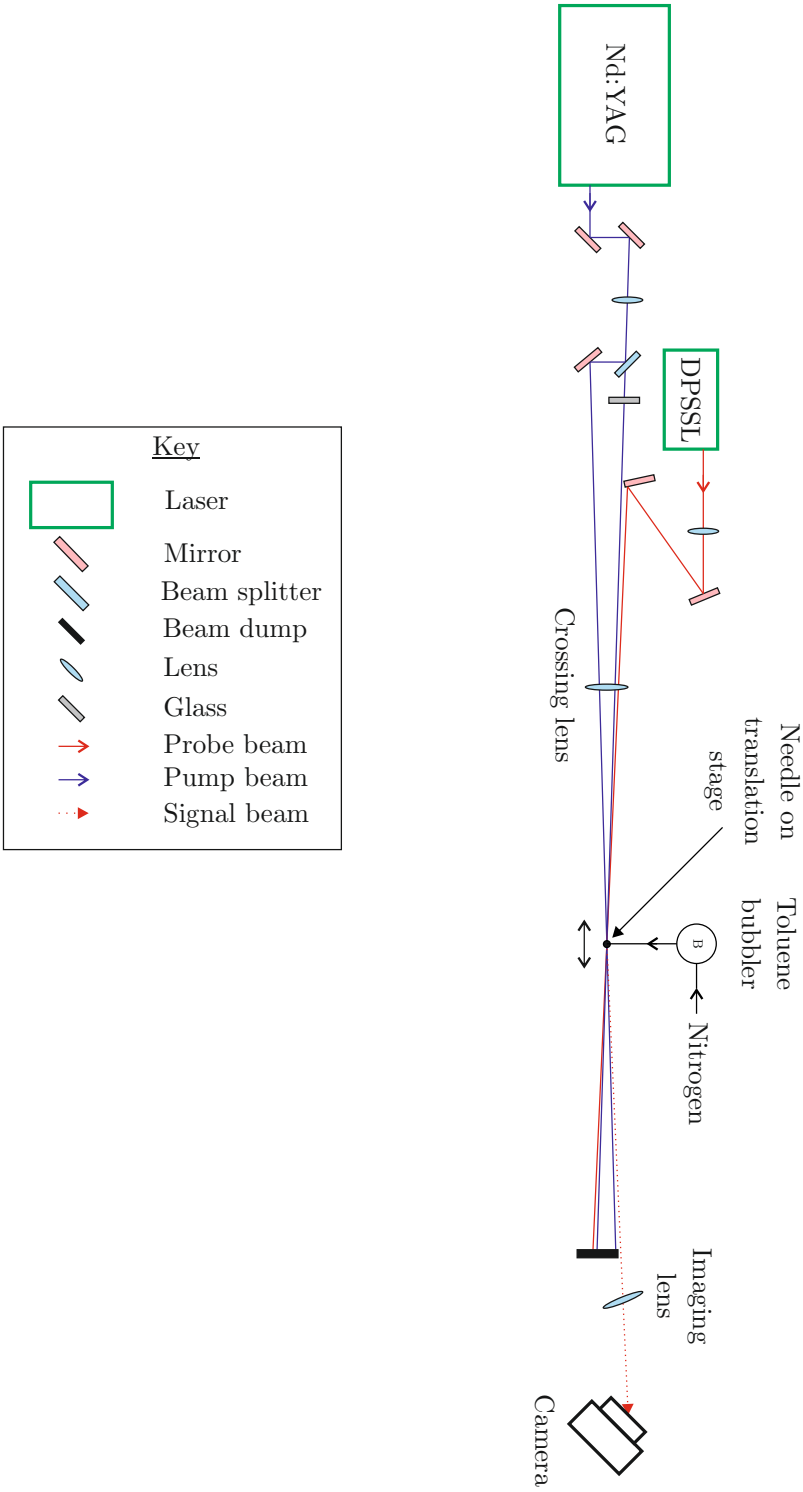


Figure A.1: Plan view of the full proof-of-concept experimental setup. Note that the needle emits a jet of nitrogen saturated with toluene in the direction out of the paper, and the laser beams pass through the jet.

First, the jet was characterised by Laser-Induced Fluorescence (LIF). The LIF image[4], presented in Figure A.2, showed the jet to be steady (with a diameter of 0.4 mm) at the height of the LITGS beams.

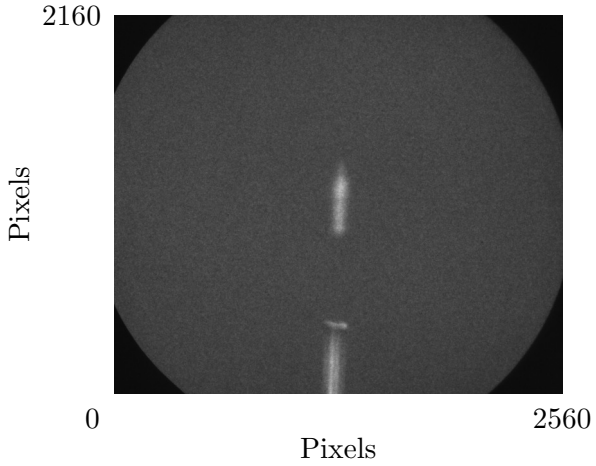


Figure A.2: LIF image of the jet of nitrogen saturated with toluene vapour.The needle, with inner diameter 0.5 mm, is visible at the bottom of the image. The fluorescence from the jet is in the centre of the frame.

A typical LITGS geometry was chosen for the experiment which would produce a signal beam at an angle of 2.8° from the grating. The desired object plane lies along the longitudinal axis of the thermal grating, which means the angle of this object plane relative to the signal beam propagation direction was fixed at 2.8°. Due to the casing around the camera sensor, the maximum angle of incoming light that the camera could accept was 45°, and so the image plane angle was fixed to that maximum. The lens used had a focal length of 200 mm and testing showed that it did not transmit light when tilted past 20°.

Having fixed the object plane tilt at 2.8°, the lens tilt at 20° and the image plane tilt at 45°, a Matlab script was written to calculate the distances that the object and image planes must be from the lens to satisfy the Scheimpflug and hinge rules. Figure A.3 shows the result, whereby the distance between the LITGS grating and the imaging lens would have to be 3.1 m.

[4]An iStar sCMOS camera from Andor was used to capture the image.

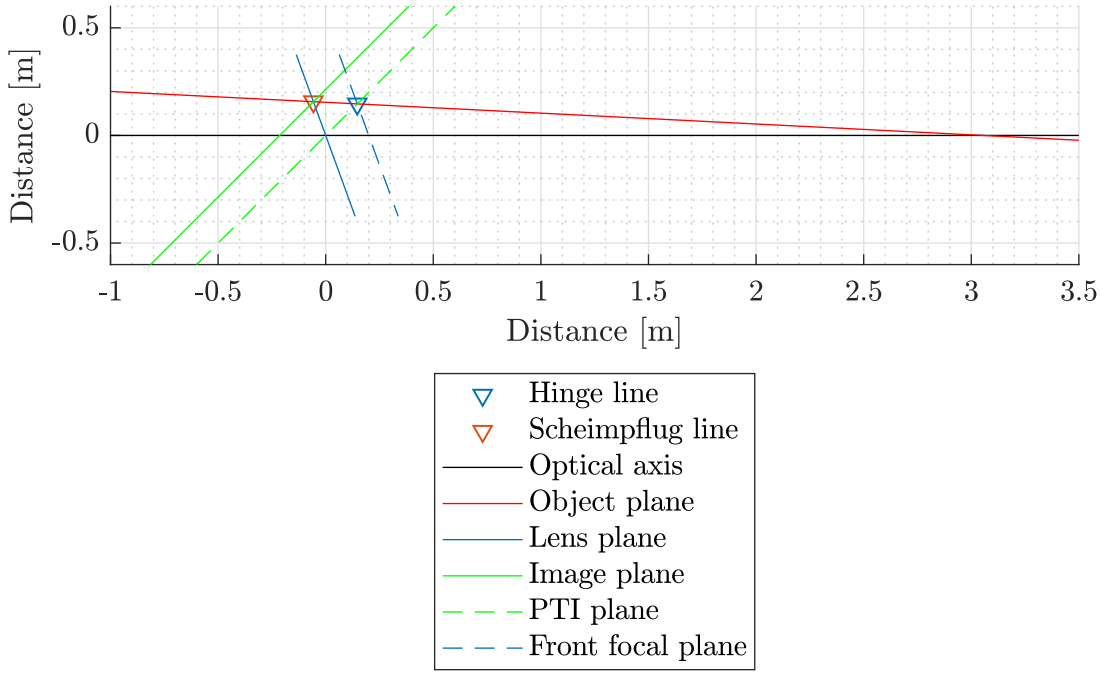


Figure A.3: Exact Scheimpflug imaging layout given practical constraints. The centre of the grating is expected to be at the intersection of the object plane with the optical axis, and the camera is situated at the intersection between the image plane and optical axis.

Due to the impracticality of this solution (being longer than the optical table), it was decided to relax the tilt of the image plane and instead fix the distances between the lens, image plane and object plane. A distance of 600 mm, along the optical axis, was chosen between the object plane and lens due to physical limitations on the optical table. Using Equation 4.1, the distance between the lens and the centre of the image plane was calculated to be 300 mm. The layout is shown in Figure A.4, where the thermal grating in the experiment lies along the object plane at an angle of 2.8° to the optical axis. The 'detector plane' is the plane along which the detector - in this case the camera sensor - is placed. Since the signal beam from the grating would be fully in focus along the image plane, it was not fully in focus on the camera sensor; however this was still an improvement from a 'standard' imaging arrangement where the detector plane would be at 90° to the optical axis.

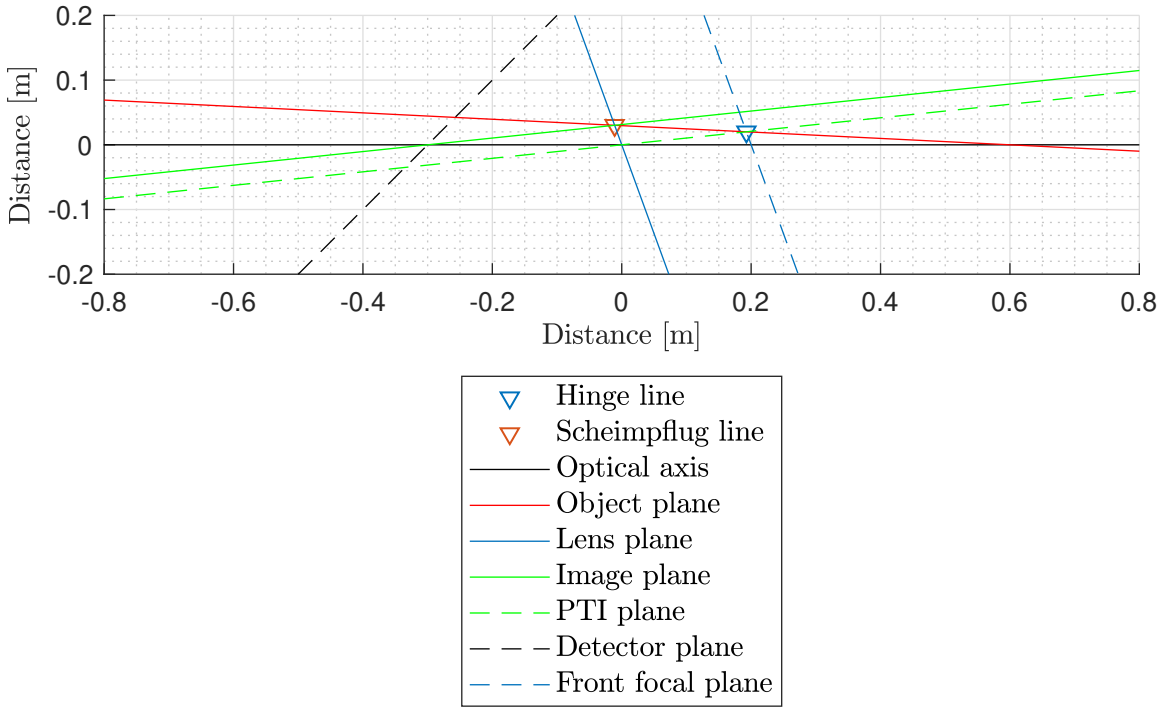


Figure A.4: Scheimpflug imaging layout given experimental constraints. The centre of the grating is expected to be at the intersection of the object plane with the optical axis, and the camera is situated at the intersection between the image plane and optical axis.

Figure A.5**a** displays the results from the experiment, where images of the signal beam were taken with the needle at three different positions (1, 2, 3). Each position was 5 mm apart along the grating. Figure A.5**b** shows the camera data, where each image is the average of 100 images taken at that position. As expected, the effect of moving the needle along the LITGS grating was a horizontal movement of the signal beam along the camera sensor.

The signal beam is brighter (higher intensity) at position 2 compared to the other two positions. This is because of the Gaussian profile of the laser beams used for the experiment, which meant that the intensity of all three beams (two pump beams and one probe beam) was highest at the centre of the LITGS grating.

The results of this experiment proved that the setup used was capable of characterising the the concept behind axially-resolved LITGS. However, the use of a camera meant that no quantitative LITGS measurements were made (since the frame rate of the camera was unable to capture the oscillations in a LITGS signal).

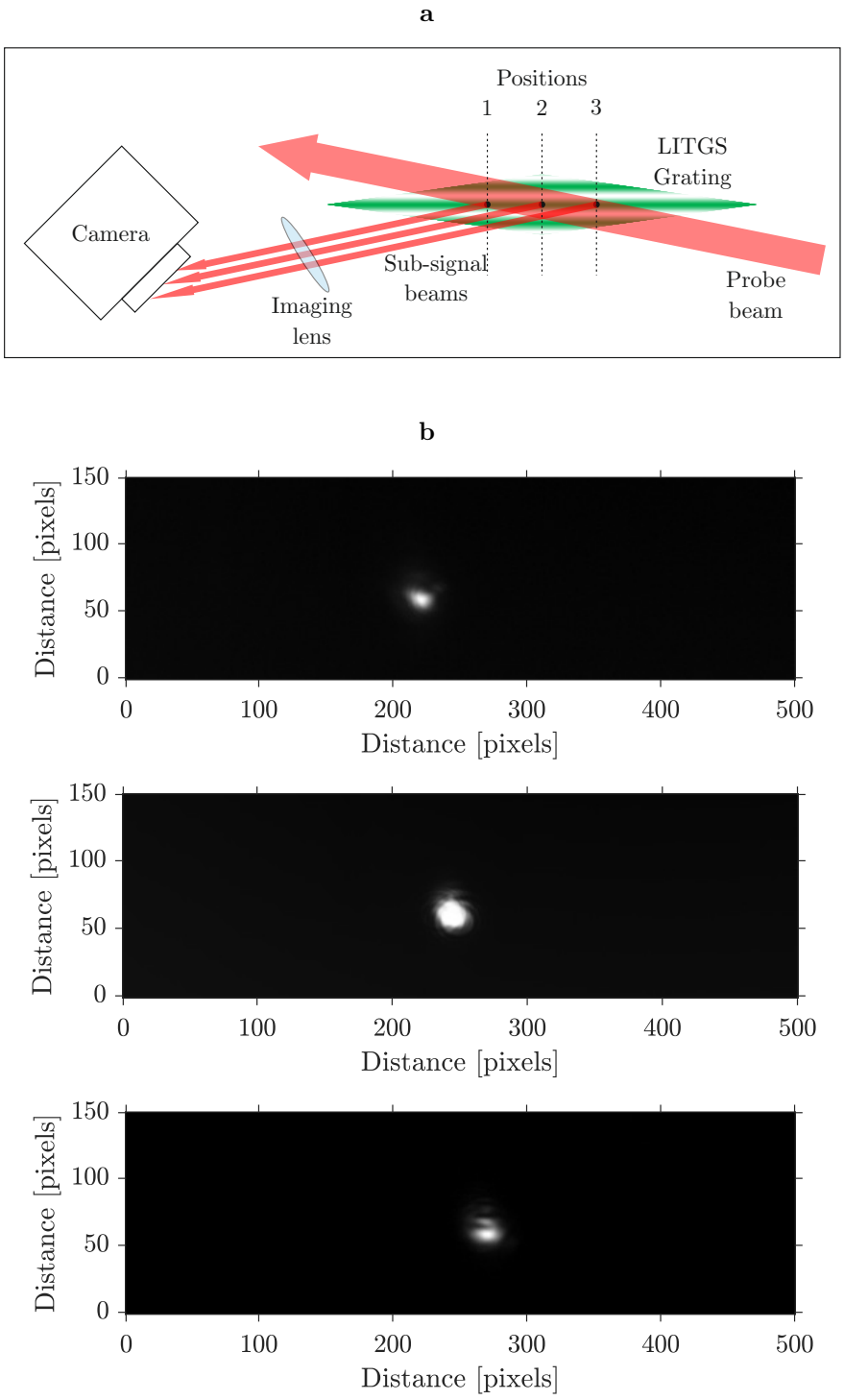


Figure A.5: Diagram **a** illustrates the three positions at which the jet was placed to obtain the results shown in **b** (the top image was taken with the jet at position 1, the middle one at position 2 and the bottom one at position 3). Each pixel in the images in **b** is 8µm by 8µm.